Measurements of $W^{\pm}$ and top-quark pair to Z-boson cross-section ratios at $\sqrt{s} = 13, 8, 7$ TeV with the ATLAS detector

Dissertation

zur Erlangung des Doktorgrades

an der Fakultät für Mathematik, Informatik und Naturwissenschaften

Fachbereich Physik

der Universität Hamburg

vorgelegt von

Artur Trofymov

aus Horlivka, Ukraine

Hamburg

2017

Gutachter der Dissertation:	PD Dr. Alexander Glazov Prof. Dr. Peter Schleper
Zusammensetzung der Prüfungskommission:	PD Dr. Alexander Glazov Prof. Dr. Peter Schleper Prof. Dr. Sven-Olaf Moch Dr. Kerstin Tackmann Prof. Dr. Dieter Horns
Vorsitzender des Prüfungsausschusses:	Prof. Dr. Sven-Olaf Moch
Datum der Disputation:	
Vorsitzender Fach-Promotionsausschusses PHYSIK:	Prof. Dr. Wolfgang Hansen
Leiter des Fachbereichs PHYSIK:	Prof. Dr. Michael Potthoff
Dekan des MIN-Fakultät:	Prof. Dr. Heinrich Graener

Abstract

Measurements of the $Z \to \ell^+\ell^-$ production cross sections, where $\ell^\pm = e^\pm, \mu^\pm$, in proton-proton collisions at $\sqrt{s} = 13$ TeV are presented using two sets of data recorded by the ATLAS experiment at the Large Hadron Collider. The data sets correspond to a total integrated luminosity of 81 pb^{-1} and 3.2 fb^{-1} collected in 2015 using the 50 ns and 25 ns bunch spacing configurations, respectively. The cross section obtained with 50 ns configuration is used for $W^\pm$ to Z cross-section ratio measurement. The W^+ to W^- boson production cross-section ratio is also measured. The ratios of measured fiducial cross sections for electron and muon decay channels of the $W^\pm$ and Z boson are evaluated and compared to the Standard Model expectations of the lepton universality.

Ratio of top-quark pair to Z-boson production cross section is measured at $\sqrt{s} = 13$ TeV using 25 ns bunch spacing data. Similar ratios are obtained at $\sqrt{s} = 8$ TeV and 7 TeV using the published ATLAS results corrected to a common phase space. Single ratios, at a given $\sqrt{s}$ for the two processes and at different $\sqrt{s}$ for each process, as well as double ratios of the two processes at different $\sqrt{s}$, are evaluated. The results are compared to calculations performed at next-to-next-to-leading-order accuracy using recent sets of parton distribution functions. The data used for $t\bar{t}$ to Z-boson cross section ratios demonstrate significant power to constrain the gluon distribution function for the Bjorken-x values near 0.1 and the light-quark sea for $x < 0.02$.

Zusammenfassung

Messungen der $Z \to \ell^+\ell^-$ Wirkungsquerschnitte, wobei $\ell^\pm = e^\pm, \mu^\pm$, werden dargestellt. Genutzt werden Proton-Proton-Kollisionen bei $\sqrt{s} = 13$ TeV, aufgezeichnet mit dem ATLAS-Experiment am Large Hadron Collider. Die Datensätze entsprechen einer integrierten Luminosität von 81 pb^{-1} bzw. 3.2 fb^{-1}, gesammelt in 2015 mit 25 ns bzw. 50 ns Abstand zwischen den Protonbündeln. Der Datensatz basierend auf 50 ns Abstand wird für eine Messung des Wirkungsquerschnittverältnisses von $W^\pm$ zu Z genutzt. Das Verhältnis von W^+- zu W^--Produktionswirkungsquerschnitt wird ebenfalls gemessen. Innerhalb der Akzeptanz des Detektors wird das Verhältnis der Wirkungsquerschnitte für Elektron- und Myonzerfälle bestimmt und mit der Vorhersage des Standardmodells zur Lepton-Universalität verglichen.

Das Verhältnis der Wirkungsquerschnitte zwischen Paarproduktion von Top-Quarks und Z-Bosonen wird bei $\sqrt{s} = 13$ TeV gemessen, dazu wird der 25 ns-Datensatz genutzt. Basierend auf publizierten Ergebnissen von ATLAS werden analoge Verhältnisse für $\sqrt{s} = 8$ TeV und $\sqrt{s} = 7$ TeV im gleichen Bereich des Phasenraums bestimmt. Einzelne Verhältnisse, bei einer bestimmten Schwerpunktsenergie für die zwei Prozesse oder bei verschiedener Schwerpunktsenergie für den gleichen Prozess, werden ermittelt. Zusätzlich werden kombinierte Verhältnisse der beiden Prozesse bei verschiedener Schwerpunktsenergie bestimmt. Die Ergebnisse werden mit Next-To-Next-To-Leading-Order-Rechnungen basierend auf aktuellen Partonverteilungsfunktionen verglichen. Der Datensatz, der für die Bestimmung des Wirkungsquerschnittverältnisses von $t\bar{t}$ zu Z-Bosonen genutzt wird, kann dazu verwendet werden, um die Gluonverteilungsfunktion für Bjorken-x um 0.1 und die Seequarkverteilung für leichte Quarks bei $x < 0.02$ genauer zu ermitteln.

Contents

Introduction

Particle physics is the study of the fundamental constituents of matter and their interactions. The beginning of this study in a recognizably modern sense takes place in 1897 with the discovery of the electron by J.J. Thompson. The next discovery of elementary particle was almost entirely theoretical. In 1905 A. Einstein argued in his photoelectric theory that under certain circumstances light behaves not as continuous waves but individual particles. He introduced the concept of "light quanta" which later was substituted with the term "photon". The developments during the period 1911-1913, among which the Geiger-Marsden experiment, its interpretation by Rutherford, and Bohr's atomic model, provided a big step in understanding of atom structure. The discovery of neutron in 1932 by J. Chadwick complemented the picture of what atoms are made of.

During the first half of the 20th century a large number of elementary particles were discovered. Systematic follow-up of these discoveries lead to the development of specialized accelerators. Since early 1950s these machines, operating at ever-higher energies, provide the main data in the experimental particle physics. Among the discoveries during the early years of accelerator physics are large number of resonances and the regularities of weak decays. These observations were incorporated into semi-phenomenological quark model of hadrons as well as theory of weak interactions. To explain the experimental observations and provide theoretical predictions the Standard Model (SM) of particle physics was developed in the mid-1970s. In 1983 the W and Z bosons, predicted by the SM, were discovered. The most massive elementary particle predicted by the SM, top quark, was discovered in 1995.

The SM classifies all observed elementary particles and describes interaction between them via electromagnetic, weak and strong forces. The electromagnetic and weak interaction are unified and described with electroweak theory, while the quantum chromodynamics describes the strong interaction. In order to test the SM predictions as well as search for possible signatures of theories beyond the SM, the Large Hadron Collider (LHC) was built at the European Organisation for Nuclear Research, CERN. It first started up on 10 September 2008, and remains the latest addition to CERNs accelerator complex. In 2012 two collaborations, ATLAS and CMS, discovered the Higgs boson in proton-proton collisions at center-of-mass energy ($\sqrt{s}$) of 7 TeV and 8 TeV at the LHC. The Higgs boson is the peace of the SM which is predicted by the theory to explain how the fundamental particles acquire mass. Currently the LHC operates at $\sqrt{s} = 13$ TeV aiming at a peak instantaneous luminosity of $\mathcal{L} = 10^{34}$ cm^{-2} s^{-1} for proton operation.

Measurements of Z-boson production at hadron colliders provide a benchmark for the understanding of quantum chromodynamic and electroweak processes. These measurements at $\sqrt{s} = 13$ TeV offer a unique opportunity to test models of parton dynamics at the LHC. Further tests may be performed by examining the $\sqrt{s}$ dependence of the cross sections. Measurements of top-quark-pair and Z-boson production at various $\sqrt{s}$ values sample different Bjorken-x regions, with higher energies sampling smaller average x. This dependence leads to a strong increase of the gluon-fusion-dominated top-pair production cross section with $\sqrt{s}$ while the increase of the quark-antiquark dominated Z-boson production cross section is more moderate.

The luminosity uncertainties as well as some of the experimental uncertainties can cancel when ratios of cross sections are evaluated. Given that the top-quark-pair and Z-boson production dynamics are driven to a large extent by different parton distribution functions (PDF), the ratio of these cross sections at a given centre-of-mass energy has a significant sensitivity to the gluon-to-quark PDF ratio. Double ratios of top-pair to Z-boson cross sections, i.e. the ratio of the ratio of the two processes at two energies, provide sensitive tests of the SM predictions which do not depend significantly on the determination of the luminosity.

This thesis is organised in the following way. Chapter 1 gives a brief overview of the theoretical background essential for the experimental studies described in this work. Theory predictions for the Z and $W^{\pm}$ boson as well as top-pair production cross sections and their ratios at different $\sqrt{s}$ are given in Chapter 2. The experimental apparatus representation, namely the LHC collider and the ATLAS detector with its supplementary detectors, is provided in Chapter 3. Chapter 4 contains information on the data and Monte Carlo samples used for the given measurements. The definition of the Z boson production cross section as well as methodology of signal event reconstruction using selection criteria and estimation of background expectations are given in Chapter 5. Methods for definition of efficiency scale factors and their uncertainties are provided in Chapter 6. Systematic uncertainties for Z-boson cross-section measurements are discussed in Chapter 7. The kinematic distributions of selected leptons and Z-boson properties as well as numbers for background-subtracted events are shown in Chapter 8. Chapter 9 provides the correlation models of systematic uncertainties for the Z, $W^{\pm}$ and $t\bar{t}$ measurements at different $\sqrt{s}$. The correlation coefficients among different measurements and method of cross-sections combination are also given in this chapter. Z and $W^{\pm}$ boson as well as $t\bar{t}$ production cross sections are presented in Chapter 10. This chapter also contains the evaluated cross-section single and double ratios compared to theoretical predictions. The ability of these data to further constrain the PDF distributions is discussed. Chapter 11 concludes the thesis.

Chapter 1

Theoretical introduction

1.1 The Standard Model of particle physics

A theory to describe the fundamental building blocks of matter and their interaction was formulated in 1970s and called the Standard Model (SM). According to this model, all mater is build of twelve fundamental particles of spin $\frac{1}{2}$: six quarks and six leptons. Particles with half-integer spin obey Fermi-Dirac statistics and were named as $fermions$ by Paul Dirac. Fundamental particles interact via electromagnetic, weak and strong forces. Adding the gravity to the SM as a fourth known force is currently an unresolved challenge. Nevertheless, it is weaker than electromagnetic force by ~ 40 orders of magnitude and therefore can be neglected in the SM calculations. The interaction between quarks and leptons is mediated by the fundamental gauge particles of spin 1. Integer-spin particles obey Bose-Einstein statistics and obtained name *bosons* from Paul Dirac. There is one such boson for the electromagnetic interaction, the massless photon (γ), which couples to the electric charge but is itself uncharged. The weak interactions happen by the exchange of the massive positively and negatively charged $W^{\pm}$ and the neutral Z^0 bosons which couple to the 3-component of the weak isospin. The strong interaction is mediated by eight massless electrically neutral gluons (g). Gluons themselves carry the colour charge (labelled red, green, blue and the corresponding anti-colours), which allows them to interact with each other. The self-interaction can explain what is commonly known as confinement [1] which describes the fact that color-charged objects can not be observed individually but only in color-neutral combinations. All three interactions are summarized in Table 1.1. In gauge theories all particles were put massless to make the theory renormalizable. However, mass terms can be obtained from spontaneous symmetry breaking, generated by the Higgs-boson field [2]. This modifies the gauge-boson sector, generates masses, and also mixes flavours.

The fermions in the SM are classified according to the way they interact or equivalently, by the charges they carry. There are six leptons: electron (e), electron neutrino (ν_e), muon

Interaction	Gauge boson	Mass (GeV)	Charge
Electromagnetic	γ	0	Electrical
Weak	$W^{\pm}$	80.4	Weak isospin
	Z	91.2	
Strong	g	0	Colours: $\mathrm{r, g, b, \bar{r}, \bar{g}, \bar{b}}$

Table 1.1: Fundamental forces and corresponding mediators with charge types described by the Standard Model.

(μ), muon neutrino (ν_μ), tau (τ), tau neutrino (ν_τ) which do not carry colour charge. Leptons are grouped into three generations (or families), each generation consisting of one (negatively) charged lepton and a neutrino. A member of each following generation has grater mass with respect to the corresponding particle in the previous generation (with the possible exception of the neutrinos). The three neutrinos do not carry electric charge, so their motion is directly influenced only by the weak force. In view of carrying an electric charge, the rest three leptons interact electromagnetically. Each lepton has antiparticle which have quantum numbers of an opposite sign. The electron, muon and tau are massive leptons while neutrinos are treated as massless in the Standard Model. However, the observation of neutrino oscillations [3–5] implies that they have non-zero mass. The current experimental bound on the neutrino mass is $m_\nu < 2$ eV [6].

There are six quarks: up (u), down (d), charm (c), strange (s), top (t), bottom (b) which carry color charge, and hence, interact via the strong interaction. Since quarks also carry electric charge and weak isospin, they interact with other fermions both electromagnetically and via the weak interaction. There exists an anti-quark to each quark which carries anti-colour. The color confinement phenomenon results in the fact that quarks do not exist as free particles in nature and are strongly bound to one another, forming color-neutral composite particles (*hadrons*). The hadrons, which consist of one quark and one anti-quark, are referred to as *mesons*, and those formed of three quarks - *baryons*. Quarks are also grouped into three generations composing one up-type (electric charge of $2/3|e|$) and one down-type (electric charge of $1/3|e|$) quark. Like in the case of leptons, the quark masses increase with the generations.

The generations of leptons and quarks are paired together. Particles of different generations differ by their flavour quantum number and mass, but their interactions are identical. The mass hierarchy in the generations causes particles of higher generations to decay via the weak interaction to the first generation particles. The fundamental fermions grouped into generations with some of the quantum numbers are listed in Table 1.2.

The fundamental interactions in the SM are described with the gauge theories, where the underlying principle is that the corresponding Lagrangian has to be invariant under certain Lie groups of local transformations. The term *gauge* refers to any specific math-

	Generations			I	I_3	$Q[e]$	Y
	I	II	III				
Leptons	$\begin{pmatrix} \nu_e \\ e \end{pmatrix}_L$	$\begin{pmatrix} \nu_\mu \\ \mu \end{pmatrix}_L$	$\begin{pmatrix} \nu_\tau \\ \tau \end{pmatrix}_L$	$\frac{1}{2}$	$+\frac{1}{2}$ $-\frac{1}{2}$	0 -1	-1
	e_R	μ_R	τ_R	0	0	-1	-2
Quarks	$\begin{pmatrix} u \\ d' \end{pmatrix}_L$	$\begin{pmatrix} c \\ s' \end{pmatrix}_L$	$\begin{pmatrix} t \\ b' \end{pmatrix}_L$	$\frac{1}{2}$	$+\frac{1}{2}$ $-\frac{1}{2}$	$+\frac{2}{3}$ $-\frac{1}{3}$	$\frac{1}{3}$
	u_R	c_R	t_R	0	0	$+\frac{2}{3}$	$\frac{4}{3}$
	d_R	s_R	b_R			$-\frac{1}{3}$	$-\frac{2}{3}$

Table 1.2: The Standard Model fermion generations and some of their quantum numbers: weak isospin (I), its third component (I_3), electric charge (Q), weak hypercharge (Y).

ematical formalism to regulate redundant degrees of freedom in the Lagrangian. Each group generator introduces a corresponding gauge field. The gauge fields included into the Lagrangian provide its invariance under local group transformations. This can be illustrated using the quantum field theory of electromagnetism. The Dirac equation for a free fermion with mass m and electric charge q

$$(i\gamma^\mu \partial_\mu - m)\psi(x) = 0 \tag{1.1}$$

can be obtained using the Lagrangian density

$$\mathscr{L} = i\bar{\psi}(x)\gamma^\mu \partial_\mu \psi(x) - m\bar{\psi}(x)\psi(x), \tag{1.2}$$

and the Euler - Lagrange equation

$$\frac{\partial}{\partial x_\mu} \frac{\partial \mathscr{L}}{\partial(\partial\bar{\psi}(x)/\partial x_\mu)} - \frac{\partial \mathscr{L}}{\partial \bar{\psi}(x)} = 0. \tag{1.3}$$

Performing a local gauge transformation of the wave function $\psi(x) \to \psi'(x)$

$$\psi'(x) = e^{i\alpha(x)q}\psi(x), \tag{1.4}$$

where $\alpha(x)$ is a phase of rotations in the Minkowski space leads to

$$\mathscr{L}' = \mathscr{L} - q\bar{\psi}(x)\gamma^\mu \partial_\mu \alpha(x)\psi(x). \tag{1.5}$$

Therefore the Lagrangian given in Equation 1.2 is not invariant under given local gauge transformation. To establish the invariance a vector field A_μ, which transforms as $A'_\mu = A_\mu - \partial_\mu \alpha(x)$ under the gauge transformation of the fermion wave function, should be introduced. The interaction of vector field A_μ with a fermion can be defined using the Lagrangian density

$$\mathscr{L}_{int} = -q\bar{\psi}(x)\gamma^\mu A_\mu \psi(x). \tag{1.6}$$

Adding the interaction with the vector field A_μ to the free-fermion Lagrangian makes it invariant under the local gauge transformation (given with Equation 1.4)

$$\mathscr{L} + \mathscr{L}_{int} = \mathscr{L}' + \mathscr{L}'_{int}. \tag{1.7}$$

The mass term $m_\gamma A_\mu A^\mu$ for the given A_μ field is not invariant under the local gauge transformation therefore it can not be introduced into the $\mathscr{L} + \mathscr{L}_{int}$. The transformation given with Equation 1.4 corresponds to the representation of $U(1)$ group with one generator. The final Lagrangian density for fermion ψ and vector field A_μ with included kinetic energy $F_{\mu\nu}F^{\mu\nu}$ (where $F_{\mu\nu} = \partial_\mu A_\nu - \partial_\nu A_\mu$) which ensures the Lagrangian invariance can be written in a form

$$\mathscr{L} = i\bar{\psi}(x)\gamma^\mu \partial_\mu \psi(x) - m\bar{\psi}(x)\psi(x) - q\bar{\psi}(x)\gamma^\mu A_\mu \psi(x) - \frac{1}{4}F_{\mu\nu}F^{\mu\nu}. \tag{1.8}$$

Quantization of the fields ψ and A_μ leads to a theory, called Quantum Electrodynamics (QED). It shows that $U(1)$ symmetry of the Lagrangian in Equation 1.8 leads to the charge conservation. The introduced massless vector field is the electromagnetic field. The QED describes the interaction of charged fermions via the exchange of photons as quanta of electromagnetic field. Given example shows that photon appears as a compensating field which is introduced to obtain theory of a free fermion, invariant under the $U(1)$ local gauge transformations. Gauge transformations provide a principle of constructing physical theories far beyond the phenomenological fields to describe a particular interaction.

Generalising given formalism, the Standard Model is described by a $SU(3)_c \otimes SU(2)_L \otimes U(1)_Y$ gauge symmetry. The $SU(3)_C$ term denotes the underlying symmetry of the strong interaction. In the group name, the notation C refers to the colour space and 3 refers to the number of possible colour states of the quarks. Due to the number of group generators there is an octet of eight gauge bosons (gluons). Since the $SU(3)$ of the strong interaction is an exact symmetry, the gluons are massless. The $SU(3)$ color symmetry forces all hadrons to be color-neutral (white). The $SU(2)_L \otimes U(1)_Y$ term incorporates the gauge symmetry of the unified electromagnetic and weak interactions and is called electroweak interaction. The $SU(2)_L$ is a left-handed group utilized to account for parity violation in the weak interaction and $U(1)_Y$ is a weak hypercharge group. Both of these are chiral groups in contrast to strong interaction group. The $SU(2)_L \otimes U(1)_Y$ local gauge symmetry is spontaneously broken to $U(1)_{EM}$, therefore the gauge $W^\pm$ - and Z - bosons are massive.

In the Standard Model the generation of the mass of the gauge bosons as well as leptons (with an exception of neutrinos) and quarks is described by the Higgs mechanism.

1.2 Electroweak Interaction and Symmetry Breaking

The experimental observations on the particle decay have to be incorporated during the building of weak interaction theory. For a long time only charge current interactions were known, where the charge of interacting leptons or quarks changes by ± 1. Therefore two of three mediators of weak interaction should have electric charges of $+1$ and -1 (W^+ and W^- bosons). The interaction can be described with combination of vector (V) and axial vector (A) operators. The contributions of both components into interaction can be introduced by coefficients c_V and c_A accordingly. To conserve parity, the interaction should equally couple to left- and right-handed particles. In such case the interaction should be either purely vectorial or axial-vectorial ($c_V = 0$ or $c_A = 0$). Therefore the parity is maximally violated if $c_V = c_A$.

Fermion's spinor u can be decomposed into left- and right-handed components. Experimentally it was found that only left-handed fermions participate in the charged currents which leads to the maximal violation of parity ($c_V = 1$ and $c_A = 1$) [7, 8]. Furthermore, the same coupling strengths were found for all the fermions. The different situation is observed in case of neutral current where the interaction is mediated by the Z boson and participating fermions do not change charges. The coupling strength depends on the charge of the fermions for the neutral currents. To explain these phenomena within unified electroweak (EW) theory a new quantum number called weak isospin (I) with appropriate formalism was introduced. The doublets are formed of left-handed fermions with weak isospin $I = 1/2$ and it's third component ($I_3 = \pm 1/2$). Since the right-handed fermions do not participate in the charged current interactions, they stay as singlets with zero weak isospin $I = I_3 = 0$.

The transition between charged left-handed leptons and neutrinos or up- and down-type quarks happens by emission of $W\pm$ boson. To explain transition between the generations, the electroweak eigenstates of down-type quarks are interpreted as a mixture of quark-mass eigenstates (d', s', b') and quark mixing matrix is introduced:

$$\begin{pmatrix} d' \\ s' \\ b' \end{pmatrix} = \begin{pmatrix} V_{ud} & V_{us} & V_{ub} \\ V_{cd} & V_{cs} & V_{cb} \\ V_{td} & V_{ts} & V_{tb} \end{pmatrix} \begin{pmatrix} d \\ s \\ b \end{pmatrix} . \tag{1.9}$$

Quark mixing matrix (also called Cabibbo-Kobayashi-Maskawa matrix) is a unitary matrix which contains information on the strength of flavour-changing weak decays. It specifies the mismatch of quantum states of quarks when they propagate freely and when they take part in the weak interactions. The diagonal elements describe the probability of transition within one generation and found to be close to unity, while transitions among families are strongly suppressed.

Due to the isospin formalism there should be a boson with $I_3 = 0$ and the same coupling to fermions which mediates transition that does not change the fermion flavour (saves I_3). $W^\pm$ and Z bosons satisfy only partially given requirements. Introduction of the fourth field which is a weak isospin singlet solves this problem. Experimentally, two bosons which do not change I_3 of the interacting fermions are observed: Z-boson and photon. One of the main ideas of electroweak unification is to express the observed bosons as a mixture of two bosons with $I_3 = 0$.

The relation between weak isospin and electric charge are given by Gell-Mann-Nishijima formula

$$Y = 2(Q - I_3), \tag{1.10}$$

which was originally based on empirical data. Value Y in the formula is the weak hypercharge. As indicated previously, the symmetry group of electroweak theory is $SU(2)_L \otimes U(1)_Y$ where weak hypercharge is a generator of $U(1)$ component. Local gauge invariance is provided with introduction of triplet vector field W^i_μ ($i = 1, 2, 3$) for $SU(2)_L$ component and single vector field B_μ for $U(1)_Y$. The physical fields of the weak bosons W^+ and W^- are identified as a superposition of W^1_μ and W^2_μ vector fields:

$$W^\pm_\mu = \frac{1}{\sqrt{2}}(W^1_\mu \pm iW^2_\mu) \tag{1.11}$$

The remaining two fields W^3_μ and B_μ couple to neutrinos and can not represent the electromagnetic field. Instead, the electromagnetic field is defined as a linear combination of the two and is orthogonal to the Z_μ term which is responsible for coupling to neutrinos:

$$\begin{pmatrix} A_\mu \\ Z_\mu \end{pmatrix} = \begin{pmatrix} cos\ \theta_W & sin\ \theta_W \\ -sin\ \theta_W & cos\ \theta_W \end{pmatrix} \begin{pmatrix} B_\mu \\ W^3_\mu \end{pmatrix}, \tag{1.12}$$

where θ_W denotes the weak mixing angle (Weinberg angle), which is related to the coupling constants q and g' for left- and right- handed fermions respectively:

$$cos\ \theta_W = \frac{g}{\sqrt{g^2 + g'^2}} \tag{1.13}$$

The mixing angle is a free parameter of the Standard Model and is measured experimentally. The coupling of all fermions to the $W^\pm$ boson (g_W) and fermion-dependent coupling to the Z boson (g_Z) are defined by:

$$g_W = gI_3 \tag{1.14}$$

$$g_Z(f) = \frac{g}{cos\ \theta_W}(I_3 - Qsin^2\ \theta_W). \tag{1.15}$$

The bosons in Equations 1.11 and 1.19 are massless since they are defined as a linear combination of massless fields. The Lagrangian for the electroweak theory before introducing boson masses can be written as:

$$\mathscr{L} = f_L^{\dagger}\gamma^{\mu}(i\partial_{\mu} + \frac{g}{2}\tau_i W_{\mu}^i + \frac{g'}{2}YB_{\mu})f_L + f_R^{\dagger}\gamma^{\mu}(i\partial_{\mu} + \frac{g'}{2}YB_{\mu})f_R - \frac{1}{4}W_{\mu\nu}^i W_i^{\mu\nu} - \frac{1}{4}B_{\mu\nu}B^{\mu\nu}, \tag{1.16}$$

where f_L and f_R are left- and right-handed fermions, τ_i are the Pauli-matrices, and the field strength tensors for the weak isospin and weak hypercharge fields are defined by:

$$W_{\mu\nu}^i = \partial_{\mu}W_{\nu}^i - \partial_{\nu}W_{\mu}^i - g\epsilon_{ijk}W_{\mu}^j W_{\nu}^k \tag{1.17}$$

$$B_{\mu\nu} = \partial_{\mu}B_{\nu} - \partial_{\nu}B_{\mu}. \tag{1.18}$$

The mass terms can be introduced by the adding two complex scalar fields ϕ^+ and ϕ^0, which form an isospin doublet ($I = \frac{1}{2}$) with hypercharge $Y = 1$:

$$\Phi = \begin{pmatrix} \phi^+ \\ \phi^0 \end{pmatrix} \tag{1.19}$$

The Lagrangian density of the Higgs doublet is given as:

$$\mathscr{L}_H = (\partial_{\mu}\Phi)^{\dagger}(\partial^{\mu}\Phi) - V(\Phi) = (\partial_{\mu}\Phi)^{\dagger}(\partial^{\mu}\Phi) - m^2\Phi^{\dagger}\Phi - \lambda(\Phi^{\dagger}\Phi)^2. \tag{1.20}$$

$\mathscr{L}_H$ is invariant under the global gauge transformation ($\Phi \to e^{i\Lambda}\Phi,\ \Lambda -$ const). The λ term is a self-interaction and m^2 is a parameter, and not a mass term. The ground state is obtained by minimizing the potential V:

$$\frac{\partial V}{\partial \Phi} = m^2\Phi^{\dagger} + 2\lambda\Phi^{\dagger}(\Phi^{\dagger}\Phi). \tag{1.21}$$

Therefore when $m^2 > 0$, the minimum occurs $\Phi^{\dagger} = \Phi = 0$. If $m^2 < 0$, however, there is a local maximum at $\Phi = 0$ and a minimum at vacuum expectation value of Φ:

$$|<0|\Phi|0>|^2 = \frac{1}{2}\begin{pmatrix} 0 \\ \frac{-m^2}{\lambda} \end{pmatrix} = \frac{1}{2}\begin{pmatrix} 0 \\ v^2 \end{pmatrix} \tag{1.22}$$

The minima of V lie along the circle $|<0|\Phi|0>|^2 = \frac{1}{2}v^2$, which form a set of degenerate vacua related to each other by rotation. The physical fields, which are excitations above the vacuum, are realized by performing perturbation about $|<0|\Phi|0>| = \frac{1}{\sqrt{2}}v$, not about $|<0|\Phi|0>| = 0$.

Choosing a particular vacuum state v and considering a small excitation:

$$\Phi = \frac{1}{\sqrt{2}}\begin{pmatrix} 0 \\ v + \eta(x) \end{pmatrix} \tag{1.23}$$

the electroweak Lagrangian can be written as:

$$\mathscr{L} = (\frac{1}{2}\partial_\mu\eta\partial^\mu\eta - \mu^2\eta^2) - \frac{1}{4}W^i_{\mu\nu}W^{\mu\nu}_i - \frac{1}{4}B_{\mu\nu}B^{\mu\nu} + \frac{1}{2}\frac{g^2v^2}{4}(|W^+_\mu|^2 + |W^-_\mu|^2) + \frac{1}{2}\frac{v^2}{4}|g'B_\mu - gW^3_\mu|^2. \tag{1.24}$$

η is a Higgs boson with mass $m_\eta = \sqrt{2}\mu$. The electromagnetic four-potential does not contain a mass term, therefore $m_\gamma = 0$. Mass of the $W^\pm$ boson is given by:

$$m_{W^\pm} = \frac{1}{2}gv, \tag{1.25}$$

and using relation $g'B_\mu - gW^3_\mu = -\sqrt{g+g'}Z_\mu$, the mass of Z boson:

$$m_Z = \frac{1}{2}v\sqrt{g^2 + g'^2}. \tag{1.26}$$

The scalar Higgs field couples fermion states of opposite helicity via Yukawa coupling generating the fermion masses.

$$m_f = \frac{1}{2}g_f v \tag{1.27}$$

with Yukawa coupling constant g_f.

Historically, the electroweak theory was built by S. Weinberg and A. Salam [9,10] based on earlier work of S.L. Glashow [11] and applying Higgs' ideas of spontaneous symmetry braking [2] to an $SU(2) \otimes U(1)$ gauge theory. Later it was shown by 't Hooft that given theory is renormalizable [12, 13].

1.3 Strong Interaction

The quantum chromodynamics (QCD) is the theory of the strong interaction between quarks and gluons. In QCD the strong force at short distances is assumed to have a similar space-time structure to QED. The quark spinor fields ψ_i ($i = 1, 2, 3$ - three colour indices) transform as triplets under $SU(3)$ in the colour space. The Lagrangian density of QCD can be formulated as

$$\mathscr{L}_{QCD} = \sum_f \bar{\psi}^i_f(i\gamma_\mu D^\mu - m_f)_{ij}\psi^j_f - \frac{1}{4}F^a_{\mu\nu}F^{\mu\nu}_a \tag{1.28}$$

where $F^a_{\mu\nu} = \partial^\mu_a - \partial^\nu_a + g_s f^{abc}A^\mu_b A^\nu_c$ is the gluon field strength tensor. The strong coupling constant $(\alpha_s)_0$ is related to the g_s coupling as:

$$(\alpha_s)_0 = \frac{g_s^2}{4\pi}. \tag{1.29}$$

The same coupling constant g_s couples the gluon fields to themselves (last term in $F_a^{\mu\nu}$ definition) and the gluon to the quark fields through the covariant derivative (D_{ij}^{μ}). This leads to special properties of strong interaction. The strength of interactions between quarks and gluons reduces as the energy scale of those interactions increases (and distance decreases). This property is called *asymptotic freedom* and makes quarks interact weakly at high energies, allowing perturbative calculations. At low energies the interaction becomes strong, leading to the confinement of quarks and gluons within composite hadrons. The strong coupling constant dependence on the energy in leading order, parametrized as momentum transfer Q, can be defined as

$$\alpha_s(Q^2) = \frac{\alpha(\mu^2)}{1 + \alpha(\mu^2) b_0 \ln\left(\frac{Q^2}{\mu^2}\right)} \tag{1.30}$$

at some scale μ^2, for which α_s is assumed to be known, with n_f denoting the number of "active" quark flavours (those with masses smaller than the scale) and coefficient $b_0 = (33 - 2n_f)/12\pi$ [14]. The fermion loops contribute $-1/6\pi$ for each quark flavour to b_0 and the gluon self-coupling loops give a positive contribution of $11/4\pi$. b_0 for QCD is positive, $\alpha_s(Q^2)$ decreases as Q^2 increases and formally $\alpha_s(Q^2) \to 0$ as $Q^2 \to \infty$ which corresponds to asymptotic freedom.

Since α_s depends on the energy scale it is called running coupling constant. The running of α_s with the scale Q^2 of the process is an effect of renormalization that is used to treat divergences arising in calculations. The reference value of strong coupling constant $\alpha_s(m_Z^2) = 0.1181(11)$ [6] is assumed at scale of Z-boson mass.

1.4 Proton-proton collisions

Since protons are composed of quarks and gluons (partons), the proton-proton (pp) collisions at high energies occur through the interaction between their constituents. Such interaction contains two processes: *hard scattering* of two partons of appropriate protons and interaction of proton remnants.

Partons which take part in the hard scattering can emit QCD radiation with gluon splitting process ($g \to q\bar{q},\ g \to gg$) or gluon radiation by quarks ($q \to qg,\ \bar{q} \to \bar{q}g$). If radiation happens before the parton-parton interaction, the process is called initial state radiation (ISR), otherwise it is a final state radiation (FSR). Gluons radiated after the interaction can trigger subsequent radiation, which leads to the "showers". The constituents of the shower recombine into the colour-neutral hadronic final states. This process is called *hadronisation*. The formed hadrons finally decay into stable particles. The ensembles of well collimated hadrons form *jets*.

Interactions of proton remnants, accompanied by production of parton showers and hadronisation process, are followed by decays to the stable particles. Proton-remnants interaction and multi-parton interaction (MPI) are the secondary interactions and collectively called *underlying event*. Secondary interactions are usually much softer than primary hard interaction. The proton-proton collision is graphically shown in Figure 1.1 on example of $t\bar{t}H$ production.

Rates and properties of the hard scattering can be precisely predicted with perturbation theory, while soft interactions are dominated mainly by non-perturbative effects and described by phenomenological models. The ISR can be treated as an underlying event if the hard process is defined at leading order of perturbation calculations. At higher orders, ISR and FSR become parts of radiative corrections to the cross-section calculation.

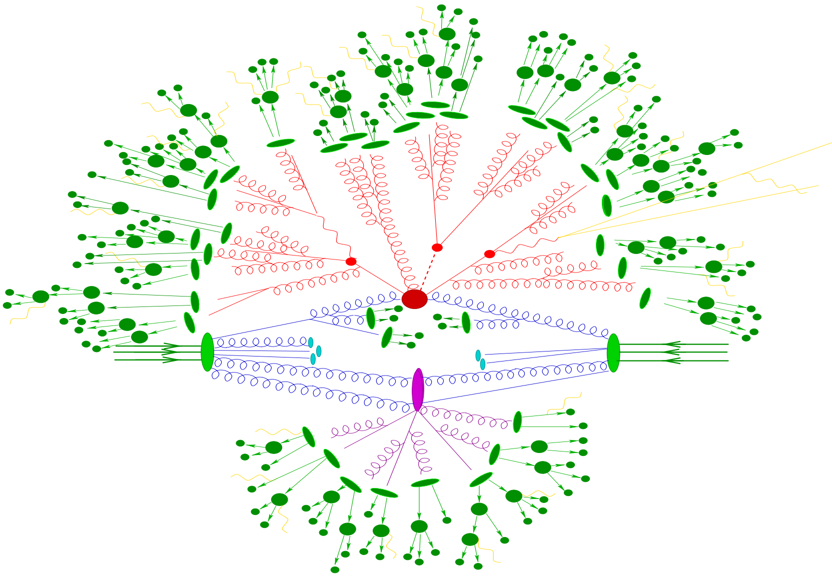

Figure 1.1: Graphical representation of pp collision. Two incoming protons are indicated by big green ellipses with three green lines for quarks. The big red circle in the top hemisphere corresponds to the hard scattering process of two partons. The small red circles denote decays of particles produced in the hard interaction (two top quarks and Higgs-boson in this example). The QCD radiation by products of hard scattering and parton showers is shown by red helices. Light-green ellipses represent colourless hadrons. Dark-green circles symbolize stable decay products of the corresponding hadrons. A secondary interaction between the remnants of the protons is shown in the bottom hemisphere with purple ellipse. A parton shower is pictured with purple helices. Yellow lines demonstrate electromagnetic radiation which occurs at any stage. [17]

1.5 Proton structure

A proton-proton collision at energies where the squared momentum transfer exceeds the rest mass of the proton, can be described in terms of the parton model [14]. Proton in this model is a bound state of two up- and one down-quark. These three quarks are called *valence quarks* and determine the quantum numbers of a proton. The valence quarks are held together by the strong force, i.e. by the exchange of gluons. These gluons can fluctuate into $q\bar{q}$ pairs, which form *quark sea*, or split into further gluons. The collisions of the two protons at a center of mass energy $\sqrt{s}$, defined by the energy of the proton beams, lead to interaction of the partons of the two protons: valence quarks, gluons or sea quarks of different flavour. Since parton carries only a fraction x of the proton longitudinal momentum, a fraction of the center of mass energy s, so called partonic center-of-mass energy, $\hat{s}$, is available in such a partonic interaction. The partonic center-of-mass energy $\sqrt{\hat{s}}$ is related to the proton beam energy as $\hat{s} = x_1 x_2 s$, where x_1 and x_2 are fractions of the proton momentum carried by the partons participating in the interaction, as introduced by Bjorken [15]. For each parton in the proton, its momentum distribution is represented by a parton distribution function (PDF) $f_p(x, Q)$, which can be interpreted as the probability to find a parton p carrying a fraction x of the proton momentum at a given energy scale Q.

The dependence of the PDFs on the scale Q with $Q > Q_0$ (evolution), is predicted in the perturbative QCD (pQCD). An analytic shape for the PDFs is assumed to be valid at some starting value of $Q^2 = Q_0^2$, which should be large enough to ensure that strong coupling is sufficiently small for perturbative calculations to be applicable. To evolve the parton distribution up to a different Q^2 values the DGLAP (Dokshitzer, Gribov, Lipatov, Altarelli and Parisi) [18–20] evolution equations are used. These represent a system of integro-differential equations and describe the dependence of the PDFs as a function of Q:

$$\frac{\partial}{\partial(\ln Q^2)}\begin{pmatrix} g_i(x,Q^2) \\ g(x,Q^2) \end{pmatrix} = \frac{\alpha_s(Q^2)}{2\pi}\sum_j \int_x^1 \frac{d\xi}{\xi}\begin{pmatrix} P_{q_iq_j}(\frac{x}{\xi},\alpha_s(Q^2)) P_{q_ig}(\frac{x}{\xi},\alpha_s(Q^2)) \\ P_{gq_j}(\frac{x}{\xi},\alpha_s(Q^2)) P_{gg}(\frac{x}{\xi},\alpha_s(Q^2)) \end{pmatrix}\begin{pmatrix} q_j(\xi,Q^2) \\ g(\xi,Q^2) \end{pmatrix}. \tag{1.31}$$

Here, g_i , q_j, g denote quarks, antiquark and gluon distributions, ξ corresponds to the momentum fraction of proton which carries a parton. The splitting functions $P_{ab}(\frac{x}{\xi}, \alpha_s(Q^2))$ describe the transition probability of the parton a into a parton b by emitting a quark or gluon. The introduced DGLAP approach is valid in the collinear factorisation [20], where the x-dependence of the PDFs is not predicted. A method of a given dependence definition is discussed in Section 1.5.2.

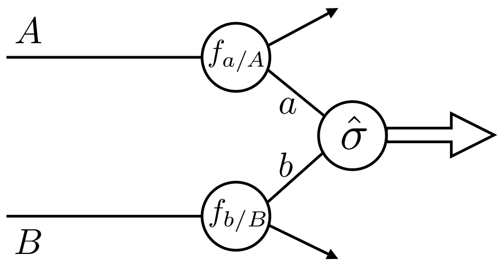

Figure 1.2: Graphical representation of the factorisation theorem for the hard hadron-hadron interaction. Adapted from [14].

1.5.1 Hadronic cross section

The PDFs are universal and independent of hard scattering process, therefore they are subject to the factorisation theorem, which states that the hadronic cross-section can be constructed from a convolution of the calculable cross-section of partonic interaction with the parton distribution functions for the incident hadrons:

$$\sigma_{AB} = \sum_{ab} \int dx_a dx_b f_{a/A}(x_a, \mu_F^2) f_{b/B}(x_b, \mu_F^2) \times [\hat{\sigma}_0 + \alpha_s(\mu_R^2)\hat{\sigma}_1 + ...]_{ab}, \tag{1.32}$$

where the term in square brackets correspond to parton-parton cross section at renormalization scale μ_R, $f_{a(b)/A(B)}$ is the momentum density of parton $a(b)$ in hadron $A(B)$ at a factorisation scale μ_F. In a given definition all large logarithms which appears in the calculation of corrections from gluon emission are factorized into the PDFs via the DGLAP equations while the finite corrections of order α_s^n are included in the parton-parton cross section term. Given approach is known as the *factorisation theorem* [14] and is illustrated in Figure 1.2.

If all orders of perturbation theory are considered in Equation 1.32, the cross section σ_{AB} is invariant under changes in μ_F and μ_R parameters. It happens due to the compensation of the scale dependence of the parton distributions and of the coupling constant. The compensation becomes more exact as more terms are included in perturbation series. For cross section-estimation is necessary to make a choice for both scales (in general μ_F and μ_R can be different). It is reasonable to choose both scales of the order of the typical energies of the hard scattering process to avoid large logarithms appearing in the perturbation series. Usually both scales are set to be equal. In case of cross-section calculation for inclusive Z-boson or $t\bar{t}$ production, the standard choices for scales are $\mu_F = \mu_R = M_{\ell\ell}$ (invariant mass of lepton pair from Z decay) and m_t (top quark mass).

1.5.2 PDF determination

As it was stated earlier, the evolution of PDFs with the change of scale Q is described with the collinear factorization and DGLAP equations, while the evolution in x-dependence can not be predicted using this approach. In practice, given dependence is parametrized by e.g. polynomial form, where the PDF parameters are chosen such that the QCD sum rules [16] hold. Constructing the predicted cross sections using these PDFs, and the DGLAP evolution equations, a fit to the corresponding measured cross sections is performed. In this fit, the χ^2 is minimized considering the uncertainties used in the theory and the measurements, and the initial PDF parameters are determined. The input PDFs at the starting scale Q_0^2 (usually in the range of $1-2$ GeV) are parametrized with analytic form $xf = A_0 x^{A_1}(1-x)^{A_2} P(x, A_3, ...)$, where $P(x, i)$ is a polynomial in x. The PDFs resulting from the fits are usually supplied on x, Q^2 grids which can be used to obtain a value of a PDF at any x and Q^2 point by interpolation.

Most of the information on PDFs are currently obtained from the fits to measured data in fixed target lepton-nucleon scattering experiments and from HERA electron-positron collider at DESY. The accessible regions of the (x, Q^2) kinematic plane for fixed target, HERA and LHC experiments are given in Figure 1.3. It demonstrates that HERA measurements cover regions down to $x \sim 10^{-5}$ at momentum transfer below hundred GeV^2. The LHC measurements provide important new information in addition to the HERA data and extend the kinematic plane for PDF determination to $x \sim 10^{-6}$. Measurements in this region enable to probe the content of the proton when the parton densities might become very large and the probability for more than one partonic interaction per event increases.

There are several PDF-fitting collaborations which regularly provide updates of their QCD analyses adding recent measurements to their fits. The most widely used PDF sets at the LHC are those provided by the ABM [23], CTEQ [24], MSTW [25], NNPDF [26], HERAPDF [27], GJR [28]. The PDFs provided by various collaborations can differ since their fits are not based on the same data sets as well as due to the different fitting parametrization, assumed values for α_s, and the approaches to treat the heavy flavours and their masses in the QCD analysis.

Figure 1.4 shows an overview of the CT14 parton distribution functions, for $Q =$ 2 GeV and 100 GeV obtained from the central fit to the global data. The function $xf(x, Q)$ is plotted versus x where it is assumed that $s(x, Q_0) = \bar{s}(x, Q_0)$. More details on parametrization and data sets used for a given fit results can be found in Ref. [29]. Given PDF distributions demonstrate that valence-quark PDFs dominate at higher x region, while the gluon and sea-quarks prevail at low x-values. The PDFs at $Q = 2$ GeV and 100 GeV indicate that an increase of the momentum transfer leads to increasing probability to find a parton with lower momentum fraction x. This behaviour is due to the probing smaller distances at higher Q, where the products of splitting processes carry smaller momentum fraction x.

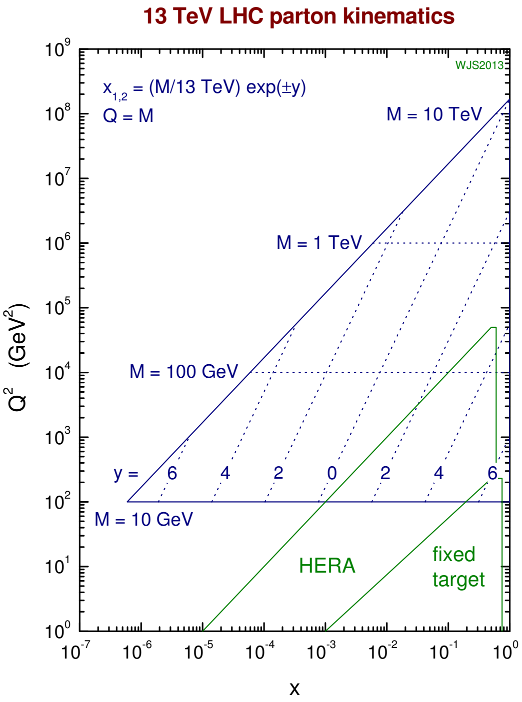

Figure 1.3: Regions in the (x, Q^2) plane covered by different experiments. The blue region represents coverage of the LHC experiments, where blue lines indicate the corresponding values of invariant mass M and rapidity y of particles produced at the center-of-mass energy of 13 TeV. Two green areas represent HERA- and fixed-target-experiments coverage. [22]

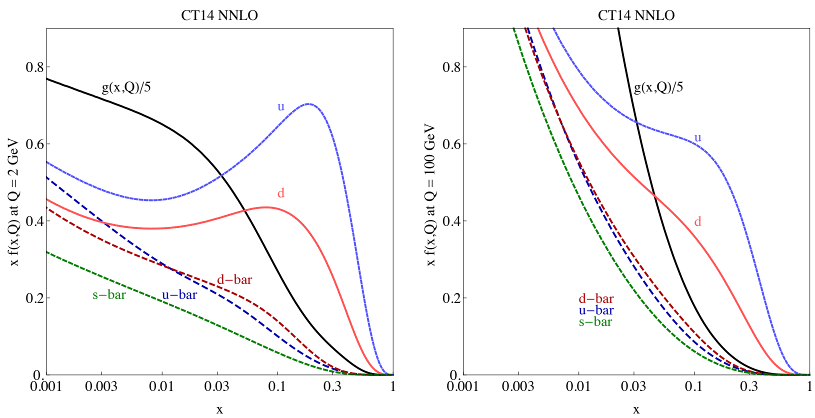

Figure 1.4: The CT14 parton distribution functions at $Q = 2$ GeV (left plot) and $Q = 100$ GeV (right plot) for $u, \bar{u}, d, \bar{d}, s = \bar{s}$, and g. [29]

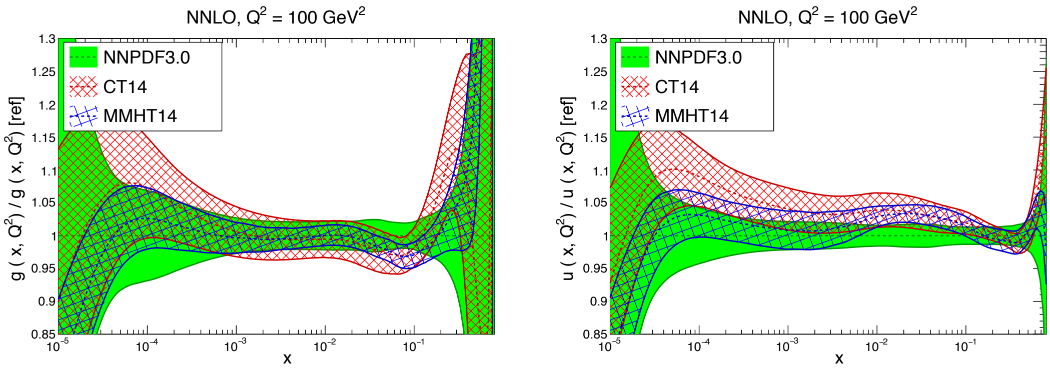

Figure 1.5: Comparison of gluon (left) and up quark (right) PDFs at $Q^2 = 10^2\text{GeV}^2$ between the NNPDF3.0, CT14 and MMHT14 sets, all of them at NNLO, with $\alpha_s(M_Z^2) = 0.118$. Results are shown normalized to the central value of NNPDF3.0. The coloured bands correspond to the PDF uncertainties. [30]

The precision of the obtained PDFs plays a very important role for their applicability. The uncertainty in the knowledge of the PDFs can be a significant or even dominant part of the overall uncertainty of the predictions. Technically, there are three widely used techniques of estimating PDF uncertainties: $Hessian$, $Offset$ and $Monte\ Carlo$ method (see Section 2.5). An example of gluon and up quark PDF distributions with PDF uncertainties provided by NNPDF, CTEQ and MMHT collaborations is shown in Figure 1.5. The comparison between these sets demonstrate good agreement within the uncertainty. The highest discrepancy is observed at small and large values of x (regions with limited kinematic coverage by the experimental data).

1.6 The Drell-Yan process

The Drell-Yan (DY) process [31] represents the production of a lepton pair of large invariant mass $M_{\ell\ell}$ in hadron-hadron collisions by the mechanism of quark-antiquark annihilation. In the basic DY mechanism, a quark and antiquark annihilate to produce a boson, e.g. virtual photon, $q\bar{q} \to \gamma^* \to \ell^+\ell^-$. At high-energy colliders, there is sufficient hadronic center-of-mass energy for the production of on-shell Z and W bosons as well. The leading order diagram of DY process is shown in Figure 1.6.

Referring to Figure 1.6, the four-momenta of the incident partons in the hadron-hadron center-of-mass frame are

$$p_a = \frac{\sqrt{s}}{2}(x_a, 0, 0, x_a), \quad p_b = \frac{\sqrt{s}}{2}(x_b, 0, 0, -x_b), \tag{1.33}$$

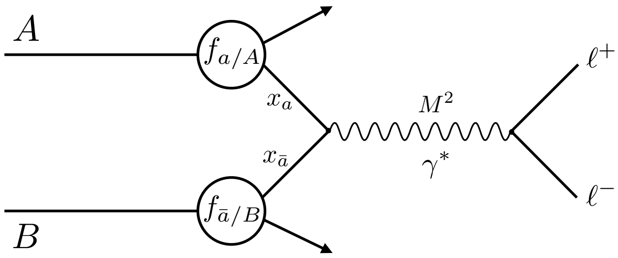

Figure 1.6: Leading order (parton model) diagram for Drell-Yan lepton pair production in hadron-hadron scattering. [14]

where $s = (p_A + p_B)^2$ and parton masses have been ignored. Then

$$M_{\ell\ell} = (p_a + p_b)^2 = x_a x_b s, \quad y = \frac{1}{2}\ln\left(\frac{E + p_z}{E - p_z}\right) = \frac{1}{2}\ln\left(\frac{x_a}{x_b}\right), \tag{1.34}$$

where $E,\ p_z$ are the energy and longitudinal momentum of the lepton pair. The parton momentum fractions x_a and x_b may also be written in terms of y as:

$$x_a = \frac{M_{\ell\ell}}{\sqrt{s}} e^{y}, \quad x_b = \frac{M_{\ell\ell}}{\sqrt{s}} e^{-y}. \tag{1.35}$$

Assuming that the hard scale is equal to $M_{\ell\ell}$, the relationship between the parton (x, Q^2) values and the kinematic variables $M_{\ell\ell}$ and y is illustrated in Figure 1.3, for the LHC collision energy $\sqrt{s} = 13$ TeV. For a given rapidity y there are two (dashed) lines, corresponding to the values of x_a and x_b. For $y = 0$, $x_a = b_b = M_{\ell\ell}/\sqrt{s}$.

For the photon exchange the cross-section for $q\bar{q} \to \ell^+\ell^-$ sub-process ($\hat{s} = x_a x_b s$) is the same as that for $e^+e^- \to q\bar{q}$:

$$\hat{\sigma}(q_a\bar{q}_a \to \ell^+\ell^-) = \frac{Q_a^2}{3}\sigma_0, \quad \sigma_0 = \frac{4\pi\alpha^2}{3\hat{s}}, \tag{1.36}$$

where Q_a is the electric charge of quark q_a.
The sub-process $q\bar{q} \to Z \to \ell^+\ell^-$ cross section can be found in the form:

$$\hat{\sigma}(q_i\bar{q}_i \to Z \to \ell^+\ell^-) = \frac{4\pi^2\alpha^2}{9}\frac{M_Z}{\Gamma_Z}k^2(v_i^2 + a_i^2)(v_\ell^2 + a_\ell^2)\delta(\bar{s} - M_Z^2), \tag{1.37}$$

where $v_i(a_i)$ is the vector (axial vector) coupling of the Z boson to the quarks, $k = \frac{\sqrt{2}G_F M_Z^2}{4\pi\alpha}$. Given formula is obtained using the the narrow resonance approximation, since $\Gamma_Z \ll M_Z$. Using the expression for the branching ratio

$$BR(Z \to \ell^+\ell^-) = \frac{G_F M_Z^3}{6\sqrt{2\pi}\Gamma_Z}(v_\ell^2 + a_\ell^2), \tag{1.38}$$

Equation 1.37 can be written as

$$\hat{\sigma}(q_i\bar{q}_i \to Z \to \ell^+\ell^-) = \hat{\sigma}(q_i\bar{q}_i \to Z)BR(Z \to \ell^+\ell^-), \tag{1.39}$$

where

$$\hat{\sigma}(q_i\bar{q}_i \to Z) = \frac{\pi}{3}\sqrt{2}G_F M_Z^2(v_i^2 + a_i^2)\delta(\hat{s} - M_Z^2). \tag{1.40}$$

The $q_i\bar{q}_j \to W$ sub-process production cross-section in the form of Equation 1.40 can be written replacing the electroweak coupling factor by the appropriate CKM matrix element $|V_{ij}|$ and boson mass:

$$\hat{\sigma}(q_i\bar{q}_j \to W) = \frac{\pi}{3}\sqrt{2}G_F M_W^2|V_{ij}|^2\delta(\hat{s} - M_W^2), \tag{1.41}$$

To calculate the rate for a leptonic final state, Equation 1.41 should be multiplied by the branching ratio

$$BR(W \to \ell\nu_\ell) = \frac{G_F M_W^3}{6\sqrt{2}\pi\Gamma_W}, \tag{1.42}$$

The amplitude for the Z boson decay to lepton pair is proportional to the vertex factor [32]:

$$\mathcal{M}_{Z\ell\ell} \propto -i\frac{g}{\cos\theta_W}\gamma^\mu\frac{1}{2}(v_\ell - a_\ell\gamma^5), \tag{1.43}$$

the vector and axial-vector coupling constants v_ℓ, a_ℓ for charged leptons are $v_\ell = -1$ and $a_\ell = -1+4\sin^2\theta_W$. The vertex factor for Z boson decay is the same for e^+e^-, $\mu^+\mu^-$, $\tau^+\tau^-$ final states. The only difference is in mass of the final state. The amplitude of the W decay into lepton and corresponding neutrino pair is proportional to the vertex factor:

$$\mathcal{M}_{W\ell\nu} \propto -i\frac{g}{\sqrt{2}}\gamma^\mu\frac{1}{2}(1 - \gamma^5). \tag{1.44}$$

This vertex factor is the same for any lepton flavour. Therefore, W decays into $e\nu_e$, $\mu\nu_\mu$, $\tau\nu_\tau$ would have similar vertex factor. This phenomenon of the Standard Model, where the coupling with leptons is the same in all three generation, is known as the lepton universality. It is one of the key assumptions in the Standard Model which means that electrons, muons and tau leptons should be produced equally often in weak decays.

Experimentally, the lepton universality can be tested by measuring the ratio of the number of decays containing one type of lepton flavour, to those containing another type of lepton flavour. Measurement of the ratios benefit from the cancellation of correlated uncertainties in contrast to measuring a simple individual rates.

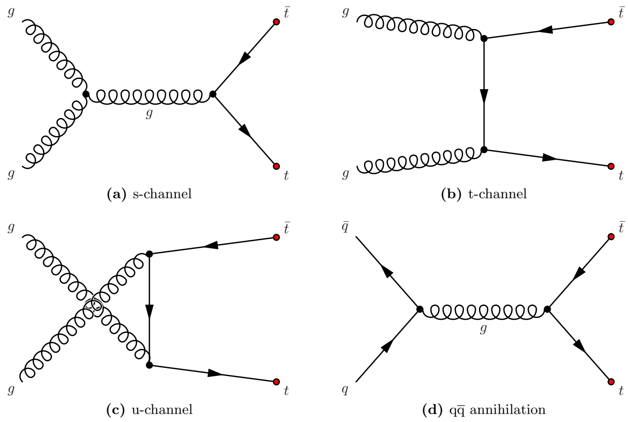

Figure 1.7: Leading order diagrams for $t\bar{t}$ production.

1.7 Top quark pair production

The top quark is the heaviest known fundamental particle ($m_t = 173$ GeV [6]). In proton-proton collisions at the LHC, the production of top-antitop pairs ($t\bar{t}$) via the strong interaction has much higher rate than single top quark production via the electroweak interaction. At leading order, pair of top and antitop quarks can be produced either via quark-antiquark annihilation ($q\bar{q} \to t\bar{t}$) or gluon-gluon fusion ($gg \to t\bar{t}$). The appropriate Feynman diagrams are showed in Figure 1.7. At the LHC top-quark pairs are dominantly produced via the gluon-gluon fusion process.

The large mass of the top quark leads to the large decay width and very short lifetime (5×10^{-25} s) which is about one order of magnitude smaller than the hadronisation time scale. Therefore, top quark does not hadronize, but decays through the weak interaction into down-type quark (most exclusively b quark) and W boson. W boson in turn has two basic types of decay: leptonic ($W \to \ell\bar{\nu}_\ell$, where $\ell = e, \mu, \tau$) and hadronic ($W \to \bar{q}_{up}q_{down}$, where $\bar{q}_{up} = \bar{u}, \bar{c}$, $q_{down} = d, s, b$). Therefore, it can be distinguished three modes of $t\bar{t}$ decay:

- Fully hadronic decay: both W bosons decay haronically. It is the most frequent $t\bar{t}$ event topology. The fully hadronic or multi-jet decay results in six (or more) jets in the final state;

- Semileptonic: one W boson decays hadronically and the other one - leptonically. The final state exhibits four jets, one charged lepton and also missing energy arising from the neutrino which passes the detector without any interaction.

- Leptonic: both W boson decay leptonically. The final state comprises two jets originating from the two b-quarks, two charged leptons and missing energy.

The dileptonic decay channels, one of which was used in this work to calculate the ratio of $t\bar{t}$ over Z-boson production cross sections, have the smallest branching fraction comparing to the semileptonic and full hadronic decay channels. Nevertheless, the smaller cross section is compensated by lower background rates. Moreover, since the charge of the leptons can be detected with much better precision than that of hadronised quarks, it is easier to reconstruct the $t\bar{t}$ system in the dileptonic channel.

Chapter 2

Theory predictions

2.1 DYNNLO and FEWZ

Theoretical computation of the W and Z boson production in hadron collisions through the DY mechanism are realized in few frameworks. DYNNLO [33,34] (and its fast version DYTURBO) and FEWZ (**F**ully **E**xclusive **W** and **Z** **P**roduction) [35] are the programs widely used for such calculations. As mentioned in Section 1.5.1 and reflected with Equation 1.32, the hadron-hadron cross section is defined with parton momentum distributions for the incident hadrons and calculable to some order of pQCD parton-level cross-section. Both DYNNLO 1.5 (as well as DYTURBO) and FEWZ 3.1 provide cross-section calculations up to the next-to-next-to-leading order (NNLO) in the strong coupling constant.

To calculate the NNLO corrections, three types of contributions are considered: two-loop double-virtual contributions, one-loop real-virtual contributions with the emission of an extra parton, and tree-level double-real contributions, with emission of two extra partons. Each contribution separately is divergent, and the calculation has to be organized such that the cancellations of the divergences are achieved when all the contributions are summed up.

The DYNNLO program calculation is based on an extension of the subtraction formalism to NNLO [36]. The computation is organized in two parts. In the first part (virtual), the contribution of the regularized virtual corrections up to two-loop order is computed. In the second part (real), the cross section for the production of the vector boson in association with at least one jet is first evaluated up to NLO (i.e. up to $O(\alpha_s^2)$). At this step the dipole formalism [37] is used. Since the vector boson + jet cross section is divergent when the transverse momentum p_T of the vector boson becomes small, a suitable counterterm must be subtracted to make the result finite as $p_T \to 0$. DYNNLO uses the counterterm introduced in the Ref. [34], and thus it completes the evaluation of the real part. Finally, virtual and real contributions are combined to obtain the full cross section.

The double-virtual and real-virtual loop integrals in FEWZ 3.1 are dealt with by decomposing the Feynman integrals into a basis of so-called master integrals [38]. Divergences due to singularities in double-real contribution are extracted with technique of sector decomposition [39]. This method involves splitting the integrand into multiple terms, called sectors, which correspond to the different singular limits of the process. It allows independently extract each singular limit. Numerical integration of Equation 1.32 within FEWZ 3.1 is performed with a Monte Carlo adaptive integrator using the Vegas routine from the the Cuba 1.7 package [40].

In the FEWZ 3.1, two input schemes, $\alpha_s(m_Z)$ and G_μ, are available. The former relies on three parameters $\alpha_s(m_Z), m_Z, m_W$, and the latter depends on parameters G_F, m_Z, m_W. DYNNLO 1.5 uses G_μ scheme only. In addition to electroweak input parameters with renormalization and factorization scales, both frameworks support cuts on W and Z boson kinematics as well as their decay products. It allows to provide calculations for total as well as fiducial phase space. FEWZ 3.1 and DYNNLO 1.5 incorporate the LHAPDF format [41,42] to allow all PDF sets of interest to be studied. Due to the limited knowledge of PDFs, the numerical result of both programs include PDF uncertainty as well as scale and α_s uncertainties through their variations.

2.2 Top++

Top++ [43] is the program for numerical evaluation of the total inclusive cross-section for producing top quark pairs at hadron colliders. Perturbative calculations of partonic cross section might be problematic due to logarithmically enhanced terms from soft gluon radiation. If the hadronic cross section is dominated numerically by these threshold logarithms, they should be summed to all orders in perturbation theory. The theoretical basis for resummation is a factorization of the partonic hard-scattering cross section in the partonic threshold region into hard and soft contributions. This approach is realized in the Top++ framework.

The Top++ calculates the $t\bar{t}$ total inclusive cross-section either in a pure fixed order perturbation theory through exact NNLO [44–47] or including soft gluon resummation performed through next-to-next-to-leading logarithmic order NNLL [48, 49] and matched through NNLO:

$$\sigma_{tot}^{(n,k)} = \sigma_{F.O.}^{(n)} + [\sigma_{res}^{(n,k)} - \sigma_{res}^{(n,k)}|_{\alpha_s^n}], \tag{2.1}$$

where n (k) denote the fixed (logarithmic) order accuracy of the result. The behaviour of the fixed order (NNLO) cross section results for the total cross section near the production threshold can be found in Ref. [46]. The resummed partonic cross section definition in

N-space has a form:

$$\sigma^{(n,k)}_{res\ part;N,\mathbf{I}} = \sum_{\mathbf{I}=1,8} \sigma^{(Coul),(n)}_{N,\mathbf{I}} \times \sigma^{(Hard),(n)}_{N,\mathbf{I}} \times \Delta^{(k)}_{N,\mathbf{I}}. \tag{2.2}$$

where functions $\sigma^{(Coul),(n)}_{N,\mathbf{I}}$ contain the threshold-enhanced bound-state contributions and have a known perturbative expansion through NNLO, $\sigma^{(Hard),(n)}_{N,\mathbf{I}}$ are hard matching functions and $\Delta^{(k)}_{N,\mathbf{I}}$ are the radiative factors containing all contributions due to soft-gluon emission. The index $\mathbf{I} = 1, 8$ corresponds to the colour configuration of the heavy quark pair. More details on the resummed partonic cross section definition are given in Ref. [48].

The Top++ uses the LHAPDF library to include PDFs in calculations. It also takes renormalization and factorization scales as well as on-shell top mass as input parameters. The ranges and steps of their variations can be specified by user.

2.3 W and Z-boson production cross sections

Theoretical predictions for fiducial (defined in Section 5.2) and total cross sections of Z and W boson times branching ratio of the decay into a lepton pair (e^+e^- or $\mu^+\mu^-$) and lepton-neutrino pair ($e^\pm\nu$ or $\mu^\pm\nu$) accordingly, are computed using DYNNLO 1.5 and FEWZ 3.1, thereby providing full NLO and NNLO QCD calculations. The electroweak corrections at NLO are calculated with FEWZ 3.1 for Z and with the MC SANC [52] for W boson cross section.

The computations are done in the G_μ EW scheme where the following input parameters were taken from PDG14 [53]: the Fermi constant, masses and widths of W and Z bosons as well as elements of the CKM matrix. The cross sections are calculated for vector-boson decays into leptons at Born level (before the decay leptons emit photons via FSR, see Section 5.2), to match the definition of the C factor used in Equation 5.1 for the determination of the measured cross sections in the data. Thus, from complete NLO EW corrections the following components are included: virtual QED and weak corrections, ISR and interference between ISR and FSR. For the Z-boson production, all the predictions include the $66 < m_{\ell\ell} < 116$ GeV requirement.

DYNNLO is used for the central values of the predictions while FEWZ is used for the PDF, QCD scale and α_s systematic variations. The reason for using two separate codes for the prediction is that studies of the W and Z boson cross section with 7 TeV data [54] revealed FEWZ to have a 1% bias in the fiducial predictions. Such disagreement between DYNNLO and FEWZ also was reported in Ref. [55]. PDF variations with respect to a given central value are not affected.

For the calculation of the Z-boson cross section, the dynamic $m_{\ell\ell}$ scale is used as a nominal renormalization μ_R and factorization μ_F scales, whereas fixed m_W is used for W cross section calculations. Both predictions are calculated using the CT14NNLO [29],

NNPDF3.0 [56], MMHT14 [57], ABM12LHC [58], HERAPDF2.0 [59], and ATLAS-epWZ12NNLO [60] PDF sets. The central values of cross sections calculated with DYNNLO 1.5 and applied EW corrections are given in Table 2.2. The corrections are treated additively in the predictions. The size of electroweak corrections is found at the level of -0.2% and -0.35% in the total and fiducial phase space, respectively. Table 2.2 contains absolute values of corrections for W and Z boson cross sections.

There are several sources of uncertainties on the computed cross sections:

- PDF uncertainties are obtained from the sum in quadrature of the differences between the central PDF values and the eigenvectors of the respective PDF sets. Where appropriate, asymmetric uncertainties are determined using separate sums of negative and positive variations. For CT14nnlo set PDF uncertainties are rescaled from 90% to 68% confidence level (CL). The absolute values of PDF uncertainties on cross section predictions obtained with different PDF sets are given in Table 2.1.

- Uncertainties due to missing higher-order corrections in the available calculations are obtained by the symmetrised envelope of variations in which the renormalization and factorisation scales are changed by factors of two with an additional constraint of $0.5 \leq \mu_R/\mu_F \leq 2$. These variations are referred further as "scale uncertainties" and are presented for the W and Z-boson cross sections in Table 2.3. A significant component of these scale uncertainties originates from the statistical precision of the integration method used to evaluate the variations. Therefore, since the values of QCD scale uncertainties contain a statistical component, as can be evidenced by the fluctuations in the values, the calculated scale uncertainties are replaced with a flat and symmetric $\pm 1.1\%$ ($\pm 1.3\%$) uncertainty for each fiducial (total) prediction. These numbers are derived from an envelope of the observed variations.

- α_s uncertainty is estimated following the prescription given with the CT14nnlo PDF, varying α_s by ± 0.001 to correspond to 68% CL. The resulting uncertainties on predicted W, Z fiducial and total cross sections are estimated with CT14NNLO PDF set and found to be at the level of $\sim 0.9\%$. The exact numbers are given in Table 2.3.

- The beam energy is assumed to be known to 1% [61] and affects the production cross sections. The uncertainty on the beam energy is found to vary the prediction for W and Z production by 1.1%. Beam energy uncertainty on W and Z cross sections is computed with CT14NNLO PDF and presented in Table 2.3.

- Intrinsic theory uncertainties are related to the limitations of NNLO calculations, internal non-perturbative parameters. It is estimated by comparing the predictions calculated with DYNNLO 1.5 and FEWZ 3.1. For the total cross-section predictions, these differences are found to be $< 0.2\%$ per process and hence are negligible.

PDF	$\sigma^{fid} \pm PDF$ [pb]				$\sigma^{tot} \pm PDF$ [pb]			
	W^+	W^-	W	Z	W^+	W^-	W	Z
CT14NNLO	4423^{+127}_{-139}	3396^{+89}_{-110}	7819^{+214}_{-247}	742^{+20}_{-25}	11540^{+318}_{-309}	8543^{+214}_{-237}	20083^{+525}_{-539}	1888^{+45}_{-50}
NNPDF3.0	4386 ± 100	3333 ± 79	7719 ± 178	734 ± 16	11359 ± 259	8402 ± 197	19761 ± 450	1857 ± 40
MMHT14NNLO	4475^{+78}_{-62}	3427^{+55}_{-53}	7903^{+131}_{-113}	753^{+15}_{-13}	11610^{+200}_{-166}	8633^{+135}_{-133}	20243^{+326}_{-293}	1906^{+31}_{-27}
ABM12LHC	4559 ± 59	3463 ± 46	8021 ± 105	761 ± 10	11743 ± 150	8584 ± 103	20327 ± 250	1914 ± 23
HERAPDF2.0	4723^{+101}_{-89}	3559^{+76}_{-54}	8282^{+173}_{-132}	779^{+26}_{-17}	12125^{+313}_{-221}	8960^{+219}_{-140}	21086^{+528}_{-354}	1978^{+57}_{-34}
ATLAS-epWZ12NNLO	4662^{+63}_{-95}	3536^{+54}_{-70}	8198^{+116}_{-163}	785^{+16}_{-16}	11885^{+182}_{-189}	8806^{+161}_{-141}	20691^{+308}_{-317}	1967^{+34}_{-31}

Table 2.1: Summary of the fiducial $\sigma^{fid}_{W,Z}$ and total $\sigma^{tot}_{W,Z}$ predictions for $W \to \ell\nu$ and $Z \to \ell\ell$ calculated with DYNNLO 1.5 using various PDF sets. The uncertainties on cross sections introduced by corresponding PDF uncertainty at 68% CL are showed. The EW corrections (size of corrections is given in Table 2.2) are applied additively.

	$\delta^{W^+}_{EW}$ [pb]	$\delta^{W^-}_{EW}$ [pb]	δ^{W}_{EW} [pb]	δ^{Z}_{EW} [pb]
Fiducial	-18	-11	-29	-3.2
Total	-27	-17	-44	-4.5

Table 2.2: The absolute values of the NLO EW corrections except QED FSR and real weak emissions.

For the fiducial cross-section predictions, these differences are larger due to a feature of the calculations involving leptons with symmetric p_T requirements, resulting in consistently larger values from FEWZ. The differences are calculated using the CT14nnlo PDF as a central value in both cases, and are up to 1.3% for the W-boson cross sections and 0.6% for the Z-boson cross section.

- The statistical uncertainties resulting from DYNNLO and FEWZ computations are negligible small.

Tables 2.1 and 2.3 indicate that systematic uncertainties in the predictions are dominated by the imperfect knowledge of the proton parton distribution functions. Obtained predictions are used for comparison to the measured data at $\sqrt{s} = 13$ TeV with 50 ns bunch spacing. The compatibility between the predictions based on different PDF sets and measurements is showed and discussed In Section 10.1.1.

2.3.1 W and Z-boson cross-section ratios

Taking the ratios of the measured Z and W-boson cross sections benefits from the cancellation of the experimental uncertainties. The ratio of W^+ to W^- cross sections is sensitive to the u_v minus d_v valence-quark distribution at low Bjorken-x while the ratio of $W^\pm$ to Z cross sections constraints the strange-quark distribution. Studies from Ref. [30] show

Source	Fiducial				Total			
	W^+ [%]	W^- [%]	W [%]	Z [%]	W^+ [%]	W^- [%]	W [%]	Z [%]
Scale	$^{+0.5}_{-1.1}$	$^{+0.7}_{-0.8}$	$^{+0.6}_{-0.1}$	$^{+0.4}_{-0.7}$	$^{+0.9}_{-1.3}$	$^{+1.0}_{-1.3}$	$^{+1.0}_{-1.3}$	$^{+0.7}_{-1.1}$
α_s	± 0.9	± 0.92	± 0.9	± 0.9	± 0.9	± 0.95	± 0.92	± 0.9
Beam energy	$^{+0.8}_{-1.0}$	± 0.7	± 0.9	± 0.8	± 1.1	± 1.0	± 1.1	± 1.0

Table 2.3: The α_s, QCD scale and beam energy uncertainties, given in %, on predicted W and Z boson cross sections. Given values are estimated with CT14NNLO PDF set.

PDF	$\sigma^{fid}_{W^+}/\sigma^{fid}_{W^-}$	$\sigma^{fid}_{W^\pm}/\sigma^{fid}_{Z}$
	value $\pm$ PDF	value $\pm$ PDF
CT14NNLO	$1.303^{+0.011}_{-0.008}$	$10.534^{+0.117}_{-0.118}$
NNPDF3.0	1.324 ± 0.007	10.668 ± 0.055
MMHT14NNLO	$1.307^{+0.010}_{-0.006}$	$10.609^{+0.098}_{-0.140}$
ABM12LHC	1.326 ± 0.004	10.594 ± 0.035
HERAPDF2.0	$1.327^{+0.010}_{-0.018}$	$10.635^{+0.159}_{-0.189}$
ATLAS-epWZ12NNLO	$1.319^{+0.005}_{-0.009}$	$10.441^{+0.119}_{-0.148}$

Table 2.4: Summary of fiducial cross section ratios $\sigma^{fid}_{W^+}/\sigma^{fid}_{W^-}$ and $\sigma^{fid}_{W^\pm}/\sigma^{fid}_{Z}$ calculated with different PDFs. Given uncertainties represent absolute values of PDF uncertainty on the central value of the ratio.

that starting from accuracy of about 2% the measurements at $\sqrt{s} = 13$ TeV begin to have significant constraining power to PDFs, compared to the modern PDF sets.

Predictions for the fiducial cross-section ratios $\sigma^{fid}_{W^+}/\sigma^{fid}_{W^-}$ and $\sigma^{fid}_{W^\pm}/\sigma^{fid}_{Z}$ are calculated along with corresponding PDF uncertainties. The QCD scale variations are not considered for the ratios since the higher-order corrections are expected to affect both the $W^\pm$ and Z bosons in a similar manner but the exact correlation is difficult to evaluate. The differences between FEWZ and DYNNLO for W^+/W and $W^\pm/Z$ are 0.4% and 0.6%, respectively. The remaining theoretical uncertainties evaluated in the fiducial cross sections, mentioned above, largely cancel in the ratio and are also neglected. The central values of computed ratios with different PDFs and corresponding PDF uncertainties are given in Table 2.4. Predicted cross-section ratios are built for comparison to the measurements at $\sqrt{s} =$ 13 TeV with 50 ns bunch spacing data. The level of agreement among predictions and measured data is discussed in Section 10.2.

2.4 $t\bar{t}$ and Z-boson production cross sections

In this section, predictions are presented at NNLO+NNLL accuracy for the production cross section of a top-quark pair and at NNLO accuracy for the production cross section of a Z boson, corrected for the branching ratio of the decay into electron or muon pair within the dilepton invariant mass. The total cross sections of these processes are calculated for the centre-of-mass energies of 13, 8, and 7 TeV. The Z-boson production cross sections are also computed within the fiducial region (defined in Section 5.2) while predictions for top-quark-pair fiducial cross sections are not yet available at NNLO accuracy. Moreover, the calculated values are used to obtain predictions for different types of cross-section ratios.

Predictions for Z boson and $t\bar{t}$ production cross sections as well as cross-section ratios are computed for comparison with measured data (25 ns bunch spacing data in case of $\sqrt{s} = 13$ TeV).

2.4.1 Z-boson cross-section predictions

Theoretical predictions of the fiducial and total Z-boson production cross sections at $\sqrt{s} = 13, 8, 7$ TeV are computed using DYTURBO, a version of DYNNLO 1.5 optimised for speed of computation, thereby providing NNLO QCD calculations. The computations are performed in the same scheme using the Born level leptons of Z decay as it is described in Section 2.3. Moreover, the same list of PDF sets, values for input parameters (the Fermi constant, masses and widths of W and Z bosons, CKM matrix elements), as well as methods and prescriptions for α_s, QCD scale and intrinsic uncertainties calculation, are used. Electroweak corrections at NNLO are calculated with FEWZ 3.1.

The central values of calculated total and fiducial cross sections at $\sqrt{s} = 13, 8$, and 7 TeV are provided in Table 2.5, where the fiducial cross sections are given in both the 13 TeV fiducial phase space and in the phase space of the original measurement (both are defined in Table 5.1). The α_s, scale and intrinsic uncertainties on predicted cross sections are estimated in % with CT14NNLO PDF set and used for predictions based on the rest PDF sets.

Uncertainties on predicted cross sections given in Table 2.5 are dominated by the limited knowledge of the proton PDFs. Such situation was observed for Z predictions given in Section 2.3 indicating the importance of PDF determination accuracy. Presented PDF uncertainties of CT14NNLO set are rescaled from 90% CL to 68% CL. The statistical uncertainties resulting from evaluations with different PDF sets are negligibly small.

The intrinsic uncertainty on computed cross sections is obtained comparing DYNNLO (not DYTURBO) and FEWZ results when fixing the p_T of one lepton at 25 GeV and varying the p_T of the second lepton. It is found that when the p_T requirements are asymmetric, the difference between DYNNLO and FEWZ results for fiducial cross section at $\sqrt{s} = 13$ TeV is at $\sim 1\%$ level, however, when the cuts become symmetric, FEWZ

PDF	7 TeV			8 TeV			13 TeV	
	Total	13 TeV fid.	Maes. fid.	Total	13 TeV fid.	Maes. fid.	Total	13 TeV fid.
	$\sigma \pm stat \pm PDF$	$\sigma \pm stat \pm PDF$	$\sigma \pm stat \pm PDF$	$\sigma \pm stat \pm PDF$	$\sigma \pm stat \pm PDF$	$\sigma \pm stat \pm PDF$	$\sigma \pm stat \pm PDF$	$\sigma \pm stat \pm PDF$
CT14NNLO	$956.3 \pm 0.7\ ^{+20.8}_{-23.9}$	$433.4 \pm 0.4\ ^{+10.6}_{-13.1}$	$482.8 \pm 0.4\ ^{+11.7}_{-14.5}$	$1112.5 \pm 0.7\ ^{+24.4}_{-28.0}$	$487.7 \pm 0.3\ ^{+12.1}_{-15.1}$	$518.2 \pm 0.5\ ^{+12.8}_{-16.1}$	$1891.0 \pm 0.5\ ^{+45.1}_{-50.3}$	$746.4 \pm 0.6\ ^{+20.3}_{-25.0}$
NNPDF3.0	$943.6 \pm 1.0\ \pm 18.7$	$426.3 \pm 0.7\ \pm 8.6$	$472.2 \pm 0.6\ \pm 9.5$	$1096.2 \pm 1.4\ \pm 21.9$	$480.8 \pm 0.7\ \pm 9.8$	$508.6 \pm 0.7\ \pm 10.4$	$1867.9 \pm 2.4\ \pm 39.6$	$734.5 \pm 1.5\ \pm 16.4$
MMHT14NNLO	$966.4 \pm 1.3\ ^{+14.5}_{-13.1}$	$437.8 \pm 0.5\ ^{+6.8}_{-6.4}$	$486.4 \pm 0.7\ ^{+7.5}_{-7.1}$	$1123.4 \pm 1.3\ ^{+16.6}_{-15.0}$	$492.9 \pm 0.7\ ^{+7.8}_{-7.3}$	$521.8 \pm 0.7\ ^{+8.3}_{-7.8}$	$1908.3 \pm 3.1\ ^{+31.2}_{-27.0}$	$756.9 \pm 1.4\ ^{+15.0}_{-12.9}$
ABM12LHC	$969.3 \pm 1.0\ \pm 10.9$	$444.0 \pm 0.6\ \pm 5.3$	$491.9 \pm 0.7\ \pm 5.8$	$1123.89 \pm 1.4\ \pm 12.8$	$500.9 \pm 0.6\ \pm 6.1$	$529.2 \pm 0.7\ \pm 6.4$	$1915.7 \pm 2.3\ \pm 23.1$	$762.6 \pm 1.3\ \pm 10.2$
HERAPDF2.0	$994.1 \pm 1.1\ ^{+31.9}_{-18.0}$	$449.4 \pm 0.6\ ^{+15.3}_{-8.7}$	$497.6 \pm 0.6\ ^{+16.7}_{-9.6}$	$1158.9 \pm 1.4\ ^{+35.8}_{-20.6}$	$506.7 \pm 0.7\ ^{+17.0}_{-9.8}$	$535.5 \pm 0.6\ ^{+17.8}_{-10.3}$	$1982.5 \pm 2.8\ ^{+58.3}_{-34.7}$	$781.5 \pm 1.9\ ^{+25.9}_{-17.2}$
ATLAS-epWZ12NNLO	$990.0 \pm 1.1\ ^{+17.0}_{-15.0}$	$449.6 \pm 0.5\ ^{+8.4}_{-8.4}$	$498.5 \pm 0.8\ ^{+9.2}_{-9.2}$	$1153.6 \pm 1.9\ ^{+19.6}_{-17.6}$	$509.2 \pm 0.7\ ^{+9.6}_{-9.7}$	$538.2 \pm 0.9\ ^{+10.1}_{-10.3}$	$1970.3 \pm 2.4\ ^{+34.6}_{-31.7}$	$788.2 \pm 1.39\ ^{+15.7}_{-16.3}$
Uncertainties [%]								
Scale	$^{+0.5}_{-0.9}$	$^{+0.7}_{-0.3}$	$^{+0.4}_{-0.8}$	$^{+0.6}_{-0.9}$	$^{+0.5}_{-0.5}$	$^{+0.3}_{-0.8}$	$^{+0.7}_{-1.1}$	$^{+0.5}_{-0.8}$
α_s	$^{+0.8}_{-0.9}$	$^{+1.0}_{-0.7}$	$^{+0.7}_{-1.1}$	$^{+0.8}_{-0.8}$	$^{+0.9}_{-0.8}$	$^{+0.8}_{-1.1}$	$^{+1.0}_{-0.9}$	$^{+0.9}_{-1.0}$
Intrinsic	< 0.2	$^{+0.7}_{-0.7}$	$^{+0.7}_{-0.7}$	< 0.2	$^{+0.7}_{-0.7}$	$^{+0.7}_{-0.7}$	< 0.2	$^{+0.7}_{-0.7}$

Table 2.5: Predictions of Z boson total and fiducial cross sections, where the fiducial region is given in both the 13 TeV fiducial phase space ("13 TeV fid.") and in the phase space of the original measurement ("Maes. fid."). Central values of cross sections with absolute values of statistical and PDF uncertainties calculated with different PDF sets are given in the top half of the table. PDF uncertainties correspond to 68% CL. The bottom half of the table contains uncertainties given in % which correspond to variations of QCD scale, α_s, intrinsic Z-boson prediction. EW corrections have not been applied to these numbers.

	δ^Z_{EW} [pb] ($\sqrt{s} = 7$ TeV)	δ^Z_{EW} [pb] ($\sqrt{s} = 8$ TeV)	δ^Z_{EW} [pb] ($\sqrt{s} = 13$ TeV)
Fiducial	-1.37 ± 0.13	1.74 ± 0.15	2.45 ± 0.24
Total	2.06 ± 0.08	2.52 ± 0.09	4.76 ± 0.18

Table 2.6: The size of the NLO EW corrections δ^Z_{EW} (in pb) at 7, 8, and 13 TeV except QED FSR and real weak emissions, given for the 13 TeV fiducial phase space and for the total phase space.

is high by $\sim 0.6\%$. This difference at $\sqrt{s} = 13$ TeV calculations is used as intrinsic uncertainty of 0.7% for all centre-of-mass energies. The level of agreement on the NNLO total cross section prediction is found to be better than $\sim 0.2\%$ and can be safely neglected.

The EW corrections should be applied to the calculated cross section predictions given in Table 2.5. The size of the corrections are given in Table 2.6 for the total and 13 TeV fiducial phase space given at $\sqrt{s} = 13, 8$, and 7 TeV.

2.4.2 $t\bar{t}$ cross-section predictions

The cross sections of inclusive $t\bar{t}$ production at $\sqrt{s} = 7, 8$ and 13 TeV times the branching ratio of the decay into opposite-sign $e\mu$ pair in the final state are computed using Top++v2.0 [43] for the central values and for all variations reflecting systematic uncer-

PDF	7 TeV	8 TeV	13 TeV
	$\sigma_{t\bar{t}}^{tot} \pm PDF$	$\sigma_{t\bar{t}}^{tot} \pm PDF$	$\sigma_{t\bar{t}}^{tot} \pm PDF$
CT14NNLO	$181.7^{+8.0}_{-6.7}$	$258.9^{+10.1}_{-8.8}$	$841.8^{+21.9}_{-22.7}$
NNPDF3.0	179.5 ± 4.6	256.5 ± 6.0	839.5 ± 15.1
MMHT14NNLO	$181.3^{+4.0}_{-5.6}$	$258.1^{+5.3}_{-7.3}$	$839.5^{+13.8}_{-17.7}$
ABM12LHC	141.5 ± 6.1	206.6 ± 8.3	721.0 ± 21.7
HERAPDF2.0	$170.1^{+5.7}_{-10.5}$	$244.2^{+7.2}_{-13.9}$	$811.8^{+15.1}_{-34.5}$
ATLAS-epWZ12NNLO	$171.5^{+5.3}_{-6.6}$	$245.1^{+7.1}_{-8.6}$	$807.1^{+20.3}_{-19.8}$
Uncertainties [%]			
Scale	$^{+2.6}_{-3.5}$	$^{+2.6}_{-3.5}$	$^{+2.4}_{-3.6}$
α_s	$^{+2.2}_{-2.1}$	$^{+2.1}_{-2.1}$	$^{+1.9}_{-1.8}$
m_t	$^{+3.1}_{-3.0}$	$^{+3.0}_{-2.9}$	$^{+2.8}_{-2.7}$

Table 2.7: Predictions of the total cross section $\sigma_{t\bar{t}}^{tot}$ at $\sqrt{s} = 7, 8$ and 13 TeV using CT14NNLO, NNPDF3.0, MMHT14NNLO, ABM12LHC, HERAPDF2.0, ATLAS-epWZ12NNLO PDF sets. The PDF uncertainties at 68% CL are given in absolute values at the top half of the table. The QCD scale, α_s and top-quark mass uncertainties are calculated with CT14NNLO PDF set and given in % at the bottom half of the table. The statistical uncertainties in the predictions are ≤ 0.1 pb and are not given in the table.

tainties, thereby providing NNLO+NNLL resummed QCD calculations. The systematic uncertainties in the predictions are performed as for those of the Z boson, with the following exceptions. The intrinsic uncertainty was not assigned to the cross-section prediction. The $t\bar{t}$ production cross section also has a significant dependence on the value of the top-quark mass, m_t. A systematic uncertainty is assessed by varying the mass of the top quark by ± 1 GeV from the baseline value of 172.5 GeV used to obtain the central value of the predictions, resulting in an uncertainty in the cross section of approximately 3%. The predictions of the total cross sections based on different PDF sets, together with their uncertainties, are given in Table 2.7. It demonstrates that top-quark mass, PDF and QCD scale uncertainties are mostly at the same level and dominate the total uncertainty.

2.4.3 Predictions for cross-section ratios

The $t\bar{t}$ to Z-boson cross section ratio has a significant sensitivity to the gluon-to-quark PDF ratio. Such type of ratio at a given center-of-mass energy provides high precision measurement through the cancellation of experimental uncertainties. The predictions given in Tables 2.5, 2.7 are used to build cross-section ratios for:

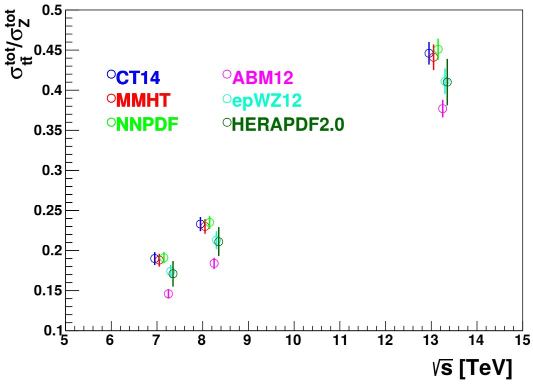

Figure 2.1: Predictions for the ratio of the total cross section $R_{t\bar{t}/Z}^{tot/fid}(i\ TeV)$, $i = 7, 8, 13$ for the four PDFs CT14NNLO, NNPDF3.0, MMHT14NNLO, ABM12LHC, HERAPDF2.0, ATLAS-epWZ12NNLO (includes only the symmetrised PDF uncertainty). Points are slightly offset at the different $\sqrt{s}$ for clarity.

- a given process at the different $\sqrt{s}$: $R_{Z_i/Z_j}^{fid(tot)} = \frac{\sigma_{Z(iTeV)}^{fid(tot)}}{\sigma_{Z(iTeV)}^{fid(tot)}}$ and $R_{t\bar{t}_i/t\bar{t}_j}^{tot} = \frac{\sigma_{t\bar{t}(iTeV)}^{tot}}{\sigma_{t\bar{t}(iTeV)}^{tot}}$,

- different processes at the same $\sqrt{s}$: $R_{t\bar{t}/Z}^{tot/fid(tot)}(i\ TeV) = \sigma_{t\bar{t}(iTeV)}^{tot}/\sigma_{Z(iTeV)}^{fid(tot)}$,

- different processes at the different $\sqrt{s}$: $R_{t\bar{t}/Z}^{tot/fid(tot)}(i/j) = \left[\frac{\sigma_{t\bar{t}(iTeV)}^{tot}}{\sigma_{Z(iTeV)}^{fid(tot)}}\right] / \left[\frac{\sigma_{t\bar{t}(jTeV)}^{tot}}{\sigma_{Z(jTeV)}^{fid(tot)}}\right]$

where $i, j = 7, 8, 13$ and all predictions for Z-boson fiducial cross sections are given in the 13 TeV phase space. The third type of ratios will be denoted as double ratios. The first set of predictions is presented in Table 2.8 while the latter two are presented in Table 2.9. Both tables contain predictions obtained with CT14NNLO PDF set. The $\sqrt{s}$ evolution of $R_{t\bar{t}/Z}^{tot/tot}(i\ TeV)$ for the listed PDF sets is shown in Figure 2.1. The comparison of the predictions to the data is discussed in Section 10.3.

The treatment of the systematic uncertainties when combining the theoretical uncertainties in the ratios is taken as follows. The PDF uncertainties are considered as correlated, eigenvector by eigenvector, between predictions. The QCD scale uncertainties are treated as uncorrelated between processes but correlated, variation by variation, at the different $\sqrt{s}$ values for a given process. The α_s uncertainties are correlated between predictions. The Z-boson intrinsic and m_t uncertainties are both considered as correlated at the different $\sqrt{s}$ values within their respective processes. In the few cases where the coherent variation of a source of systematic uncertainty in the numerator and in the denominator of a ratio results in variations of the same sign, only the largest variation is added in the total uncertainty of the corresponding sign.

	$R^{fid}_{Z_i/Z_j}$			$R^{tot}_{Z_i/Z_j}$			$R^{tot}_{t\bar{t}_i/t\bar{t}_j}$		
i/j	13/7	13/8	8/7	13/7	13/8	8/7	13/7	13/8	8/7
Central value	1.722	1.531	1.125	1.977	1.699	1.163	4.634	3.251	1.425
Uncertainties [%]									
PDF	$^{+1.0}_{-0.9}$	$^{+0.8}_{-0.7}$	$^{+0.22}_{-0.21}$	$^{+0.9}_{-0.8}$	$^{+0.7}_{-0.6}$	$^{+0.18}_{-0.17}$	$^{+1.9}_{-2.3}$	$^{+1.4}_{-1.8}$	$^{+0.5}_{-0.6}$
Scale	$^{+0.03}_{-0.60}$	$^{+0.02}_{-0.29}$	$^{+0.02}_{-0.31}$	$^{+0.21}_{-0.30}$	$^{+0.20}_{-0.25}$	$^{+0.19}_{-0.05}$	$^{+0.19}_{-0.26}$	$^{+0.13}_{-0.19}$	$^{+0.05}_{-0.07}$
α_s	$^{-0.1}_{-0.4}$	$^{-0.1}_{-0.3}$	$^{-0.1}_{-0.1}$	$^{+0.2}_{-0.1}$	$^{+0.2}_{-0.1}$	$^{-0.1}_{+0.1}$	$^{-0.32}_{+0.29}$	$^{-0.25}_{+0.22}$	$^{-0.08}_{+0.07}$
m_t	N/A	N/A	N/A	N/A	N/A	N/A	$^{+0.29}_{-0.29}$	$^{+0.22}_{-0.22}$	$^{+0.07}_{-0.07}$
Total	$^{+1.0}_{-1.2}$	$^{+0.8}_{-0.8}$	$^{+0.22}_{-0.40}$	$^{+0.9}_{-0.9}$	$^{+0.8}_{-0.7}$	$^{+0.27}_{-0.20}$	$^{+1.9}_{-2.4}$	$^{+1.4}_{-1.8}$	$^{+0.5}_{-0.6}$

Table 2.8: Predictions of the cross-section ratios $R^{fid(tot)}_{Z_i/Z_j}$ and $R^{tot}_{t\bar{t}_i/t\bar{t}_j}$ at different $\sqrt{s}$ values where $i/j = 13/7, 13/8, 8/7$ using the CT14 PDF. The uncertainties, given in %, correspond to variations of: CT14 eigenvector set at 68% CL, QCD scale, α_s and m_t. The statistical uncertainties in the predictions are ≤ 0.002 for the Z process and ≤ 0.001 for the $t\bar{t}$ process and are not given in the table. The notation N/A means "not applicable".

	$R^{tot/fid}_{t\bar{t}/Z}(i\ TeV)$			$R^{tot/tot}_{t\bar{t}/Z}(i\ TeV)$			$R^{tot/fid}_{t\bar{t}/Z}(i/j)$			$R^{tot/tot}_{t\bar{t}/Z}(i/j)$		
i or i/j	7	8	13	7	8	13	13/7	13/8	8/7	13/7	13/8	8/7
Central value	0.421	0.533	1.132	0.190	0.233	0.446	2.691	2.124	1.267	2.344	1.913	1.225
Uncertainties [%]												
PDF	$^{+7}_{-5}$	$^{+7}_{-5}$	$^{+6}_{-5}$	$^{+6}_{-5}$	$^{+6}_{-5}$	$^{+5}_{-5}$	$^{+1.5}_{-2.0}$	$^{+1.1}_{-1.6}$	$^{+0.4}_{-0.5}$	$^{+1.8}_{-2.2}$	$^{+1.4}_{-1.7}$	$^{+0.4}_{-0.6}$
Scale	$^{+2.7}_{-3.6}$	$^{+2.6}_{-3.5}$	$^{+2.6}_{-3.6}$	$^{+2.8}_{-3.5}$	$^{+2.7}_{-3.6}$	$^{+2.7}_{-3.7}$	$^{+0.62}_{-0.27}$	$^{+0.32}_{-0.20}$	$^{+0.31}_{-0.07}$	$^{+0.35}_{-0.34}$	$^{+0.38}_{-0.28}$	$^{+0.09}_{-0.21}$
α_s	$^{+1.1}_{-1.5}$	$^{+1.1}_{-1.3}$	$^{+0.9}_{-0.8}$	$^{+1.4}_{-1.3}$	$^{+1.4}_{-1.3}$	$^{+0.9}_{-0.9}$	$^{-0.22}_{+0.70}$	$^{-0.22}_{+0.50}$	$^{-0.00}_{+0.20}$	$^{-0.49}_{+0.36}$	$^{-0.49}_{+0.35}$	$^{-0.00}_{+0.01}$
m_t	$^{+3.1}_{-3.0}$	$^{+3.0}_{-2.9}$	$^{+2.8}_{-2.7}$	$^{+3.1}_{-3.0}$	$^{+3.0}_{-2.9}$	$^{+2.8}_{-2.7}$	$^{+0.29}_{-0.29}$	$^{+0.22}_{-0.22}$	$^{+0.07}_{-0.07}$	$^{+0.29}_{-0.29}$	$^{+0.22}_{-0.22}$	$^{+0.07}_{-0.07}$
Total	$^{+8}_{-7}$	$^{+8}_{-7}$	$^{+7}_{-7}$	$^{+8}_{-7}$	$^{+7}_{-7}$	$^{+7}_{-7}$	$^{+1.8}_{-2.1}$	$^{+1.3}_{-1.6}$	$^{+0.5}_{-0.5}$	$^{+1.9}_{-2.3}$	$^{+1.5}_{-1.8}$	$^{+0.4}_{-0.6}$

Table 2.9: Predictions of the cross-section ratios $R^{tot/fid(tot)}_{t\bar{t}/Z}(i\ TeV)$ and $R^{tot/fid(tot)}_{t\bar{t}/Z}(i/j)$ at the different $\sqrt{s}$ values, where $i, j = 13, 8, 7$ using the CT14 PDF. The uncertainties, given in %, correspond to variations of: CT14 eigenvector set at 68% CL, α_s QCD scale, intrinsic Z-boson prediction, and top-quark mass. The statistical uncertainties in the predictions are ≤ 0.001 for $R^{tot/fid(tot)}_{t\bar{t}/Z}(i\ TeV)$ and ≤ 0.003 (≤ 0.002) for $R^{tot/fid(tot)}_{t\bar{t}/Z}(i/j)$ and are not given in the table.

2.5 xFitter

The QCD analysis framework, xFitter [27, 62, 63], is an open-source package for the determination of the parton distribution functions of the proton and the extraction of fundamental parameters of QCD such as the heavy quark masses and the strong coupling constant. A variety of theory predictions and different phenomenological approaches are implemented for calculating PDF-dependent cross section predictions corresponding to the measurements. It also provides a framework for the comparison of different theoretical approaches and can be used to test the impact of new experimental data on the PDFs and SM parameters.

The xFitter structure and functionality can be divided into four main blocks: *data*, *theory*, *QCD Analysis* and *Results*. In the *data* block results of measurements from various processes (such as DY, single top, top-quark pair, DIS processes, jets, etc.) at different experiments (LHC, HERA, Tevatron) are provided including the information on their uncorrelated and correlated uncertainties. Moreover, HERA inclusive scattering data are the basis of any proton PDF extraction and are used in all current PDF sets from ABM, CTEQ, MSTW, NNPDF, GJR, HERAPDF groups.

In the *theory* block, the PDFs are parametrised at a starting scale, Q_0^2, using a functional form and a set of free parameters. There are several predefined functional forms and flavour decompositions in the xFitter: the standard polynomial for parametrization the x-dependence of PDFs, bi-log-normal form as a generalisation of the standard polynomial for multi-particle statistics, Chebyshev polynomials which can be employed for the gluon and sea distributions. More details on parametrisation functions are given in Ref. [62]. Parametrised PDFs are evolved to the scale of the measurements Q^2, $Q^2 > Q_0^2$. By default, the evolution uses the DGLAP formalism but alternatively can use the CCFM [64] evolution. xFitter also provides the possibility to access external PDF sets from LHAPDF library for cross sections computation. The prediction of the cross section for a particular process is obtained using the factorisation formalism.

In the *QCD Analysis* block, the PDFs are determined in a least squares fit: a χ^2 function, which compares the input data and theory predictions, is minimised with the MINUIT [65] program. There are various choices for the treatment of experimental uncertainties in the χ^2 definition. Correlated experimental uncertainties can be accounted for using a nuisance parameter or a covariance matrix method. In the covariance matrix representation for a data point μ_i with a corresponding theory prediction m_i, the χ^2 is defined in the form

$$\chi^2(m) = \sum_{i,k}(m_i - \mu_i)C_{ik}^{-1}(m_k - \mu_k) \tag{2.3}$$

where the experimental uncertainties are given as a covariance matrix C_{ik} for measurements in bins i and k. The covariance matrix is given by a sum of statistical, uncorrelated and correlated systematic contributions $C_{ik} = C_{ik}^{stat} + C_{ik}^{uncorr} + C_{ik}^{corr}$. This representation does not allow to distinguish the effect of each source of systematic uncertainty. In the nuisance parameter representation, the χ^2 is expressed as

$$\chi^2(m,b) = \sum_i \frac{\left[\mu_i - m_i(1-\sum_j \gamma_j^i b_j)\right]^2}{\delta_{i,uncorr}^2 m_i^2 + \delta_{i,stat}^2 \mu_i m_i (1-\sum_j \gamma_j^i b_j)} + \sum_j b_j^2, \tag{2.4}$$

where $\delta_{i,stat}$ and $\delta_{i,uncorr}$ denote the relative statistical and relative uncorrelated systematic uncertainties of the measurement i. γ_j^i quantifies the sensitivity of the measurement to the correlated systematic source j. b_j is a set of nuisance parameters. Such χ^2 definition is obtained under the assumption of normal distribution of the nuisance parameters. This assumption results in the trailing term, $\sum_j b_j^2$, expressing the penalty for correlated shifts away from the central values. Given representation allows to distinguish the effect of different sources of systematic uncertainties.

The Hessian, Offset, and Monte Carlo methods are implemented in xFitter for propagating experimental uncertainties to PDFs. In the first method the Hessian matrix is defined by the second derivatives of χ^2 on the fitted PDF parameters, therefore matrix dimension is equal to the number of free parameters in the fit. The resulting matrix diagonalized resulting in orthonormal eigenvector directions which provide the basis for the determination of the PDF error. Due to orthogonality, eigenvectors correspond to independent sources of uncertainty in the obtained PDFs. In the offset method the inversion of a large measurement covariance matrix is avoided. Only uncorrelated uncertainties are taken into account in the χ^2 function for the central fit [62,66], therefore goodness of the fit can no longer be judged from the χ^2. The correlated uncertainties are propagated into the PDF uncertainties by performing fits where each systematic parameter is offset by its assumed error. The resulting deviations of the PDF parameters from the ones obtained in the central fit are statistically independent, and are added in quadrature to derive a total PDF systematic uncertainty. Uncertainties estimated with this method are generally larger than those from the Hessian method. In the MC method [67] the PDF uncertainties are estimated using randomly generated pseudo-data replicas of the measured central values with their statistical and systematic uncertainties taking into account point-to-point correlations. The QCD fit is performed for each replica. The PDF central values and their experimental uncertainties are obtained taking the mean values and standard deviations over the replicas. Gaussian distributions of statistical and systematic uncertainties are assumed in a given approach.

As an alternative to performing a QCD fit, xFitter allows quantitatively estimate the impact of a new data set on a given PDF set with a $profiling$ procedure [68]. The profiling technique is performed using a χ^2 function which includes both the experimental uncertainties and the theoretical ones arising from PDF variations:

$$\chi^2(\vec{b}_{exp}, \vec{b}_{th}) = \sum_{i=1}^{N_{data}} \frac{\left[\sigma_i^{exp} - \sigma_i^{th}(1 - \sum_\alpha \gamma_{i\alpha}^{exp} b_{\alpha,exp} - \sum_\beta \gamma_{i\beta}^{th} b_{\beta,th})\right]^2}{\Delta_i^2} + \sum_{\alpha=1}^{N_{exp.sys}} b_{\alpha,exp}^2 + \sum_{\beta=1}^{N_{th.sys}} b_{\beta,th}^2. \tag{2.5}$$

The index i runs over all N_{data} data points. The measurements and the theory predictions are given by σ_i^{exp} and σ_i^{th}, respectively. The correlated experimental and theoretical uncertainties are included using the nuisance parameter vectors $\vec{b}_{exp}$ and $\vec{b}_{th}$, respectively. Their influence on the data and theory predictions is described by the matrices $\gamma_{i\alpha}^{exp}$ and $\gamma_{i\beta}^{th}$, where the index α (β) corresponds to the $N_{exp.sys}$ experimental ($N_{th.sys}$ theoretical) nuisance parameters. Both the correlated and uncorrelated systematic uncertainties are treated as multiplicative. The estimation of the statistical uncertainties is protected against statistical fluctuations in data using the expected rather than the observed number of events and the denominator is hence calculated as

$$\Delta_i^2 = \delta_{i,stat}^2 \sigma_i^{exp} \sigma_i^{th} + (\delta_{i,uncor} \sigma_i^{th})^2. \tag{2.6}$$

The χ^2 function of Equation 2.5 can be generalised to account for asymmetric PDF uncertainties [69]:

$$\gamma_{i\beta}^{th} \to \gamma_{i\beta}^{th} + \omega_{i\beta}^{th} b_{\beta,th}, \tag{2.7}$$

where $\gamma_{i\beta}^{th} = 0.5(\gamma_{i\beta}^{th+} - \gamma_{i\beta}^{th-})$ and $\omega_{i\beta}^{th} = 0.5(\gamma_{i\beta}^{th+} + \gamma_{i\beta}^{th-})$ are determined from the shifts of predictions corresponding to up $\gamma_{i\beta}^{th+}$ and down $\gamma_{i\beta}^{th-}$ PDF uncertainty eigenvectors.

The minimisation of Equation 2.5 leads to a system of linear equations. The generalised function, with asymmetric PDF uncertainties, is minimised iteratively where the values of $\gamma_{i\beta}^{th+}$ are updated with $b_{\beta,th}$ from the previous iteration. The value of the χ^2 function at its minimum provides a compatibility test of the data and theory. The values of the nuisance parameters at this minimum, $b_{\beta,th}^{min}$, can be interpreted as an optimization of PDFs to describe the data. The profiled PDF set f_0' is given by:

$$f_0' = f_0 + \sum_\beta b_{\beta,th}^{min} \Big(\frac{f_\beta^+ - f_\beta^-}{2} + b_{\beta,th}^{min} \frac{f_\beta^+ + f_\beta^- - 2f_0}{2} \Big), \tag{2.8}$$

where f_0 is the central PDF set, $f_\beta^\pm$ are up and down variations of the original eigenvector sets. Explicitly, $f_0 = f_0(x, Q^2)$, where $f_0 = u, \bar{u}, d, \bar{d}, ...g$ for the central set. f_0 and $f_\beta^\pm$ for LHAPDF parametrisations are given as tables for fixed x and Q^2 values.

The profiled PDF sets have reduced uncertainties and the eigenvectors are no longer orthogonal. The eigenvectors can be transformed to the orthogonal representation with

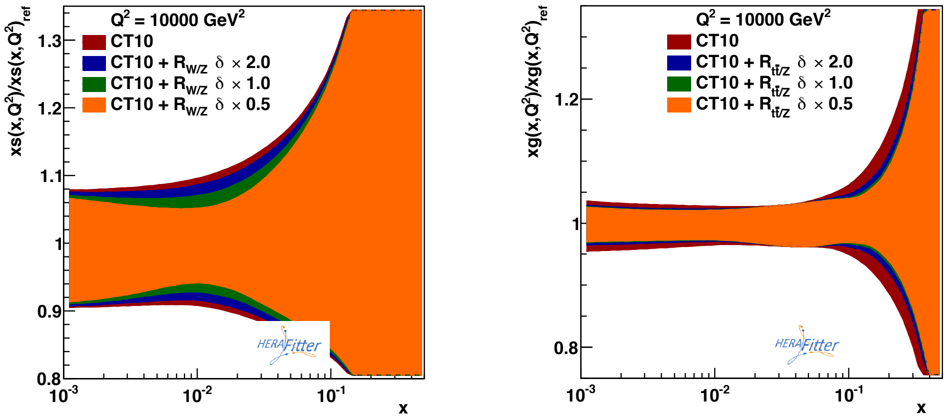

Figure 2.2: Relative uncertainty of the strange-quark (left) and gluon (right) distribution as a function of x for $Q^2 = 10^4\text{GeV}^2$ estimated based on CT10NNLO PDF set. The outer uncertainty band corresponds to the original PDF uncertainty. The embedded bands represent results of the PDF profiling using $R_{W/Z}$ (for strange-quark distribution) and $R_{t\bar{t}/Z}$ (for gluon distribution) pseudo-data at 13 TeV corresponding to three variations for size of uncertainties. [30]

a standard diagonalization procedure [70]. Given method can be extended to PDF sets with asymmetric uncertainties.

Figure 2.2 demonstrates the example of PDF profiling for estimating the impact of a pseudo-data on the CT10NNLO [71] PDF set. For this test, the inclusive W, Z and $t\bar{t}$ production are considered [30]. To reduce the correlations among the observables, the cross-section ratios were used instead of absolute cross-sections. The central values of the pseudo-data are equal to the central values of the predictions, while the uncertainties are taken from Run I results of W, Z [72–74] and $t\bar{t}$ measurements [75]. In a given test, there are three scenarios depending on the size of the uncertainties for pseudo-data considered: data uncertainties are similar to those from Run I; data uncertainties are scaled by a factor of two; data uncertainties are scaled by a factor of 0.5.

The strange-quark distribution shows that biggest impact of the $R_{W/Z}$ pseudo-data is in the region $x \sim 0.01$. The PDF uncertainty of the profiled PDF set reduces with increasing the precision of the pseudo-data. Therefore, the highest reduction of PDF uncertainty is observed for profiled set using data with uncertainties scaled by a factor of 0.5. Profiling of the $R_{t\bar{t}/Z}$ pseudo-data demonstrates the largest reduction of PDF uncertainties for gluon distribution in the regions $x < 0.01$ and $x \geq 0.1$. In this case, the difference in pseudo-data precision does not change the gluon density uncertainty significantly.

More studies of such impact on different PDF sets can be found in Ref. [30]. Plots in Figure 2.2 demonstrate the example of graphical representation of output in the *results* block of the xFitter. In case of full QCD analysis (QCD fit), a new PDF set is produced in a format ready to be used by the LHAPDF library as well as graphical representation of parton density distributions (the example can be found in Ref. [54]).

Chapter 3

Experimental apparatus

Progress in our understanding of nature comes through the interplay between theory and experiment. Experiment in particle physics primary depends on particle accelerators with complex detectors. Starting from the early 1930s the collision energy is gradually increasing over time allowing to test theory at previously inaccessible scale. The Standard Model is one of the theories is designed to explain observations at such experimental facilities. During the last thirty years several major results predicted with Standard Model are obtained at different colliders. In 1983 at the Super Proton Synchrotron (SPS) at Conseil Europén pour la Recherche Nucléaire (CERN), the Z and W bosons were discovered studying $p\bar{p}$ collisions at $\sqrt{s} = 450$ GeV by UA1 and UA2 collaborations [76–78]. In 1995 the top quark was discovered in $p\bar{p}$ collisions at $\sqrt{s} = 1.8$ TeV with Tevatron collider in the Fermi National Accelerator Laboratory by the CDF and D0 collaborations [79, 80]. Results from Tevatron showed that SM predicted Higgs boson should have mass higher than 114.4 GeV [81]. Therefore, the accelerator with higher center-of-energy had to be built. Such a high-intensity accelerator started up in 2008 and is called the Large Hadron Collider (LHC). In 2012 the Higgs boson was discovered in pp collisions at $\sqrt{s} = 7$ and 8 TeV at the LHC by the ATLAS and CMS collaborations [82, 83]. Currently the LHC operates at $\sqrt{s} = 13$ TeV allowing to increase precision of already measured SM constituents and test theories beyond the SM. The scientific programme of the LHC spans over the next twenty years and includes an ambitious series of upgrades that will result in increasing the total number of collisions at $\sqrt{s} = 14$ TeV. A more powerful LHC would provide more accurate measurements and enable observation of rare processes that occur below the current sensitivity level.

Following chapters provide a brief overview of the LHC as well as the ATLAS detector with its currently installed components used for the physics analyses.

3.1 The Large Hadron Collider

The LHC [84] is a two-ring, superconducting accelerator and collider installed in 26.7 km tunnel with center of mass collision energies of up to 14 TeV aiming at the measurements of SM parameters in hitherto inaccessible regions of phase space as well as reveal the physics beyond the SM. Number of events that the LHC generates per second is defined as:

$$N_{event} = \mathcal{L}\sigma_{event}, \tag{3.1}$$

where $\mathcal{L}$ is the instantaneous machine luminosity and σ_{event} is the cross section of the studied event. Luminosity has the dimension of $[\mathcal{L}] = cm^{-2}s^{-1}$. For the Gaussian beam distribution the machine luminosity is defined in a form [85]:

$$\mathcal{L} = \frac{N_b^2 n_b f \gamma}{4\pi\epsilon\beta^*}F \tag{3.2}$$

where N_b is the number of particles per bunch, n_b the number of bunches in one beam, f the beam revolution frequency, γ the relativistic gamma factor, ϵ the normalized transverse beam emittance, β^* the beta function at the collision point, and F the geometric luminosity reduction factor due to the crossing angle at the interaction point. In equation 3.2, the beams are assumed to be round and have equal parameters. Number of bunches in one beam can reach 2808 and the number of particles per bunch can exceed 10^{11}. To measure the amount of data produced in a certain period of time, the integrated over time luminosity $\int \mathcal{L}$ is used. It is measured in the inverse cross section units.

There are two high luminosity experiments at the HLC, ATLAS (A Toroidal LHC ApparatuS) [86] and CMS (Compact Muon Solenoid) [87], aiming at a peak instantaneous luminosity of $\mathcal{L} = 10^{34}cm^{-2}s^{-1}$ for proton operation. Both ATLAS and CMS are general-purpose detectors designed to investigate the largest range of physics possible. LHC also has low-luminosity experiments, among which LHCb [88], MoEDAL [90], TOTEM [91], LHCf [89], and ALICE [92]. LHCb is designed to exploit the large number of b hadrons produced at the LHC in order to make precision studies of CP asymmetries and of rare decays in the B-meson systems, aiming at a peak luminosity of $\mathcal{L} = 10^{32}cm^{-2}s^{-1}$. MoEDAL is the LHC's newest experiment (start data taking in 2015) which shares an interaction point with the LHCb experiment. It is designed to significantly expand the discovery horizon of the general-purpose LHC detectors with searches for magnetic monopoles or massive (pseudo-) stable charged particles. The TOTEM [91] detectors are located on both sides of the interaction point at CMS experiment to takes precise measurements of protons as they emerge from collisions at small angles to the beam pipe, aiming at a peak luminosity of $\mathcal{L} = 2 \times 10^{29}cm^{-2}s^{-1}$. This region is known as the 'forward' direction and is inaccessible by the CMS detector. Its physics programme aims at a deeper understanding of the proton structure as well as monitoring the LHC luminosity. The

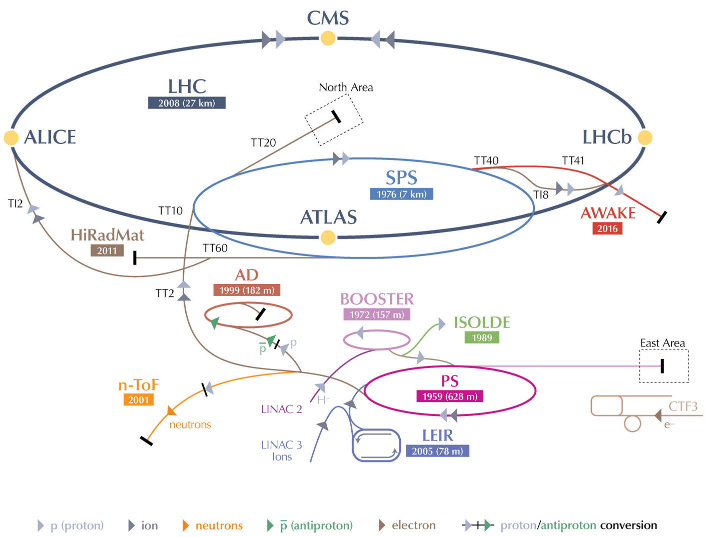

Figure 3.1: The LHC accelerator complex. [93]

LHCf [89] detectors also designed to measure very forward particles emitted at nearly zero degrees to the direction of the proton beam, optimized to operate with luminosity below $\mathcal{L} = 10^{30}cm^{-2}s^{-1}$. LHCf's detectors are located along the LHC beam line, at 140 metres either side of the ATLAS collision point. The physics goal of this experiment is to provide data for calibrating the hadron interaction models that are used in the study of Extremely High-Energy Cosmic-Rays. ALICE [92] is designed as a dedicated heavy-ion experiment with the prime aim to study nuclear collisions at LHC. It is aimed for operating at the peak luminosity of $\mathcal{L} = 10^{27}cm^{-2}s^{-1}$ for nominal lead-lead ion operation. The high-energy heavy-ion collisions at LHC provide a possibility to study the transition from hadronic matter to a plasma of deconfined quarks and gluons.

The location of the biggest detectors at the LHC and the the CERN accelerator complex for proton beams are schematically shown in Figure 3.1. Before getting into the LHC, the protons are accelerated in several steps with the smaller accelerating complex. Proton beam formation starts with ionizing hydrogen gas which yields to bare protons which are directed into the linear accelerator LINAC 2 and accelerated to 50 MeV. Then protons are injected into the BOOSTER where they reach an energy of 1.4 GeV. The protons are further accelerated with the Proton Synchrotron (PS) to 25 GeV and then sent to the Super Proton Synchrotron (SPS) which pushes the beam to 450 GeV. After the SPS, protons are injected into the two beam pipes of the LHC where they are to be accelerated up to 7 TeV per beam. In one of the pipes beam circulates clockwise while in the another pipe - anti-clockwise. Since the protons are not the only particles accelerated in the LHC, the lead ion collisions start from a source of vaporized lead and enter Linac 3 before being collected and accelerated in the Low Energy Ion Ring (LEIR). They then follow the same route to maximum energy as the protons [94]. The two beams in the LHC are brought into collision inside the four detectors (ATLAS, CMS, LHCb and ALICE).

3.2 The ATLAS detector

3.2.1 General information

Coordinate system and useful variables

The nominal interaction point within the ATLAS detector determines the origin of the coordinate system, while the beam direction defines the z-axis and $x-y$ plane is transverse to the beam direction. The positive x-axis points from the interaction point to the center of the LHC ring and the positive y-axis points upwards such that coordinate system is right-handed. The detector is split into two side where side-A is defined as that with positive z and side-C is that with negative z. The symmetry of the detector makes cylindrical coordinates useful. The azimuthal angle ϕ is the angle in xy-plane originating from the x-axis and increases clockwise when looking down the positive z-direction. The polar angle θ is defined as the angle with the positive z-axis. Instead of polar angle the pseudo-rapidity $\eta = -ln(tan\ \frac{\theta}{2})$ is often used, in the case of massive objects the rapidity is used. The rapidity is defined as $y = \frac{1}{2}ln\left(\frac{E+p_z}{E-p_z}\right)$ where E is the energy and p_z the longitudinal momentum of the object. In the limit where the particle is travelling close to the speed of light (highly relativistic particles), or equivalently in the approximation that the mass of the particle is negligible, pseudo-rapidity converges to the definition of rapidity ($m \ll p \Rightarrow \eta \simeq y$).

The distance in $\eta\phi$-plane is often used quantity and defined as $\Delta R = \sqrt{\Delta\eta^2 + \Delta\phi^2}$. The object's momentum in the xy plane is called transverse momentum and defined with x and y momentum components $p_T = \sqrt{p_x^2 + p_y^2}$.

Detector overview

ATLAS is a magnetic spectrometer with a forward-backward symmetry with respect to the interaction point which is designed to exploit the full physics potential of LHC. The detector consists of several components made of different materials aimed at detecting different types of particles. ATLAS is divided into four main parts: the inner detector(ID), calorimeter, muon spectrometer and magnet system. ID is the closest detector layer to the collision point which is aimed to reconstruct the position of an interaction (*vertex*) as well as trajectories of charged particles (*tracks*) and identify electrons. It is immersed in a solenoidal field created by surrounding superconducting solenoid. The calorimeter consists of two detectors: liquid-argon (LAr) electromagnetic calorimeter and hadronic calorimeter providing electromagnetic and hadronic energy measurements. All particles except muons and neutrino are stopped inside the calorimeter. The calorimeter is surrounded by the

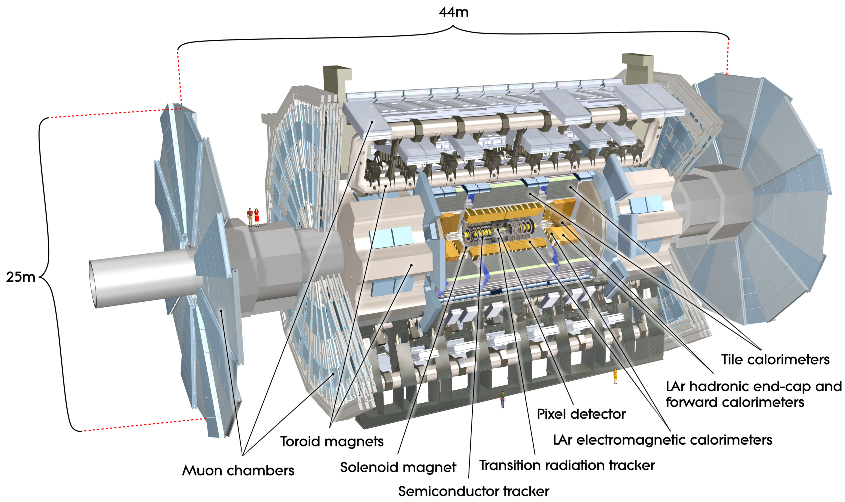

Figure 3.2: Cut-away view of the ATLAS detector. [95]

muon spectrometer. The muon system is submerged into magnetic field created with the air-core toroid system consists of barrel and two end-cap magnets. It minimises a multiple-scattering effects thereby increasing the muon momentum resolution of all three layers of tracking chambers. The muon instrumentation also includes, as a key component, trigger chambers. The muon spectrometer defines the overall dimensions of the ATLAS detector [86]. A cut-away view of the ATLAS detector is given in Figure 3.2.

3.2.2 The magnet system

The ATLAS magnet system (see Figure 3.3) consists of one solenoid and three toroids (one barrel and two end-caps). The central solenoid (CS) is designed to produce an axial magnetic field of 2 T at the center of the ID. Outside the CS the electromagnetic calorimeter is situated, therefore the solenoid's winding is designed as transparent as possible for traversing particles, resulting in the solenoid assembly contributing a total of ~ 0.66 radiation lengths at normal incidence. The single-layer coil wound with a high-strength Al-stabilised $NbTi$ conductor. The solenoid is 0.1 m thick and its axial length is 5.8 m. The barrel and two end-cap toroids produce a magnetic field of approximately 0.5 T and 1 T for the muon detectors in the central and end-cap regions, respectively. The barrel toroid surrounds calorimeters and both end-cap toroids. It consists of eight coils encased in individual racetrack-shaped, stainless-steel vacuum vessels. The size of the barrel toroidal system is 25.3 m in length with inner and outer diameters of 9.4 m and 20.1 m, correspondingly. The magnetic field generated by end-cap toroids is required for optimizing the bending power in the end-cap muon spectrometer regions. Each end-

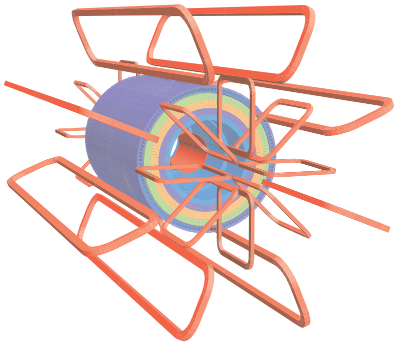

Figure 3.3: Schematic diagram of the ATLAS magnet system (in red). The eight barrel toroid coils and eight pairs of end-cap coils are showed. The solenoid winding is inside the calorimeter volume which is modelled by four layers and outside return yoke (discussed in Section 3.2.4). [86]

cap toroidal magnet consists of eight coils with a length of 5.0 m and with inner and outer diameters of 1.65 m and 10.7 m. The conductor (Al-stabilised $Nb/Ti/Cu$) and coil-winding technology in the barrel and end-cap toroids are essentially the same.

3.2.3 The inner detector

The Inner detector is located inside the solenoid magnet, which provide the magnetic field to bend the charged particles for the momentum measurements. It consists of three sub-detectors: the pixel and silicon micro-strip (SCT) trackers and the transition radiation tracker (TRT). Pixel and SCT cover pseudo-rapidity region $|\eta| < 2.5$, while TRT covers up to $|\eta| < 2$. The ID components are subdivided into a barrel part, forming concentric cylinders around the beam pipe, and two end-caps, where they are grouped in disks perpendicular to the beam axis. A schematic layout of the ID and its components are shown in Figure 3.4.

The Pixel Detector

The Pixel Detector [96, 97] is the inner-most part of the ATLAS tracking system. It consists of four layers of barrel pixel detector and two end-caps of three pixel disks each. The pixel end-caps and three outer barrel layers were installed into ATLAS originally in 2007 and referred as 3-Layer Pixel Detector system. The innermost barrel pixel layer is a newly constructed high-resolution pixel detector and called Insertable Barrel Layer (IBL) [98]. It was installed in 2013-2014 after replacing the beam pipe with the smaller one. The IBL is located approximately 5 mm away from the beam pipe. Figure 3.5 shows the 4-Layer ATLAS Pixel Detector for LHC Run-2 and the radial placement of the pixel

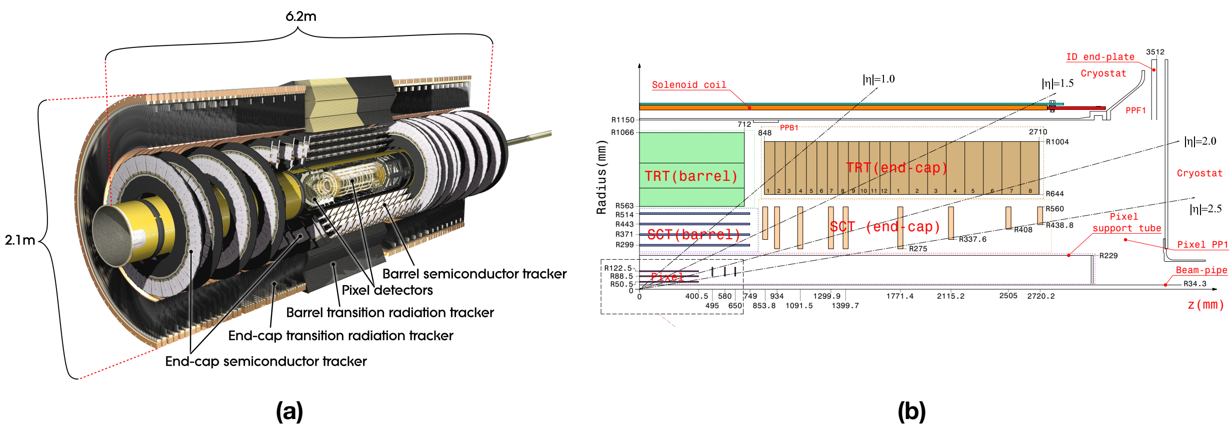

Figure 3.4: Schematic cut-away view of the ATLAS ID (a) and its quarter-section plan view indicating η coverage of each sub-detector. The labels PP1, PPB1 and PPF1 indicate the patch-panels for the ID services. [86]

barrels.

The initial 3-Layer Pixel Detector is designed to have a high granularity and spatial resolution for precise measurements of primary and secondary vertices. The pixel sensors of the detector have a minimum size of $50 \times 400\ \mu m^2$. The intrinsic accuracy of the barrel layers (end-cap discs) are $10\ \mu m$ in $R - \phi$ and $115\ \mu m$ in z (in R). The sensors are $250\ \mu m$ thick detectors which have the oxygenated n-type bulk with high positive p^+ and negative n^+ dose regions on each side of the silicon wafer. The readout pixels are placed on the n^+-implanted side of the detector. Such design has several important advantages. The n^+ implants allow the detector operate with high charge-collection efficiency after type inversion even below the depletion voltage. The highly oxygenated material has the increased radiation tolerance to charged hadrons. The sensors are initially operate at the bias voltage of $150\ V$ and temperature of $-5\ C^\circ$, but after ten years of operation the bias voltages of up to $600\ V$ will be increased, while the operating temperature will be decreased down to $-10\ C^\circ$.

The IBL is designed for operating at the peak luminosity of $> 2 \times 10^{34} cm^{-2}s^{-1}$ and high number of over-lapping interactions in a single bunch-crossing at different operation modes ($25\ ns$ and $50\ ns$ bunch spacing). Furthermore, the IBL provides the increased robustness in pattern recognition and tracking if efficiency is lost due to radiation damage or faults on individual modules [98]. It is designed to withstand 250 MRad of ionizing and $5 \times 10^{15} n_{eq}/cm^2$ non-ionizing dose.

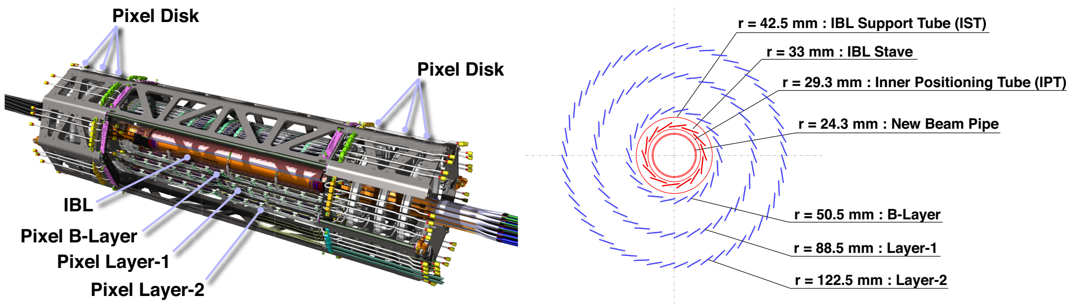

Figure 3.5: Schematic cut-away of 4-Layer Pixel Detector system (left) and the radial placement of pixel barrels, beam pipe and support carbon-fibre cylinders (IPT, IST) (right). [97]

The Semiconductor Tracker

The Semiconductor Tracker (SCT) is a silicon micro-strip detector. It consists of a barrel made of four cylinders and two end-caps each of nine disks. In the barrel region each layer consists of two set of strips with a small stereo angle of 40 $mrad$ with respect to each other, which allows two-dimensional (in $\phi - z$) position measurement. One set of strips in each layer are parallel to the beam direction. In the end-cap discs one set of strips runs radially from the beam pipe. For the SCT, the single-sided p-in-n silicon sensors with AC-coupled readout strips are used. The sensor thickness is of 285 ± 15 mm. The spatial resolution of the barrel (end-cap) region is 17 μm in $R - \phi$ and 580 μm in z (R). The initial bias voltage for the sensors is ~ 150 V, but after ten years of operation it will be between 250 V and 350 V depending on the sensor position, the integrated luminosity and the length of warm-up periods. To reduce a leakage current, which increase the detector noise, and to prevent the annealing of the sensors, the SCT operates at -7 C°. Sensors are designed to withstand radiation doses of up to 2×10^{14} n_{eq}/cm^2 and operate stably at bias voltage of up to 500 V.

The Transition Radiation Tracker

The Transition Radiation Tracker is the outermost and largest of the three tracking subsystems of the ATLAS ID. Its basic elements are thin-walled drift tubes, which are bonded back-to-back and called *strawtubes* or simply *straws*. Straws in the barrel part of TRT are 144 cm in length and oriented parallel to the beam, whereas 37 cm in length straws in barrel part are radially aligned to the beam axis. Due to the detector geometry, particles cross $35 - 40$ straws in a pseudorapidity interval from 0 to 2, providing continuous tracking at larger radii of the ID while enhancing its pattern recognition ability. The straw (cathode) tube wall is made of two layers of a 35 μm thick Kapton 100VN multilayer film [99]. The anodes in the center of each tube are made of 31 mm diameter tungsten

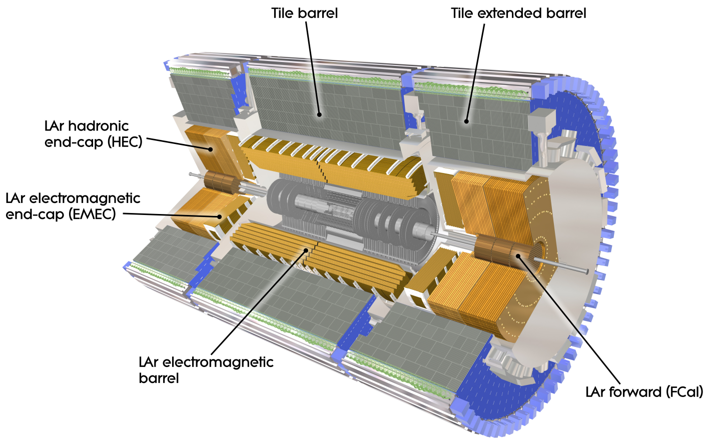

Figure 3.6: Cut-away view of the ATLAS calorimeter system. [101]

wires plated with 0.50.7 mm gold and supported at the straw end by an end-plug. Straws are filled with the gas mixture of 70% Xe, 27% CO_2, 3% O_2. Charged particles traversing the TRT ionise the gas inside the straws. The resulting free electrons drift towards the wire, where they are amplified and read out. The spaces between the straws are filled with polymer fibres in the barrel and foils in the end-caps. Highly relativistic charged particles emit the transition radiation traversing a material boundary. Given effect depends on the relativistic factor $\gamma = E/m$ and is strongest for electrons. Therefore, the emission of transition radiation is much more likely for an electron than for a pion of the same momentum. The use of different thresholds provides the electronhadron discrimination over a wide energy range.

3.2.4 The calorimeter system

The ATLAS calorimeter system [86, 100] consists of electromagnetic (EM) and hadronic subsystems which covers pseudorapidity ranges $|\eta| < 3.2$ and $|\eta| < 4.9$, correspondingly. Over the η region matched to the ID, the EM calorimeter has a fine granularity suited for precision measurements of electrons and photons, while coarser granularity is used for the rest calorimeter parts which is sufficient for the reconstruction of jets and missing transverse energy. Calorimeter system also provide a containment for electromagnetic and hadronic showers, limiting punch-through into the muon detectors. Therefore, the thickness of calorimeter detectors in terms of radiation lengths (X_0) is important for their design. The thickness of EM calorimeter in the barrel is $> 22X_0$ and $> 24X_0$ in the end-caps, which correspond to approximately 9.7 and 10 interaction lengths, respectively. Figure 3.6 shows a cut-away view of the calorimeter systems.

The Electromagnetic Calorimeter

The Electromagnetic Calorimeter is divided into tree parts: barrel, which covers $|\eta| < 1.475$, and two end-caps (EMEC), which cover $1.375 < |\eta| < 3.2$. Each EMEC is divided into two coaxial wheels, an outer wheel covers the region $1.375 < |\eta| < 2.5$, while an inner wheel covers the region $2.5 < |\eta| < 3.2$. The EM calorimeter is a lead-LAr detector with accordion-shaped kapton electrodes and lead absorber plates. Due to accordion geometry the EM calorimeter is symmetric in ϕ and does not have azimuthal cracks. The lead thickness in the absorber plates is chosen as a function of η for energy resolution optimization.

In the region $|\eta| < 2.5$, relevant for precision physics, the EM calorimeter is longitudinally segmented into three layers. The first layer is finely segmented along η allowing for a precise position measurements. It also gives an opportunity for individual photon reconstruction. The second layer collects the largest fraction of the electromagnetic shower energy, while the third layer collects the tail of the shower, therefore it is less segmented in η.

Similarly to EM calorimeter, the precision region in the end-cap electromagnetic calorimeters, $1.5 < |\eta| < 2.5$, is divided into three longitudinal layers. The front layer is $4.4X_0$ thick and segmented along η direction. The middle layer has the same cell size as the barrel EM and the back layer has a twice coarser granularity. The outermost region $|\eta| < 1.5$ of the outer wheel and the inner wheel are segmented in two longitudinal layers and have a coarser transverse granularity [86].

The Hadronic Calorimeter

The ATLAS hadronic calorimeter covers the pseudorapidity range of $|\eta| < 5$. It consists of three main parts: tile calorimeter, hadronic end-cap calorimeter and forward calorimeter, which are suited for the different requirements and radiation environment.

The tile calorimeter is split into the barrel part, covers $|\eta| < 1.0$, and two extended barrels which cover the range $0.8 < |\eta| < 1.7$. It is a sampling calorimeter, which consists of layers of steel absorber and scintillating tiles as the active material. Tile calorimeter is segmented in depth into three layers. For the barrel part the thickness of each segment is 1.5λ, 4.1λ and 1.8λ, while for the extended barrel it is 1.5λ, 2.6λ and 3.3λ. This thickness is sufficient to reduce the punch-through below the irreducible level of prompt or decay muons.

The hadronic end-cap calorimeter (HEC) comprises two wheels per end-cap. It covers pseudorapidity range $1.5 < |\eta| < 3.2$ thereby overlapping with the forward and tile calorimeters. Cooper plates are used as an absorber, they are interleaved with LAr gaps, which provide an active medium. The thickness of the plates are 25 mm for the inner wheels, while 50 mm for the outer wheels. The LAr gaps for both wheels is 8.5 mm.

The Forward Calorimeters (FCal) are located in the same cryostat as the end-cap

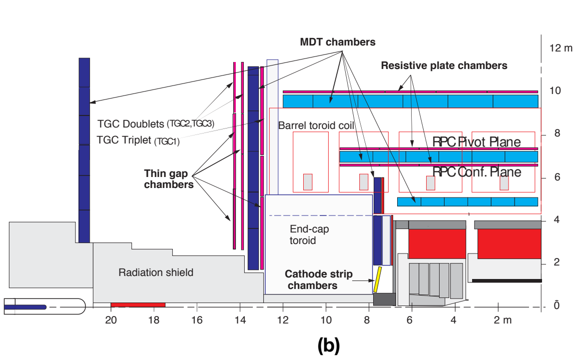

Figure 3.7: Schematic view of the muon spectrometer in the $x - y$ (a) and $z - y$ (b) projections. [102]

calorimeter and provide coverage in the region $3.1 < |\eta| < 4.9$. Each FCal end-cap consists of three modules: the first, made of cooper, is optimized for electromagnetic measurements, and the rest two, made of tungsten, measure predominantly hadronic energy deposition. Due to the high particle fluxes, FCal modules have small LAr gaps, comparing to 2 mm in electromagnetic barrel calorimeter, to avoid ion build-up problems and to provide at the same time the highest possible density.

3.2.5 The muon spectrometer

The muon spectrometer [86] is the outermost part of the ATLAS detector which is designed for detecting charged particles that comes out from the calorimeter detectors and measuring their momentum in the pseudorapidity range $|\eta| < 2.7$ as well as triggering on these particles in $|\eta| < 2.4$. Spectrometer integrates four detector subsystems, among which the monitored drift tube (MDT), cathode strip chambers (CSC), resistive plate chambers (RPC), thin gap chambers (TGC), as well as barrel and end-cap toroid magnets (introduced in Section 3.2.2). The muon tracking chambers in the barrel region are located between and on the eight coils of the barrel toroid magnet, whereas the end-cap chambers are in front and behind the two end-cap toroid magnets. Symmetry of the toroids in ϕ is reflected in the symmetry of the muon chamber system. The muon track momentum measurements are based on track deflection in the muon chambers by virtue of the magnetic field created with toroid magnets. Schematic view of the muon spectrometer is given in Figure 3.7. There is a gap in the chamber coverage at the center of the detector ($|\eta| \approx 0$), which has been left open for the services for the solenoid magnet, the calorimeters and the inner detector. The gap size varies from sector to sector, depending on the service necessities. There are additional gaps in the acceptance in sectors 12 and 14 due to the detector support structure.

The MDT chambers cover pseudorapidity range $|\eta| < 2.4$ with exception for the innermost end-cap layer, which covers $|\eta| < 2.0$. The chambers are made of multi-layers of drift tubes which are filled with the gas mixture 73% Ar, 7% CO_2 and have tungsten-rhenium anode in the center of each tube. The resolution per tube is 80 μm and about 35 μm per chamber.

The CSC's cover the forward region $2 < |\eta| < 2.7$ and are used in the innermost tracking layer due to their higher rate capability and time resolution. The resolution of chambers is 40 μm in the bending plane and about 5 mm in the transverse plane.

Muon tracking chambers are complemented with a system of fast trigger chambers, RPC and TGC, capable of delivering information in $15 - 20$ ns after particle passage. Thus, they can be used to tag the beam-crossing. RPC covers barrel pseudorapidity range $|\eta| < 1.05$, while TGC covers end-cap region $1.05 < |\eta| < 2.4$. The trigger chambers measure coordinates of the track in the η (bending) and ϕ (non-bending) planes.

3.2.6 Forward detectors

There is a smaller set of detectors located in a very forward region at larger distance from the interaction point comparing to the introduced main ATLAS detector systems. The closest detector is LUCID (LUminosity measurement using Cerenkov Integrating Detector), it is located at the distance of 17 m on either side of the interaction point. LUCID is a relative luminosity detector in ATLAS. Its main purpose is to detect inelastic $p - p$ scattering in the forward direction, in order to measure the integrated luminosity and to provide monitoring of the instantaneous luminosity and beam conditions [86].

The second after LUCID is the Zero-Degree Calorimeter (ZDC), located at the distance of ± 140 m from the interaction point, where the LHC beam-pipe is divided into two separate pipes. Its main purpose is to detect forward neutrons with $|\eta| > 8.3$ in heavy-ion collisions.

The farthest detector, located at approximately 240 m on either side of the interaction point, is the ALFA (Absolute Luminosity For ATLAS). It consists of scintillating-fibre trackers located inside Roman pots. ALFA is used for the measurement of elastic pp-scattering and small angles in the Coulomb-Nuclear Interference region.

3.2.7 The trigger and data acquisition system

To reduce the data flow from $\sim$ 60 million megabytes per second to manageable levels, where only events with distinguishing characteristics that make them interesting for physics analyses are selected, ATLAS uses a specialised multi-level Trigger System. The ATLAS trigger system carries out the selection process in three stages: Level-1, Level-2 and event filter. The Level-1 (L1) trigger is implemented using custom-made electronics, while Level-2 (L2) and event filter, which together form the High-Level Trigger (HLT), are almost entirely based on commercially available computers and networking hardware [86]. A block diagram of the trigger and data acquisition systems is shown in Figure 3.8.

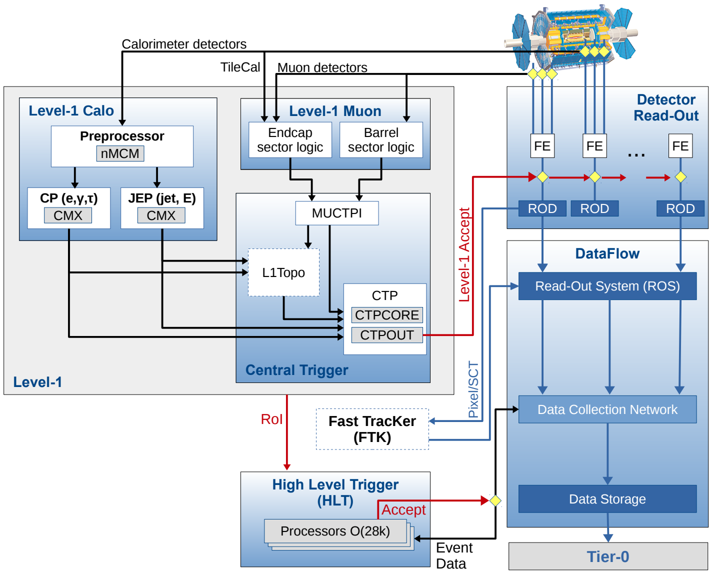

Figure 3.8: Block diagram of the ATLAS trigger and data acquisition systems. [103]

The L1 trigger decision is formed by the Central Trigger Processor (CTP), which receives information from calorimeter (electromagnetic and hadronic) and muon (RPC and TGC) detectors. The L1 Calorimeter Trigger (L1Calo) identifies objects with high transverse energy, such as electrons, photons, jets, τ-leptons decaying into hadrons, as well as events with large missing and total transverse energy. Additional isolation requirement for electrons, photons, jets and τ triggers can be required to provide angular separation from any significant energy deposit in the same trigger. The L1 muon trigger (L1Muon) searches for hit patterns consistent with high-p_T muons which originate from the interaction region. It has six programmable p_T thresholds, therefore for each bunch crossing L1Muon trigger uses information of muon multiplicity for each p_T threshold.

The CTP is also responsible for applying preventive dead-time. It limits the minimum time between two consecutive L1 accepts ($simple\ dead - time$) to avoid overlapping readout windows, and restricts the number of L1 accepts allowed in a given number of bunch-crossings ($complex\ dead - time$) to avoid front-end buffers from overflowing [103].

After the event acceptance by L1 trigger, it is buffered in the Read-Out System (ROS). The HLT receives Region-of-Interest (RoI) information from L1 which is used for regional reconstruction in the trigger algorithms. RoI are the regions of the ATLAS detector where L1 identified possible trigger objects within the event. Basing on RoI information (coordinates, energy, type of signature), L2 trigger limits the amount data which will be transferred from the detector readout.

To reduce the event rate from the pp collisions with the LHC luminosity of $2 \times 10^{34} cm^{-2} s^{-1}$, the ATLAS trigger system is under upgrading with a new Fast TracKer

(FTK). Its installation to ATLAS started in 2013 and full integration planned to be completed in 2018 [104]. The FTK [103, 105] is an electronics system that finds and reconstructs tracks in the pixel and SCT detectors for every event that passes the L1 trigger. After processing, FTK fills ROSs with the helix parameters and hits for all tracks with p_T above a minimum value, typically 1 GeV. Therefore, FTK enables the L2 trigger to have early access to tracking information in a RoI of the ID.

Each event which has been selected by the L2 trigger is assigned by the DataFlow Manager (DFM) to an event-building node, which builds a single event-data structure, *event*. Then the full event structure is sent to the event filter for further selection and classification. The classified event files are subsequently transferred to CERN's central data-recording facility.

Chapter 4

Data and Monte Carlo

4.1 Data samples

During 2015 year LHC was running with 50 ns and 25 ns bunch spacings, therefore there are two types of data sets. Each of them is used for the separate $Z \to \ell^+\ell^-$ analyses. During the data taking period, the conditions were changing. Some data are collected with toroid and IBL off or with special b-jet trigger conditions. Cosmic and detector calibration data were taken also as separate runs. Thus, each data set is divided into periods with some specifications. The data periods with all ATLAS detector components turned on and operating at nominal conditions for both data sets are used in $Z \to \ell^+\ell^-$ analyses.

A different data taking efficiency for runs in each period is caused by different detector issues: appearing of the noisy or dead channels in the readout systems of sub-detectors, high voltage trips, LAr noise bursts, wrong trigger settings. To reflect the overall quality of the data, special status flags are introduced in the *GoodRunsLists* [106] package. The Data Quality (DQ) flags represent the sub-detector-, trigger-, and reconstruction-level. Combined performance flags define good physics objects: electron, muon, jets, etc.), therefore different requirements for the flags are used for various analyses. The flags are assigned for every subsystem per luminosity block (minute data peace of run). The filtering on DQ flags is provided in the Athena framework [107]. Using filtered DQ flags, the lists of runs, called as Good-Run List (GRL) [108], are constructed for each type of analysis. Thereby, usage of GRL in the data analyses provides a preselection step. Each GRL file for a data set contains all runs which are divided on flagged luminosity blocks (LBs). The integrated luminosity of data set is calculated due to selected flags of luminosity blocks in an appropriate GRL file.

Period	Run number	# LBs	Luminosity [pb^{-1}]
A4	267638	637	3226.58
	267639	514	2853.44
C2-C5	270806	48	744.88
	270953	333	4403.29
	271048	489	6458.93
	271298	425	9581.48
	271421	322	13057.52
	271516	315	18945.42
	271595	227	15951.15
	271744	142	6042.88
Total		3452	81.27

Table 4.1: 13 TeV 50 ns bunch spacing pp collision runs used in $Z \to \ell^+\ell^-$ analyses. Number of luminosity blocks per run correspond to good luminosity blocks recorded in the good runs list. The integrated luminosity per run as well as the total integrated luminosity is shown.

4.1.1 Data at 50 ns bunch spacing

50 ns bunch spacing data were collected between June 13 and July 16, 2015. Data periods A4 and C2-C5 were used for both $Z \to e^+e^-$ and $Z \to \mu^+\mu^-$ analyses. In these periods the LHC circulated 6.5 TeV proton beams. The peak delivered instantaneous luminosity in period A4 was $\mathcal{L} = 1.5 \times 10^{32} cm^{-1} s^{-1}$, and the peak mean number of pileup events, $< \mu >= 27$. In periods C2-C5, the peak of delivered instantaneous luminosity was $\mathcal{L} = 17.2 \times 10^{32} cm^{-1} s^{-1}$ (see Figure 4.1), measured during C4 period, and the peak mean number of pileup was $< \mu >= 28$. The average pileup during full 50 ns data taking period was found at the level of $< \mu >= 20$, (see Figure 4.2).

To preselect "good" events from the data samples, the $GRL^{(50ns)}$ file [1] is used for both electron and muon channels. Preselected runs and corresponding luminosities for each period as well as total integrated luminosity of the data used in $Z \to \ell^+\ell^-$ analyses are showed in the Table 4.1. The total integrated luminosity of the data used in the analyses is $\int \mathcal{L} = 81 pb^{-1}$. The measurement of the integrated luminosity has a 2.1% uncertainty. It is derived, following a methodology similar to that detailed in [109], from a calibration of the luminosity scale using xy beam separation scans performed in August 2015.

4.1.2 Data at 25 ns bunch spacing

The data collected between August 16 and November 03, 2015, during periods D-J, when the LHC circulated 6.5 TeV proton beams with 25 ns bunch spacing, are used

[1] data15_13TeV.periodAllYear_DetStatus-v63-pro18-01_DQDefects-00-01-02_PHYS_StandardGRL_All_Good.xml

Period	Run numbers	# LBs	Luminosity $[pb^{-1}]$
D	276954, 276952, 276790, 276778, 276689 276511, 276416, 276336, 276329, 276262	1602	71.81
E	278880, 278912, 278968, 279169, 279259, 279279, 279284, 279345, 279515, 279598, 279685, 279764, 279813, 279867, 279928	5466	441.86
F	279932, 279984, 280231, 280273, 280319, 280368	2487	279.18
G	280423, 280464, 280500, 280520, 280614 280673, 280753, 280853, 280862, 280950, 280977, 281070, 281074, 281075	5085	716.88
H	281317, 281385, 281411	1251	220.52
J	282625, 282631, 282712, 282784, 282992, 283074, 283155, 283270, 283429, 283608, 283780, 284006, 284154, 284213, 284285, 284420, 284427, 284484	7393	1427.88
Total		23284	3158.13

Table 4.2: 13 TeV 25 ns bunch spacing pp collision runs used in $Z \to \ell^+\ell^-$ analyses. Number of luminosity blocks per run correspond to good luminosity blocks recorded in the good runs list. The integrated luminosity per run as well as the total integrated luminosity is shown.

for $Z \to \ell^+\ell^-$ analyses. In these periods, the peak instantaneous luminosity was $\mathcal{L} = 5.1 \times 10^{33} cm^{-1} s^{-1}$ (is shown in Figure 4.1) and the average number of pileup events was $<\mu>= 17$ (see Figure 4.2).

The GRL file $GRL^{(25ns)}$ [2] is used to select "good" luminosity blocks in the runs of all collected data at the periods D-J. The total integrated luminosity after the preselection with GRL is $\int \mathcal{L} = 3.16\ fb^{-1}$. The luminosity uncertainty is similar to 50 ns runs. Detailed list of data periods, run numbers and corresponding luminosities is expressed in Table 4.2. The distribution of cumulative luminosity collected during data taking periods with 50 ns and 25 ns bunch spacings in 2015 year as a function of time, is shown in Figure 4.1.

4.2 Monte Carlo samples

Monte Carlo (MC) simulations are used to optimize the data selection criteria, evaluate the selection efficiency for signal events, estimate the contribution of background processes

[2] data15_13TeV.periodAllYear_DetStatus-v73-pro19-08_DQDefects-00-01-02_PHYS_StandardGRL_All_Good_25ns.xml

to the analysed data set and assess the systematic uncertainties. Due to the difference in pileup conditions for 50 ns and 25 ns bunch spacing, two Monte Carlo productions are performed. The result of $MC15a$ Monte Carlo production [110] is used for $Z \to \ell^+\ell^-$ signal and background descriptions at 50 ns bunch spacing, whereas $MC15b$ [111] samples are used for 25 ns bunch spacing analyses. The MC15b is build upon the MC15a campaign but with an improved μ profile in reconstruction. The MC15a samples are created with the release 20.1.4.4 of `AtlasProduction` using the setup for 50 ns bunch spacing, while MC15b are produced in 20.1.5.10.1 release with the setup for 25 ns bunch spacing. The comparison of mean number of interactions per bunch crossing at 50 ns and 25 ns bunch spacing conditions derived from the data is shown in Figure 4.2. However, due to the sameness of the physics processes and the rest conditions at both bunch spacings, MC15a and MC15b productions are performed with the same generator, at the same perturbation order.

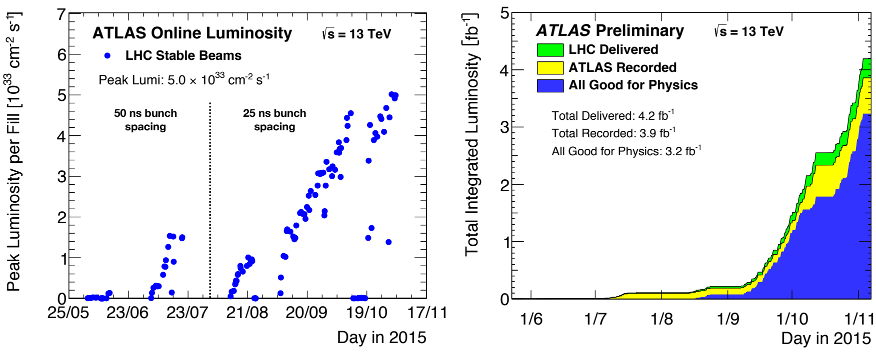

Figure 4.1: The peak instantaneous (left plot) and cumulative (right plot) luminosity delivered to ATLAS during stable beams for pp collisions at 13 TeV centre-of-mass energy for each LHC fill as a function of time in 2015.

The ATLAS MC production consists of few main steps: generation, simulation and digitalization. MC generation starts with calculation of decay matrix elements (at some order of α_s and α_{EW}), then parton showers calculation takes place. When parton showers calculation done, the hadronization of the generated partons with further decays of produced hadron is computed. At the simulation step all generated particles are propagated through the ATLAS detector. This step describes the interaction of the generated particles with detecting material using GEANT4 [112] package. The digitalization exposes the GEANT4 hits to the detector response to produce the digital signal in terms of ADC and TDC. After MC sample is produced, the reconstruction of simulated events takes place.

In $Z \to \ell^+\ell^-$ analyses several Monte Carlo samples for signal and background determination are produced with different generators. All of the signal, $Z \to e^+e^-$ $(Z \to \mu^+\mu^-)$, and single-boson electroweak background samples are generated with the POWHEG program [113–115], interfaced with the Pythia v8.1 parton shower program [116]. The CT10

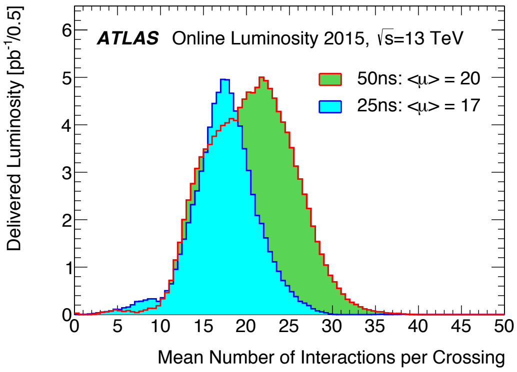

Figure 4.2: Luminosity-weighted distribution of the mean number of interactions per bunch crossing for the 2015 pp collision data at 13 TeV centre-of-mass energy.

parton distribution functions [24] are used. For bottom and charm hadronization properties, the EvtGen v1.2.0 [118] program is used. The Photos++ v3.52 [119] generated QED radiation from electroweak vertices and charged leptons. The di-boson events are generated with Sherpa v2.1.1 program [120].

The $t\bar{t}$ events are generated with Powheg-Box v2 [113–115] , which uses the four-flavour scheme for the NLO matrix element calculations together with fixed four-flavour PDF set CT10f4. The parton shower and fragmentation are simulated using Pythia 6.4 [123] with the CTEQ6L1 PDF sets and the corresponding Perugia 2012 tune [121]. The generated distributions are normalized to the cross sections calculated with the Top++ 2.0.

Multiple overlaid proton-proton collisions are simulated with the soft QCD processes of Pythia v.8.1 [116] using the A2 [122] tune and the MSTW2008LO PDF. The pileup distributions of the generated MC samples are reweighted due to the measured (see Section 6.4). A full list of all simulated event samples used in the $Z \to \ell^+\ell^-$ analyses of 50 ns and 25 ns bunch spacing data is shown in the Table 4.3.

Channel	Dataset ID	Generator	Order	$\sigma \cdot \mathrm{BR} \cdot \epsilon_{\mathrm{filter}}$ (pb)	Theo unc.(%)
$Z \to ee$	361106	POWHEG Box [113–115] + PYTHIA8 [116]	NNLO	1892	5
$Z \to \mu\mu$	361107			1892	
$Z \to \tau\tau$	361108			1892	
$W^+ \to e\nu$	361100			11501	
$W^+ \to \mu\nu$	361101			11501	
$W^- \to e\nu$	361103			8579	
$W^- \to \mu\nu$	361104			8579	
$WZ \to qqll$	361084	SHERPA2.1.1 [120]	NLO	3.76	7
$ZZ \to qqll$	361086			$16.59 \cdot 0.14$	5
$WW \to l\nu l\nu$	361600			10.63	5
$t\bar{t}$	410000	POWHEG Box [113–115] + PYTHIA6 [123]	NNLO + NNLL	451	6

Table 4.3: Simulated event samples used in this measurement and their predicted cross sections as given in the AMI database (and so are only NLO for the signal samples).

Chapter 5

Measurement of $Z \to \ell\ell$ integrated cross section

The inclusive cross section definition as well as the methodology of signal-event reconstruction using a selection of lepton candidates and an estimation of background expectation are described in this chapter. The aim of Z production cross-sections measurements is to use it for the calculation of ratios with the $t\bar{t}$ and W cross sections. For this purpose the Z event selection software packages are fully synchronized to the ones used for the $t\bar{t}$ and W analyses.

5.1 Cross-section definition

The inclusive cross section times the branching ratio (BR) for the process $Z \to \ell\ell$ is determined with the formula:

$$\sigma_Z^{fid} \times BR(Z \to \ell\ell) = \sigma_Z^{tot} \times BR(Z \to \ell\ell) \cdot A_Z = \frac{N - B}{C_Z \cdot E_Z \cdot \mathcal{L}}, \tag{5.1}$$

where σ_Z^{fid} is the Z-boson cross section in the fiducial phase space of the measurement and σ_Z^{tot} denotes the cross section in the full phase space. N is defined as the number of reconstructed signal-event candidates and B is an estimated number of background events. C_Z corrects the number of reconstructed events to all events in the fiducial volume of the detector. A_Z is an acceptance factor which extrapolates from fiducial to total phase space of the cross-section measurement. E_Z is the extrapolation factor from fiducial volume of the measurement to the common phase space. This factor contributes to the combination of measurements at different fiducial volumes. $\mathcal{L}$ is the integrated luminosity. Definitions of C_Z, A_Z and E_Z factors as well as fiducial volume are given in Section 5.2.

	7 TeV	8 TeV	13 TeV
$p_{T,\ell} >$	20 GeV	20 GeV	25 GeV
$\lvert\eta_\ell\rvert <$	2.5	2.4	2.5
$\lvert y_{\ell\ell}\rvert <$	-	2.4	-
$m_{\ell\ell}$	66-116 GeV	66-116 GeV	66-116 GeV

Table 5.1: Z-boson fiducial-volume definition at 7, 8, and 13 TeV.

	50ns		25ns	
	Electron channel	**Muon channel**	**Electron channel**	**Muon channel**
	value ± stat ± syst	value ± stat ± syst	value ± stat ± syst	value ± stat ± syst
C_Z	$0.552 \pm 0.0003\ ^{0.0055}_{-0.0055}$	$0.711 \pm 0.0003\ ^{0.0075}_{-0.0075}$	$0.5536 \pm 0.0002\ ^{+0.0028}_{-0.0029}$	$0.7064 \pm 0.0003\ ^{+0.0057}_{-0.0057}$

Table 5.2: Central values of C_Z correction factors for electron and muon channels, its statistical and total systematic uncertainty (for 50 ns and 25 ns analyses).

5.2 C_Z, A_Z, E_Z and the fiducial-volume definition

A fiducial volume of the measurement is the part of the phase space covered by the detector, where events are considered as measurable. Lepton transverse momentum (p_T^ℓ), pseudorapidity (η_ℓ), rapidity (y_ℓ) and an invariant mass of a lepton pair ($m_{\ell\ell}$) are used for the fiducial volume definition for $Z \to \ell\ell$ analyses at different center-of-mass energies. Table 5.1 contains definitions of a Z-boson fiducial volume definitions for center-of-mass energies of 7 TeV, 8 TeV and 13 TeV.

The C_Z correction factor is defined as a ratio of number of reconstructed events which passed all selection criteria (Table 5.4) to the total number of generated events within the fiducial volume (Equation 5.2). Such definition provides connection between generator and reconstruction level objects. Thus, C_Z factor corrects measured cross section to events that contain lepton candidates which are in detector acceptance but were not reconstructed due to different effects.

$$C_Z = \frac{N_{MC}^{rec}}{N_{MC}^{gen,fid\ vol}}. \tag{5.2}$$

All corrections applied to the reconstructed-event (lepton) candidates are included in a given definition (N_{MC}^{rec} contains efficiency scale factors which are discussed in Chapter 6). They introduce appropriate systematic and statistical uncertainties to the cross section. Contributions from these uncertainties are discussed in Chapter 7. Because of different reconstruction methodologies, the C_Z factor is calculated for electron and muon channels separately. Central values of C_Z with total uncertainties at 13 TeV are listed in the Table 5.2.

Due to the same reconstruction conditions and methods of the measurements with 50 ns and 25 ns bunch spacing, C_Z factors are very close for the same channels. Electron channels at both bunch spacing have lower C_Z values due to overall worse reconstruction efficiency comparing to muons.

The geometrical acceptance A_Z is defined as a ratio of number of generated events within the fiducial volume to the number of events generated within the invariant-mass window:

$$A_Z = \frac{N_{MC}^{gen,fid\ vol}}{N_{MC}^{gen,mass\ cut}}. \tag{5.3}$$

Having both total and fiducial cross sections calculated using generated events, A_Z as an extrapolation factor from a fiducial to a total cross section, can be calculated as their ratio ($\sigma^{fid}/\sigma^{tot}$). Such approach is used to calculate A_Z factors at 13 TeV (50 ns and 25 ns). The central value of A_Z and its PDF, scale, α_S uncertainties for Z boson analysis with 50 ns data are calculated using the total and fiducial cross sections computed with DYNNLO 1.5 and CT14NNLO PDF set. Following similar approach the A_Z factor for Z analysis with 25 ns data is calculated with DYTURBO (fast version of DYNNLO 1.5). The central values of A_Z factors with total uncertainties are listed in Table 5.3. Geometrical acceptance is very close for both measurements at 13 TeV. It is observed that the acceptance factors tend to decrease as $\sqrt{s}$ increases.

Both C_Z and A_Z definitions use generator level events which are constructed of particle-level objects. The use of such objects reduces model dependence and provides an interface between experiment and theory. Generated final-state leptons which do not originate from hadrons (but from a Z boson as the mother particle in case of Z analysis) also called prompt leptons. Given that charged leptons can emit photons via QED final state radiation (QED FSR) processes, the definition of prompt charged leptons can be of three kinds: Born, bare, and dressed.

The Born leptons are pre-FSR leptons which correspond to the lowest-order diagram in the electromagnetic coupling. The bare leptons are post-FSR objects which contain QED FSR corrections. Dressed leptons are objects after partial QED radiation, they contain cone of photons around the direction of the bare lepton. In case of single Z or W analysis interference effects between initial and final state QED radiation for Born leptons can be neglected.

Born leptons are used as generated particle-level objects in Z analyses at 13 TeV. In A_Z definition generated leptons before QED FSR are used. Born level for leptons is best suited for NNLO predictions which usually do not include QED radiation. Such A_Z definition provides channel independence, therefore it gives similar number for electron and muon channels at the same center-of-mass energy and simplifies their combination procedure. Lepton-energy losses due to QED FSR are taken into account through the C_Z factor.

	$13\ TeV(50ns)$	$13\ TeV(25ns)$	$8\ TeV$	$7\ TeV$
A_Z	0.393 ± 0.007	0.395 ± 0.007	0.466 ± 0.008	0.505 ± 0.009
E_Z	-	-	0.941 ± 0.001	0.898 ± 0.001

Table 5.3: The extrapolation factors from fiducial to total phase space, A_Z, and from fiducial to common fiducial phase space, E_Z.

To have compatible fiducial Z-boson cross sections at different center-of-mass energies as well as their ratios and allow for a proper combination, E_Z factor has been introduced. It is defined as a ratio of cross section calculated in common fiducial volume for all measurements to the cross section calculated in fiducial volume of a given measurement:

$$E_Z = \frac{\sigma_{pred}^{common\ fid\ vol}}{\sigma_{pred}^{meas\ fid\ vol}}, \tag{5.4}$$

Components for E_Z definition are computed at Born level with DYNNLO 1.5 [34] for 50 ns analysis and DYTURBO for 25 ns analysis using CT14NNLO PDF set. Therefore, E_Z is also channel independent and cross sections used for its definition computed for $Z \to \ell\ell$ without splitting to electron and muon channels.

Fiducial volume of 13 TeV measurements was chosen as a common, therefore two E_Z factors were introduced ($E_Z^{8\ TeV}$ and $E_Z^{7\ TeV}$). The central values E_Z factors with total uncertainties are listed in the Table 5.3. Full list of total uncertainty components and methods of their calculation are discussed in the Section 7.3.

5.3 Event reconstruction and selection

The event selection can be naturally split into online and offline selection. The online selection is based on ATLAS trigger system, while the offline selection operates with already recorded objects into data samples. The connection between objects generated with trigger algorithms and offline recorded objects is realized with trigger matching. The offline preselection starts with the requiring quality conditions on the recorded data, monitored during the data-taking. Information about good quality runs are stored in GRL and used for Z analyses.

This section describes full selection of Z-boson candidates at electron and muon channels. The detailed electron selection and general muon selection are introduced. More details about muon selection are given in [124]. Summarized list of selection criteria for $Z \to e^+e^-$ and $Z \to \mu^+\mu^-$ events at 25 ns and 50 ns bunch spacing is expressed in the Table 5.4.

<table>
<tr><td>Cut name</td><td>50 ns</td><td>25 ns</td></tr>
<tr><td>GRL</td><td>GRL^{50ns}</td><td>GRL^{25ns}</td></tr>
<tr><td rowspan="2">Vertex and tracks</td><td colspan="2">one primary vertex with two associated tracks</td></tr>
<tr><td></td><td>$e: \ |S_{d_0}| < 5$ and $|\Delta z_0 \sin(\theta)| < 0.5\ mm$
$\mu: \ |S_{d_0}| < 3$ and $|\Delta z_0 \sin(\theta)| < 0.5\ mm$</td></tr>
<tr><td>ID</td><td colspan="2">e : Medium LH
μ : Medium Muon</td></tr>
<tr><td>ISO</td><td colspan="2">e : Gradient OP
μ : Gradient OP</td></tr>
<tr><td>Trigger</td><td>e : HLT_e24_lhmedium_iloose_L1EM20VH or HLT_e60_lhmedium

μ : HLT_mu20_iloose_L1MU15 or HLT_mu50</td><td>e (data): HLT_e24_lhmedium_L1EM20VH or HLT_e60_lhmedium or HLT_e120_lhloose
e (MC): e24_lhmedium_L1EM18VH or HLT_e60_lhmedium or HLT_e120_lhloose
μ : HLT_mu20_iloose_L1MU15 or HLT_mu50</td></tr>
<tr><td>Trigger matching</td><td colspan="2">At least one lepton candidates is required to match the lepton that triggered the event</td></tr>
<tr><td>p_T^ℓ</td><td colspan="2">> 25 GeV</td></tr>
<tr><td>η</td><td colspan="2">$e: \ |\eta| < 2.47$ and not $1.37 < |\eta| < 1.52$
$\mu: \ |\eta| < 2.4$</td></tr>
<tr><td>N leptons</td><td colspan="2">two oppositely charged leptons with the same flavour</td></tr>
<tr><td>Invariant mass window</td><td colspan="2">$66\ GeV < m_{\ell\ell} < 116\ GeV$</td></tr>
</table>

Table 5.4: Overview of the event selection criteria for $Z \to e^+e^-$ and $Z \to \mu^+\mu^-$ analyses of 25 ns and 50 ns bunch spacing data.

5.3.1 Track and vertex reconstruction

Due to the large number of charged particles produced in the proton-proton collisions, resulting in a large number of in the ATLAS inner detector, the track reconstruction algorithm has to distinguish the hits from different particles and define the trajectories that best match these hits. Detailed description of the tracks reconstruction in the Inner Detector is described in Ref. [126], [127].

Track finding strategy

Track reconstruction in ATLAS passes in several stages: clusterization, iterative combinatorial track finding, ambiguity-solving stage, neural-network pixel clustering, track fitting. A connected component analysis (CCA) [128] groups pixels and strips in a given sensor, where deposited energy yields a charge above threshold, into clusters. From these clusters, three-dimensional measurements referred to as $space-points$ are created. There are two types of clusters: $single\ particle\ clusters$ (created by charge deposited by one particle) and $merged\ clusters$ (created by multiple particles). Sets of three space-points are used to form track seeds. A combinatorial Kalman filter [129] is used to build track candidates from the chosen seeds and additional space-points from the remaining layers of the silicon detectors (Pixel and SCT). Filter creates multiple track candidates per seed where some number of space-points overlap. Such situation necessitate an ambiguity-solving stage. The ambiguity solver saves track candidates in descending order of track score, where clusters assigned to a track increase its score while existence of intersections of reconstructed track trajectory with an active detector area that does not contain matching clusters (*holes*), reduce the score. After the track scores have been calculated, the ambiguity solver limits number of shared clusters and clusters used in multiple track candidates. It also applies quality criteria [126] on the cinematic properties of the track and number of clusters and holes.

The neural-network (NN) pixel clustering [130] is used to minimize the efficiency losses due to limitations on the number of shared clusters per track. The network is trained to identify merged clusters. To improve its performance information about position of pixels in the cluster, measured charge, particle's incident angles is used as additional input information.

A high resolution fit is performed for track candidates which passed the selection implemented in ambiguity solver. The position and uncertainty of each cluster used in determined with additional NNs [130]. Fitted track which pass the ambiguity solver without modifications are added to the final track collection.

Track parametrization

A track reconstructed in the ATALS Inner Detector can be approximated as a helix (trajectory of charged particle in the magnetic field) and parametrized with respect to some arbitrary reference point. In the ATLAS the reference point is the global origin of the coordinate system as described in the Section 3.2.1. Perigee parametrization is used for helix representation, where the perigee of the track ($P(x_P, y_P, z_P)$) is defined as a point of closes approach to z-axis of the coordinate system. A detailed description of the track parametrisation is given in [131]. There are five perigee parameters:

- d_0 - transverse impact parameter. Defined as the signed distance of closest approach to the beam-line (z-axis) at the transverse plane ($X - Y$)
- z_0 - z-coordinate of the track at the point of closest distance in the transverse plain
- ϕ_0 - azimuthal angle of the track at the perigee point and x-axis
- θ - polar angle of the track at the perigee point and z-axis
- $\frac{q}{p}$ - ratio of particle charge to its momentum magnitude

The sign of d_0 parameter is negative if the track has positive angular momentum around the beam line. Perigee parametrization of the track in the ATLAS detector schematically shown at the Figure 5.1.

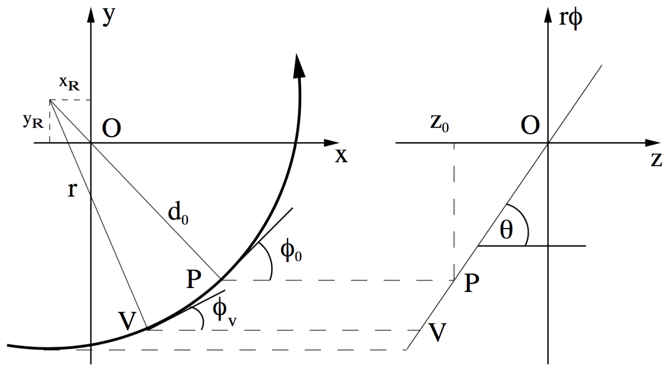

Figure 5.1: Illustration of track parametrization in ATLAS detector with perigee parameters in the transverse (left) and RZ plane (right).

Vertex reconstruction

Finding common intersection points between sets of reconstructed tracks allows to identify the proton-proton interaction point as well as decay vertices of unstable particles produced in the collisions. Most of the reconstructed tracks from proton-proton collision in ATLAS originate from the collision point, indicating the *primary vertex* of that collision. The reconstruction of primary vertices can be divided in two stages: primary vertex finding and fitting. Primary vertex finder provides association of reconstructed tracks to a particular vertex candidate, while fitter is a tool which takes some input tracks and eventual additional information and returns a vertex. Therefore, vertex finder is a client of a vertex fitter, it gives tracks to the fitter and receives a reconstructed vertex.

Containers with selected vertices are stored in the data and MC samples (introduced in Chapter 4) used in $Z \to \ell\ell$ analyses. Each primary vertex has highest sum of track p_T^2, with at least two associated tracks with $p_T > 400$ MeV. Information about number of primary vertices and associated tracks to it for each event is saved in these containers. To pre-select $Z \to \ell\ell$ signal events at both 50 ns and 25 ns bunch spacing, requirement to have at least one hard scatter vertex with at least two associated tracks was applied. Due to short life-time of Z-boson [134], primary vertex in $Z \to \ell\ell$ analysis coincides with Z-boson candidate decay point. Therefore, such criterion ensures that selected event can have at least one vertex of Z-boson candidate decay and two associated tracks originating from this vertex.

For $Z \to \ell\ell$ analysis at 25 ns bunch spacing additional lepton-vertex association criteria using track parameters z_0, θ and significance of d_0 is added. d_0 significance is defined as a ratio of d_0 absolute value to its uncertainty:

$$S_{d_0} = \frac{|d_0|}{\Delta_{d_0}}. \tag{5.5}$$

Lepton-vertex association criteria for electron and muon-candidates expressed with the next requirements:

- $|S_{d_0}| < 5$ for electron-candidates,
- $|S_{d_0}| < 3$ for muon-candidates,
- $|\Delta z_0 \sin(\theta)| < 0.5\ mm$ for electron and muon-candidates,

which are implemented in the `TrackVertexAssociationTool` [135]. Δz_0 is the difference between z_0 of the track and the primary vertex when expressed at the beam line. $\Delta z_0 \sin(\theta)$ instead of Δz_0 is used in the tool to avoid rejecting tracks with an expected larger uncertainty in the forward region.

5.3.2 Electron selection

Electron reconstruction

The reconstruction of electrons in ATLAS detector relies on the signal from the inner detector and the electromagnetic calorimeter. There are three reconstruction algorithms implemented in offline ATLAS software which are integrated in a single pakage `EGamma` [136]. The first algorithm (referred as a standard algorithm and seeded from the electromagnetic calorimeters) starts from clusters reconstructed in the calorimeters and then builds the identification variables based on information from the inner detector and the EM calorimeters. The second algorithm, seeded from the inner detector tracks, is optimized for electrons with low energy (at the level of few GeV) and selects good-quality tracks matching them to isolated energy deposition in the EM calorimeters. The third algorithm is available for the reconstruction of forward electrons. The standard algorithm is used for Z boson analyses at 13 TeV to reconstruct electron candidates in the ATLAS central region ($\eta < 2.47$).

The standard algorithm is organized in the few steps. For the reconstruction of electromagnetic clusters it uses a sliding window method [137] which consists of mapping the calorimeter cells into towers and moving a window of 3×5 towers on this grid. A cluster seed is found when the transverse energy in the window is greater than 2.5 GeV.

Once seed clusters are reconstructed, a search is performed for inner detector tracks which are loosely matched to the clusters (angular distance between the cluster barycentre and intersection point of extrapolated track with the second sampling layer of calorimeter is smaller than 0.05 along ϕ in direction of track bending and smaller than 0.05 along η for tracks with hits in Pixel and SCT). After rescaling track momentum to cluster energy, the similar matching procedure is applied (difference along ϕ should be smaller than 0.1) for efficient selection of low-momentum tracks, which may have substantial bremsstrahlung before calorimeter. Tracks which are loosely matched to the cluster and have hits in the silicon detectors are refitted using a `Gaussian Sum Filter` algorythm (GSF) [138], [139] and retained for reconstruction of electrons and converted photons. Track matching is realised in `EMTrackMatchBuilder` package [140].

After tracks are reconstructed in the inner detector they are loosely matched to seed clusters. Tracks which correspond to the origin from a photon conversion are used to create conversion vertex candidates. Finding and reconstruction of the conversion vertices is realised in the `InDetConversionFinderTools` tool [141]. After reconstruction, conversion vertex candidates are matched to the clusters in the calorimeter in the same way as reconstructed tracks.

At this point the object in the container could be either an electron or a photon. The separation between the photon and electron hypotheses for the reconstructed EM clusters is performed with EGammaAmbiguityTool [142]. If no track with at least four hits (one hit at one Si layer) is matched to the EM cluster or if vertex is found and the electron track is a part of the vertex and has no pixel hits, clusters are considered as photon candidates. If the track is not matched to the conversion vertex candidate, if it reconstructed from object with $p_T \geq 2$ GeV, $E/p < 10$ (E being the cluster energy, p - the track momentum), and has hits in b-layer or at least two pixel hits, clusters reconstructed as electron candidates.

Electron identification

To define if the reconstructed electron candidates are signal or background-like objects such as hadronic jets or converted photons, electron identification (ID) technique is applied. This technique uses quantities related to track properties (reconstructed in the inner detector), calorimeter clusters and shower shapes, information from the transition radiation tracker, track-to-cluster matching, variables measuring bremsstrahlung effects. ID algorithms use number of tracks in the IBL for discriminating between electrons and converted photons. To distinguish between electrons and hadrons, the TRT likelihood method introduce discriminant variable `eprobabilityHT` based on high-threshold probability of each TRT hit [143].

The ID algorithms are based on likelihood methods (LH) which use multivariate analysis technique (MVA). The MVA technique simultaneously uses several properties of electron candidate to take a selection decision. As an electron properties LH method uses signal and background probability density functions of discriminative variables for definition of the discriminant. Applying requirements on the discriminant allows to separate signal and background. On top of the MVA technique, simple selection cuts are applied for the variables corresponding to the number of track hits.

There are thee working points provided for electron identification: *Loose*, $Medium$ and $Tight$. Each of three operating points uses the same variable to define LH discriminant, but has different selection on it. *Loose* selection has the weakest background rejection power, while $Medium$ has stronger reducing power than *Loose* but weaker than $Tight$, and

	Efficiency		
Operating point	calorimeter isolation	track isolation	total efficiency
Loose	99%	99%	$\sim 98\%$
Tight	96%	99%	$\sim 95\%$
Gradient	$0.1143\% \times E_T + 92.14\%$	$0.1143\% \times E_T + 92.14\%$	90/99% at 25/60 GeV

Table 5.5: Efficiency targeted operating points definitions for electron isolation. For Gradient working point , E_T is in GeV.

$Tight$ has the strongest reducing power. According to such definition, electron candidates selected at $Medium$ operating point are all selected at *Loose*, and candidates selected at $Tight$ are selected at $Medium$.

For identification of electron candidates at $Z \to e^+e^-$ analyses of both 50 ns and 25 ns bunch spacing data at 13 TeV, $Medium$ LH operating point is used. The efficiencies of the identification method are discussed in Chapter 6.

Electron isolation

For further discrimination between signal and background events, on top of reconstruction and identification criteria, the isolation requirements are applied. Electron isolation allows to disentangle prompt electrons from non-isolated electron candidates originating from converted photons, heavy flavour hadron decays, and light hadrons misidentified as electrons. There are two discriminative variables used for electron isolation: calorimetric isolation energy $E_T^{cone0.2}$ and track isolation momentum $p_T^{varcone0.2}$ [143]. $E_T^{cone0.2}$ is defined as the sum of transverse energy of the clusters within a cone of $\Delta R = 0.2\ mm$ around the electron-candidate cluster. E_T contained in the cluster of size $\Delta\eta \times \Delta\phi = 0.125 \times 0.175$ around the electron-candidate cluster barycentre is subtracted. $p_T^{varcone0.2}$ is defined as the sum of transverse momenta of all tracks within a cone of $\Delta R = min(0.2, 10\ GeV/E_T)$ satisfying quality requirements, originating from primary vertex of hard scattering, excluding electron associated tracks (electron track and tracks from converted bremsstrahlung photons).

Introduced discriminative variables are used for constructing isolation criteria. Isolation operating points are divided into two classes: efficiency targeted operating points, based on cut maps derived from $Z \to \ell\ell$ simulated events, and fixed requirement operating points, optimized by maximizing sensitivity of $H \to 4\ell$ searches.

There are three frequently used isolation operation points: *Loose*, $Tight$ and $Gradient$. First two points have a flat efficiency. Detailed definition of these working points is given in Table 5.5. The isolation working points are implemented in the `IsolationSelectionTool` of the `IsolationSelection` package [144].

Gradient working point is used for electron isolation selection in $Z \to e^+e^-$ analyses at 13 TeV for synchronization with electron isolation at $t\bar{t}$ analysis. Such synchronization leads to increasing of the correlation between the channels at the combination stage as well as accuracy of the the cross-sections ratio.

Electron trigger

The ATLAS online data processing reconstructs and identifies electron candidates at the L1 and the HLT trigger levels. The L1 trigger algorithm identifies RoI as a 2×2 trigger tower cluster (core) surrounded with isolation ring of 12 towers in the electromagnetic calorimeter [145]. The size of one trigger tower is $\Delta\eta \times \Delta\phi = 0.1 \times 0.1$, therefore, size of the RoI is $\Delta\eta \times \Delta\phi = 0.4 \times 0.4$. The sum of the transverse energy from at least one of four possible pairs of the nearest neighbour towers inside the core cluster should exceed a predefined threshold. Isolation-veto threshold can be applied for the electromagnetic isolation ring, as well as for hadronic tower sums in central 2×2 core behind the electromagnetic cluster and and in the hadronic isolation ring around it.

After L1 trigger selection, the events are processed by the HLT using finer-granularity calorimeter information, precision measurements from the inner detector, which are not available at L1. The tracking HLT trigger is split into $fast\ tracking$ and $precision\ tracking$ stages [146]. The fast tracking stage consists of trigger-specific pattern recognition algorithms, while precision tracking stage relies on offline tracking algorithms. The calorimeter reconstruction also consists of two stages. The first stage provides unpacking the data from the calorimeter. The unpacked data is then converted into collection of cells. To reconstruct clusters of energy deposited in the calorimeter by electron candidate, the sliding-window algorithm (see Section 5.3.2) is used. The size if rectangular clustering window is $\Delta\eta \times \Delta\phi = 0.75 \times 0.175$ in the barrel and 0.125×0.125 in the end-caps. Electron candidates are required to have tracks from the fast tracking stage with $p_T >$ 1 GeV and to match clusters within $\Delta\eta < 0.2$. The second stage relies on offline-like algorithms. Electron identification realized with likelihood method and multivariate analysis technique as described in Section 5.3.2. The composition of likelihood is the same as in offline identification with exception of momentum loss due to bremsstrahlung which is not accounted for the online environment. Requirements on electron isolation at the trigger, using discriminative variables and working points introduced in the previous section, are also applied.

At $Z \to e^+e^-$ analysis with 50 ns bunch spacing data two single electron-triggers are used. The first `HLT_e24_lhmedium_iloose_L1EM20VH` is the lowest-threshold single-electron trigger. It applies 24 GeV transverse energy threshold (indicated by `24` in the name) end requires the electron to pass LH identification requirement at medium working point (denoted by `lhmedium`) as well as isolation requirement at loose working point (introduced with criterion $p_T^{cone20}/E_T < 0.1$ and marked as `iloose`). This trigger is seeded by `L1EM20VH`, which requires $E_T > 20$ GeV and applies E_T dependent veto on energy deposit in the hadronic calorimeter behind the electromagnetic cluster of electron candidate (denoted by `H` in the name). The E_T threshold varies slightly as a function of η to compensate for passive material in front of calorimeter (denoted by `V`). To recover possible efficiency losses at higher transverse energy regime, additional trigger `HLT_e60_lhmedium` with threshold above 60 GeV, with medium LH identification and no isolation criterion is used. Events are required to pass at least one of two triggers, thus providing at least one triggered electron-candidate in the selected event. Trigger requirement with such logic was applied for both data and Monte Carlo event selection.

For $Z \to e^+e^-$ analysis with 25 ns bunch spacing data trigger selection is slightly modified comparing to described 50 ns selection. Low-threshold non-isolated trigger `e24_lhmedium_L1EM20VH` for data and `e24_lhmedium_L1EM18VH` for Monte Carlo is used. Middle-threshold `HLT_e60_lhmedium` trigger as well as additional high-E_T `e120_lhloose` trigger are applied in both data and Monte Carlo selection. The logic of using the single-electron triggers is the same as at 50 ns analysis, therefore, trigger-selected event contains at least one electron which passed one of three (low-threshold, middle-threshold, hight-threshold) triggers.

The trigger selection for 50 ns and 25 ns analyses was applied due to *Egamma Trigger Signature Group* recomendations [147] based on trigger rates as a function of the instantaneous luminosity studies and trigger efficiency measurements with tag-and-probe method. Such combination of triggers at both analyses provides the optimal performance at full electron transverse energy range.

Electron trigger matching

Trigger matching determines the relationship between offline reconstructed objects and objects generated by the trigger algorithms. The defined relationship provides information if reconstructed offline electron cause the given trigger chain to fire. Matching of these two object is realized using the minimization of squared distances between them via the maximum likelihood algorithm in the `TrigEgammaMatchingTool` [148] tool.

The logic of the electron trigger matching selection is the same as at trigger selection: at least one of the offline reconstructed electron-candidate in the event should be matched to at least one of the trigger containers. Therefore, for 50 ns analysis one of the two electron-candidates should be matched to `HLT_e24_lhmedium_iloose_L1EM20VH` or `e120_lhloose`, while for 25 ns analysis should be matched to `e24_lhmedium_L1EM20VH` (`e24_lhmedium_L1EM18VH` for MC) or `HLT_e60_lhmedium`, or `e120_lhloose`. The trigger matching criterion is also used in the electron trigger efficiency definition for both analyses (described in Section 6.2).

Z boson selection

Electrons from central region of the ATLAS detector are used for Z-boson selection, therefore $|\eta_e| < 2.47$ requirement is applied. Central electrons detected in the crack region between EMB and EMEC, $1.37 < |\eta_e| < 1.52$, are excluded from the measurement.

The central electrons also should have $p_T > 25$ GeV. To reconstruct Z-boson candidate in electron-pair invariant mass window of 66 GeV $< M_{ee} <$ 116 GeV, two oppositely charged same flavour leptons are used. The summarized selection for $Z \to e^+e^-$ analyses is presented in Table 5.4. The numbers of $Z \to e^+e^-$ event candidates remaining in data after each major requirement are given in Table 5.6. A total of 35009 for 50 ns data and 1367026 for 50 ns data candidates pass all requirements in the electron channel within the invariant mass window.

5.3.3 Muon selection

Muon reconstruction is performed independently in the inner detector and muon spectrometer. After muon is reconstructed in both sub-detectors, information is combined to form the muon tracks which are used in the analysis. In the ID muon tracks are reconstructed as any other charged particles [149]. Muon reconstruction in MS starts with search for hit patterns in each muon chamber to form segments. Hits in MDT and nearby trigger chambers are aligned on the trajectory in detector bending plane using $Hought$ transform [150]. The RPC or TGC hits measure coordinate orthogonal to the bending plane. Segments in CSC are reconstructed with separate combinatorial search in η and ϕ detector planes. When segments in all chambers are formed, muon track candidates are built by fitting hits from segments in different layers. After muon track reconstructed in MS it combines with track reconstructed in ID. There are various algorithms of combining track information from different sub-detectors, therefore four muon "types" are exist: Combined (CB), Segment-tagged (ST), Calorimeter-tagged (CT), Extrapolated (ME). In $Z \to \mu^+\mu^-$ 50 ns and 25 ns analyses CB muons are used. Track reconstruction of such muons performed independently in ID and MS, and a combined track is formed from the global refit that uses hits from ID and MS. A detailed description of muon reconstruction methods can be found in Ref. [151].

To select prompt muons and suppress background contamination muon identification based on track quality requirements is applied. For CB muons identification, the discriminative variables are: $q/p\ significance$, defined as an absolute value of the difference between ratio of muon charge and momentum measured in the ID and MS divided by sum in quadrature of the corresponding uncertainties; ρ - absolute value of the difference between p_T measured in ID and MS; χ^2 of the combined track fit. Using these variables and number of hits in MS chambers, four main working points of muon identification are introduced: $Medium$, $Loose$, $Tight$, and $High - p_T$. In both 50 ns and 25 ns $Z \to \mu^+\mu^-$ analyses the Medium working point is used. Such selection minimises the systematic uncertainties associated with muon reconstruction and calibration. At this working point CB muons are required to have equal or more then three hits in at least two MD layers, except for tracks in region of $|\eta| < 0.1$, where tracks with at least one MDT layer and no more then one MDT hole are required.

The muon isolation is a powerful tool for background rejection. The principle of its realization is the same as in electron case. For muon isolation track-based and calorimeter-based variables are used. $p_T^{varcone30}$ is the track-based isolation variable which defined as a scalar sum of transverse momenta of the tracks with $p_T > 1$ GeV in a cone of size $\Delta R = min(0.3, 10GeV/p_T^{\mu})$ around the muon of p_T^{μ}, excluding the muon track itself. $E_T^{topocone20}$ is the calorimeter-based variable, it is defined as a sum of transverse energy in a cone of size $\Delta R < 0.2$ around the muon, after subtracting energy from muon contribution itself. Similarly to electron case, there are three general muon isolation working points. The *Gradient* working point is used for $Z \to \mu^+\mu^-$ analyses with 50 ns as well as for 25 ns data. $p_T^{varcone30}/p_T^{\mu}$ and $E_T^{topocone20}/p_T^{\mu}$ are used as discriminative variables at this working point. The efficiency of Gradient isolation is 90(99)% at $p_T = 25(60)$ GeV.

Level-1 muon trigger identifies muons by spatial and temporal coincidence of hits in the RPC or TGC chambers. There are six p_T thresholds depending on the number of layers with coincided hits. L1 muon trigger algorithm identifies RoI with dimensions of 0.1×0.1 (0.03×0.03) in $\Delta\eta \times \Delta\phi$ in RPCs and TGCs. The HLT receives this information and makes use of the precision muon chambers for further selection. The HLT muon reconstruction is split into *fast* and *precision* stages. At the fast stage track fit is performed using MDT information, creating MS-only muon candidates, which are back-extrapolated to the interaction point and combined with ID tracks. In the precision stage the RoIs defined at the fast stage are used to reconstruct segments and tracks. The precision stage uses the same logic as at the fast stage: initially MS-only muon candidates are formed and subsequently combined with ID tracks. The lowest-threshold single-muon trigger `HLT_mu20_iloose_L1MU15` and additional trigger `HLT_mu50` with logical "or" between them are used in both 25 ns and 50 ns $Z \to \mu^+\mu^-$ analyses. The `HLT_mu20_iloose_L1MU15` requires transverse momentum of 20 GeV for combined muon candidate in addition to loose isolation: the scalar sum of track p_T in a cone size $\Delta R = 0.2$ around muon candidate is required to be smaller than 12% of the muon transverse momentum. The trigger is seeded by `L1MU15` which requires transverse momentum above 15 GeV. At a transverse momentum above 50 GeV this trigger is complemented by `HLT_mu50` trigger, to cover a small efficiency loss in the high transverse momentum region.

The connection between objects generated with trigger algorithms and offline reconstructed muon candidates is defined with the trigger matching algorithm. The same approach as for electron trigger matching is realized for muons in `TrigMuonMatching` tool [152], where criterion of ΔR between offline reconstructed muon and RoI with HLT muon object is applied. At least one of the two offline reconstructed muon candidate in the event are matched either to `HLT_mu20_iloose_L1MU15` or `HLT_mu50` trigger object.

The muon candidates which pass presented above selection are considered for $|\eta| < 2.4$ with $p_T > 25$ GeV. To select events containing Z-boson candidate, exactly two selected oppositely charged muon candidates with an invariant mass of 66 $GeV < M_{\mu^+\mu^-} < 116$ GeV are required. The summarized selection for $Z \to \mu^+\mu^-$ analyses is presented in the Table 5.4. The numbers of $Z \to \mu^+\mu^-$ event candidates in data after each major selection requirement are summarized in Table 5.6. A total number of 44898 event candidates with

Requirement	Number of candidates			
	50 ns		25 ns	
	$Z \to e^+e^-$	$Z \to \mu^+\mu^-$	$Z \to e^+e^-$	$Z \to \mu^+\mu^-$
Trigger	141600	445400	7928180	8011110
Lepton identification	42680	59300	1605610	2180740
Lepton isolation	36900	46910	1447460	1832100
Opposite charge ee or $\mu\mu$ pair	36370	46880	1412720	1809920
Invariant mass window	35009	44898	1367026	1735197

Table 5.6: Number of $Z \to e^+e^-$ and $Z \to \mu^+\mu^-$ candidates in data, remaining after each major requirement.

50 ns data and 1735197 with 25 ns data have passed all selection criteria in muon channel within the invariant mass window.

In the same way as for electron analysis, the muon identification, isolation and trigger selection is synchronized with the $t\bar{t}$ analysis which leads to increasing of the correlation between the measurements in the combination as well as accuracy of the the cross-sections ratio determination.

5.4 Background expectations

The selection described in the previous section defines the $Z \to \ell^+\ell^-$ signal event candidates. However, the background contribution to the selected data events should be estimated. The background sources in Z-analysis can be split into two categories. The first category is the electroweak (single-boson and di-boson events) and top (single top and top-quark pair production) backgrounds. The electroweak and top background processes have cross-sections compatible with $Z \to e^+e^-$ ($\mu^+\mu^-$) process (see Table 4.3) and, therefore, can be simulated by MC with the sufficient statistics. The second category is the QCD backgrounds (also called multijet). The QCD background originates from the semileptonic decays of heavy quarks, misidentification of hadronic jets as isolated leptons, and, in case of electron channel, electrons from photon conversion. Since the multijet background has the cross section six order of magnitude higher than the electroweak processes, it could not be simulated by MC with sufficient statistics, and therefore the data-driven method is used for estimation of its contribution.

5.4.1 Electroweak and top backgrounds

The electroweak and top background sources for $Z \to e^+e^-$ ($\mu^+\mu^-$) process are: $W \to \ell\nu$, $Z \to \tau\tau$, $WZ \to qq\ell\ell$, $ZZ \to qq\ell\ell$, $WW \to \ell\nu\ell\nu$, $t\bar{t}$. Contributions from $WZ \to l\nu qq$,

	50 ns		25 ns	
	$Z \to e^+e^-$ % MC	$Z \to \mu^+\mu^-$ % MC	$Z \to e^+e^-$ % MC	$Z \to \mu^+\mu^-$ % MC
$Z \to \tau\tau$	0.04	0.05	0.04	0.04
Diboson	0.12	0.12	0.15	0.15
$t\bar{t}$	0.24	0.24	0.27	0.24
$W \to e\nu$	0.00	0.00	0.00	0.00
$W \to \mu\nu$	0.00	0.01	0.00	0.00

Table 5.7: Electroweak background contributions estimated from simulation. Expectations are expressed as a percentage of the total simulated events coming from the sources listed in the table and passing signal selection in each channel.

$ZZ \to ll\nu\nu$, $ZZ \to llll$ and single-top processes are ignored due to its insignificance. The full list of MC samples used for each background contribution estimation is summarized in the Table 4.3.

To assess contribution from each source, events of each background MC sample have passed the signal event selection 5.4 and normalized to the appropriate process cross-sections. As can be seen from the Table 4.3 in both 50 ns and 25 ns analyses the same MC samples for background estimation were used. The expected contributions of individual background process were estimated for each Z channel and listed in the Table 5.7. The highest contribution for both channels at 25 ns and 50 ns bunch spacings belongs to $t\bar{t}$ and diboson processes at the level of 0.2% and 0.1%. The total electroweak and top background event rate contributing to $Z \to \ell^+\ell^-$ selection in both channels is approximately 0.5%.

The systematic uncertainties introduced by the method of electroweak and top background estimation are assessed by varying of background cross-section by the corresponding cross-section uncertainty (shown in Table 4.3). The breakdown of background systematic uncertainties on the Z-boson cross sections is shown in the Table 5.8. The resulting uncertainties for both channels at 50 ns and 25 ns are found to be at the level of 0.02%. Taking into account the luminosity, beam energy, and C_Z systematic sources, the electroweak and top systematic uncertainties contribute negligibly to the experimental cross-section uncertainty.

5.4.2 QCD backgrounds

The QCD multijet background measurement for both electron and muon channels is performed with data-driven method. The basic idea of the method is that background template constructed from data by suppressing the signal events with changing the nominal selection, is used for appropriate background description for data with the nominal selection. To gain multijet events to the template in $Z \to \ell^+\ell^-$ analyses, the lepton iso-

	50 ns		25 ns	
	$Z \to e^+e^-$ δ (%)	$Z \to \mu^+\mu^-$ δ (%)	$Z \to e^+e^-$ δ (%)	$Z \to \mu^+\mu^-$ δ (%)
$Z \to \tau\tau$	0.00	0.00	0.00	0.00
Diboson	0.01	0.01	0.01	0.01
$t\bar{t}$	0.02	0.02	0.02	0.02
$W \to \ell\nu$	0.00	0.00	0.00	0.00

Table 5.8: Electroweak and top background systematic uncertainties on the $Z \to e^+e^-$ and $Z \to \mu^+\mu^-$ cross sections at 50 ns and 25 ns bunch crossing.

lation requirement should be inverted (all events which failed the isolation requirement are used instead of those which passed). The additional inversion/cuts can be applied depending on the channel. Another important component of the method is the discriminative variable which is used to distinguish between signal and background contribution in the signal sample. For both electron and muon channels the transverse impact parameter d_0 multiplied by lepton charge is used as the discriminative variable.

The detailed description of multijet background estimation for $Z \to \mu^+\mu^-$ channel with 50 ns and 25 ns data is given in [124]. The current section provides description of multijet background estimation in $Z \to e^+e^-$ channel with both bunch crossing periods data.

$Z \to e^+e^-$ 25 ns analysis

The multijet template in the data-driven method is determined by inverting the isolation and the offline identification requirements for both electron candidates. The inverted cut accepts all events which were removed by the "normal" cut and reduce events which were accepted by "normal" cut. The same single electron trigger as for the signal selection is used for the template, thus one of the two electron candidates passes the online medium-ID selection and isolation requirements. Therefore, in terms of cut names given in Table 5.4 template selection uses GRL, Vertex and tracks, Trigger, Trigger matching, p_T^e, η^e, N leptons, Invariant mass window, inverted ID and inverted ISO cuts. Figure 5.2 shows that the events selected for the multijet template do not display large deviations for the η distribution and do not show an enhancement around the nominal Z-boson mass. Small spikes at $|\eta| = 0$ and $|\eta| = 1.40$ are likely due to the change of ID requirements for these regions. Given that total amount of events in these spikes is below 10% they can not bias the template selection in a significant way.

The $d_0 \cdot Q$, where d_0 is the transverse impact parameter and Q is the electron charge, is chosen as the discriminating variable. The distribution of $d_0 \cdot Q$ for $Z \to e^+e^-$ events has an asymmetric shape due to photon radiation: the large negative values of $d_0 \cdot Q$

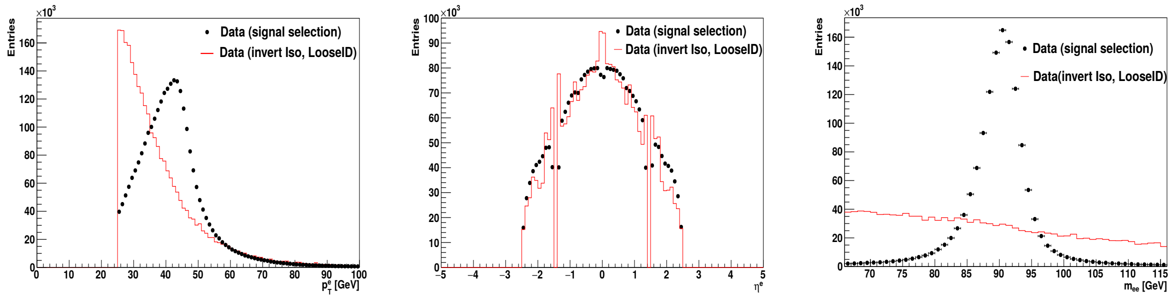

Figure 5.2: Comparisons of the p_T (left), η (middle) and $m_{\ell\ell}$ (right) distributions for the signal and multijet template selection (all normalized to the number of events in data).

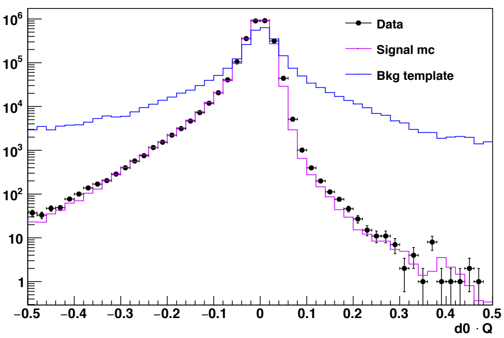

Figure 5.3: Distribution of the charge times track d_0, $d_0 \cdot Q$, for the data signal selection, signal Monte Carlo simulation, and multijet selection. All distributions are normalized to the number of events in data.

are significantly more populated, from the bias to the electron track caused by radiation. Thus the multijet fits exploit the positive tail of the distribution. Figure 5.3 shows the $d_0 \cdot Q$ distribution for the nominal selection of data and MC simulation as well as selected multijet template. The simulation describes the radiative tail well. As expected, the multijet background has a significant contribution for large positive $d_0 \cdot Q$ values.

χ^2 fitting method definition Initially, TFractionFitter [153] is used to determine the background normalization. The fitting procedure is tested using a simplified closure test. The pseudo-data are produced as the sum of the signal MC and a given fraction of the multijet background template. Therefore, the amount of background was exactly known and the shapes of the distributions were reproduced by construction. Both components (signal MC and multijet background template) are fitted together to the pseudo-data constructed with different fractions of the multijet template inside. Significant instabilities of the fits are observed, with many fits failing to converge even in this ideal case. As an additional test, fits in different regions of $d_0 \cdot Q$ distribution are performed. The differences in the resulting background fractions are found at the level of 20 %. The instabilities are caused by the complex treatment of the signal MC and background template uncertainties and the usage of the Minuit package.

Given that the multijet background template as well as the signal MC distribution have enough statistics, the template statistical uncertainties can be neglected and a simple χ^2 method can be used instead. For $N_{templates}$ number of templates with α_j scale factor for each template, χ^2 function can be defined as:

$$\chi^2(\alpha) = \sum_{i=1}^{N_{\text{bins}}} \left(\frac{N_i^{data} - \sum_{j=1}^{N_{\text{templates}}} N_{i,j}^{\text{template}} \alpha_j}{\sigma_i} \right)^2 , \tag{5.6}$$

where N_i^{data} is the number of events in bin i of the data distribution, σ_i is the statistical uncertainty for the bin i of the data distribution, and $N_{i,j}^{\text{template}}$ is the number of events in the bin i of the template j. This χ^2 definition takes into account only data statistical uncertainties (template uncertainties are neglected). Analytic minimization of $\chi^2(\alpha)$ allows to find α for each template. In the case of two templates (signal MC and multijet background template) the result of minimization can be written as

$$\begin{pmatrix} \sum_{i=1}^{N_{\text{bins}}} \frac{N_i^{\text{mc}} N_i^{\text{mc}}}{\sigma_i^2} & \sum_{i=1}^{N_{\text{bins}}} \frac{N_i^{\text{mc}} N_i^{\text{bkg}}}{\sigma_i^2} \\ \sum_{i=1}^{N_{\text{bins}}} \frac{N_i^{\text{mc}} N_i^{\text{bkg}}}{\sigma_i^2} & \sum_{i=1}^{N_{\text{bins}}} \frac{N_i^{\text{bkg}} N_i^{\text{bkg}}}{\sigma_i^2} \end{pmatrix} \begin{pmatrix} \alpha^{\text{mc}} \\ \alpha^{\text{bkg}} \end{pmatrix} = \begin{pmatrix} \sum_{i=1}^{N_{\text{bins}}} \frac{N_i^{\text{data}} N_i^{\text{mc}}}{\sigma_i^2} \\ \sum_{i=1}^{N_{\text{bins}}} \frac{N_i^{\text{data}} N_i^{\text{bkg}}}{\sigma_i^2} \end{pmatrix} . \tag{5.7}$$

The solution of this system of two linear equations gives the scale factors α^{mc} and α^{bkg} that correspond to the fractions of signal and background events, respectively.

χ^2 validation procedure The χ^2 method is validated using the pseudo-data, in the same manner as for TFractionFitter. All fits yielded stable results. The resulting fits with different background fractions in the pseudo-data are shown in Figure 5.4 and Table 5.9 while results for different fitting region are shown in Figure 5.5 and Table 5.10.

Further validation tests are performed using the real data with relaxed isolation and identification criteria, to increase the amount of multijet background. Three data samples with different reduced/relaxed cuts in comparison to the nominal selection (Table 5.4) are prepared. The first sample corresponds to the nominal selection with removed the isolation criterion. The second sample is created using the nominal selection with removed isolation requirement and Loose LH identification instead of Medium LH. The the third

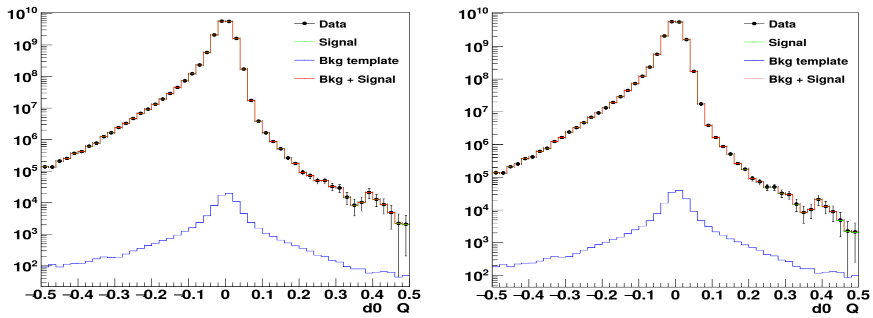

Figure 5.4: Fitted $d_0 \cdot Q$ distribution with the different amounts of multijet background in the pseudo-data. For the left panel, the pseudo-data are obtained by summing the signal MC and multijet background template with equal weights. For the right panel, the amount of multijet background is increased by a factor of two.

Fit results	Normal MJ background fraction in pseudo-data	2 $\times$ Normal MJ background fraction in pseudo-data
χ^2/NDF	6.1×10^{-11} / 47	2.1×10^{-10} / 47
Background fraction	5.2×10^{-6}	1.0×10^{-5}

Table 5.9: Fit results using different amounts of multijet background in the pseudo-data.

Fit results	$[-0.5; 0.5]$ region for fit	$[0.04; 0.5]$ region for fit	$[0.1; 0.5]$ region for fit
χ^2/NDF	6.1×10^{-11} / 47	9.8×10^{-13} / 47	0 / 47
Background fraction	5.2×10^{-06}	5.2×10^{-06}	5.2×10^{-06}

Table 5.10: Fit results to the pseudo-data using different fit regions.

one constructed using VeryLoose LH identification comparing to the second sample selection. For all three cases, the nominal single electron trigger is used to select the events, thus one of the two electron candidates is required to pass the online medium-ID and isolation requirements.

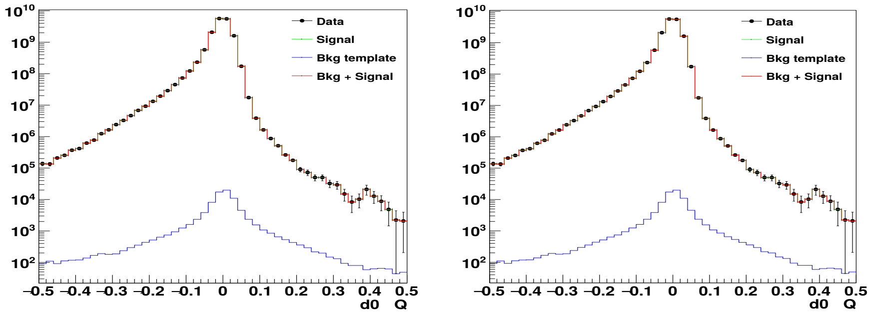

Figure 5.5: Fitted $d_0 \cdot Q$ distribution using different ranges for fit applying. The left plot corresponds to a fit in the region from 0.04 to 0.5. The right plot corresponds to a fit in the region from 0.1 to 0.5. In both cases, the full distributions are scaled to the numbers extracted from corresponding fits.

The comparison plots of the invariant mass distributions using three modified and the nominal selection, are presented in Figure 5.6. The same comparison in terms of $d_0 \cdot Q$ is shown in Figure 5.7. All the distributions are normalized to the number of events with the nominal selection.

The distributions indicate that simple removing of the isolation requirement from the nominal selection does not produce substantial increasing in the background. However, the additional relaxation of the identification working point from Medium LH to Loose LH allows to gain a significant amount of background. Further changing identification working point from the Loose LH to the VeryLoose LH increase the background fraction.

Exclusion of the isolation requirement and relaxation of the identification selection to Loose LH working point in the nominal selection of the data template was chosen for the χ^2 method validation. To reduce the deficiency in the resolution description of the signal MC around the peak region of $d_0 \cdot Q$ distribution, the Gaussian smearing for the positive values of $d_0 \cdot Q$ in MC distribution is applied (detailed description is given in

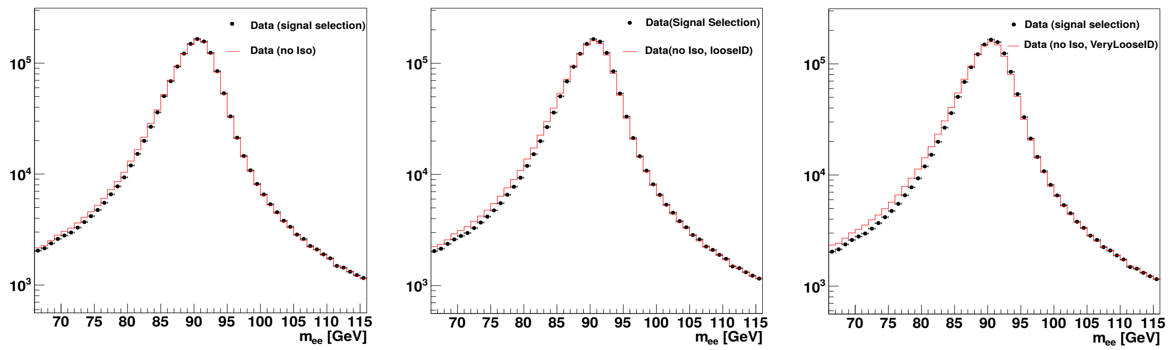

Figure 5.6: Data mass distributions using different selection modification (points - nominal selection, line - modified selection). The top left plot corresponds to removing the isolation requirement. The top right plot corresponds to removing the isolation requirement and using the LooseLH identification. The bottom plot corresponds to removing the isolation requirement and using the VeryLooseLH identification.

Ref. [124]). To fix the signal rate and avoid a dependence on the resolution description, the $d_0 \cdot Q$ distribution was rebinned such that all bins below $d_0 \cdot Q < 0.1$ are combined together. The resulting fit for $d_0 \cdot Q$ distribution is presented in Figure 5.8. The fit yields a good $\chi^2/NDF = 17.0/18$. The background fraction is 0.0044 ± 0.0002. In the region of $d_0 \cdot Q > 0.18$, the multijet background dominates over signal.

The Final $d_0 \cdot Q$ fit Due to successfully performed validation fits, the background fraction determine with the final fit. The data and the signal MC events for the final fit are selected with the nominal selection. The fitted $d_0 \cdot Q$ distribution are shown in Figure 5.9. The fit quality is $\chi^2/NDF = 37.4/18$ and the multijet background fraction is found to be at the level of -0.0005 ± 0.0001. Given that the fit yields a negative background fraction, the statistical uncertainty is used to set an upper limit on the background contamination. Determining the limit at 90% confidence level, it is concluded that the multijet background contamination for the nominal selection is below 0.02% and can be neglected.

χ^2 method cross-check Using the data template with a known expected fraction of multijet events, it is possible to estimate the accuracy of the described fitting method. One of the techniques to assess the expected fraction of multijet events for the same conditions (selection) under which the fit was performed, is to use only part of all the selected events (i.e. part of the kinematic region). It is convenient to choose regions where the contribution of multijet events is increased. The dielectron invariant mass tails are used as such regions. The tails are defined as the regions from 66 GeV to 80 GeV and 102 GeV to 116 GeV ("*bkg reg*") of dielectron invariant mass. To check the enhancement of multijet contribution in *bkg reg* region, the comparison of $d_0 \cdot Q$ distributions using data

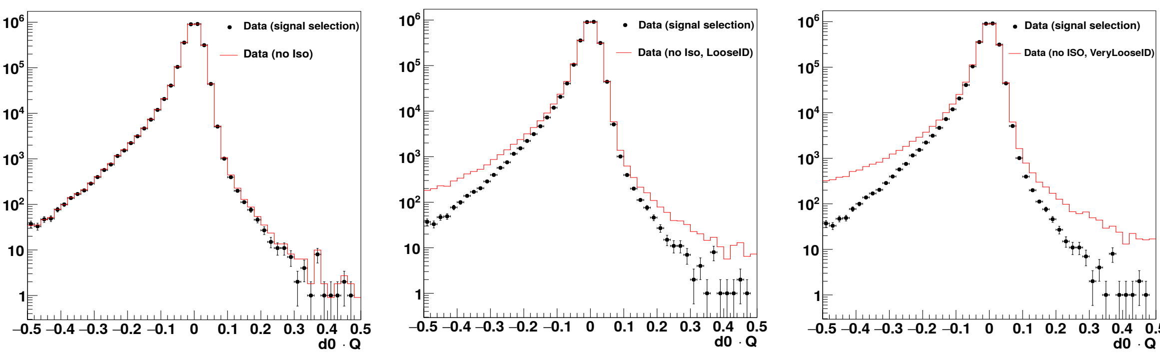

Figure 5.7: $d_0 \cdot Q$ distributions using different selection modifications (points - nominal selection, line - modified selection). The top left plot corresponds to removing the isolation requirement. The top right plot corresponds to removing the isolation requirement and using the LooseLH identification. The bottom plot corresponds to removing the isolation requirement and using the VeryLooseLH identification.

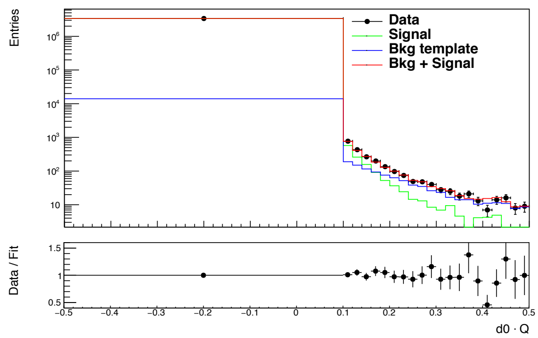

Figure 5.8: Fitted $d_0 \cdot Q$ distribution. The data points represent events selected with the nominal selection without the isolation requirement using the Loose LH identification. The signal MC corresponds to the nominal selection.

events from full invariant mass window and invariant mass tails is produced (Figure 5.10). The comparison illustrates a higher population at $d_0 \cdot Q$ tails for events from the *bkg reg* region with respect to events from the full mass window.

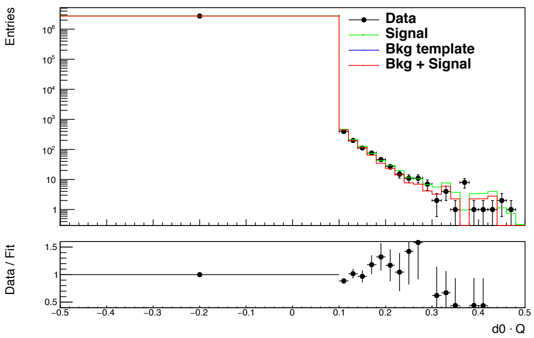

Figure 5.9: Fitted $d_0 \cdot Q$ distribution. The data and the signal MC correspond to the nominal selection.

The ratio defined as

$$R = \left(\frac{N^{\text{bkg reg}}_{\text{bkg templ}}}{N^{\text{full distr}}_{\text{bkg templ}}}\right) / \left(\frac{N^{\text{bkg reg}}_{\text{signal templ}}}{N^{\text{full distr}}_{\text{signal templ}}}\right), \tag{5.8}$$

where $N^{\text{bkg reg}}_{\text{signal templ}}$ is the number of signal template events in the region with enhanced multijet contribution, $N^{\text{full distr}}_{\text{signal templ}}$ - number of signal template events in the full window of dielectron invariant mass distribution (66 GeV - 116 GeV), $N^{\text{bkg reg}}_{\text{bkg templ}}$ and $N^{\text{full distr}}_{\text{bkg templ}}$ are the multijet background template events correspondingly, is used for estimation of $d_0 \cdot Q$ fitting accuracy. The product of R and the fraction of multijet background, obtained from the fit using events in the full 66 GeV $-$ 116 GeV invariant mass window, gives the expected fraction of multijet background in the "*bkg reg*" region. Using the resulting number from the χ^2 validation procedure in the full invariant mass window (0.0044 ± 0.0002), the expected fraction of multijet background events in the *bkg reg* region is found to be $R \cdot 0.44\% = 3.2\%$.

To check the accuracy of χ^2 fitting method, the predicted value of multijet background and value obtained from the fit should be compared. The $d_0 \cdot Q$ distribution of data events obtained using nominal selection without isolation with Loose LH identification in the *bkg reg* region was fitted with the same background and signal MC templates as were used for obtaining multijet fraction of 0.0044 ± 0.0002. The resulting fit is shown in Figure 5.11. The fit yields a $\chi^2/NDF = 31.9/22$. The multijet background fraction extracted from the fit amounts to 0.022 ± 0.0012, i.e. 2.2% to be compared to 3.2%. The difference between these fraction is 50% of extracted number from the fit. Adding 50% to the estimated multijet background contamination using the nominal selection, results in

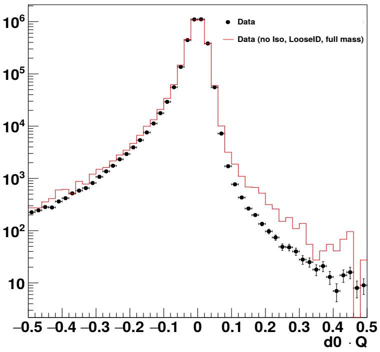

Figure 5.10: $d_0 \cdot Q$ distributions comparison. The points correspond to data events obtained using nominal selection without isolation with LooseLH identification in the full invariant mass region. The red line corresponds to data with the same selection but in *bkg reg* region only. Red line distribution is normalized to the area of the black points distribution.

a background fraction of 0.03% and can be neglected comparing to electroweak and top background contaminations.

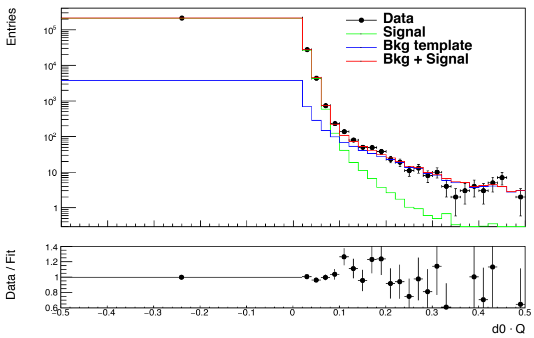

Figure 5.11: Fitted $d_0 \cdot Q$ distribution. The data events assessed with the nominal selection without isolation criterion, with Loose LH identification in the di-electron invariant mass tails ($66\ GeV - 80\ GeV$ and $102\ GeV - 116\ GeV$). The signal MC events have passed the nominal selection.

In order to properly cover all possible mismodellings of this number which is challenging to measure due to its smallness, the systematic uncertainty on multijet background is assigned to be 0.05%. Similar estimation of multijet background for analysis with 50 ns data is given in Ref. [154].

Chapter 6

Efficiency scale factors

The accuracy of Monte Carlo (MC) simulation to model the efficiency of lepton selection plays a fundamental role for the Z-boson cross-section measurements. To achieve a reliable result, the MC simulation should be corrected to reproduce the measured data efficiency. The methods of definition of the efficiency scale factors and their uncertainties are discussed in this Chapter. It also contains results for the measured efficiencies and their correlations between the W, Z and $t\bar{t}$, Z measurements.

6.1 The tag-and-probe method

Selection of unbiased, well defined sample of objects (leptons) is one of the main challenges of the efficiency measurement. Approach used to select such sample is implemented in the tag-and-probe method. It uses known mass resonance to select a lepton pair of the desired type, e.g. Z-boson mass in $Z \to \ell\ell$ analysis. "Tag" is an object that passes a tight selection (full chain of selection cuts), which provides a clean sample. A set of "probes", potentially pass very loose criteria, is selected by pairing them with the tags such that one tag-and-probe pair invariant mass is consistent with the mass of the corresponding resonance. A probe object definition depends on the specific analysis selection that is used for the resonance reconstruction.

In the $Z \to \ell\ell$ analysis one lepton is used to tag an event. Tag-lepton is required to pass full a chain of selection criteria listed in Table 5.4. Initially, the first lepton in the pair is checked whether it is a tag and the second lepton is saved as a probe consequently, then the second lepton is checked if it is a tag and the first lepton is saved as a probe.

6.2 Efficiency definition

Using the tag-and-probe method, efficiency, ϵ_{cut}, of the cut of interest can be defined as a ratio of number of probes that have passed this cut to the number of probes that have not:

$$\epsilon_{cut} = \frac{N_{probes}^{passed\ cut}}{N_{probes}^{all}}, \tag{6.1}$$

In $Z \to e^+e^-$ analysis, the efficiencies of the electron identification (ϵ_{ID}), isolation (ϵ_{ISO}) and trigger (ϵ_{TG}) are introduced. Each of these efficiencies is measured relatively to the previous one, therefore efficiency of the individual lepton can be expressed in a factorized way:

$$\epsilon_\ell = \epsilon_{ID} \cdot \epsilon_{ISO} \cdot \epsilon'_{TG}. \tag{6.2}$$

The trigger efficiency (ϵ'_{TG}), however, does not correspond to the individual lepton efficiency, but rather into the overall Z-boson event efficiency. Therefore, probability that at least one of the daughter leptons in the event have passed the trigger selection can be defined in the next way:

$$\epsilon'_{TG} = \epsilon_{TG}^{\ell_1} + (1 - \epsilon_{TG}^{\ell_1})\epsilon_{TG}^{\ell_2}, \tag{6.3}$$

where $\epsilon_{TG}^{\ell_{1,2}}$ are the trigger efficiencies for each of two leptons in the event.

To define the introduced efficiencies, there are four types of probes: 1) probes that passed lepton reconstruction selection; 2) probes that passed lepton reconstruction and identification selection; 3) probes that passed lepton reconstruction, identification, and isolation selection; 4) probes that passed lepton reconstruction, identification, isolation, and trigger selection. For the trigger efficiency measurement, the trigger requirement for the probe-lepton contains the trigger matching cut. Therefore, such probes are associated with the objects that have passed the trigger cut. The definitions for the electron identification, isolation and trigger efficiencies are given by

$$\epsilon_{ID} = \frac{N_{probes}^{passed\ Reco+ID}}{N_{probes}^{passed\ Reco}}, \tag{6.4}$$

$$\epsilon_{ISO} = \frac{N_{probes}^{passed\ Reco+ID+ISO}}{N_{probes}^{passed\ Reco+ID}}, \tag{6.5}$$

$$\epsilon_{TG} = \frac{N_{probes}^{passed\ Reco+ID+ISO+TG}}{N_{probes}^{passed\ Reco+ID+ISO}}. \tag{6.6}$$

Due to the detector geometry (see Section 3.2), it is convenient to measure efficiency as a function of lepton pseudo-rapidity η^ℓ and transverse momentum p_T^ℓ (or azimuthal angle ϕ^ℓ for muons). The electron identification, isolation and trigger efficiencies as a function of the electron η are shown in Figure 6.1. The electron identification efficiency is obtained using Formula 6.4, where $N_{probes}^{passed\ Reco}$ is the number of probes that have passed electron reconstruction selection, and $N_{probes}^{passed\ Reco+ID}$ have passed electron identification requirement atop. The electron isolation and trigger efficiencies are obtained with Formula 6.5 and 6.6, respectively, using similar logic. The efficiency distributions in Figure 6.1 reflect the calorimeter and inner detector structure and the material distribution of the detector. The efficiency to identify an electron varies from 80% to 92% between the end-cap and barrel regions, while for the electron isolation it stays at the level of 92% due to the gradient working point. The trigger selection efficiency varies from 0.7% to 0.92%. The MC efficiencies are not corrected with the appropriate scale factors and show best agreement with the data for isolation selection, while the disagreement between the data and simulation for the identification and trigger efficiencies reaches up to 5% in the end-cap regions.

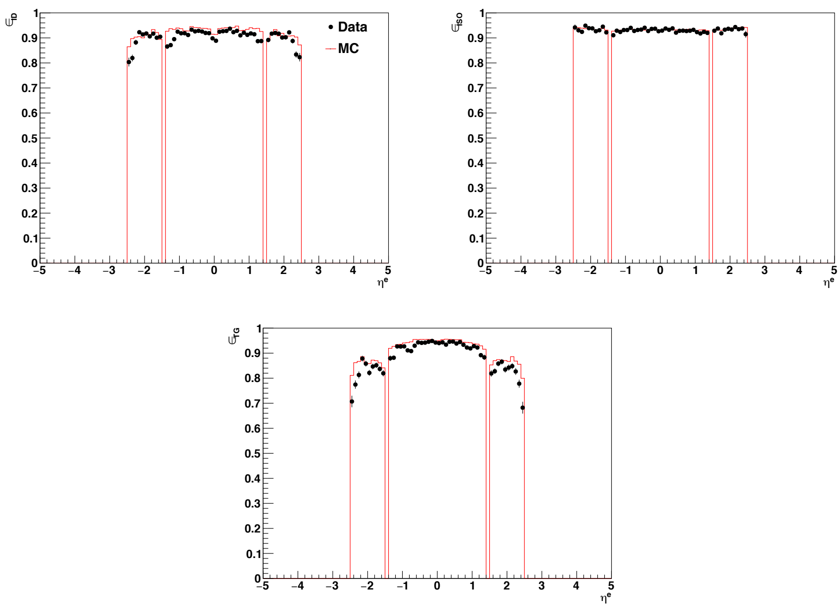

Figure 6.1: Data (black points with statistical uncertainties) and Monte Carlo (red line) comparison of electron efficiencies for identification (top left), isolation (top right) and trigger (bottom plot) as a function of electron pseudo-rapidity.

The efficiency distributions as a function of electron transverse momentum are shown in Figure 6.2. The efficiency increases with p_T for all three selection criteria. In the region of $p_T < 40$ GeV, the simulated efficiency for electron identification and trigger is higher than measured one. The region of $p_T > 80$ GeV has low statistics, therefore the efficiency fluctuations as well as increased statistical uncertainties and some empty bins are observed in the data.

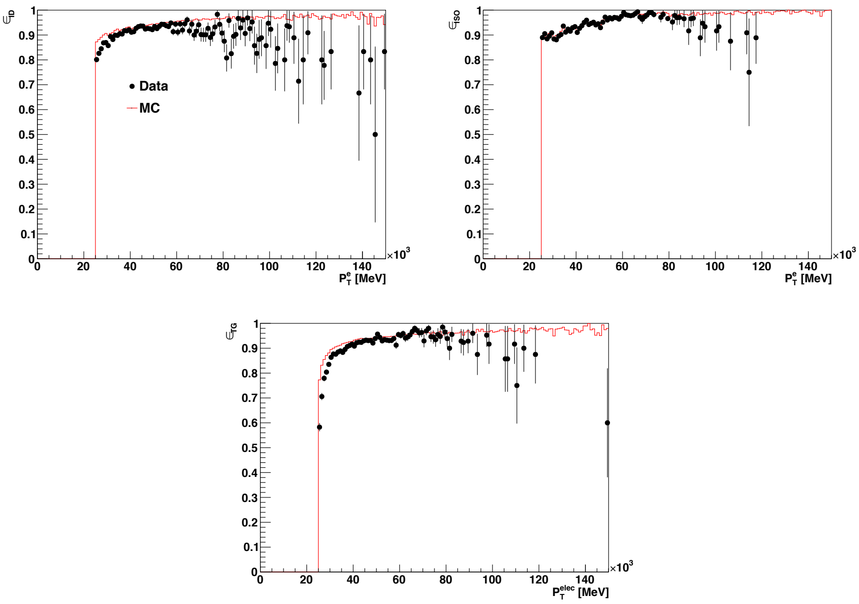

Figure 6.2: Data (black points with statistical uncertainties) and Monte Carlo (red line) comparison of electron efficiencies for identification (top left), isolation (top right) and trigger (bottom plot) as a function of electron transverse momentum.

The two-dimensional η vs p_T distributions for the MC simulation and data for the electron probes that have passed the full selection without the trigger matching requirement are shown in Figure 6.3. These distributions are filled with the probes that correspond to a denominator in Equation 6.6. Probes that have also passed trigger matching (correspond to a numerator in Equation 6.6) are shown in Figure 6.4. The pairwise ratios provide the MC simulation and data trigger efficiencies, shown in Figure 6.5. The two-dimensional plots demonstrate the highest trigger efficiency for electrons in the barrel region with $p_T > 40$ GeV. The efficiency in the regions removed by selection cuts on η and p_T is set manually to unity.

6.3 Efficiency scale factor definition

The efficiency scale factor as a function of lepton η and p_T is defined as a ratio of efficiency measured in data to efficiency obtained with the MC simulation:

$$SF(\eta, p_T)_i = \frac{\epsilon(\eta, p_T)_i^{data}}{\epsilon(\eta, p_T)_i^{MC}}, \tag{6.7}$$

where i is a type of cut of interest. The constructed efficiency scale factors provide corrections for a simulated efficiency with respect to the measured result. The example

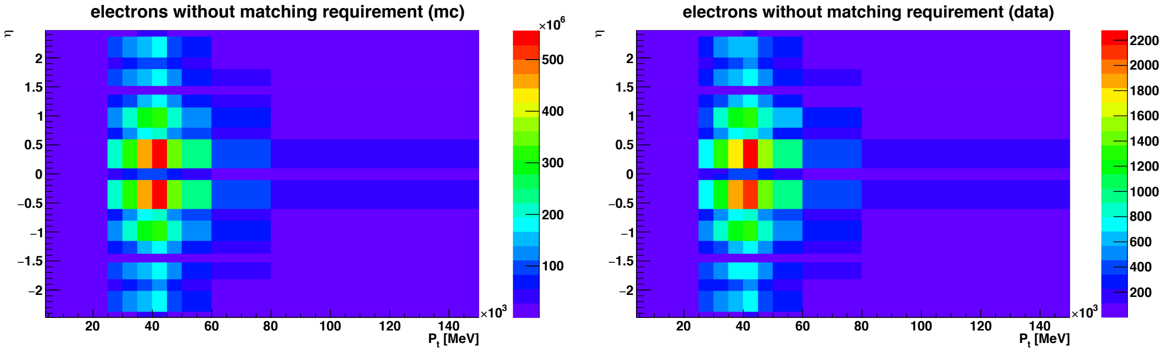

Figure 6.3: Monte Carlo (left) and data (right) η vs p_T distributions for electron probes that have passed common selection, identification and isolation criteria.

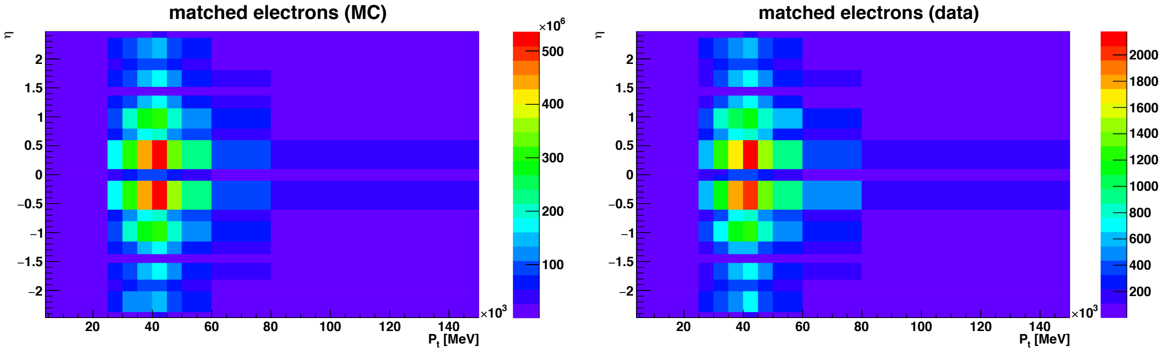

Figure 6.4: Monte Carlo (left) and data (right) η vs p_T distributions for electron probes that have passed common selection, identification, isolation and trigger matching criteria.

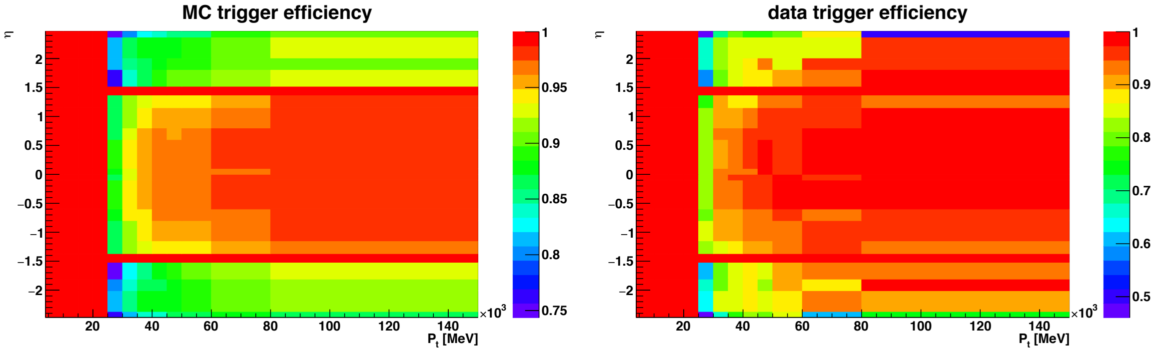

Figure 6.5: Electron trigger efficiency for Monte Carlo (left) and data (right) in bins of η vs p_T.

of corrected electron identification efficiency as a function of electron η and p_T is given in Figure 6.6. It is compared to the measured as well as simulated efficiency before correction. Given distributions demonstrate the improvement of the agreement between the measured and simulated efficiencies after applying scale factor correction.

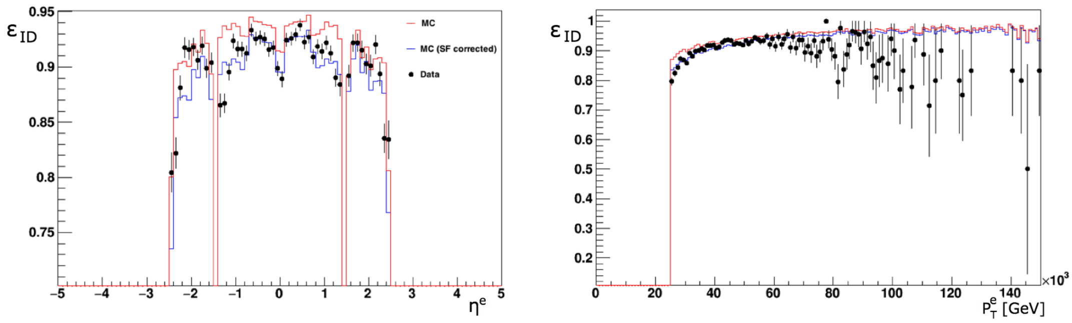

Figure 6.6: Monte Carlo (left) and data (right) η vs p_T distributions for electron probes that have passed common selection, identification and isolation criteria.

Using the scale factor definitions, provided with Formula 6.7, and the trigger efficiency for the event with two leptons, given with Formula 6.3, the trigger efficiency scale factor can be expressed as:

$$SF(\eta, p_T)^{event}_{TG} = \frac{\epsilon^{\ell_1,data}_{TG} + (1 - \epsilon^{\ell_1,data}_{TG})\epsilon^{\ell_2,data}_{TG}}{\epsilon^{\ell_1,MC}_{TG} + (1 - \epsilon^{\ell_1,MC}_{TG})\epsilon^{\ell_2,MC}_{TG}}. \tag{6.8}$$

The $Z \to e^+e^-$ analysis specification allows to have MC trigger efficiencies ($\epsilon^{e_1,MC}_{TG}$, $\epsilon^{e_2,MC}_{TG}$) and scale factors ($SF^{e_1,MC}_{TG}$, $SF^{e_2,MC}_{TG}$) for both leptons calculated using the ElectronEfficiencyCorrectionTool [156]. Using this information it is possible to calculate the trigger efficiency for separate electrons in data and scale factor for the whole event ($SF(\eta, p_T)^{event}_{TG}$). Due to the scale factor definition

$$\epsilon^{e_i,data}_{TG} = SF^{e_i,MC}_{TG} \times \epsilon^{e_i,MC}_{TG}, \tag{6.9}$$

the trigger scale factor for the $Z \to e^+e^-$ channel can be written as

$$SF(\eta, p_T)^{event}_{TG} = \frac{SF^{e_1,MC}_{TG}\epsilon^{e_1,MC}_{TG} + (1 - SF^{e_1,MC}_{TG}\epsilon^{e_1,MC}_{TG})SF^{e_2,MC}_{TG}\epsilon^{e_2,MC}_{TG}}{\epsilon^{e_1,MC}_{TG} + (1 - \epsilon^{e_1,MC}_{TG})\epsilon^{e_2,MC}_{TG}}. \tag{6.10}$$

The example of $SF(\eta, p_T)^{event}_{TG}$ calculated as a function of η and p_T for the electron channel is shown in Figure 6.7. The left plot contains central values of the trigger scale factor and the right plot shows statistical uncertainties. Statistical uncertainties are treated as uncorrelated between the bins.

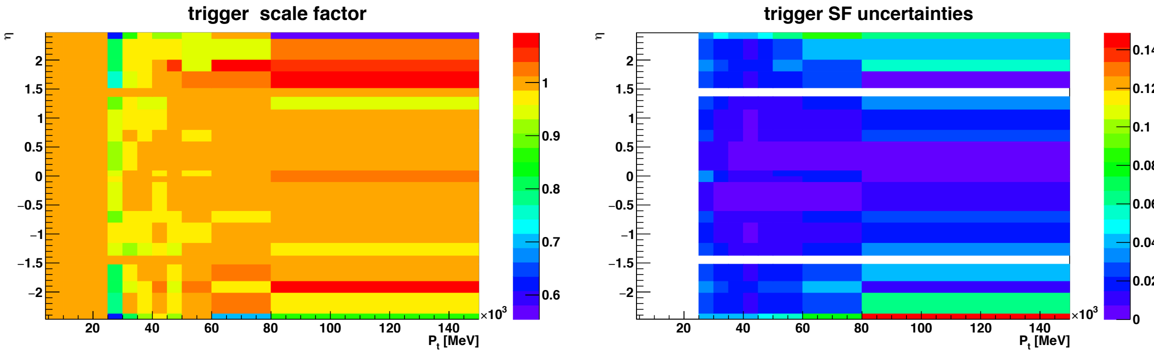

Figure 6.7: Trigger scale factor for $Z \to e^+e^-$ events (left plot) with the statistical uncertainties (right plot) as a function of η and p_T.

There is an alternative way to estimate a trigger scale factor for the $Z \to e^+e^-$ event, using only $SF_{TG}^{e_{1,2},MC}$:

$$SF(\eta, p_T)_{TG}^{event} = SF_{TG}^{e_1,MC} + SF_{TG}^{e_2,MC} - SF_{TG}^{e_1,MC} SF_{TG}^{e_2,MC} \tag{6.11}$$

This method, as well as the previous, takes into account logic of the trigger and trigger matching cuts. The feature of a given method is that in case if one of the electrons was not trigger matched then the corresponding $SF_{TG}^{e_i,MC}$ is zero and $SF(\eta, p_T)_{TG}^{event}$ becomes equal to the scale factor of the remaining electron.

The difference between the resulting trigger scale factors for $Z \to e^+e^-$ events using both methods is estimated. Figure 6.8 shows this difference for each event in the sample. Most of the points are in the band of 3 %. Points with the high deviation from zero correspond to events where one of the two electrons was not matched and the remaining electron has a small scale factor. The comparison demonstrates a good agreement between the two methods.

The total weight for the $Z \to e^+e^-$ events is constructed of four efficiency scale factors:

$$W_{event} = SF_{Reco} \times SF_{ID} \times SF_{ISO} \times SF_{TG}, \tag{6.12}$$

where SF_{Reco} is the lepton reconstruction efficiency scale factor, which is provided by ElectronEfficiencyCorrection tool. The uncertainty on W_{event} includes uncertainties from each multiplier in Equation 6.12 as independent sources. In the analysis all these uncertainties are included as components of C_Z factor uncertainty.

The systematic uncertainties on the efficiency scale factors contain bin-to-bin correlated and uncorrelated components. There are several methods for the systematic uncertainties estimation. One of them is the offset method, which is based on the the variation of the central value of the efficiency scale factors. "Up" variation is provided by adding the upper limit of the systematic uncertainty, and the "down" variation implies adding

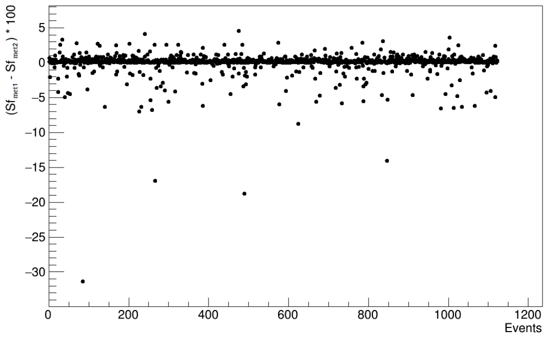

Figure 6.8: Difference between scale factors calculated using two methods. Y-axis corresponds to difference between scale factors calculated using two methods multiplied by 100 and X-axis to the event number.

the lower limit to the central value. This method is used for the propagation of bin-to-bin correlated uncertainties. Another approach is the toy Monte Carlo method, which is used for uncorrelated uncertainties. There is also the combined toy Monte Carlo method that includes both correlated and uncorrelated uncertainties. The toy Monte Carlo method is further discussed in Section 6.5.

6.4 Systematics introduced by pileup reweighting

For the $Z \to \ell\ell$ analysis, the MC pile-up reweighting is performed for $\langle\mu\rangle$ distribution and implemented using the `PileupReweighting tool` [157]. Additional scale factor of 1/1.16 is applied on top of the reweighting for the $\langle\mu\rangle$ distribution. This correction factor was estimated by the ATLAS Tracking CP group to take into account the fraction of inelastic activity, which is differently described in the MC simulation with respect to the measured data, and match the number vertices vs $\langle\mu\rangle$.

The systematic uncertainty on the C_Z factor due to the 1/1.16 scaling is evaluated by varying this factor, where the upper variation limit is 1.23 and the lower is 1.09 [158]. Variation of pileup scale factor affects lepton isolation and identification efficiencies, which are determined in a data-driven way and have dedicated uncertainties. The change in the C_Z due to change in the efficiency scale factors should be thus subtracted, to avoid a double counting of the uncertainties.

A dedicated tag-and-probe study is performed to evaluate the impact of the pileup reweighting variation on the isolation scale factors. The efficiencies measured in data are compared to those estimated with MC simulation. The MC samples are considered with the standard $s_p = 1/1.16$ and modified pileup scaling factors ($s_p = 1.0, 1/1.09, 1/1.23$). It is observed that the changes in the s_p factor leads to a significant change in the isolation efficiency, while other efficiencies are not affected significantly.

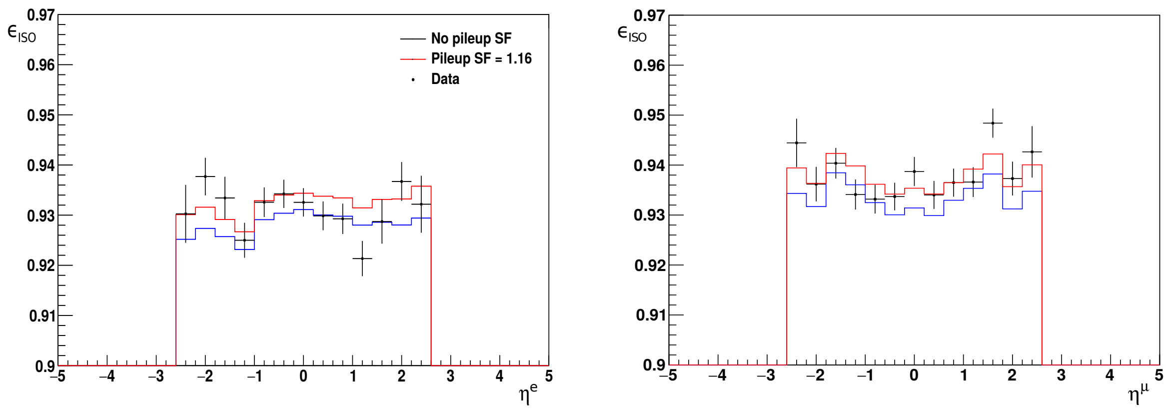

Figure 6.9: Isolation requirement efficiency as a function of the lepton rapidity as determined using tag-and-probe method. The left (right) plot shows efficiency for the electrons (muons). The data are shown as dots with error bars. The solid red (blue) histogram shows MC efficiency using $s_p = 1/1.16$ ($s_p = 1$).

The electron and muon isolation efficiencies ϵ_{ISO} as a function of lepton pseudorapidity, measured in data and MC simulated, with the pile-up scaling factors of $s_p = 1/1.16$ and $s_p = 1$ are given in Figure 6.9. One can see the consistent change of the isolation efficiency of about 0.4%, similar for electrons and muons. The overall shift is determined using a constant function to fit the ratio of the two efficiencies. The corrected systematic uncertainty in C_Z factor due to the pileup scaling factor variation is determined as

$$\Delta C_Z^{s_p,corr} = \Delta C_Z^{s_p} - 2 \times (\Delta\epsilon_{ID} + \Delta\epsilon_{ISO}), \tag{6.13}$$

where $\Delta C_Z^{s_p}$ stands for the raw change of C_Z due to variation in s_p and $\Delta\epsilon_{ID}, \Delta\epsilon_{ISO}$ stand for the change in the identification and isolation efficiencies. Table 6.1 summarises the changes in the isolation efficiency, as well as raw and corrected changes of C_Z for the electron and muon channel for different values of s_p. Based on these variations, the resulting systematic uncertainty is summarised in Table 6.2.

6.5 The Toy Monte Carlo method

The toy Monte Carlo method is an approach used for the efficient propagation of statistical and bin-to-bin uncorrelated uncertainties. The efficiency scale factors, SF_i, have two types of uncertainties: statistical, δ_i, which is uncorrelated for different bins, i, and correlated systematic, s_{ij}, which can be characterised by M nuisance parameters, j.

s_p variation	1.00 %	1.09 %	1.23 %
$\Delta\epsilon_{ID}$ (electrons)	-0.025	-0.013	0.001
$\Delta\epsilon_{ISO}$ (electrons)	-0.423	-0.182	0.139
$\Delta\epsilon_{ISO}$ (muons)	-0.436	-0.172	0.170
$\Delta C_Z^{s_p}$ $(Z \to ee)$	-0.908	-0.381	0.274
$\Delta C_Z^{s_p}$ $(Z \to \mu\mu)$	-0.919	-0.354	0.307
$\Delta C_Z^{s_p,corr}$ $(Z \to ee)$	-0.012	0.009	-0.006
$\Delta C_Z^{s_p,corr}$ $(Z \to \mu\mu)$	-0.047	-0.010	-0.034

Table 6.1: Changes of the identification and isolation efficiencies, C_W and C_Z factors, before and after correction using equation 6.13

Channel	Uncertainty up %	Uncertainty down %
$Z \to e^+e^-$	0.009	-0.006
$Z \to \mu^+\mu^-$	-0.010	-0.034

Table 6.2: Summary of the systematic uncertainties in $C_{W,Z}$ due to pileup reweighting

There are two modifications of the toy MC approach for propagation of uncertainties binned in the detector level variables to the final observable:

- **Statistical toy MC propagation.** In this method the correlated scale factor uncertainties are propagated using nuisance parameters while statistical uncertainties are evaluated using the toy MC method. The toy efficiency maps are defined as

$$SF_i^t = SF_i + r_i^t \delta_i \tag{6.14}$$

  where r_i^t is a random number drawn from a Gaussian distribution with the mean of zero and standard deviation of one[1]. The number of toy efficiency maps, T, can be optimised depending on N and number of observable bins, O, typically $O < T < N$. The r.m.s. for the observable o determined using the toy efficiency maps can be employed to determine the statistical uncertainty $\sigma(o)$:

$$\begin{aligned} \overline{o} &= = \tfrac{1}{T} \textstyle\sum_{t=1}^{T} o^t \,, \\ \sigma(o) &= \tfrac{1}{T-1} \sqrt{\textstyle\sum_{t=1}^{T} \left(o^t - \overline{o}\right)^2} \,. \end{aligned} \tag{6.15}$$

[1]In general, toy MC method can be extended to arbitrary distribution of random numbers. E.g. for efficiency scale factors log-normal distribution may be more appropriate. However, if $\delta_i < 10\%$, the difference between Gaussian and log-normal distributions is insignificant.

A correlation coefficient ρ_{12} between the two observables o_1 and o_2 can be estimated as

$$\rho_{12} = \frac{1}{\sigma(o_1)\sigma(o_2)} \cdot \frac{1}{T-1} \sum_{t=1}^{T} \left(o_1^t - \bar{o}_1\right)\left(o_2^t - \bar{o}_2\right) \ . \tag{6.16}$$

- **Combined toy MC propagation**. This is an extension of the statistical toy MC method, where the correlated systematic uncertainties are also included in the toy preparation:

$$SF_i^t = SF_i + r_i^t \delta_i + \sum_{j=1}^{M} r_j^t s_{ij} \, . \tag{6.17}$$

For this method, Equation 6.15 and 6.16 yield total uncertainty of the observable o and the total correlation coefficient between the observables o_1 and o_2, respectively.

6.5.1 The Toy Monte Carlo method in Z, W and $t\bar{t}$ measurements

For the Z, W and $t\bar{t}$ measurements the statical and combined toy MC methods have been implemented for the lepton efficiency scale factors which have the largest uncertainties. These include the electron identification, isolation, trigger, and reconstruction [2] efficiencies as well as the muon trigger efficiency. The muon trigger SF uncertainties have split statistical and systematic components, and the toy MC method is applied only to the statistical one, while in the electron case the combined toy MC method is applied.

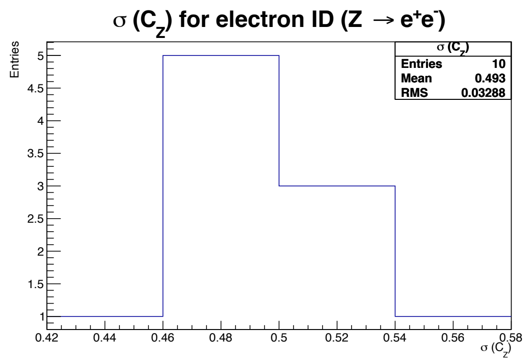

Figure 6.10: Distribution of $\sigma(C_Z)$ for $Z \to e^+e^-$ events for the toy MC samples generated for electron identification scale factors with $T = 40$ replica.

A large number of toy replica may require substantial computational resources, therefore to assess the number of the required replicas to estimate uncertainty for C_Z factor

[2]The toy MC method was applied for the electron reconstruction scale factor uncertainty definition only for $Z \to e^+e^-$ boson measurements with 25 ns bunch spacing data.

Sample and source of C_Z uncertainties	Up/down variation evaluation %	toy MC evaluation %
$Z \to e^+e^-$, electron trigger	0.42/-0.55	0.05
$Z \to e^+e^-$, electron identification	3.73/-3.66	0.48
$Z \to e^+e^-$ electron isolation	0.99/-0.98	0.29
$Z \to \mu^+\mu^-$, muon trigger (stat.)	0.87/-1.00	0.10

Table 6.3: Uncertainty of C_Z determined for various lepton efficiency sources using up/down variation and toy MC methods.

($\sigma(C_Z)$) with about 10% accuracy, the dedicated study was performed. Figure 6.10 shows the $\sigma(C_Z)$ for $Z \to e^+e^-$ determined with 10 independent toy sets of identification scale factors, each of them contains 40 replica. One can see that the r.m.s. of the distribution is 7% which assumes that $T = 40$ is sufficient to measure uncertainty with better than 10% accuracy.

The results of the electron identification, isolation, trigger as well as the muon trigger efficiency scale factor uncertainties calculated with the toy MC method are given in Table 6.3. The numbers are compared to similar results obtained with "up" and "down" variations of selection criteria used in efficiency SF definition and provided by `EGamma` tool. The uncertainties estimated with the toy MC method demonstrate a significant reduction compared to the variations.

The correlation coefficients between the correction factors $C_{Z\to\ell\ell}$, $C_{W^+\to\ell^+\nu}$, $C_{W^-\to\ell^-\nu}$ (with 50 ns data), and $C_{Z\to\ell\ell}$, $t\bar{t}$ (with 25 ns data) for different sources of uncertainty are determined using Equation 6.16. The resulting correlation coefficients are shown in Figure 6.11 and 6.12. The highest correlation is observed between the W^+ and W^- measurements, but it is smaller than 100% because of differences in p_T and η distributions.

The detailed list of the toy MC replicas (in percentage) for $C_{Z\to\ell\ell}$, $C_{W^+\to\ell^+\nu}$, $C_{W^-\to\ell^-\nu}$ with 50 ns data using the `ElectronEfficiencyCorrectionTool` [156] is presented in Table A.1 of Appendix A. Similar result for $C_{t\bar{t}}$, $C_{Z\to\ell\ell}$ with 25 ns data is given in Table A.2.

6.5.2 Uncertainties on correlation coefficients between C_Z, C_{W^+}, C_{W^-}

The cross section ratio $\sigma_{W^\pm}/\sigma_Z$ is proportional to the correction factors ratio $C_Z/C_{W^\pm}$, therefore the uncertainty of the cross section ratio depends on the uncertainties for correction factors and level of their correlation. If the uncertainties on C_Z and $C_{W^\pm}$ would be 100% correlated, they are completely cancelled. The results of correlations between C_Z, C_{W^+}, and C_{W^-} for systematic sources estimated with the toy MC method demonstrate high but not 100% correlation, which leads to a partial cancellation of uncertainties in the ratio. The influence of the level of correlation between the systematic sources on the

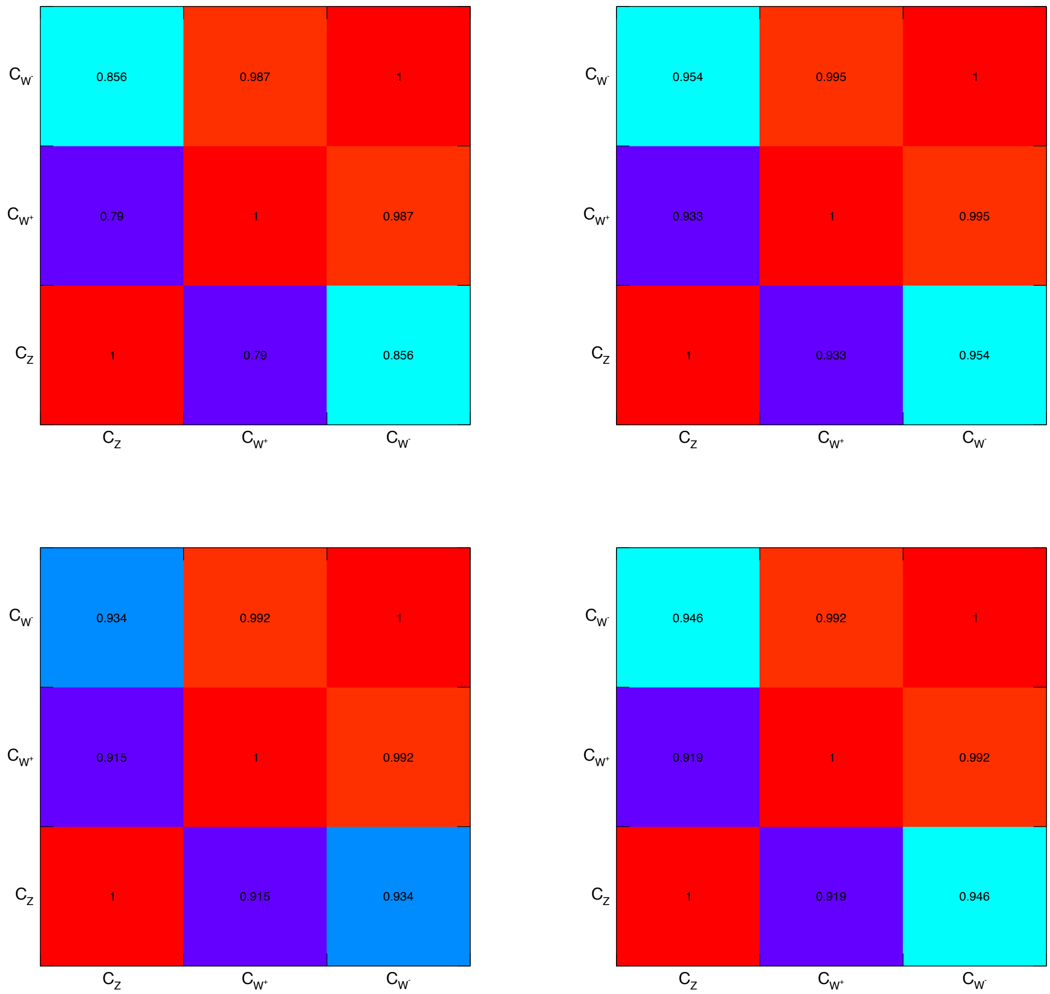

Figure 6.11: Correlation coefficients between C_Z, C_{W^+} and C_{W^-} for electron trigger (top left), electron identification (top right), electron isolation (bottom left), and muon trigger (bottom right) scale factor uncertainties using $50ns$ data.

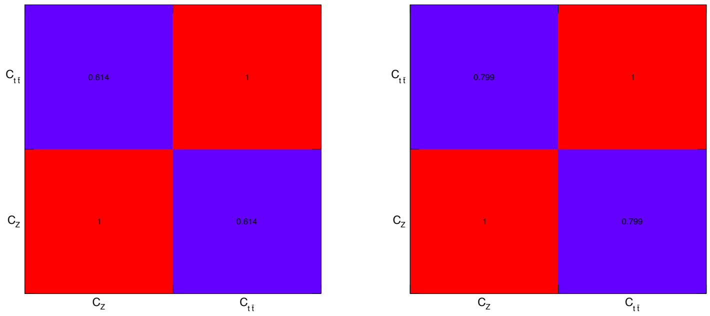

Figure 6.12: Correlation coefficients between C_Z and $C_{t\bar{t}}$ for the electron reconstruction (left) and electron identification (right) scale factor uncertainties using $25ns$ data.

cross section ratio can be shown with the formula

$$\sigma^2(f(a,b)) = \left(\sigma_a \frac{\partial f}{\partial a}\right)^2 + \left(\sigma_b \frac{\partial f}{\partial b}\right)^2 + 2\rho_{ab}\frac{\partial f}{\partial a}\frac{\partial f}{\partial b}\sigma_a\sigma_b, \tag{6.18}$$

where $f(a,b)$ corresponds to $C_Z/C_{W^\pm}$ and a, b correspond to C_Z, $C_{W^\pm}$, respectively. The uncertainties σ_a and σ_b are at the same level and the correlation coefficient ρ_{ab} is large. Therefore, the accuracy of correlation coefficient determination plays an important role for precision of the ratio measurement.

The calculation of the level of correlation using the toy MC introduces an additional statistical uncertainty due to the limited number of toy MC replica. This uncertainty can be estimated by artificial decorrelation of different number of C factors in one pair of toy MC replicas. For example, for $\rho_{C_Z C_{W^+}}$ calculation several components of toy MC replicas from the full list (provided in Table A.1) can be decorrelated. It can be simply achieved rearranging "Toy MC replica 1" and "2" for C_Z, while the rest replicas for C_Z, as well as C_{W^+}, stay on their original places.

The statistical accuracy of such determination depends on the number of possible decorrelations. For a toy MC set with n replicas, this number is given by the amount of derangements D_n e.g. permutation of the elements of a set, such that no element appears in its original position.

$$D_n = !n\,, \tag{6.19}$$

where $!n$ is a subfactorial function, that defined as:

$$!n = n!\sum_{i=0}^{n}\frac{(-1)^i}{i!}\,. \tag{6.20}$$

For $n \geq 1$ subfactorial can be defined as:

$$!n = \left[\frac{n!}{\gamma}\right], \tag{6.21}$$

where $\left[\frac{n!}{\gamma}\right]$ is the is the nearest integer function of $\frac{n!}{\gamma}$, and γ is the Euler's constant.

For the toy MC sets with $n \sim 100$, D_n is a very large number allowing for detailed statistical tests. In practice, far fewer number of permutations is required for sufficiently accurate determination of the uncertainties. A method to obtain these permutations is described below.

The first step of the method is cyclic permutations with no fixed points for all replicas (left scheme in Figure 6.13). Number of such derangements is $n-1$. The second step consists in one by one permutation of the first element in the chain of the toy MC replica with all other (except permutation with itself, and with element that stays at the original position of currently first element) elements for each of $n-1$ derangements (right scheme in Figure 6.13). In such a way there are $(n-3)(n-2)+(n-2-k)$ derangements at the second step, where $k=0$ if n is even, and $k=1$ if n is odd. Described method produces N derangements for n elements:

$$N = (n-2)(n-3) + (2n-3-k)\,. \tag{6.22}$$

Thereby, number of derangements for $n = 100$ is $N = 9703$.

Figure 6.13: Schematic representation of the method of permutation without fixed points for n elements (left scheme shows clockwise cyclic permutations for all elements, right scheme shows permutations of the first element with all other elements for each result of clockwise cyclic permutations).

Using the described method, the distributions for $C_Z C_Z$, $C_Z C_{W^+}$, and $C_Z C_{W^-}$ correlations, when all toy MC replicas are decorrelated, were obtained. Given distributions for the electron identification are shown in Figure 6.14. The rest correlation distributions are given in Appendix B. As expected, no correlation is observed on average, while the spread of the results corresponds to the statistical uncertainty.

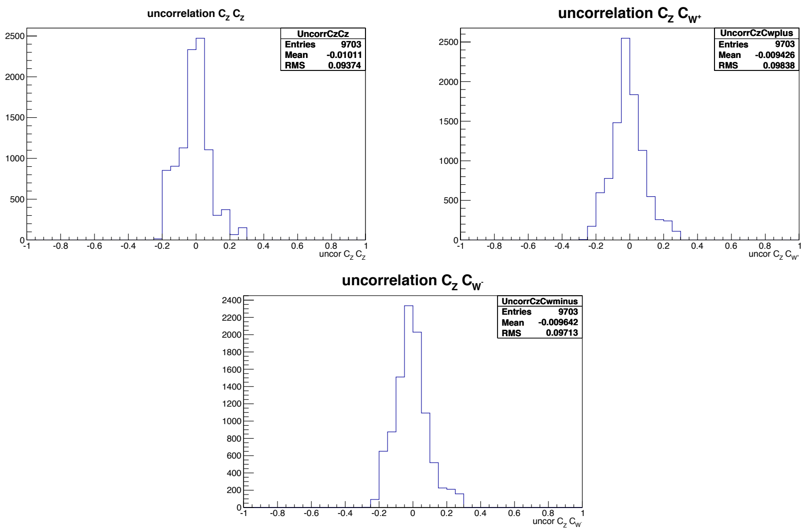

Figure 6.14: Correlation of $C_Z C_Z$, $C_Z C_{W^+}$, $C_Z C_{W^-}$ factors in case of full decorrelation for all MC toys for electron identification source of systematics.

The correlation behaviour with the different number of decorrelated replicas for the electron identification is given in Figure 6.15. It demonstrates a linear dependence of the mean value of the correlation distribution as a function of the number of correlated replicas. Similar behaviour was observed for electron isolation and trigger systematics sources.

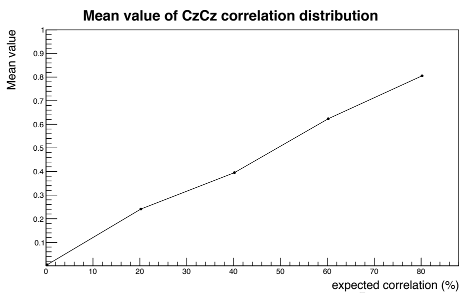

Figure 6.15: Mean value of correlation distribution with different number of decorrelated MC toys (for electron identification in $Z \to e^+e^-$ channel.)

	syst. uncertainty deviation (%)	
Channel	$\sigma_{W^+}/\sigma_{W^-}$	$\sigma_{W^\pm}/\sigma_Z$
e-channel	1.8	0.20
μ-channel	0.0	0.09
combined	0.0	0.05

Table 6.4: Deviation of systematic uncertainties (after variation of the correlation coefficients within its uncertainty) of the fiducial cross sections for the electron, muon and combined measurements.

The estimation of behaviour of the uncertainty on correlation factor is provided using the r.m.s. values of the correlation distributions with different number of decorrelated replicas. The r.m.s. as a function of expected correlation for the electron isolation are shown in Figure 6.16. Similar results for the electron identification, trigger, as well as muon trigger are shown in Figures B.2, B.3, and B.4, respectively.

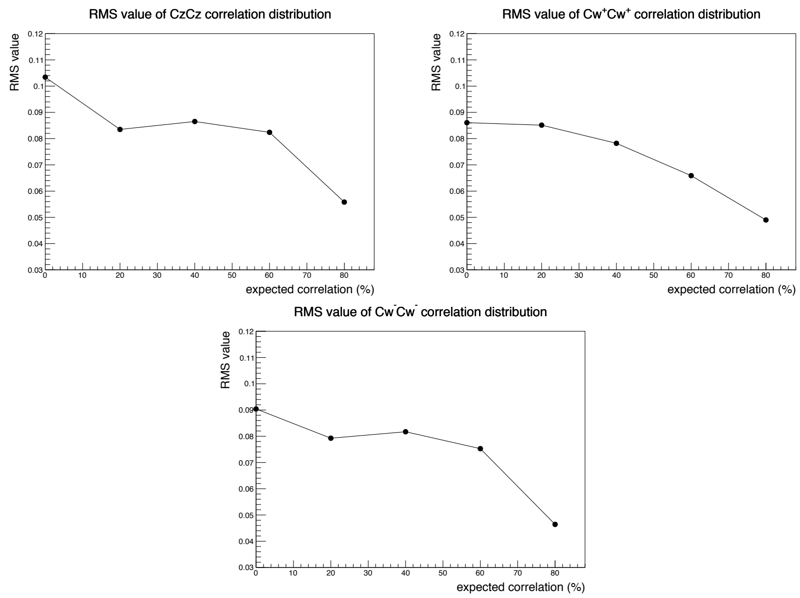

Figure 6.16: $C_Z C_Z$ (left), $C_{W^+}C_{W^+}$ (middle), $C_{W^-}C_{W^-}$ (right) RMS as a function of number of correlated toys for electron isolation systematics source.

For the electron and muon efficiency scale factors, 100 toy MC experiments allow to measure the correlation coefficients with the accuracy of $\sim 0.1\%$ ($\sim 0.05\%$) for 0% (80%) level of correlation. The impact of the correlation coefficient uncertainties on the systematic uncertainties on the cross-section ratios is estimated. The deviations of systematic uncertainties from the central values of W/Z and W^+/W^- cross-section ratios are obtained using the variation of correlation coefficients within its uncertainty. Given effect is found to be negligibly small (see Table 6.4) and can be ignored, which means that chosen number of toy MC replicas is sufficient for given measurements.

Chapter 7

Systematics uncertainties on correction factors

7.1 Systematic uncertainties on C_Z factor (50 ns bunch spacing)

7.1.1 $Z \to e^+e^-$ analysis

Systematic uncertainties on the C_Z correction factor for $Z \to e^+e^-$ cross section measurement with 50 ns bunch spacing data are introduced by the electron reconstruction, identification, isolation, and trigger efficiency scale factor uncertainties obtained with the tag-and-probe method. Also uncertainties on the electron energy scale, resolution and charge identification make contribution. Table 7.3 contains full list of systematic sources and the corresponding contributions to C_Z uncertainty. The total systematic uncertainty on C_Z factor is calculated as the sum in quadrature of uncertainties originated from different sources, since they are statistically independent. The names of the systematics in Table 7.3 are similar to the original names provided by appropriate tools.

- **Electron reconstruction** systematic uncertainty is estimated by applying variations on the selection parameters (tag identification, Z-mass peak window, template definition). Systematic uncertainty of SF_{Reco} on C_Z is $^{+0.77}_{-0.76}\,\%$.

- **Electron identification, isolation, and trigger** systematics are estimated using the combined toy MC method, as described in Section 6.5. Systematic uncertainties of SF_{ID}, SF_{ISO}, SF_{Trig} on C_Z are $^{+0.48}_{-0.48}\,\%$, $^{+0.29}_{-0.29}\,\%$, and $^{+0.05}_{-0.05}\,\%$, respectively.

- **Electron energy scale and resolution** systematic uncertainties are obtained using the systematic variations in the energy calibration using the simplified scheme, where all the effects are considered as fully correlated in η and summed in quadrature. Systematic uncertainty of electron energy scale is $^{+0.22}_{-0.23}\,\%$ and for energy resolution is $^{-0.02}_{+0.01}\,\%$.

- **Opposite charge requirement** causes a systematic uncertainty due to the charge identification inefficiency. The electron charge can be misidentified in case if one electron-candidate of the pair from Z decay emits photon which converts into another electron pair before passing the inner tracker, whereupon one electron candidate (similarly charged as the second electron candidate from first pair) from the second pair is reconstructed as high p_T track. Such reconstructed track can be associated with the calorimeter cluster, thereby selected event will contain two reconstructed electron candidates with the same charge. Fraction of such events is well predicted in signal MC (1.41 % in data vs 1.42 % in MC simulation). It is found that sample with same-signed reconstructed electrons has background contamination below 10 % [154]. To cover potential background in the fraction of same-signed events and difference between the data and MC (0.01 %), the systematic uncertainty of 0.15 % is assigned.

- **Pileup** scale factor for average number of pp interactions per bunch crossing, $\langle\mu\rangle$, is varied according to the ATLAS Tracking CP group recommendations (see Section 6.4). The resulting pileup scale factor uncertainty on C_Z factor is $^{+0.009}_{-0.006}\,\%$.

- **PDF** systematic uncertainty is the theoretical uncertainty based on CT10nlo calculation, since Z signal MC is simulated with CT10nlo. This PDF set contains 26 free parameters therefore there are 52 uncertainties (up and down variations). Total uncertainty is calculated by summing all eigenvectors in quadrature. Brake down of all eigenvectors as well as a total PDF uncertainty for C_Z and A_Z factors is presented in Table 7.1.

The central value of C_Z factor for electron channel with 50 ns bunch spacing data is 0.552, while its the total uncertainty is $^{+1.0}_{-0.99}\,\%$. The main contribution to C_Z uncertainty comes from the electron reconstruction and identification efficiencies.

7.1.2 $Z \to \mu^+\mu^-$ analysis

The uncertainties on C_Z factor for $Z \to \mu^+\mu^-$ analysis originate from the lepton-related efficiency systematics as well as pileup and PDF determination. The lepton systematic uncertainties are based on estimations and recommendations provided by the ATLAS Muon CP group [159].

- **Muon reconstruction** systematic uncertainty arises due to the several limitations of measurement: 1) statistical limitation for tracks with p_T much higher or lower

Eigenvector	C_Z Up(%)	C_Z Down(%)	A_Z Up(%)	A_Z Down(%)
1	-0.002	0.002	-0.218	0.200
2	-0.001	0.000	0.105	-0.115
3	0.013	-0.012	-0.001	-0.008
4	0.018	-0.024	0.235	-0.327
5	-0.003	0.004	-0.096	0.127
6	-0.006	0.004	-0.174	0.104
7	-0.043	0.077	-0.449	0.720
8	0.002	-0.001	-0.081	0.067
9	-0.002	0.006	0.229	-0.058
10	0.036	-0.013	0.538	-0.188
11	0.051	-0.027	0.316	-0.158
12	0.013	0.015	0.240	0.005
13	0.003	-0.005	-0.008	0.008
14	-0.016	0.013	-0.259	0.142
15	-0.012	0.010	-0.078	0.069
16	0.012	-0.003	0.081	0.022
17	-0.004	0.003	-0.006	-0.023
18	0.044	0.019	0.416	0.185
19	0.010	-0.009	0.146	-0.090
20	0.009	0.030	0.222	0.260
21	-0.040	0.037	-0.454	0.369
22	-0.010	0.011	-0.148	0.175
23	0.026	-0.032	0.312	-0.314
24	0.044	-0.010	0.324	-0.122
25	0.022	-0.018	0.206	-0.289
26	0.048	-0.004	0.547	-0.477
Total uncertainty	0.145	-0.085	1.470	-1.102

Table 7.1: Summary of the different variations of PDF contributing to the uncertainty on C_Z and A_Z for electron final states (for 50ns analysis).

than 50 GeV (causes significant effect of $^{+0.61}_{-0.61}$ % uncertainty), 2) biases introduced through the tag-and-probe method for muon efficiency definition related to discrepancy between probe and truth-level efficiencies at muon spectrometer crack region, $|\eta| < 0.1$, for low p_T which was propagated to efficiency scale factor, 3) systematic uncertainty due to transfer factor T [160] used for estimation of multijet background, 4) systematic uncertainty on the cone size ΔR around the probe is estimated by varying central value 0.05 between 0.025 and 0.1. Given systematic sources for muon reconstruction introduce $^{0.64}_{-0.64}$ % uncertainty on C_Z factor.

- **Muon isolation scale factor** uncertainty is estimated by varying related selection criteria: 1) Z-mass window, 2) isolation working point for tag and quality of the probe, 3) ΔR between two muons and between the probe muon and closest jet (for background events), 4) transfer factor T. All sources used for variations are taken as uncorrelated, therefore resulting isolation scale factor uncertainty calculated as sum in quadrature and found to be $^{+0.29}_{-0.29}$ %.

- **Muon Trigger** statistical uncertainty is estimated using the toy MC method and found to be $^{+0.1}_{-0.1}$ % . The systematic component is $^{+0.17}_{-0.17}$ %.

- **Muon energy scale and resolution** systematic uncertainties are estimated using the variations for parameters of reconstructed muons in the inner detector (ID) and muon spectrometer (MS) : 1) $M_{\mu\mu}^{ID,MS}$ window variation to take into account ISR

Eigenvector	C_Z Up(%)	C_Z Down(%)	A_Z Up(%)	A_Z Down(%)
1	-0.003	0.002	-0.218	0.200
2	0.001	-0.001	0.105	-0.115
3	-0.002	0.001	-0.000	-0.008
4	0.004	-0.005	0.235	-0.328
5	-0.002	0.003	-0.096	0.127
6	-0.003	0.001	-0.175	0.104
7	-0.003	0.003	-0.449	0.720
8	-0.001	0.001	-0.082	0.067
9	0.009	-0.004	0.227	-0.058
10	0.007	-0.002	0.537	-0.187
11	-0.002	0.002	0.315	-0.158
12	0.006	-0.004	0.240	0.005
13	-0.000	0.001	-0.008	0.008
14	-0.004	0.002	-0.259	0.142
15	0.001	-0.001	-0.079	0.070
16	-0.002	0.003	0.081	0.023
17	-0.002	0.000	-0.006	-0.023
18	-0.002	0.004	0.416	0.185
19	0.002	-0.001	0.146	-0.090
20	0.001	0.002	0.223	0.259
21	-0.005	0.003	-0.453	0.370
22	-0.003	0.003	-0.147	0.175
23	0.003	-0.003	0.311	-0.313
24	0.002	-0.001	0.324	-0.121
25	-0.000	-0.002	0.205	-0.275
26	0.004	-0.002	0.547	-0.477
Total uncertainty	0.017	-0.013	1.469	-1.097

Table 7.2: Summary of the different variations of PDF contributing to the uncertainty on C_Z and A_Z for muon final states (for 50ns analysis).

and FSR for events far from Z mass peak, 2) background normalization variation ($t\bar{t}$, ZZ, $Z \to \tau\tau$) by factor of 2 and 0.5, 3) simultaneously up(down) variation of correction factors for ID and MS reconstructed p_T of muons, 4) separate ID and MS resolution variation which provides over/under smearing of muon tracks with regard to nominal correction.

- **Pileup** scale factor for average number of pp interactions is varied in the same way as for electron channel. Pileup systematic uncertainty is estimated at the level of ${}^{-0.01}_{-0.03}\,\%$.

- **PDF** systematic uncertainty is based on CT10 PDF set with 26 eigenvectors and estimated using similar approach as for electron channel. The detailed list of all eigenvectors for C_Z and A_Z with the total uncertainty is shown in Table 7.2.

Table 7.4 contains full list of muon systematics. The main contribution to the total systematic uncertainty on C_Z factor is provided by the muon reconstruction and isolation sources. The central value of C_Z factor for muon channel with 50 ns bunch spacing data is 0.711, and its total uncertainty is ${}^{+1.05}_{-1.05}\,\%$.

Parameter	50ns		25ns	
	Up(%)	Down(%)	Up(%)	Down(%)
Statistics	0.05	-0.05	0.03	-0.03
EG_RESOLUTION_ALL__1	-0.02	0.01	-0.04	0.01
EG_SCALE_ALL__1	0.22	-0.23	0.24	-0.25
EL_EFF_ID_COMBMCTOY__1	0.48	-0.48	0.38	-0.38
EL_EFF_Iso_COMBMCTOY__1	0.29	-0.29	0.14	-0.14
EL_EFF_Reco_TotalCorrUncertainty__1	0.77	-0.76	-	-
EL_EFF_Reco_COMBMCTOY__1	-	-	0.05	-0.05
EL_EFF_Trig_COMBMCTOY__1	0.05	-0.05	0.01	-0.01
Opposite charge requirement	-0.15	0.15	-0.15	0.15
Z p_T mismodeling	-	-	-0.07	0.07
Pileup	0.01	-0.01	0.01	-0.01
PDF	0.14	-0.08	0.10	-0.10
Total	1.00	-0.99	0.51	0.52

Table 7.3: Summary of the different terms contributing to the uncertainty on C_Z for electron final states.

7.2 Systematic uncertainties on C_Z factor (25 ns bunch spacing)

7.2.1 $Z \to e^+e^-$ analysis

Most of the systematic sources for Z-boson measurement with 25 ns data are similar to 50 ns analysis. The p_T^Z mismodelling is only the additional source. Its effect is estimated at the level of 0.07% and included into C_Z systematic sources list. Calculation of electron reconstruction efficiency scale factor uncertainty is performed using the toy MC method unlike to 50 ns analysis where the selection criteria variations are applied. Uncertainties introduced by the electron identification, isolation and trigger efficiency scale factors are also estimated with the toy MC method. The PDF systematic uncertainty calculation is based on NNPDF3.0 set with 100 MC replicas. The total PDF uncertainty on C_Z factor is $^{+0.1}_{-0.1}$%. More details on systematic sources and methods of their evaluation for 25 ns analysis can be found in Ref. [124].

Table 7.3 contains uncertainties on C_Z factor introduced by each systematic source. The total systematic uncertainty is found to be two times smaller comparing to 50 ns analysis result, mostly due to applying toy MC method for electron reconstruction efficiency uncertainty and reducing statistical component. The central value for C_Z factor is 0.5536, while its total uncertainty is $^{+0.51}_{-0.52}$%.

7.2.2 $Z \to \mu^+\mu^-$ analysis

The muon track to vertex association and p_T^Z mismodelling are the two additional systematic sources, compared to 50 ns analysis, where the first was found to be negligible. For PDF uncertainty estimation the NNPDF3.0 PDF set is used. The detailed list of systematics for muon channel is provided in Table 7.4. The central value for C_Z factor is

Parameter	50ns		25ns	
	Up(%)	Down(%)	Up(%)	Down(%)
Statistics	0.05	-0.05	0.04	-0.04
MUONS_ID__1	-0.05	-0.01	-0.01	-0.00
MUONS_MS__1	-0.01	0.00	-0.01	-0.00
MUONS_SCALE__1	-0.07	0.06	-0.07	0.04
MUON_EFF_STAT__1	0.61	-0.61	0.33	-0.33
MUON_EFF_SYS__1	0.64	-0.64	0.59	-0.59
MUON_EFF_TrigSystUncertainty__1	0.17	-0.17	0.12	-0.12
MUON_EFF_TrigStatTOYUncertainty__1	0.10	-0.10	0.03	-0.03
MUON_ISO_STAT__1	0.49	-0.48	0.07	-0.07
MUON_ISO_SYS__1	0.22	-0.21	0.40	-0.40
MUON_TTVA_STAT__1	-	-	0.00	0.00
MUON_TTVA_SYS__1	-	-	0.00	0.00
Opposite charge requirement	-0.00	0.00	-0.00	0.00
Z p_T mismodeling	-	-	-0.03	0.03
Pileup	-0.01	-0.03	-0.01	-0.03
PDFCT10	0.02	-0.01	0.02	-0.02
Total	1.05	-1.05	0.80	0.81

Table 7.4: Summary of the different terms contributing to the uncertainty on C_Z for muon final states.

0.7064, while its total uncertainty is ${}^{0.80}_{-0.81}$ %. More details on systematic sources for 25 ns data analysis can be found in Ref. [124].

7.3 Systematic uncertainties on A_Z and E_Z factors

The A_Z extrapolation factors for 50 ns and 25 ns analyses are computed using the theoretical predictions for total and fiducial cross sections, as it is explained in Section 5.2. Similarly to $\sqrt{s} = 13$ TeV analyses, the A_Z factors for measurements at $\sqrt{s} = 7$ TeV and $\sqrt{s} = 8$ TeV are calculated using the DYTURBO program and CT14NNLO PDF set to achieve the uniformed ratio calculations of total Z-boson cross sections. The NLO EW corrections are also estimated with FEWZ3.1.

The statistical uncertainties on A_Z factors are negligible, whereas main role in systematic uncertainty plays limited knowledge of proton PDFs. There are systematic sources that are taken into account in A_Z calculation: PDF, scale and α_s.

- **PDF** uncertainty is estimated using the “up” and “down” variations for each of 26 eigenvectors of CT14NNLO PDF set. “Up” variations can provide negative uncertainty and vice versa for some eigenvectors, therefore “up” uncertainty for each eigenvector is taken as a biggest positive signed value from the up/down pair and the “down” is the smallest negative signed value. “Up” uncertainties added in quadrature provide the total “up” PDF uncertainty, while the same sum of “down” uncertainties is the total “down” PDF uncertainty with minus sign. Such calculation represents the envelope of the PDF variations.

- **Scale** uncertainty is estimated by the envelope of the scale variations where the scales are changed by a factor of two. Variations of μ_f and μ_r are done separately

A_Z^i/A_Z^j	A_Z^{8TeV}/A_Z^{13TeV}	A_Z^{7TeV}/A_Z^{13TeV}	A_Z^{7TeV}/A_Z^{8TeV}
value	1.180 ± 0.004	1.279 ± 0.006	1.084 ± 0.002

Table 7.5: A_Z factors ratio at different center-of-mass energies with the total uncertainty. A_Z^{13TeV} factor corresponds to 25ns data analysis.

as well as simultaneously and both effects are taken into account.

- Uncertainty due to the α_s is estimated by varying α_s by $\pm$ 0.001. The total uncertainty due to the α_s is calculated as sum in quadrature of resulting "up" and "down" uncertainties.

All uncertainties are rescaled from 90% CL to 68% CL. The resulting A_Z factors with the total uncertainty for all center-of-mass energy are shown in Table 5.3. For the Z boson total cross section ratios at different center-of-mass energies, ratios A_Z^i/A_Z^j, where i, j - different $\sqrt{s}$, are calculated. The PDF uncertainties on the A_Z ratios are computed eigenvector-by-eigenvector. The uncertainty for k eigenvector of A_Z^i/A_Z^j ratio is calculated using the formula

$$\Delta\left(\frac{A_Z^i}{A_Z^j}\right)_k = \frac{(\sigma_{centr}^i + \Delta\sigma_{PDF}^{i,k})_{fid} \cdot (\sigma_{centr}^i + \Delta\sigma_{PDF}^{j,k})_{tot}}{(\sigma_{centr}^i + \Delta\sigma_{PDF}^{i,k})_{tot} \cdot (\sigma_{centr}^i + \Delta\sigma_{PDF}^{j,k})_{fid}} - \frac{\sigma_{centr,fid}^i \cdot \sigma_{centr,tot}^j}{\sigma_{centr,tot}^i \cdot \sigma_{centr,fid}^j}, \tag{7.1}$$

where σ_{centr} is the central value of the cross section calculated with DYTURBO, $\Delta\sigma_{PDF}^k$ is the uncertainty for eigenvector with index k (up and down variation for the same eigenvector has different k index). The total PDF uncertainty on the A_Z factors ratio is estimated as an envelope of all eigenvectors. The symmetrized PDF uncertainty is calculated as $\Delta\sigma^{sym} = \frac{1}{2}\big(\Delta\sigma^{up} - \Delta\sigma^{down}\big)$, where $\Delta\sigma^{up}$ is the positive signed total "up" uncertainty and $\Delta\sigma^{down}$ is the negative signed total "down" uncertainty.

The components of uncertainties from scale and α_s variations are uncorrelated between fiducial and total phase spaces and not included into A_Z^i/A_Z^j uncertainty. The results of acceptance factors ratio at different center-of-mass energies with the total uncertainties are given in Table 7.5.

The systematic uncertainties for E_Z factors are estimated following similar approach. Therefore, E_Z uncertainty for k eigenvector of the PDF set is defined as

$$\Delta(E_Z)_k = \frac{\sigma_{centr,fid}^{13TeV\ vol} + \Delta\sigma_{fid,k}^{13TeV\ vol}}{\sigma_{centr,fid}^{meas\ vol} + \Delta\sigma_{fid,k}^{meas\ vol}} - \frac{\sigma_{centr,fid}^{13TeV\ vol}}{\sigma_{centr,fid}^{meas\ vol}}, \tag{7.2}$$

where $\Delta\sigma_{fid,k}^{13TeV(meas)\ vol}$ is the uncertainty of PDF eigenvector with index k. The resulting E_Z factors with the total uncertainties are given in Table 5.3.

Chapter 8

Kinematic distributions and background-subtracted events

8.1 Kinematic distributions

Kinematic distributions of selected leptons and reconstructed Z-bosons in the $Z \to \ell^+\ell^-$ channels are provided separately for 50 ns and 25 ns bunch spacing conditions. The data distributions are compared to $Z \to e^+e^-$ and $Z \to \mu^+\mu^-$ Monte Carlo (MC) simulated samples, generated with POWHEG+Pythia (details are in Section 4.2), and the background expectations. All electroweak and $t\bar{t}$ backgrounds are taken from MC simulations, whereas QCD multi-jet contribution is extracted using the data-driven method. The data-to-expectations comparison plots (also referred to as control distributions) do not include W and multi-jet background contributions for both $Z \to e^+e^-$ and $Z \to \mu^+\mu^-$ channels with 50 ns and 25 ns data analyses due to their negligible contributions. The control distributions for diboson simulated data ($WZ \to qqll$, $ZZ \to qqll$, $WW \to l\nu l\nu$) are combined together to emphasize their contribution and compatibility with the $t\bar{t}$ deposit. The non-negligible $Z \to \tau\tau$ background fraction is also shown in the control distributions. The background processes for electron and muon channels for both bunch spacing data samples are heavily suppressed and, therefore, are not visible on the distributions on a linear scale.

The plots show the MC samples stacked on top of each other and compared to the black data points. The signal MC simulations are normalised to the measured cross sections. The remaining simulations are normalised to the predictions of the highest-order available QCD calculations with uncertainties provided in Table 4.3. The contribution of all systematic uncertainties, described in Section 7, for the signal distributions are combined with the background expectation uncertainties and plotted as the shaded band at the data to prediction ratio part for each control distribution. The statistical uncertainty contributions are shown on the data point. The luminosity and beam energy uncertainties are not included into the control distributions.

8.1.1 Kinematic distributions for 50 ns bunch spacing data

The transverse momentum distributions of the electrons and muons are shown in Figure 8.1 on a linear scale. Monte Carlo simulation describes data well in full p_T spectrum although statistics are poor in the tail of the distributions. The p_T-distributions for electrons and muons have a maximum in the region of $\sim$ 43 GeV and fall steeply. The contribution of background processes is higher in the low-p_T region and decreases steadily with p_T. The η-distributions for electron and muon candidates are shown in Figure 8.2. The pseudo-rapidity distributions demonstrate the expected shape for highly energetic events, which are typically central. Most of the entries are at small absolute values of pseudo-rapidity η and the distributions falls towards larger absolute values. The small dip in the muon η-spectrum in the region $|\eta| < 0.1$ is expected and corresponds to the Muon Spectrometer crack region (see Section 3.2.5). Due to the coarse bin width of the distributions, driven by the efficiency scale factors binning, the empty regions of $1.37 < |\eta| < 1.52$ cut are not observed for electron pseudo-rapidity. Discrepancies observed at high $|\eta_e|$ for both electrons and muons are also due to mismatch of the binning for the control plots and efficiency scale-factor distributions. The reconstructed dilepton invariant mass distributions, shown in Figure E.2, are sensitive to the track momentum scale and resolution since the dilepton mass is reconstructed using the measured lepton momenta. Thus, the systematic uncertainty bands for both channels are dominated by corresponding lepton energy (momentum) scale and resolution variation. Therefore, the wider uncertainty band for dielectron than for dimuon invariant mass is due to the difference in uncertainty introduced by energy scale for electrons and momentum scale for muons. The top processes shows a flat distribution in $m_{\ell\ell}$, while spectrum for $Z \to \tau^+\tau^-$ have a monotonously falling shape. The invariant mass for the diboson processes naturally features a peak at the Z-mass. The transverse momentum of the lepton pair, determined using p_T of each leptons, is given in Figure 8.4. Similarly to single lepton p_T distributions, it demonstrates increasing of uncertainties as well as discrepancy between the data and MC simulated distribution in the high-p_T region due to statistical limitations. The background contribution is also dominated in the region of low p_T. All control distributions for data and MC simulations show a good agreement within the uncertainties. More kinematic distributions with data to MC comparison are given in Appendix E.

8.1.2 Kinematic distributions for 25 ns bunch spacing data

Since the 25 ns bunch spacing data set contains higher statistics, the data point fluctuations as well as statistical uncertainties in the tails of p_T^{ℓ} and $p_T^{\ell\ell}$ distribution are reduced compared to similar results with 50 ns data. The total systematic uncertainty is reduced due to the implementation of Toy MC method for broader list of systematic

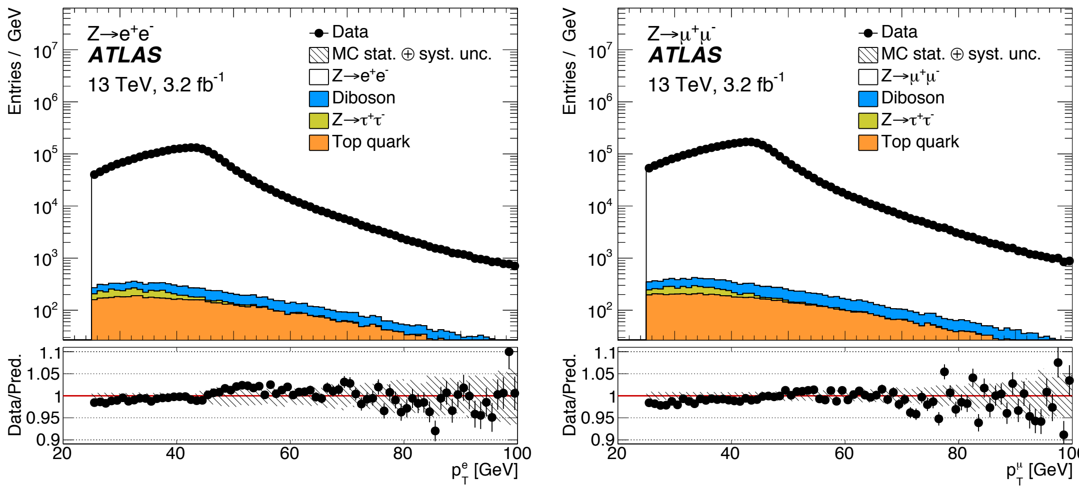

Figure 8.1: Lepton transverse momentum distributions from the $Z \to e^+e^-$ selection (left) and the $Z \to \mu^+\mu^-$ selection (right). Systematic uncertainties for the signal and background distributions are combined in the shaded band, and statistical uncertainties are shown on the data points. Luminosity uncertainties are not included. There are two lepton entries in the histogram for each candidate event.

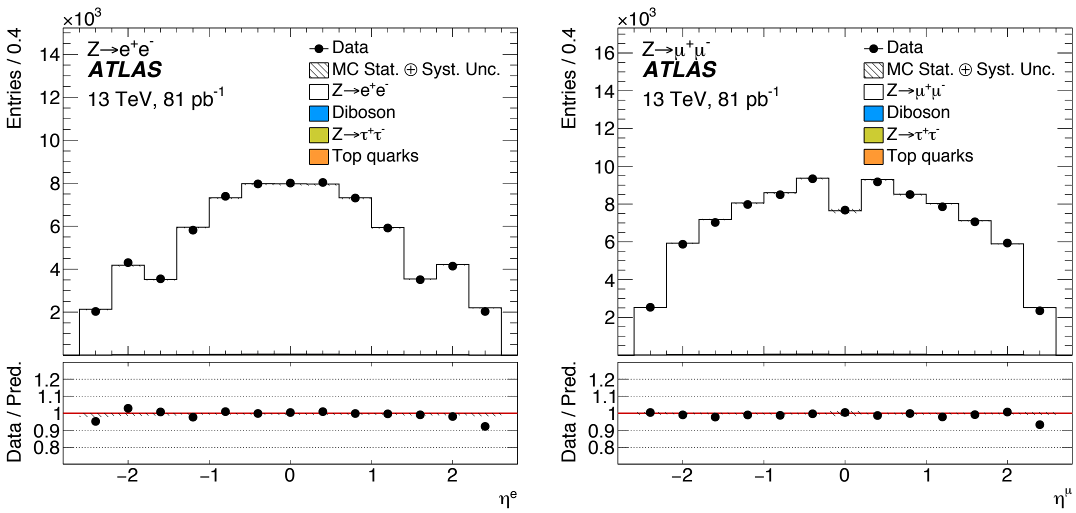

Figure 8.2: Lepton pseudo-rapidity distribution from the $Z \to e^+e^-$ selection (left) and the $Z \to \mu^+\mu^-$ selection (right). Systematic uncertainties for the signal and background distributions are combined in the shaded band, and statistical uncertainties are shown on the data points. Luminosity uncertainties are not included. There are two lepton entries in the histogram for each candidate event.

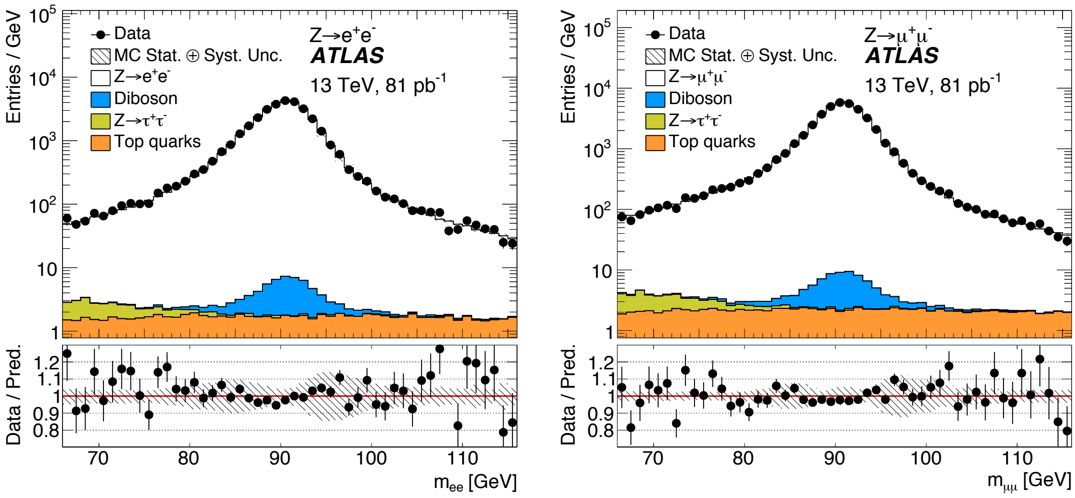

Figure 8.3: Dilepton mass distribution after the $Z \to e^+e^-$ selection (left) and the $Z \to \mu^+\mu^-$ selection (right). Systematic uncertainties for the signal and background distributions are combined in the shaded band, and statistical uncertainties are shown on the data points. Luminosity uncertainties are not included.

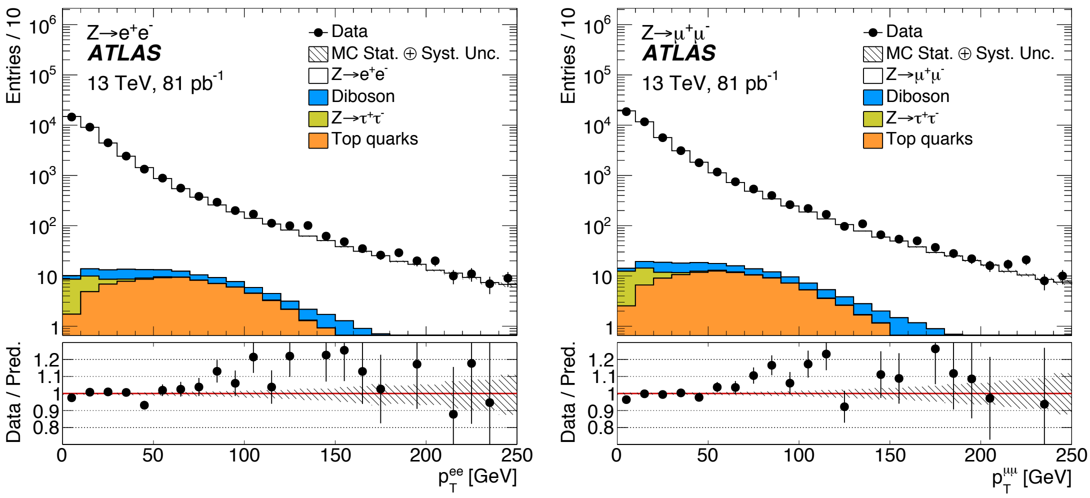

Figure 8.4: Z boson transverse momentum distribution after the $Z \to e^+e^-$ selection (left) and the $Z \to \mu^+\mu^-$ selection (right). Systematic uncertainties for the signal and background distributions are combined in the shaded band, and statistical uncertainties are shown on the data points. Luminosity uncertainties are not included.

sources comparing to the analysis of 50 ns data. The comparison of measured and MC simulated distributions for lepton transverse momentum as well as invariant mass and transverse momentum of lepton pair is given in Figures 8.5, 8.6, and 8.7, respectively, and demonstrate a high level of agreement. Moreover, control distributions obtained with 25 ns and 50 ns data sets show similar shape indicating good compatibility among the measurements. More control distributions obtained with 25 ns data are given in Ref. [124].

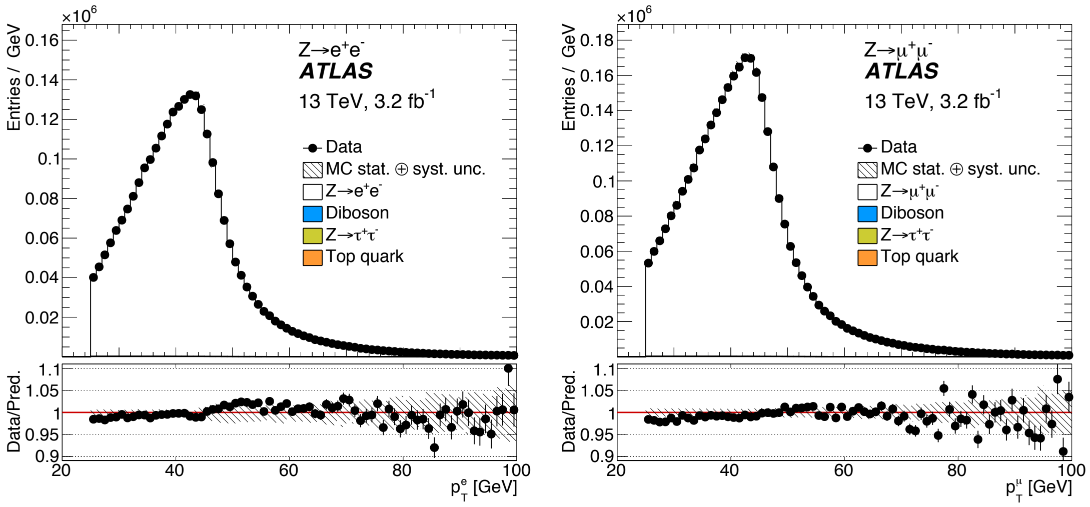

Figure 8.5: Lepton transverse momentum distributions from the $Z \to e^+e^-$ selection (left) and the $Z \to \mu^+\mu^-$ selection (right). The systematic uncertainties for the signal and background distributions are combined in the shaded band, and the statistical uncertainties are shown on the data points. The luminosity uncertainties are not included. There are two lepton entries in the histogram for each candidate event. The systematic error bands and statistical uncertainties are often hidden by the symbols and lines.

8.2 Background-subtracted Z candidate events

Given that for all the control distributions the data is well described by the simulation, the number of background subtracted event candidates can be calculated. Table 8.1 summarises the numbers of observed candidate events for the $Z \to e^+e^-$, $Z \to \mu^+\mu^-$ channels with 50 ns and 25 ns data. It also contains the number of expected background events from both the multi-jet and electroweak including top processes as well as the number of background-subtracted signal events. The higher statistics in the 25 ns data set allowed to determine the multi-jet background expectations more precisely. The multi-jet background is estimated to have less than 0.1% contribution for 50 ns data and less than 0.01% for 25 ns data. However, the level of multi-jet background is neglected in both cases. For

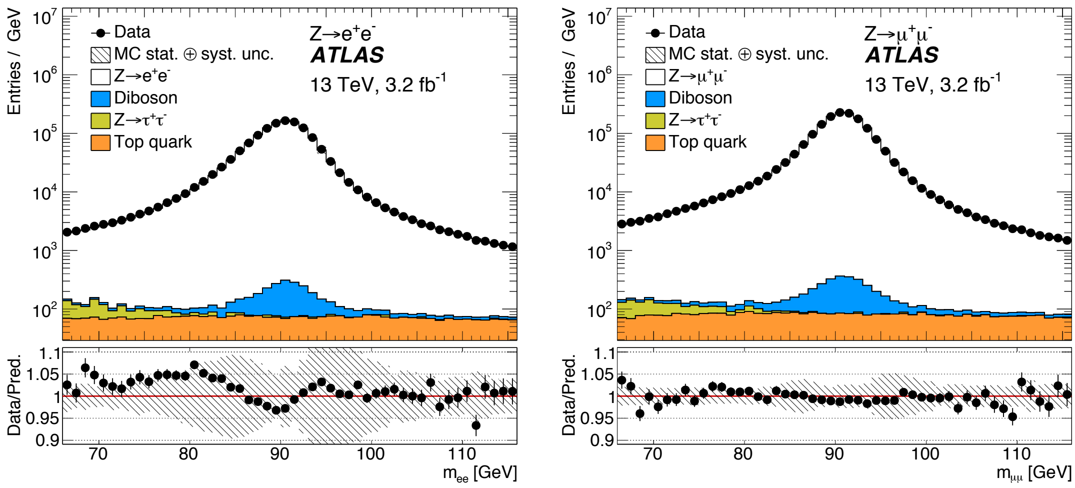

Figure 8.6: Dilepton mass distribution after the $Z \to e^+e^-$ selection (left) and the $Z \to \mu^+\mu^-$ selection (right). The systematic uncertainties for the signal and background distributions are combined in the shaded band, and the statistical uncertainties are shown on the data points. The luminosity uncertainties are not included. The systematic error bands and statistical uncertainties are often hidden by the symbols and lines.

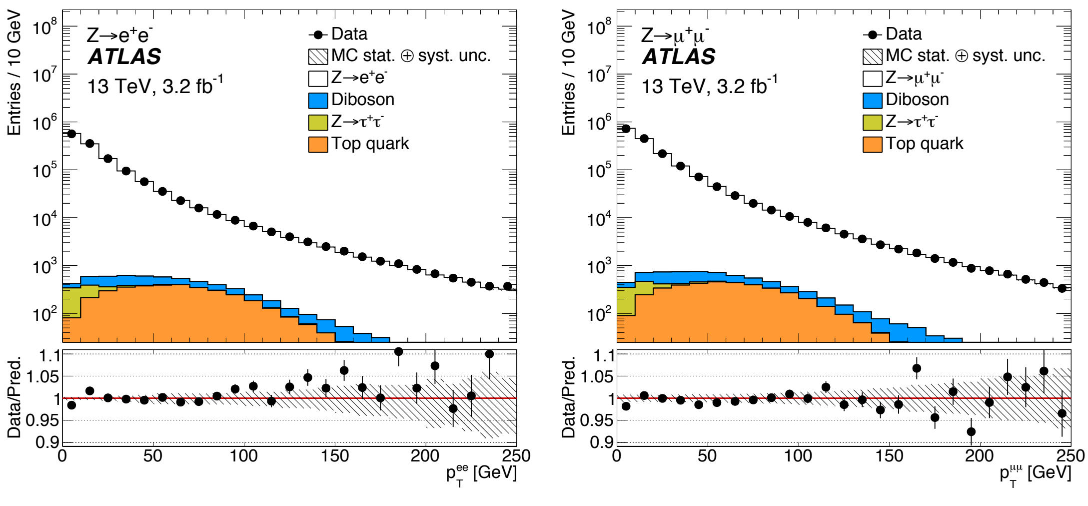

Figure 8.7: Z boson transverse momentum distribution after the $Z \to e^+e^-$ selection (left) and the $Z \to \mu^+\mu^-$ selection (right). The systematic uncertainties for the signal and background distributions are combined in the shaded band, and the statistical uncertainties are shown on the data points. The luminosity uncertainties are not included. The systematic error bands and statistical uncertainties are often hidden by the symbols and lines.

Data	Channel	Observed candidates	EW + top background value ± stat ± syst	Multijet background	Background-subtracted candidates value ± stat ± syst ± lumi
50 ns	e^+e^-	35009	$144 \pm 1 \pm 8$	$< 0.1\%$	$34865 \pm 187 \pm 7 \pm 3$
	$\mu^+\mu^-$	44898	$191 \pm 1 \pm 10$	$< 0.1\%$	$44707 \pm 212 \pm 9 \pm 4$
25 ns	e^+e^-	1,367,026	$6344 \pm 43 \pm 761$	$< 0.02\%$	$1,360,682 \pm 1169 \pm 762 \pm 133$
	$\mu^+\mu^-$	1,735,197	$7500 \pm 48 \pm 952$	$< 0.02\%$	$1,727,698 \pm 1317 \pm 953 \pm 158$

Table 8.1: Number of observed candidate events for the electron end muon channels with 50 ns and 25 ns data. Fractions of electroweak (EW) plus top background events are showed with statistical and systematic uncertainty, additional 2.1% uncertainty on the luminosity determination is applicable. The multi-jet background estimations are listed in percentage.

the background-subtracted event candidates the statistical uncertainty is quoted first, followed by the total systematic uncertainty, derived from the electroweak plus top and multi-jet background, considering the sources as uncorrelated. The luminosity determination uncertainty of 2.1% is applicable to the electroweak and top backgrounds and is given for the background-subtracted events. The increase of background-subtracted candidates for 25 ns data set comparing to 50 ns data in both channels is proportional to the increase of the luminosity.

Chapter 9

Analysis of correlations and combinations

The correlation model for systematic uncertainties is an important component for the evaluation of the combined cross section for $Z \to e^+e^-$ and $Z \to \mu^+\mu^-$, for the Z-boson measurements, as well as $W^+ \to e^+\nu_e$, $W^- \to e^-\bar{\nu}_e$, $W^+ \to \mu^+\nu_\mu$, and $W^- \to \mu^-\bar{\nu}_\mu$ for the W-boson measurements. Moreover, the level of correlation between the systematic sources plays a key role in the uncertainty cancellation in the cross-section ratio calculation. These correlations arise from the use of electrons, muons, or E_T^{miss} reconstructed in the same way for different channels, but also due to similar or identical analysis techniques, e.g. in the signal and background estimation.

9.1 W and Z correlation model

Given that the same tools were used for the lepton selection in the Z and W analyses of 50 ns bunch spacing data, the lepton-related systematic sources for the same flavour channels are treated as correlated. Thus the muon reconstruction, identification, isolation, momentum scale, and trigger systematic sources are correlated between the $Z \to \mu^+\mu^-$, $W^+ \to \mu^+\nu_\mu$ and $W^- \to \mu^-\bar{\nu}_\mu$ measurements. The muon trigger systematic uncertainties are estimated using the Toy MC method for both of the W and Z analyses, as described in Section 6.5, and due to differences in the p_T^ℓ and $\left|\eta^\ell\right|$ distributions the correlation is found to be below 100% level. The charge-dependent part of the trigger systematics for the W^+ and W^- muon channels is taken into account separately and treated as correlated between W^+ / W^-, and uncorrelated with the Z channel.

The correlations for lepton reconstruction, identification, isolation, and trigger systematics for the electron channels $Z \to e^+e^-$, $W^+ \to e^+\nu_e$, and $W^- \to e^-\bar{\nu}_e$ are estimated with the Toy MC method, and the correlation coefficients are given in Section 6.5. Each of these systematic uncertainty sources is represented with three nuisance parameters, where the first two are correlated components and the third is anti-correlated. The other two electron-related systematics, electron energy scale and resolution, are treated as 100% correlated between all three channels. All discussed lepton-related sources are naturally uncorrelated between the electron and muon channels.

The systematic uncertainties which affect only the $W^{\pm}$ measurements, such as jet-related sources (jet energy scale, reconstruction, resolution, vertex tagging) and missing energy reconstruction, are treated as fully correlated between all four channels for W decay. Such an approach is used following the pre-recommendations based on the 2012 jet energy scale uncertainties [162]. For the E_T^{miss} reconstruction for both electron and muon channels the `METSystematicsTool` tool was used, where the systematics were estimated using different Monte Carlo generators instead of data-driven techniques.

The systematic uncertainties from the electroweak and top background estimations are treated as uncorrelated between the W and Z analyses, and fully correlated among different flavour decay channels of the W and Z boson. The multi-jet background for the W channels is non-negligible. It is described by 10 nuisance parameters, 5 parameters per each lepton flavour. The 5 parameters are split into 3 correlated and 2 anti-correlated components. Details of the multi-jet background correlation model for the W channels are given in Ref. [154].

Two of the systematic sources, PDF and Pileup, are taken as fully correlated between all six channels. Both the W and Z analyses use the CT10nlo PDF set with 26 eigenvector variations. The common methodology for evaluating the pileup uncertainty for the W and Z channels was used, and is described in Section 6.4. The same normalisation uncertainty due to the luminosity calibration, as well as beam energy uncertainty, are excluded for the combination of the channels.

The simplified form of the correlation model with a grouped list of systematic sources is given in Table 9.1, and the values of these uncertainty sources are listed in Table 9.2. The correlation between the electron and muon decay channels of the W boson is introduced mainly by the jet- and lepton-related systematics, whereas the correlation between the W^+ and W^- measurements with the same decay channel is based on jet-related and multi-jet background systematic sources. The dominant contribution to the correlation between the electron and muon channels for Z boson decays, as well as the correlation between the W and Z measurements, originates from the lepton-related systematics. The groups listed in Tables 9.1 and 9.2 are represented by several nuisance parameters. A full list of the nuisance parameters for the different decay modes is given in Appendix C.

The introduced correlation model allows the combination of the electron and muon decay channels, as well as the opposite charge W channels. The combination procedure is described in Section 9.3. The correlation coefficients between the combined channels were also assessed (see Section 9.4).

Source	Muon channel			Electron channel		
	Z	W^+	W^-	Z	W^+	W^-
Beam energy	A	A	A	A	A	A
Muon trigger	A	A^*	A^*	—	—	—
Muon reconstruction/ID	A	A	A	—	—	—
Muon isolation	A	A	A	—	—	—
Muon momentum scale	A	A	A	—	—	—
Electron trigger	—	—	—	A	A	A
Electron reconstruction/ID	—	—	—	A	A	A
Electron isolation	—	—	—	A	A	A
Electron energy scale	—	—	—	A	A	A
Jet-related	—	A	A	—	A	A
E_T^{miss} reconstruction	—	A	A	—	A	A
EWK + top bkg	A	B	B	A	B	B
Multi-jet bkg	—	A	A	—	B	B
PDF	A	A	A	A	A	A
Pileup	A	A	A	A	A	A

Table 9.1: The correlation model for the grouped systematic uncertainties for the measurements of Z and W-boson production. The entries in different rows are uncorrelated with each other. Entries within a row with the same letter are fully correlated. Entries within a row with a starred letter are mostly correlated with the entries with the same letter (most of the individual sources of uncertainties within a group are taken as correlated). Entries with different letters within a row are either fully or mostly uncorrelated with each other.

Source	Muon channel			Electron channel		
	δ_Z^{fid}[%]	δ_{W+}^{fid}[%]	δ_{W-}^{fid} [%]	δ_Z^{fid}[%]	δ_{W+}^{fid}[%]	δ_{W-}^{fid}[%]
Muon trigger	0.2	0.6	0.6	—	—	—
Muon reconstruction/ID	0.9	0.4	0.4	—	—	—
Muon isolation	0.5	0.3	0.3	—	—	—
Muon momentum scale	0.1	0.1	0.1	—	—	—
Electron trigger	—	—	—	0.1	0.3	0.3
Electron reconstruction/ID	—	—	—	0.9	0.4	0.4
Electron isolation	—	—	—	0.5	0.3	0.3
Electron energy scale	—	—	—	0.1	0.1	0.1
Jet-related	—	1.6	1.7	—	1.7	1.7
E_T^{miss} reconstruction	—	0.1	0.1	—	0.1	0.1
EWK + top bkg	0.03	0.27	0.35	0.03	0.13	0.14
Multijet bkg	—	0.9	1.1	—	2.0	3.3
PDF	<0.1	0.1	0.1	0.1	0.1	0.1
Pileup modelling	<0.1	0.2	0.2	<0.1	0.4	0.3

Table 9.2: Systematic uncertainties, δ, in % for the measurement of Z and W-boson production. Values listed as "—" have no corresponding uncertainty.

9.2 $t\bar{t}$ and Z correlation model

The correlation between the Z boson and $t\bar{t}$ cross-section measurements at different center-of-mass energies is expected to be more complicated than the correlation model for the W and Z measurements at the same $\sqrt{s}$. [1] The correlation model is given in a simplified form in Table 9.3. The groups listed in the table may be represented by a single source, or by several individual sources, of systematic uncertainties (nuisance parameters). The size of the uncertainties is summarized in Table 9.4. The groups of sources are:

- *Luminosity*: this uncertainty is considered to be correlated for the measurements performed at the same center-of-mass energy. This is ensured by using the same luminosity database-tag and similar data-quality requirements as used for the measurements. It is taken as uncorrelated between measurements at different $\sqrt{s}$, as the luminosity uncertainties are dominated by machine optics related effects and variations of the luminosity calibrations with time, and is therefore considered uncorrelated between 2011 and 2012 of run-I and run-II.

[1] Since the luminosity and beam energy uncertainties are not negligible for all measurements and can provide dominant contribution to some of cross-section ratios, they must be taken into account in the construction of the correlation model.

- *Beam energy*: this uncertainty is 0.66% of the beam-energy value [125] and is considered to be fully correlated for all data sets [2].

- *Muon and electron trigger*: these uncertainties are introduced by using a single nuisance parameter for the $t\bar{t}$ cross section measurements at $\sqrt{s} = 7$ TeV and $\sqrt{s} = 8$ TeV. This nuisance parameter is treated as uncorrelated to the trigger uncertainties for the $t\bar{t}$ measurement at $\sqrt{s} = 13$ TeV and for all Z-boson measurements. The other measurements of Z boson production at $\sqrt{s} = 13, 8$ and 7 TeV, and $t\bar{t}$ at $\sqrt{s} = 13$ TeV are treated as correlated between themselves.

- *Muon reconstruction and identification*: the treatment of these uncertainties is fully synchronised, in terms of selection methods and tools, for the Z and $t\bar{t}$ measurements at $\sqrt{s} = 13$ TeV. Therefore, these measurements are considered to be correlated. The Z-boson measurements at $\sqrt{s} = 7$ TeV and $\sqrt{s} = 8$ TeV are treated as uncorrelated with each other, and with all $t\bar{t}$ measurements. The muon reconstruction and identification uncertainties between $t\bar{t}$ measurements at $\sqrt{s} = 7$ TeV and $\sqrt{s} = 8$ TeV are assumed to be correlated due to the similarity of the reconstruction algorithms.

- *Muon isolation*: this is a small source of uncertainty for all Z-boson measurements, and similar between them, thus it is considered to be correlated among all center-of-mass energies. For the $t\bar{t}$ analysis, the muon isolation is determined in-situ, to account for a different hadronic environment, with a significant statistical uncertainty. Thus, it is considered to be uncorrelated among the $t\bar{t}$ measurements at different $\sqrt{s}$ as well as to the Z-boson measurements.

- *Muon momentum scale*: this is a moderate source of uncertainty for all measurements. It is validated in-situ by comparing the invariant mass distributions of muon pairs in data and simulation. Similar levels of agreement are observed for all data-taking periods, and thus all measurements are considered to be correlated.

- Following similar line of reasoning as in muon case, *the electron trigger uncertainties* are taken as correlated between all Z-boson and $t\bar{t}$ measurements at $\sqrt{s} = 13$ TeV, but uncorrelated to the other $t\bar{t}$ measurements. The electron trigger uncertainty is sub-dominant for all measurements.

- The treatment for *electron reconstruction and identification* uncertainties is fully synchronised for the $\sqrt{s} = 13$ TeV data analyses thus, these measurements are considered to be correlated. Furthermore, the Toy MC method was used for the electron reconstruction and identification uncertainty estimation for both the Z and $t\bar{t}$ measurements with 13 TeV data. Therefore, these measurements are not 100%

[2]The relative uncertainty on the beam energy is updated in 2017 and determined to be 0.1%.

correlated, and introduce additional nuisance parameters. The level of correlation between the measurements for electron reconstruction and identification is shown in Figure 6.12. The Z-boson measurements at $\sqrt{s} = 7$ TeV and 8 TeV are considered to be uncorrelated with each other, and to the $t\bar{t}$ measurement at run-I, and to the $\sqrt{s} = 13$ TeV measurements, due to the difference in algorithms used. As long as identical reconstruction techniques and identification working points are used in the $t\bar{t}$ measurements at $\sqrt{s} = 7$ TeV and 8 TeV, the corresponding systematic sources are taken as correlated.

- The *electron isolation* and *energy scale* uncertainties are treated similarly to the muon isolation and momentum scale, respectively.

- *Jet energy scale*: this uncertainty only affects the $t\bar{t}$ measurements, and is described by several nuisance parameters. The uncertainty is correlated for $\sqrt{s} = 7$ TeV and 8 TeV data, following the prescription in Ref. [75], and mostly uncorrelated with 13 TeV data, in part due to the in-situ corrections. The impact of this source on the $t\bar{t}$ measurements is small.

- $B - tagging$ also only affects the $t\bar{t}$ measurements. This source is considered to be correlated for $\sqrt{s} = 7$ TeV and 8 TeV data, but uncorrelated with the $\sqrt{s} = 13$ TeV data, since the installation of the new insertable B-layer in the inner detector and re-optimised b-tagging algorithms used at $\sqrt{s} = 13$ TeV resulted in significantly improved B-tagging performance.

- The *background* is treated as fully correlated for all $\sqrt{s}$ within a given process. The main uncertainty for this source is driven by the theoretical uncertainties in the cross sections of the background processes. The leading background sources are very different for the Z-boson and $t\bar{t}$ measurements.

- The *signal modelling* uncertainty is small for the fiducial Z-boson measurements. The extrapolation factor from fiducial to total cross section, A_Z, however, has a sizeable uncertainty which is treated as correlated for data at different $\sqrt{s}$ values. The signal modelling is the leading source of uncertainty for the $t\bar{t}$ measurements. It is considered to be to be correlated between the $\sqrt{s} = 7$ TeV and $\sqrt{s} = 8\ TeV$ measurements. An additional source of uncertainty is included only for the $t\bar{t}$ measurement at $\sqrt{s} = 13$ TeV, due to the level of agreement observed in events with at least three b-tagged jets [175]. Therefore, the signal modelling for the $t\bar{t}$ measurement at $\sqrt{s} = 13$ TeV, is represented with a starred letter in Table 9.3, and is less correlated to the $\sqrt{s} = 7$ TeV and $\sqrt{s} = 8$ TeV results.

Tables 9.3 and 9.4 indicate that the main contribution to the correlation between the Z and $t\bar{t}$ measurements at the same center-of-mass energy is expected to be from the luminosity uncertainty, while the beam energy, lepton momentum and energy scale uncertainties

Source / $\sqrt{s}$ [TeV]	$\delta\sigma_Z^{fid}$ 13	8	7	$\delta\sigma_{t\bar{t}}^{tot}$ 13	8	7
Luminosity	A	B	C	A	B	C
Beam energy	A	A	A	A	A	A
Muon (lepton) trigger	A	A^*	A	A	B	B
Muon reconstruction/ID	A	B	C	A	D	D
Muon isolation	A	A	A	B	C	D
Muon momentum scale	A	A	A	A	A	A
Electron trigger	A	A	A	A	—	—
Electron reconstruction/ID	A	B	C	A	D	D
Electron isolation	A	A	—	B	C	D
Electron energy scale	A	A	A	A	A	A
Jet energy scale	—	—	—	A	B	B
B-tagging	—	—	—	A	B	B
Background	A	A	A	B	B	B
Signal modelling (incl. PDF)	A	A	A	B^*	B	B

Table 9.3: The correlation model for the systematic uncertainties, δ, of the measurements of Z-boson and $t\bar{t}$ production at $\sqrt{s} = 13, 8$ and 7 TeV. Entries in different rows are uncorrelated with each other. Entries within a row with the same letter are fully correlated. Entries within a row with a starred letter are mostly correlated with the entries with the same letter (most of the individual sources of uncertainties within a group are taken as correlated). Entries with different letters within a row are either fully or mostly uncorrelated with each other.

dominantly contribute to correlation among Z and $t\bar{t}$ at different $\sqrt{s}$. The correlation between the Z and $t\bar{t}$ measurements at $\sqrt{s} = 13$ TeV mostly arise from the lepton-related systematic uncertainties, since the lepton selection for these two measurements is synchronized in terms of analysis tools usage. It is also a primary source of correlation among the Z measurements at different $\sqrt{s}$. The correlation of the $t\bar{t}$ measurements at different center-of-mass energies mostly originates from the signal and background modelling uncertainties.

9.3 Combination procedure

The combination of the integrated cross sections for the electron and muon channels for Z and W decays, as well as the combination of W^+ and W^- measurements, are performed simultaneously using the code developed at HERA for the combination of DIS cross section data [164]. The combination requires an understanding of the correlations

Source / $\sqrt{s}$ [TeV]	$\delta\sigma_Z^{fid}$ 13	8	7	$\delta\sigma_{t\bar{t}}^{tot}$ 13	8	7
Luminosity	2.10	1.90	1.80	2.31	2.10	1.98
Beam energy	0.69	0.62	0.60	1.50	1.72	1.79
Muon (lepton) trigger	0.12	0.55	0.05	0.05	0.17	0.19
Muon reconstruction/ID	0.68	0.45	0.30	0.44	0.42	0.31
Muon isolation	0.41	0.04	0.15	0.27	0.22	0.44
Muon momentum scale	0.06	0.03	0.03	0.04	0.01	0.14
Electron trigger	0.01	0.19	0.04	0.14	—	—
Electron reconstruction/ID	0.41	0.80	0.26	0.34	0.41	0.13
Electron isolation	0.14	0.00	—	0.39	0.30	0.59
Electron energy scale	0.25	0.07	0.08	0.20	0.51	0.21
Jet energy scale	—	—	—	0.38	0.72	0.40
B-tagging	—	—	—	0.53	0.40	0.46
Background	0.08	0.15	0.08	1.09	1.04	1.04
Signal modelling (incl. PDF)	0.12	0.08	0.27	2.98	1.70	1.81

Table 9.4: Systematic uncertainties, δ, in % for the measurement of Z-boson and $t\bar{t}$ production at $\sqrt{s} = 13, 8$ and 7 TeV. Values listed as 0.0 are $< 0.05\%$. Values listed as "-" have no corresponding uncertainty. The entry "(lepton)" in "Muon (lepton) trigger" refers to the $t\bar{t}$ trigger for the $\sqrt{s} = 7$ and 8 TeV data set which quotes a single uncertainty for the combined effects of the uncertainties in the electron and muon triggers. There is therefore a corresponding entry "-" for the electron trigger for the $\sqrt{s} = 7$ and 8 TeV $t\bar{t}$ data set.

in the systematic uncertainties across data sets. Therefore, the correlation models for the W and Z and the Z and $t\bar{t}$ measurements are used for their respective combinations.

The data are combined by using a simultaneous averaging. The procedure distinguishes sources that are fully uncorrelated between channels and those that are fully correlated. Partial correlations between channels are handled by splitting sources into fully correlated and fully uncorrelated components. This approach is used for uncertainties estimated with the Toy MC method. The examples of split nuisance parameters are given in Tables C.1 and D.1.

9.3.1 Linear Averaging

For a measurement, μ, with uncertainty, Δ, assuming a Gaussian shape of the uncertainty, the measurement can be considered to be a probability distribution function for a quantity

m [165, 166]:

$$P(m) = \frac{1}{\sqrt{2\pi}\Delta} e^{-\frac{(m-\mu)^2}{2\Delta^2}}. \tag{9.1}$$

The χ^2 function can be extracted by taking $-2log$:

$$\chi^2(m) = \frac{(m-\mu)^2}{\Delta^2}. \tag{9.2}$$

The averaging procedure uses a χ^2 minimisation. The minimum of the χ^2 function is reached at:

$$\frac{\partial \chi^2}{\partial m} = 0. \tag{9.3}$$

For a single data set, the χ^2 function can be constructed in the nuisance parameter representation in the form:

$$\chi^2(\vec{m}, \vec{b}) = \sum_i \frac{(m_i - \mu_i - \sum_j \Gamma_i^j b_j)^2}{\Delta_i^2} + \sum_j b_j^2, \tag{9.4}$$

where i sums over the measurements and j sums over all systematic sources correlated between the measurements, $\vec{b}$ defines a vector of nuisance parameters b_j, and Γ_i^j is the absolute correlated systematic uncertainty. Δ_i is the uncorrelated systematic uncertainty, which can be separated into statistical and uncorrelated components:

$$\Delta_i^2 = \Delta_{i,stat}^2 + \Delta_{i,uncorr}^2. \tag{9.5}$$

Γ_i^j is a representation of the correlated systematic uncertainties where the uncertainty is considered proportional to the central value: $\Gamma_i^j = m_i \gamma_i^j$, where

$$\gamma_i^j = \frac{1}{\mu_i} \frac{\partial \mu_i}{\partial \alpha^j}, \tag{9.6}$$

and α^j is the central value of systematic uncertainty j. The relationship $\partial \mu_i / \partial \alpha^j$ can be interpreted as the sensitivity of measurement μ_i to the systematic uncertainty source j. To combine several different data sets, a more general form of Equation 9.4 is used:

$$\chi_{tot}^2(\vec{m}, \vec{b}) = \sum_e \sum_{i=1}^{N_M} \frac{(m_i - \mu_{i,e} - \sum_{j=1}^{N_S} \Gamma_{i,e}^j b_j)^2}{\Delta_{i,e}^2} w_{i,e} + \sum_{j=1}^{N_S} b_j^2, \tag{9.7}$$

where the sum over e runs over all data sets. The factor $w_{i,e}$ is equal to 1 if the data set e contains a measurement at point i, and is 0 otherwise. The factor $\Gamma_{i,e}^j$ similarly quantifies the sensitivity of a measurement i for data set e to the systematic uncertainty j.

9.3.2 Iterative Procedure of Minimisation

Uncertainties that are considered functions of the value of the central measurement, m, to which they apply, are treated using a multiplicative approach. As mentioned in Section 9.3.1, this is represented in the correlated systematic uncertainty case as:

$$\Gamma_i^j = m_i \gamma_i^j \tag{9.8}$$

For the uncorrelated systematic and statistical cases respectively:

$$\begin{aligned} \Delta_{i,unc} &= \delta_{i,unc} m_i \\ \Delta_{i,stat} &= \delta_{i,stat} \sqrt{\mu_i m_i exp(-\sum_{j=1}^{N_S} \gamma_i^j b_j)}. \end{aligned} \tag{9.9}$$

Therefore, Equation 9.6 takes the form:

$$\Delta_i^2 = \delta_{i,stat}^2 \mu_i m_i exp(-\sum_{j=1}^{N_S} \gamma_i^j b_j) + \delta_{i,unc}^2 m_i^2 \tag{9.10}$$

and $\chi^2(\vec{m}, \vec{b})$ can be written as:

$$\chi^2(\vec{m}, \vec{b}) = \sum_i \frac{(m_i - \mu_i - \sum_j^{N_S} \gamma_i^j m_i b_j)^2}{\delta_{i,stat}^2 \mu_i m_i exp(-\sum_{j=1}^{N_S} \gamma_i^j b_j) + \delta_{i,unc}^2 m_i^2} + \sum_{j=1} b_j^2. \tag{9.11}$$

Using an iterative minimization procedure, initial approximations for the average $\mu_{i,ave}$ and $b_{j,ave}$ are obtained by applying Equation 9.4. The obtained $\mu_{i,ave}$ and $b_{j,ave}$ are used to recalculate uncertainties Γ_i^j and Δ_i, given with Equations 9.8 and 9.10, and the determination of $\mu_{i,ave}$ is then repeated iteratively minimizing Equation 9.4 with these recalculated uncertainties.

9.4 Correlation coefficients

The combination of the W and Z measurements with 50 ns data yields $\chi^2/N_{d.f.} = 3.0/3$ indicating a good compatibility of the measurements. The correlation coefficients among the combined W^+, W^-, and Z fiducial cross section measurements are calculated and reported in Table 9.5. The W^+ and W^- cross sections are highly correlated, whereas the correlation between the W and Z measurements is much lower, originating mainly from lepton systematic sources.

To highlight the role of the luminosity and beam energy uncertainties in combination of the $t\bar{t}$ and Z-boson cross section measurements at $\sqrt{s} = 13$ TeV, 8 TeV, and 7 TeV, the correlation coefficients are calculated twice: once including and once omitting these two

	W^+	W^-	Z
W^+	1.	0.93	0.19
W^-		1.	0.18
Z			1.

Table 9.5: Correlation coefficients between W^+, W^-, and Z-boson production fiducial cross-section measurements, excluding the common normalisation uncertainty due to the luminosity calibration.

	Z 13 TeV	$t\bar{t}$ 13 TeV	Z 8 TeV	$t\bar{t}$ 8 TeV	Z 7 TeV	$t\bar{t}$ 7 TeV
Z 13 TeV	1.	0.612	0.097	0.156	0.100	0.145
$t\bar{t}$ 13 TeV		1.	0.105	0.324	0.106	0.312
Z 8 TeV			1.	0.679	0.097	0.138
$t\bar{t}$ 8 TeV				1.	0.149	0.542
Z 7 TeV					1.	0.620
$t\bar{t}$ 7 TeV						1.

Table 9.6: Correlation coefficients between the $t\bar{t}$ total and Z-boson combined fiducial cross-section measurements, at different center-of-mass energies.

uncertainties from the combination procedure. The resulting correlation coefficients are given in Table 9.6 and 9.7, respectively. The combination of the nine measurements yields $\chi^2/N_{d.f.} = 0.6$ for $N_{d.f.} = 3$, indicating an excellent compatibility of the measurements. The combination of the electron and muon decay channels of the Z-boson at different $\sqrt{s}$ affects the $t\bar{t}$ cross sections, which take part in the combination, insignificantly. Details on the resulting $t\bar{t}$ cross sections after combination are provided in Appendix G.

The correlation coefficients in Table 9.6 demonstrate the highest correlation, at the level of 60%, for measurements at the same center-of-mass energy. The sharp decrease in correlation among the $t\bar{t}$ and Z measurements at different $\sqrt{s}$ in Table 9.7, compared to the numbers in Table 9.6, demonstrates the significance of the beam energy uncertainty in the correlation between given measurements. The correlation between same-channel measurements at different $\sqrt{s}$ does not change dramatically when omitting the luminosity and beam energy uncertainties from the combination. The largest correlation between same-channel analyses is observed for the $t\bar{t}$ measurements at $\sqrt{s} = 8$ TeV and $\sqrt{s} = 7$ TeV due to the synchronised approaches for these measurements. The correlation between the $t\bar{t}$ and Z measurements is the largest at $\sqrt{s} = 13$ TeV.

	Z 13 TeV	$t\bar{t}$ 13 TeV	Z 8 TeV	$t\bar{t}$ 8 TeV	Z 7 TeV	$t\bar{t}$ 7 TeV
Z 13 TeV	1.	0.132	0.091	0.084	0.123	0.031
$t\bar{t}$ 13 TeV		1.	0.013	0.315	0.002	0.274
Z 8 TeV			1.	0.009	0.090	0.004
$t\bar{t}$ 8 TeV				1.	0.002	0.674
Z 7 TeV					1.	0.002
$t\bar{t}$ 7 TeV						1.

Table 9.7: Correlation coefficients between the $t\bar{t}$ total and Z-boson combined fiducial cross-section measurements at different center-of-mass energies, excluding the luminosity and beam energy uncertainties.

Chapter 10

Results

This chapter presents Z and W boson production cross sections measured at $\sqrt{s} = 13$ TeV using 50 ns bunch spacing data, as well as Z boson cross sections at $\sqrt{s} = 13$ TeV using 25 ns, $\sqrt{s} = 8$ TeV, $\sqrt{s} = 7$ TeV. The Z and W boson cross sections for the electron and muon decay channels, together with the correlations in the systematic uncertainties, are used for the measurements of the ratios $R_{W^\pm} = \sigma^{fid}_{W^\pm\to e\nu}/\sigma^{fid}_{W^\pm\to\mu\nu}$ and $R_Z = \sigma^{fid}_{Z\to e^+e^-}/\sigma^{fid}_{Z\to\mu^+\mu^-}$ which allow the Standard Model expectations of lepton universality to be tested. Combined cross sections for electron and muon decay channels are used for comparison to previous measurements as well as examination of their energy dependence. The following ratios are also considered in this Chapter: R_{W^+/W^-}, $R_{W/Z}$ at $\sqrt{s} = 13$ TeV with 50 ns data, $R^{fid,tot}_{Z_i/Z_j}$, $R^{tot}_{t\bar{t}_i/t\bar{t}_j}$, $R^{tot/fid}_{t\bar{t}/Z}(i \text{ TeV})$, $R^{tot/fid}_{t\bar{t}/Z}(i/j \text{ TeV})$, where $i, j = 13(25 \text{ ns}), 8, 7$ and $i \neq j$. The impact of the ATLAS data, used for $t\bar{t}$ and Z boson ratios calculation, on the PDF uncertainties is quantified and presented.

10.1 Cross-section measurements

10.1.1 Z and W boson cross sections at $\sqrt{s} = 13$ TeV (50 ns)

The measured $Z \to e^+e^-$, $Z \to \mu^+\mu^-$, and combined fiducial and total cross sections with 50 ns data at $\sqrt{s} = 13$ TeV are reported in Table 10.1, along with their statistical, systematic, and luminosity uncertainties. Results for the W^+, W^-, $W^\pm$ cross sections are given in Table 10.2 in the same style. The fiducial cross sections are extrapolated to the total phase space using the geometrical acceptance factors A_Z, given in Table 5.3, and A_W, which can be found in Ref. [167]. Additional uncertainties introduced by acceptance factors are included into systematic uncertainty on the total cross sections.

Cross sections for the electron and muon channels are combined using the correlation model presented in Table 9.1 and the combination procedure introduced in Section 9.3. The combined results are obtained by minimising the χ^2 function, which was constructed

	Electron channel	**Muon channel**	**Combined**
	value ± stat ± syst ± lumi	value ± stat ± syst ± lumi	value ± stat ± syst ± lumi
Fiducial cross section [pb]	$780.8 \pm 4.2 \pm 7.7 \pm 16.4$	$777.0 \pm 3.7 \pm 8.2 \pm 16.3$	$778.6 \pm 2.8 \pm 5.6 \pm 16.4$
Total cross section [pb]	$1986.9 \pm 10.7 \pm 40.5 \pm 41.7$	$1977.1 \pm 9.4 \pm 40.9 \pm 41.5$	$1981.2 \pm 7.0 \pm 38.1 \pm 41.6$

Table 10.1: Results for $Z \to e^+e^-$, $Z \to \mu^+\mu^-$, and combined cross sections in the fiducial and total phase space using 50 ns data. The cross sections are shown with absolute values of statistical, systematic, and luminosity uncertainties quoted in that order.

Phase space	**Cross section [pb]**	**Electron channel**	**Muon channel**	**Combined**
		value ± stat ± syst ± lumi	value ± stat ± syst ± lumi	value ± stat ± syst ± lumi
Fiducial	W^+	$4684.4 \pm 10.4 \pm 136.3 \pm 102.5$	$4500.2 \pm 9.8 \pm 93.0 \pm 102.2$	$4530.8 \pm 7.1 \pm 90.7 \pm 95.1$
	W^-	$3582.1 \pm 9.1 \pm 141.0 \pm 78.9$	$3482.4 \pm 8.7 \pm 78.7 \pm 80.1$	$3497.9 \pm 6.2 \pm 72.7 \pm 73.5$
	$W^\pm$	$8266.6 \pm 13.6 \pm 255.9 \pm 173.6$	$7982.6 \pm 13.2 \pm 164.7 \pm 167.6$	$8028.7 \pm 9.5 \pm 160.7 \pm 168.6$
Total	W^+	$12230.8 \pm 27.2 \pm 419.1 \pm 267.7$	$11749.8 \pm 25.5 \pm 324.2 \pm 266.8$	$11829.8 \pm 18.6 \pm 320.7 \pm 248.4$
	W^-	$9000.2 \pm 23.0 \pm 388.1 \pm 198.2$	$8749.8 \pm 21.8 \pm 250.5 \pm 201.1$	$8788.7 \pm 15.7 \pm 239.3 \pm 184.6$
	$W^\pm$	$21250.9 \pm 35.0 \pm 760.9 \pm 446.3$	$20520.8 \pm 33.9 \pm 561.8 \pm 430.9$	$20639.3 \pm 24.4 \pm 555.6 \pm 433.4$

Table 10.2: Results for the fiducial and total cross sections for W^+, W^-, and $W^\pm$ in the electron, muon and combined channels using 50 ns data.. The observed numbers of signal events after background subtraction are shown for each channel. The cross sections are shown with absolute values of statistical, systematic, and luminosity uncertainties quoted in that order.

with Z and W results for electron and muon channels, where the nuisance parameters originate from systematic sources of both measurements. The combination is performed separately for the fiducial and total cross sections. Since the luminosity uncertainty is taken as 100% correlated between channels, it is excluded from the combination procedure. Table 10.1 demonstrates that the uncertainties on the individual and combined fiducial cross sections are dominated by the luminosity determination, while for the total cross sections the impact of the luminosity uncertainty is at the same level as the sum of the rest of the systematic sources due to the precision of A_Z (A_W).

The measured cross sections are compared to the theoretical predictions employing four PDF sets: CT14NNLO, NNPDF3.0, MMHT14NNLO68CL, and ABM12LHC, and illustrated at Figure 10.1. The central values and uncertainties of the predictions are given in Tables 2.1, and 2.3 in Section 2.3, where they are discussed further. Most of the predictions demonstrate good compatibility with the measured cross sections within the uncertainties. The theoretical uncertainties are dominated by the PDF uncertainty for most of the predictions. The experimental precision is comparable to the PDF uncertainties which provides an indication of the ability of these measurements to further constrain the PDF distributions.

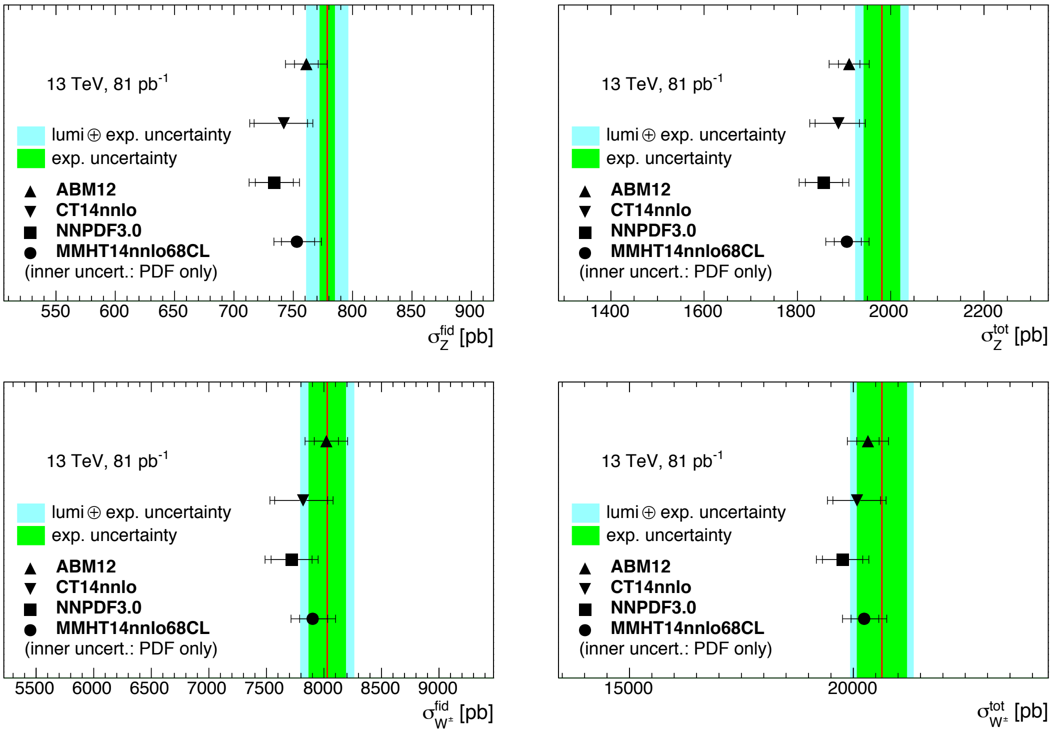

Figure 10.1: Measured fiducial (left) and total (right) cross sections of Z (top) and $W^{\pm}$ boson (bottom) compared to the predictions based on four PDF sets: CT14NNLO, NNPDF3.0, MMHT14NNLO68CL, and ABM12LHC. The green (cyan) band corresponds to the experimental uncertainty without (with) the luminosity uncertainty. The inner error bar of the predictions is the PDF uncertainty while the outer error bar is the total uncertainty.

10.1.2 Test of electron-muon universality

The measured Z and W-boson cross sections given in Tables 10.1, and 10.2 are used to test electron-muon universality in the weak interaction sector. Taking into account the constructed correlation model between the electron and muon decay channels of Z and W bosons given in Table 9.1, the fiducial cross-section ratios $\sigma_{Z\to e^+e^-}/\sigma_{Z\to\mu^+\mu^-}$ and $\sigma_{W^\pm\to e\nu}/\sigma_{W^\pm\to\mu\nu}$ are calculated. The given cross-section ratios represent the ratios of branching fractions:

$$\begin{aligned} R_Z = \frac{\sigma_Z^e}{\sigma_Z^\mu} &= \frac{BR(Z \to ee)}{BR(Z \to \mu\mu)} \\ &= 1.0050 \pm 0.0072\,(\text{stat}) \pm 0.0145\,(\text{syst}) \\ &= 1.0050 \pm 0.0162. \end{aligned} \tag{10.1}$$

The result is in agreement with the current PDG world average of $R_Z^{PDG} = 0.9991 \pm 0.0024$ [168], which is derived using the fit of the LEP results [169].

The extracted ratio for W-boson cross sections

$$\begin{aligned} R_W = \frac{\sigma_W^e}{\sigma_W^\mu} &= \frac{BR(W \to e\nu)}{BR(W \to \mu\nu)} \\ &= 1.0356 \pm 0.0024\,(\text{stat}) \pm 0.0287\,(\text{syst}) \\ &= 1.0356 \pm 0.0288 \end{aligned} \tag{10.2}$$

also agrees with the world average of $R_W^{PDG} = 1.007 \pm 0.0193$ [168] within the uncertainty of the measurement.
Taking into account the correlations between the W and Z measurements, the experimental results for R_Z and R_W are used to construct a correlation ellipse. A comparison of the experimental ellipse for the R_W and R_Z uncertainties with the Standard Model expectation of (1,1) and PDG values is shown in Figure 10.2. The center of the ellipse in the (R_W, R_Z) plane correspond to the crossing point of the R_W and R_Z central values, while its axes represent the total uncertainties on R_W and R_Z accordingly. The orientation of the ellipse represents the positive correlation among R_W and R_Z. The measured result agrees well with both the PDG and Standard Model values confirming the lepton ($e - \mu$) universality in the weak vector-boson decays. More details on methods and ellipse parameters are given in Appendix I.

10.1.3 Energy dependence of Z and W boson cross sections

The combined measured electron and muon total cross sections at $\sqrt{s} = 13$ TeV given in Tables 10.1 and 10.2. These are compared to theoretical predictions, as well as previous measurements of the total W and Z-production cross sections by: ATLAS [72], CMS [73, 74], UA1 [170], UA2 [171] experiments at $\sqrt{s} = 0.63$ TeV at the CERN SppS, the CDF [172] and D0 [173] experiments at $\sqrt{s} = 1.8$ TeV and $\sqrt{s} = 1.96$ TeV at the Fermilab, and the W production cross-section measurement by the PHENIX [174] experiment in proton-proton collisions at $\sqrt{s} = 0.5$ TeV at the RHIC collider. The theoretical calculations are performed with the FEWZ program using the CT14nnlo NNLO PDF set. The renormalisation scale and factorisation scale are chosen to be $\mu_R = \mu_F = m_W$. The comparisons for Z and W cross sections are presented in Figure 10.3. The theoretical

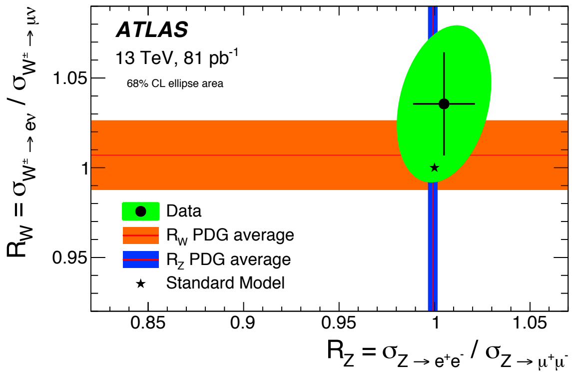

Figure 10.2: Ratio of the electron- and muon-channel $W^\pm$ and Z-boson production fiducial cross sections, compared to the expected values of the Standard Model of $R_W = R_Z = 1$ (neglecting mass effects that contribute at a level below 10^{-5}), and previous experimental verifications of lepton universality for on-shell $W^\pm$ and Z bosons, shown as PDG average bands [168, 169]. The PDG average values and the ATLAS measurement are shown with total uncertainties. The green shaded ellipse represents the 68% CL for the correlated measurement of R_W and R_Z, while the black error bars give the one dimensional standard deviation.

predictions are in good agreement with all measurements. The energy dependence of the measured total W and Z production cross sections is well described by theory predictions.

10.1.4 Z-boson and $t\bar{t}$ cross sections at different $\sqrt{s}$

Z-boson cross sections at $\sqrt{s} = 13$ TeV (25 ns)

The measured Z-boson cross-sections for the electron, muon, and combined decay channels using 25 ns data are given in Table 10.3. The uncertainties of the proton beam energy and luminosity determination are shown separately since these sources were taken into account in the combination procedure. The combined values demonstrate the reduction of the experimental systematic uncertainty with respect to the individual channels, as was observed for results with 50 ns bunch spacing data. The beam energy and luminosity uncertainties are at the same level as for the separate channels. The systematic uncertainties for the total cross sections are increased compared to the fiducial cross sections. The measured cross sections with 25 ns bunch spacing data show excellent compatibility, within the statistical uncertainty, with results based on 50 ns data. The precision of the results with 25 ns data is higher due to the increased statistics in the data, see Section 4.1 and Table 5.6, as well as improved methods of systematic uncertainty estimation. More details on the comparison of the results between the two measurements are given in Ref. [124].

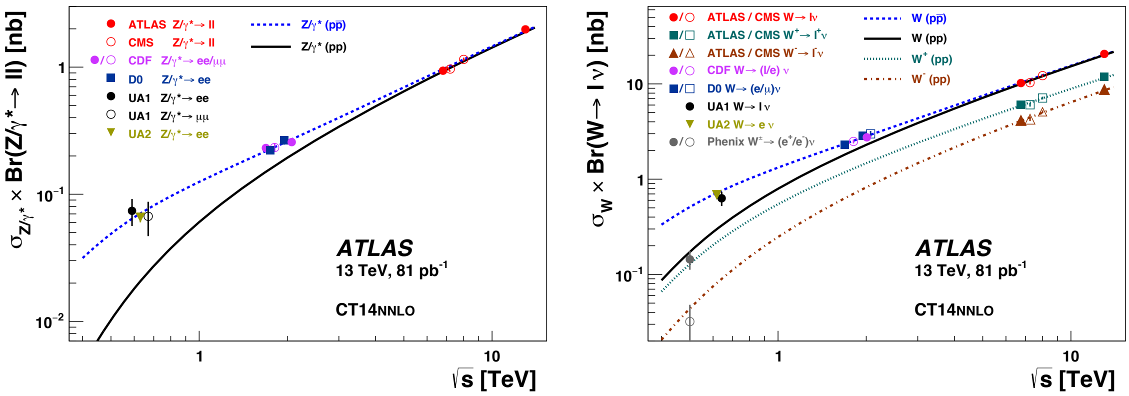

Figure 10.3: The measured value of $\sigma_Z \times BR(Z \to \ell\ell)$ (left) and $\sigma_W \times BR(W \to \ell\nu)$ for W^+, W^-, and their sum (right) where the electron and muon channels have been combined, compared to theoretical predictions based on NNLO QCD calculations. The predictions are shown for both proton-proton and proton-antiproton colliders as a function of $\sqrt{s}$. In addition, previous measurements at proton-antiproton colliders are shown. The data points at the various energies are staggered to improve readability. All data points are displayed with their total uncertainty. The theoretical uncertainties are not shown.

	Electron channel	**Muon channel**	**Combined**
	value ± stat ± syst ± beam ± lumi	value ± stat ± syst ± beam ± lumi	value ± stat ± syst ± beam ± lumi
Fiducial cross section [pb]	$778.3 \pm 0.7 \pm 4.0 \pm 5.4 \pm 16.3$	$774.4 \pm 0.6 \pm 6.2 \pm 5.3 \pm 16.3$	$777.3 \pm 0.5 \pm 3.4 \pm 5.4 \pm 16.3$
Total cross section [pb]	$1970.3 \pm 1.7 \pm 36.5 \pm 13.6 \pm 41.4$	$1960.6 \pm 1.5 \pm 38.3 \pm 13.5 \pm 41.2$	$1969.0 \pm 1.2 \pm 35.9 \pm 13.6 \pm 41.3$

Table 10.3: Results for $Z \to e^+e^-$, $Z \to \mu^+\mu^-$, and combined cross sections in the fiducial and total phase space using 25 ns data. The cross sections are shown with absolute values of statistical, systematic, and luminosity uncertainties quoted in that order.

$\sqrt{s}$	Cross section	Electron channel	Muon channel	Combined
		value ± stat ± syst ± beam ± lumi	value ± stat ± syst ± beam ± lumi	value ± stat ± syst ± beam ± lumi
8 TeV	**Common fiducial (13 TeV phase space) [pb]**	$509.99 \pm 0.20 \pm 4.36 \pm 3.14 \pm 9.63$	$504.74 \pm 0.15 \pm 3.94 \pm 3.13 \pm 9.59$	$505.80 \pm 0.12 \pm 2.77 \pm 3.13 \pm 9.61$
	Total [pb]	$1156.50 \pm 0.46 \pm 22.20 \pm 7.17 \pm 21.97$	$1151.37 \pm 0.34 \pm 21.70 \pm 7.14 \pm 21.88$	$1153.50 \pm 0.28 \pm 20.83 \pm 7.14 \pm 21.92$
7 TeV	**Common fiducial (13 TeV phase space) [pb]**	$451.17 \pm 0.45 \pm 1.59 \pm 2.71 \pm 8.12$	$450.02 \pm 0.34 \pm 1.96 \pm 2.70 \pm 8.10$	$450.76 \pm 0.28 \pm 1.44 \pm 2.71 \pm 8.11$
	Total [pb]	$995.75 \pm 0.99 \pm 18.09 \pm 5.98 \pm 17.92$	$993.22 \pm 0.75 \pm 18.23 \pm 5.96 \pm 17.88$	$994.77 \pm 0.62 \pm 17.99 \pm 5.98 \pm 17.89$

Table 10.4: Results for $Z \to e^+e^-$, $Z \to \mu^+\mu^-$, and combined cross sections in the common fiducial phase space of $\sqrt{s} = 13$ TeV measurements and total phase space of Z-boson cross sections measured at $\sqrt{s} = 8$ TeV and 7 TeV. The cross sections are shown with absolute values of statistical, systematic, and luminosity uncertainties quoted in that order.

Z-boson cross sections at $\sqrt{s} = 8$ and 7 TeV

The measured fiducial cross sections at $\sqrt{s} = 8$ TeV and 7 TeV are taken from Ref. [161] and Ref. [54] and extrapolated with E_Z and A_Z factors from the phase space of their original measurement to the phase of the $\sqrt{s} = 13$ TeV Z-boson measurements as well as total phase space. The E_Z and A_Z factors are calculated with DYNNLO using the CT14NNLO PDF set and are given in Table 5.3. The uncertainties introduced by the extrapolation factors are small and are included in the systematic part of the cross-section uncertainties. The resulting separate and combined cross sections are given in Table 10.4. The accuracy of the measured fiducial cross sections is dominated by the precision of the luminosity determination, while for the total cross sections the systematic uncertainty is comparable to the luminosity uncertainty.

$t\bar{t}$ cross sections at $\sqrt{s} = 13$, 8, and 7 TeV

The results of the measured inclusive and fiducial $t\bar{t}$ production cross-sections at $\sqrt{s} =$ 13 TeV, 8 TeV, and 7 TeV, along with list of systematic uncertainties used in correlation model, are taken from Ref. [75, 175]. These measurements were performed using dilepton $t\bar{t}$ events with an opposite-sign $e\mu$ pair in the final state, and additional jets tagged as containing b-hadrons. Each lepton in the $e\mu$ pair is produced directly from $t \to W \to \ell$ or via a leptonic τ decay $t \to W \to \tau \to \ell$. For the measurements at $\sqrt{s} = 13$ TeV, data with 25 ns bunch spacing were used. The measured total and fiducial $t\bar{t}$ production cross-sections are given in Table 10.5. The $t\bar{t}$ fiducial space has remained unchanged at $\sqrt{s} = 13$ TeV, 8 TeV, and 7 TeV: $p_T^\ell > 25$ GeV and $\left|\eta^\ell\right| < 2.5$.

	$\sqrt{s} = 13$ TeV	$\sqrt{s} = 8$ TeV	$\sqrt{s} = 7$ TeV
	value $\pm$ stat $\pm$ syst $\pm$ beam $\pm$ lumi	value $\pm$ stat $\pm$ syst $\pm$ beam $\pm$ lumi	value $\pm$ stat $\pm$ syst $\pm$ beam $\pm$ lumi
Fiducial cross section [pb]	$11.32 \pm 0.10 \pm 0.29 \pm 0.26 \pm 0.17$	$3.45 \pm 0.03 \pm 0.07 \pm 0.11 \pm 0.06$	$2.62 \pm 0.04 \pm 0.06 \pm 0.05 \pm 0.05$
Total cross section [pb]	$818.0 \pm 8.0 \pm 27.0 \pm 19.0 \pm 12.0$	$242.4 \pm 1.7 \pm 5.5 \pm 7.5 \pm 4.2$	$182.9 \pm 3.1 \pm 4.2 \pm 3.6 \pm 3.3$

Table 10.5: Measured fiducial and total $t\bar{t}$ production cross sections at $\sqrt{s} = 13$ TeV, 8 TeV, and 7 TeV. The cross sections are shown with absolute values of statistical, systematic, and luminosity uncertainties quoted in that order.

Comparison with predictions

To compare the measured cross sections, including the correlation information, to the theory predictions, the two-dimensional contours of σ_Z^{fid} vs. $\sigma_{t\bar{t}}^{tot}$ at the three $\sqrt{s}$ values were evaluated. Since the Z-boson fiducial cross-section measurements are found to be more precise compared to the total cross sections, the σ_Z^{fid} are used.

Figure 10.4 shows the measured two-dimensional 68% CL contours, overlayed with the theoretical cross-section predictions calculated from the error sets associated with each specific PDF. For the measured contours, the correlation coefficient between the $t\bar{t}$ and Z measurements given in Tables 9.6 and 9.7 are used. The measurement contours overlay with most of the theoretical ellipses, indicating good compatibility between experimental and predicted results. The correlations of the measured cross sections are opposite in sign to those of the predicted cross sections (with exception of ABM12 set, which has a small positive correlation), providing discriminating input to the determination of the PDFs. The data ellipses visually show the domination of the luminosity uncertainty in the formation of correlations between the $t\bar{t}$ and Z measurements at the given center-of-mass energy.

10.2 W and Z cross sections ratios at $\sqrt{s} = 13$ TeV (50 ns)

To obtain the cross-section ratios of W over Z, first the electron and muon channels were combined and then the ratios of combined results were calculated. The correlation model presented in Table 9.1 was used. The results for the ratios of fiducial cross sections for W^+- to W^--boson production and $W^\pm$- to Z-boson production are given in Table 10.6. As a cross check, the ratios for the electron and muon channels separately were calculated and are given in Appendix F.

The systematic uncertainties on the ratio measurements are largely uncorrelated between the electron and muon channels, apart from the common luminosity uncertainty.

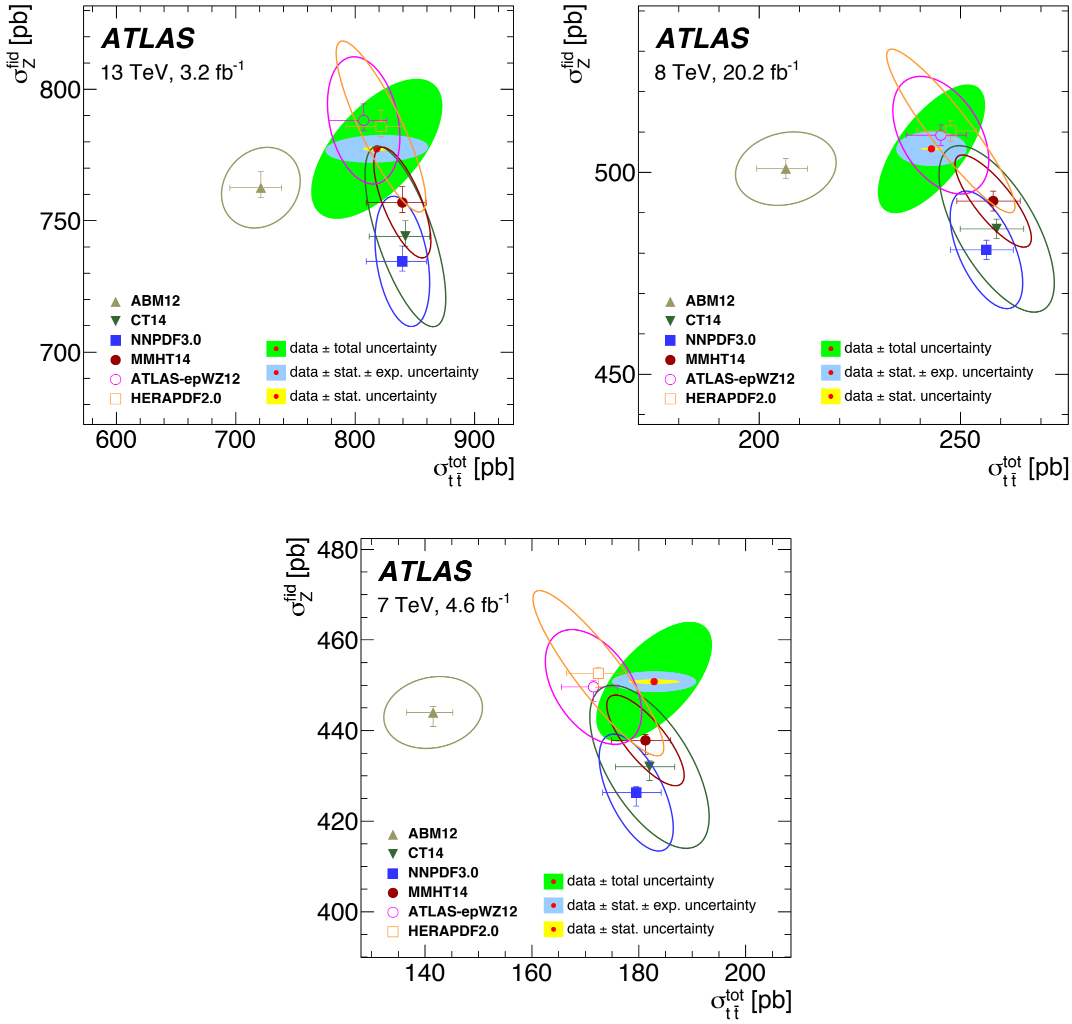

Figure 10.4: Two-dimensional 68% CL contours of σ_Z^{fid} vs. $\sigma_{t\bar{t}}^{tot}$ at $\sqrt{s} = 13$ TeV (top, left), 8 TeV (top, right), and 7 TeV (bottom). The solid red circle shows the result of the combination, the yellow ellipse represents the statistical uncertainty, the blue ellipse adds the experimental uncertainty, while the green ellipse is the total uncertainty. The results are overlaid with the theoretical cross-section predictions calculated from the error sets associated with each specific PDF, also plotted at 68% CL. The ellipses correspond to the PDF uncertainties, the asymmetric error bars inside the ellipses represent the scale uncertainties, and the coloured markers are the central values.

Channel	$\sigma^{fid}_{W^+}/\sigma^{fid}_{W^-}$	$\sigma^{fid}_{W^\pm}/\sigma^{fid}_{Z}$
	value $\pm$ stat $\pm$ syst	value $\pm$ stat $\pm$ syst
e**-channel**	$1.3078 \pm 0.0044 \pm 0.0306$	$10.5867 \pm 0.0598 \pm 0.3229$
μ**-channel**	$1.2923 \pm 0.0043 \pm 0.0099$	$10.2737 \pm 0.0512 \pm 0.2101$
Combined	$1.2953 \pm 0.0031 \pm 0.0097$	$10.3117 \pm 0.0385 \pm 0.2044$

Table 10.6: Ratios of the W^+ to W and $W^\pm$ to Z fiducial cross sections for the electron, muon, and combined measurements. The cross-section ratios are shown with absolute values of statistical and systematic uncertainties.

However, there is a strong correlation between the W^+ and W^--boson measurements, and between the $W^\pm$ and Z-boson results for the same-flavour measurement. The results for the measured W^+/W^- and $W^\pm/Z$ ratios of fiducial production cross sections in the combined electron and muon channels are given in Table 10.6. The measured ratios are compared to the the corresponding NNLO QCD predictions based on various PDF sets as described in Section 2.3 and presented in Figure 10.5. The dominant components of the systematic uncertainty in the $W^\pm/Z$ ratio are from the multijet background and the jet-energy scale/resolution, while for the W^+/W^- ratio it is the uncorrelated part of the multijet background uncertainty. The experimental ratio gains from the partial cancellation of lepton identification and trigger systematic uncertainties. For the ratios $R_{W^+/W^-} = \sigma^{fid}_{W^+}/\sigma^{fid}_{W^-}$ and $R_{W^\pm/Z} = \sigma^{fid}_{W^\pm}/\sigma^{fid}_{Z}$, several predictions agree within quoted uncertainties, although all predictions are above the central value for the data in both cases. For the ratio R_{W^+/W^-} the accuracy of the experimental result is comparable to the PDF uncertainties indicating the constraining power of the measured data on PDF precision. The spread of some predictions such as HERAPDF2.0nnlo and CT14nnlo for R_{W^+/W^-} are larger than the uncertainty of the data, therefore the measurements are seen to discriminate between different PDF choices and to provide information to reduce PDF uncertainties [163].

10.3 Z and $t\bar{t}$ cross-sections ratios at $\sqrt{s} = 13$, 8, and 7 TeV

Using the results for Z-boson and $t\bar{t}$ production cross sections at $\sqrt{s} = 13$ TeV, 8 TeV, and 7 TeV given in Tables 10.3, 10.4, and 10.5, including the correlation information presented with Table 9.2, the cross-section ratios are calculated. There are three types of ratios as introduced in Section 2.4.3: 1) cross-section ratios for a given process at the different $\sqrt{s}$ ($R^{fed(tot)}_{Z_i/Z_j}$ and $R^{tot}_{t\bar{t}_i/t\bar{t}_j}$), 2) for different processes at the same $\sqrt{s}$ ($R^{tot/fid(tot)}_{t\bar{t}/Z}$ i TeV), and

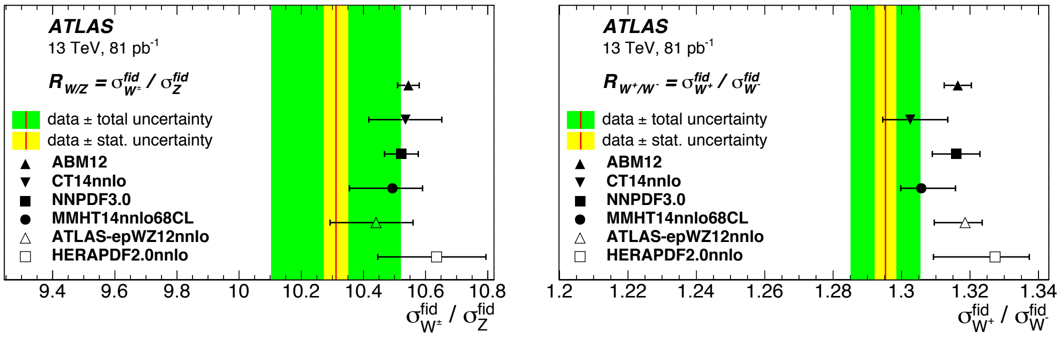

Figure 10.5: Ratios (red line) of $W^\pm$ to Z boson (left) and W^+ to$W$ boson (right) combined production cross sections in the fiducial region, compared to predictions based on different PDF sets. The inner (yellow) shaded band corresponds to the statistical uncertainty while the outer (green) band shows statistical and systematic uncertainties added in quadrature. The theory predictions are given with only the corresponding PDF uncertainties shown as error bars.

3) for different processes at the different $\sqrt{s}$ ($R^{tot/fid(tot)}_{t\bar{t}/Z}$ i/j TeV, also referred as double ratios). The $t\bar{t}$ over Z single ratios, as well as double ratios, are split into three categories depending on the phase space used for the cross-section measurement: 1) total over total, 2) fiducial over fiducial, and 3) total over fiducial ("mixed") ratios. The $t\bar{t}$ over $t\bar{t}$ and Z over Z at different $\sqrt{s}$ are divided into two categories: 1) total over total, and 2) fiducial over fiducial cross-section ratios. The results of the single and double cross-section ratios are given in Table 10.7 and 10.8, respectively.

The ratios of fiducial cross sections have the smallest experimental uncertainty since the geometrical acceptance factors are not used for such ratio calculations, however they are more difficult to predict accurately, especially for $t\bar{t}$ production where only the total cross section is currently available at NNLO+NNLL. The ratios of total cross sections gain from the smallest theoretical uncertainty. The mixed ratios have experimental uncertainties compatible to fiducial ratios and are predicted at the same formal accuracy as the ratio of the total cross sections.

10.3.1 Ratios of $t\bar{t}$ to Z cross sections at a given $\sqrt{s}$

The $t\bar{t}$ to Z-boson cross section ratio at a given center-of-mass energy, $R_{t\bar{t}/Z}$, is defined as

$$R_{t\bar{t}/Z} = \frac{\sigma_{t\bar{t}}}{0.5(\sigma_{Z\to ee} + \sigma_{Z\to\mu\mu})}, \tag{10.3}$$

where $\sigma_{t\bar{t}}$ is the inclusive $t\bar{t}$ production cross-section, $\sigma_{Z\to ee}$ and $\sigma_{Z\to\mu\mu}$ are the inclusive Z-boson production cross-sections measured in dielectron and dimuon channels multiplied by their appropriate branching fractions. The use of equal weights for the electron and

	$\sigma^{tot}/\sigma^{tot}$	$\sigma^{tot}/\sigma^{fid}$	$\sigma^{fid}/\sigma^{fid}$
	value ± stat ± syst ± lumi	value ± stat ± syst ± lumi	value ± stat ± syst ± lumi
$\sigma_{t\bar{t}}^{13\ \text{TeV}}/\sigma_Z^{13\ \text{TeV}}$	0.416 ± 0.004(0.92%) ± 0.016(3.83%) ± 0.001(0.21%)	1.053 ± 0.010(0.92%) ± 0.036(3.39%) ± 0.002(0.21%)	0.01280 ± 0.00012(0.91%) ± 0.00033(2.61%) ± 0.00003(0.21%)
$\sigma_{t\bar{t}}^{8\ \text{TeV}}/\sigma_Z^{8\ \text{TeV}}$	0.211 ± 0.001(0.71%) ± 0.007(3.09%) ± 0.000(0.20%)	0.480 ± 0.003(0.71%) ± 0.012(2.57%) ± 0.001(0.20%)	0.00602 ± 0.00004(0.72%) ± 0.00014(2.35%) ± 0.00001(0.20%)
$\sigma_{t\bar{t}}^{7\ \text{TeV}}/\sigma_Z^{7\ \text{TeV}}$	0.184 ± 0.003(1.69%) ± 0.006(3.14%) ± 0.000(0.18%)	0.406 ± 0.007(1.69%) ± 0.011(2.59%)± 0.001(0.18%)	0.00511 ± 0.00009(1.68%) ± 0.00013(2.46%) ± 0.00001(0.18%)
$\sigma_Z^{13\ \text{TeV}}/\sigma_Z^{8\ \text{TeV}}$	1.707 ± 0.001(0.06%) ± 0.013(0.77%) ± 0.048(2.83%)	–	1.537 ± 0.001(0.06%) ± 0.010(0.67%) ± 0.044(2.83%)
$\sigma_Z^{13\ \text{TeV}}/\sigma_Z^{7\ \text{TeV}}$	1.979 ± 0.002(0.09%) ± 0.014(0.71%) ± 0.055(2.77%)	–	1.724 ± 0.001(0.09%) ± 0.009(0.52%) ± 0.048(2.77%)
$\sigma_Z^{8\ \text{TeV}}/\sigma_Z^{7\ \text{TeV}}$	1.160 ± 0.001(0.07%) ± 0.007(0.63%) ± 0.030(2.62%)	–	1.122 ± 0.001(0.07%) ± 0.007(0.61%) ± 0.029(2.62%)
$\sigma_{t\bar{t}}^{13\ \text{TeV}}/\sigma_{t\bar{t}}^{8\ \text{TeV}}$	3.365 ± 0.039(1.16%) ± 0.112(3.34%) ± 0.105(3.12%)	–	3.270 ± 0.038(1.16%) ± 0.086(2.62%) ± 0.102(3.12%)
$\sigma_{t\bar{t}}^{13\ \text{TeV}}/\sigma_{t\bar{t}}^{7\ \text{TeV}}$	4.470 ± 0.086(1.92%) ± 0.149(3.33%) ± 0.136(3.04%)	–	4.322 ± 0.083(1.91%) ± 0.116(2.69%) ± 0.131(3.04%)
$\sigma_{t\bar{t}}^{8\ \text{TeV}}/\sigma_{t\bar{t}}^{7\ \text{TeV}}$	1.328 ± 0.024(1.83%) ± 0.015(1.11%) ± 0.038(2.89%)	–	1.322 ± 0.024(1.83%) ± 0.015(1.12%) ± 0.038(2.89%)

Table 10.7: Summary of the Z-boson and $t\bar{t}$ production cross-section single ratios at $\sqrt{s} = 13, 8$ and 7 TeV. The beam-energy uncertainty, which largely cancels in the ratios, is included in the systematic uncertainty.

	R^{tot}/R^{tot}	R^{tot}/R^{fid}	R^{fid}/R^{fid}
	value ± stat ± syst ± lumi	value ± stat ± syst ± lumi	value ± stat ± syst ± lumi
$\frac{\sigma_{t\bar{t}}^{13\ \text{TeV}}}{\sigma_Z^{13\ \text{TeV}}} / \frac{\sigma_{t\bar{t}}^{8\ \text{TeV}}}{\sigma_Z^{8\ \text{TeV}}}$	1.975 ± 0.023(1.16%) ± 0.067(3.38%) ± 0.006(0.29%)	2.193 ± 0.026(1.16%) ± 0.074(3.36%) ± 0.008(0.37%)	2.131 ± 0.025(1.16%) ± 0.057(2.67%) ± 0.006(0.29%)
$\frac{\sigma_{t\bar{t}}^{13\ \text{TeV}}}{\sigma_Z^{13\ \text{TeV}}} / \frac{\sigma_{t\bar{t}}^{7\ \text{TeV}}}{\sigma_Z^{7\ \text{TeV}}}$	2.260 ± 0.044(1.93%) ± 0.075(3.33%) ± 0.007(0.32%)	2.594 ± 0.050(1.93%) ± 0.086(3.30%) ± 0.008(0.30%)	2.508 ± 0.048(1.91%) ± 0.067(2.66%) ± 0.008(0.32%)
$\frac{\sigma_{t\bar{t}}^{8\ \text{TeV}}}{\sigma_Z^{8\ \text{TeV}}} / \frac{\sigma_{t\bar{t}}^{7\ \text{TeV}}}{\sigma_Z^{7\ \text{TeV}}}$	1.145 ± 0.021(1.83%) ± 0.015(1.28%) ± 0.003(0.28%)	1.184 ± 0.022(1.83%) ± 0.015(1.27%) ± 0.003(0.27%)	1.178 ± 0.022(1.83%) ± 0.015(1.28%) ± 0.003(0.29%)

Table 10.8: Summary of the Z-boson and $t\bar{t}$ production cross-section double ratios at $\sqrt{s} = 13, 8$ and 7 TeV. The beam-energy uncertainty, which largely cancels in the ratios, is included in the systematic uncertainty. The luminosity uncertainty mostly cancels in this ratio.

muon channels in the denominator ensures the best cancellation of systematic uncertainties related to lepton reconstruction, identification, and the trigger with respect to the numerator, which involves one electron and one muon.

Ratios at $\sqrt{s} = 13$ TeV

The first result of $R^{tot/tot}_{t\bar{t}/Z}$ is obtained using the 50 ns data at $\sqrt{s} = 13$ TeV. This ratio is determined using the measurement of $t\bar{t}$ in the $e\mu$ decay channel described in Ref. [176]. The ratio defined in Equation 10.3 is measured to be:

$$R^{50ns}_{t\bar{t}/Z}(tot/tot) = 0.445 \pm 0.027 \text{ (stat)} \pm 0.028 \text{ (syst} \oplus \text{lumi)}.$$

corresponding to a relative uncertainty of 8.8%. A detailed breakdown of the uncertainties on the ratio, together with those on the $t\bar{t}$ and Z-boson cross-section measurement, is given in Ref. [177]. The uncertainty on the ratio is found to be significantly smaller than that on the $t\bar{t}$ cross-section, mostly because of the almost complete cancellation of the uncertainty on the integrated luminosity. The statistical and systematic uncertainties on $R^{50ns}_{t\bar{t}/Z}$ are of similar size, and the latter is dominated by $t\bar{t}$ modelling uncertainties.

The ratio obtained with 25 ns data at $\sqrt{s} = 13$ TeV is measured to be:

$$R^{25ns}_{t\bar{t}/Z}(tot/tot) = 0.416 \pm 0.004 \text{ (stat)} \pm 0.016 \text{ (syst)} \pm 0.001 \text{ (lumi)},$$

which have significantly reduced statistical and systematic uncertainties compared to the results based on 50 ns data. However, both results demonstrate good compatibility within $1.1\sigma_{stat}$. The other two types of ratios, $R_{t\bar{t}/Z}(tot/fid)$ and $R_{t\bar{t}/Z}(fid/fid)$, obtained with 25 ns data are given in Table 10.7. All three measurements are dominated by systematic uncertainties, while luminosity uncertainty is at the level of 0.2%.

A detailed breakdown of the uncertainties on the ratio $R_{t\bar{t}/Z}(tot/tot)$, together with those on the $t\bar{t}$ and Z cross-section measurements, is given in Table J.1 of Appendix J. It demonstrates almost complete cancellation of the uncertainty on the integrated luminosity as well as significant cancellations of the beam energy uncertainty and lepton systematics. Similar to the ratio with 50 ns data, the total uncertainty on the ratios with 25 ns data is significantly smaller than that on the $t\bar{t}$ cross-section. The systematic uncertainty on the ratio is dominated by the $t\bar{t}$ modelling systematic sources (2.8%).

Ratios at $\sqrt{s} = 8$ and 7 TeV

In contrast to $t\bar{t}$ and Z cross sections measurements at $\sqrt{s} = 13$ TeV, measurements at run-I of LHC operation at $\sqrt{s} = 8$ TeV and 7 TeV were not fully synchronised, therefore several lepton reconstruction sources of uncertainty which have a similar origin are treated as uncorrelated in the correlation model (see Section 9.2). Since these sources have relatively small impact on the $t\bar{t}$ cross-section measurement, the increase of the uncertainty on the

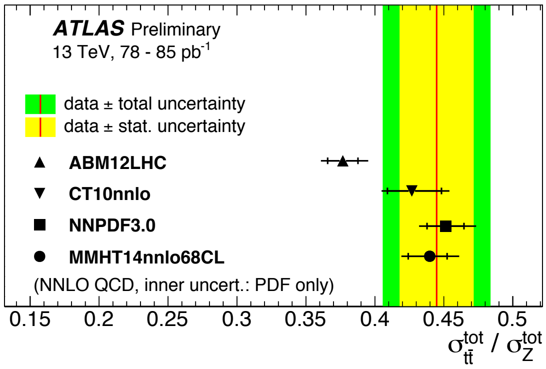

Figure 10.6: Measured cross-section ratio $R_{t\bar{t}/Z}^{50ns}$ compared to NNLO predictions at $\sqrt{s} =$ 13 TeV based on the ABM12LHC, CT10, NNPDF3.0 and MMHT14 PDF sets. The inner shaded band corresponds to the statistical uncertainty on the measurement, whilst the outer shaded band includes both statistical and systematic uncertainties. The inner error bars on the predictions correspond to PDF uncertainties only, whilst the outer error bars also include QCD scale and α_s uncertainties.

ratio is low. The detailed break-down of the systematic sources for each channel as well as ratio is given in the Tables J.2 and J.3. The precisions of both ratios are higher than the corresponding $t\bar{t}$ cross-section measurement used in the ratio definition. Additional studies for the influence of the the correlation model for lepton-related systematic sources between $t\bar{t}$ and Z measurements on the ratio calculations at $\sqrt{s} = 8$ TeV and 7 TeV are provided and discussed in Appendix H.

Comparison to theory predictions

The ratio $R_{t\bar{t}/Z}(tot/tot)$ measured with 50 ns data is compared to predictions obtained at NNLO accuracy in QCD with leading-order electroweak corrections for Z production with FEWZ, and at NNLO+NNLL accuracy for $t\bar{t}$ production with Top++. Figure 10.6 demonstrates the level of compatibility among the measured result and predictions. The experimental result agrees with predictions based on the CT10NNLO, NNPDF3.0, and MMHT14nnlo68CL PDF sets. However, they are only marginally consistent with the prediction using the ABM12LHC PDF set.

The single ratios $R_{t\bar{t}/Z}^{tot/tot}$ and $R_{t\bar{t}/Z}^{tot/fid}$ at $\sqrt{s} = 13$ TeV (50 ns), 8 TeV and 7 TeV are compared in Figure 10.7 to the theoretical predictions based on different PDF sets. The predictions follow a similar pattern for all center-of-mass energies. The ABM12 set yields the lowest values of the ratios. The three PDF sets used in the PDF4LHC prescription [30] (CT14nnlo, NNPDF3.0, and MMHT14nnlo) predict the largest ratios. The HERA-data based PDF sets, HERAPDF2.0 and ATLAS-epWZ12, are in the middle. Such spread of the predictions is beyond the PDF uncertainties for the three groups of

PDFs. The quoted PDF uncertainties are similar in size, with HERAPDF2.0 errors being the largest and ABM12 the smallest. This pattern can be explained by the differences in the gluon density and the α_s value used in the PDF sets. ABM12, HERAPDF2.0 and ATLAS-epWZ12 do not include jet data which typically yields a low gluon density for the Bjorken-x values where the $t\bar{t}$ data at the LHC are sensitive to it. The ABM12 set uses a low value of α_s in addition. The size of the error bars depends on the data sets used in the PDF fits and also on the statistical model used for the analysis.

The ATLAS data are more accurate than most of the theory predictions, indicating that the data have a strong constraining power. The systematic uncertainties dominate the total uncertainty for the measured ratios, while the luminosity uncertainties almost entirely cancel. The statistical uncertainties are sub-dominant for most of the ratios, except for the ratios at $\sqrt{s} = 7$ where they are sizeable. The systematic uncertainty for the measurement at $\sqrt{s} = 13$ TeV is larger compared to the run-I results, mostly due to the larger $t\bar{t}$ NLO-modelling uncertainty. The highest precision of measured cross section ratios is at $\sqrt{s} = 8$ TeV.

For the most precise measurement at $\sqrt{s} = 8$ TeV the data are in the best agreement with the HERAPDF2.0 and ATLAS-epWZ12 PDF sets. The experimental results at $\sqrt{s}$ = 8 TeV deviate by $1.6 - 2.1\ \sigma$ from the PDF4LHC PDFs and by 2.6 σ from the ABM12 PDF, where σ is the total uncertainty on the measured ratio. A similar pattern is observed for the results at $\sqrt{s} = 13$ TeV, however with less significance. The measured ratios at $\sqrt{s}$ = 7 TeV are most consistent with the MMHT14nnlo PDF set. The data are in between the PDF4LHC PDFs and the HERA-based PDFs, deviating from ABM12 more.

10.3.2 Ratios of $t\bar{t}$ and Z cross sections at different $\sqrt{s}$

To obtain the single same-channel ratios, $R^{tot/tot}_{Z_i/Z_j}$ and $R^{fid/fid}_{Z_i/Z_j}$, the electron and muon channels are first combined and then the ratios of the combined cross sections are calculated. The combination is performed separately for each single ratio with respect to the correlation model. Measurements at both $\sqrt{s}$ used in the ratio definition take part in the combination procedure simultaneously, which is conceptually similar to the $W^{\pm}$ over Z ratio calculation (see Section 10.2). Each of the combinations were performed with an exclusive χ^2 function, and introduce a single χ^2 value as well as a combined cross section. Such an approach also provides a test of stability of the combination method.

The χ^2 method of averaging was also used for the $R^{tot/tot}_{t\bar{t}_i/t\bar{t}_j}$ and $R^{fid/fid}_{t\bar{t}_i/t\bar{t}_j}$ ratio calculations. In this case the cross sections for a given ratio were not combined but shifts of the systematic nuisance parameters of measurements at different $\sqrt{s}$ with respect to the correlation model were provided. The detailed systematic uncertainty break-down for the cross-section ratios is given as a part of Table D.1.

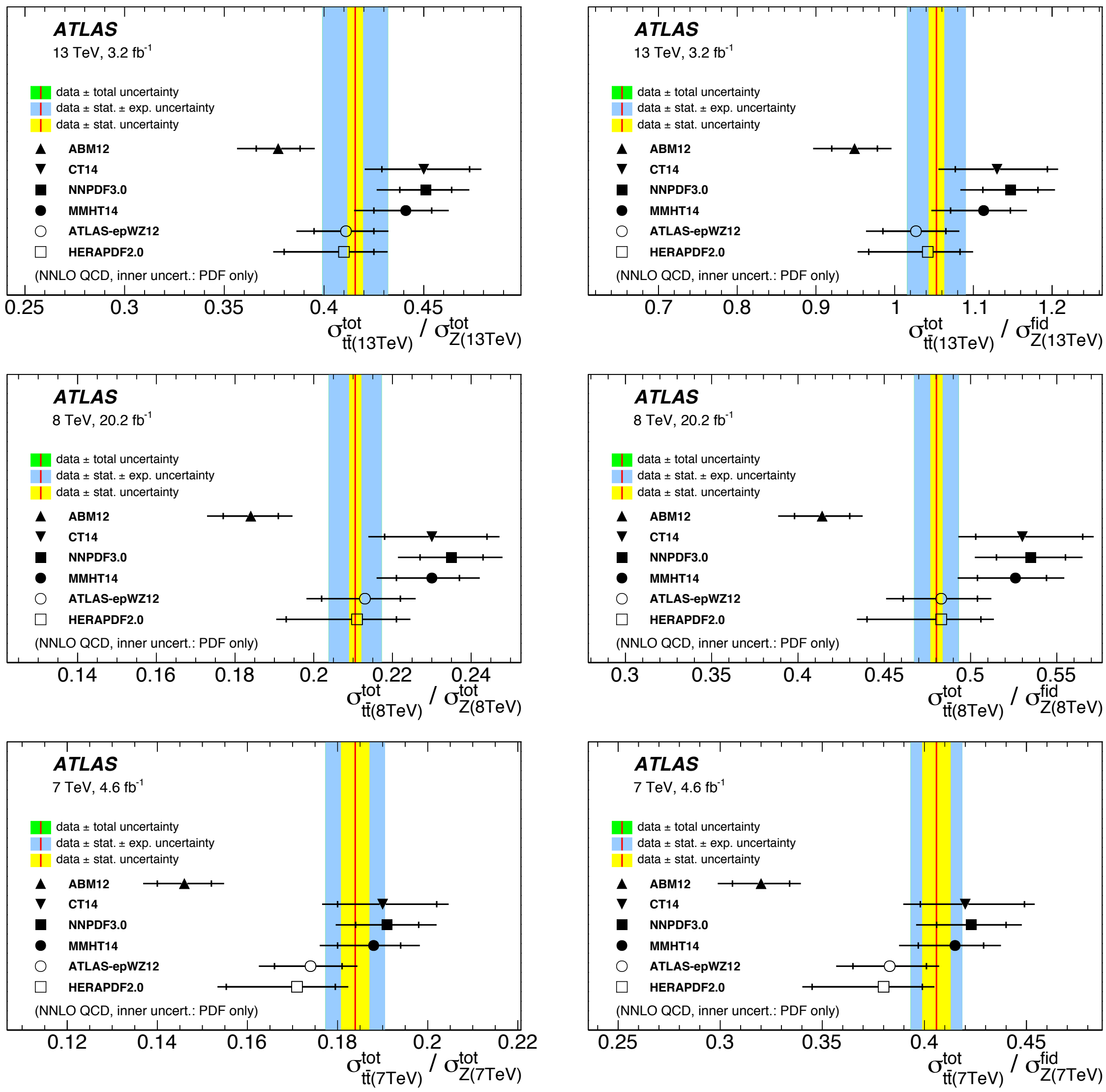

Figure 10.7: $\sigma^{\rm tot}_{t\bar{t}}$(13 TeV) to $\sigma^{\rm tot}_{Z}$(13 TeV) (top left), $\sigma^{\rm tot}_{t\bar{t}}$(13 TeV) to $\sigma^{\rm fid}_{Z}$(13 TeV) (top right), $\sigma^{\rm tot}_{t\bar{t}}$(8 TeV) to $\sigma^{\rm tot}_{Z}$(8 TeV) (middle left), $\sigma^{\rm tot}_{t\bar{t}}$(8 TeV) to $\sigma^{\rm fid}_{Z}$(8 TeV) (middle right), $\sigma^{\rm tot}_{t\bar{t}}$(8 TeV) to $\sigma^{\rm tot}_{Z}$(8 TeV) (bottom left), $\sigma^{\rm tot}_{t\bar{t}}$(8 TeV) to $\sigma^{\rm fid}_{Z}$(8 TeV) (bottom right) ratios of production cross sections compared to predictions based on different PDF sets. The inner shaded band corresponds to the statistical uncertainty, the middle band to the statistical and experimental systematic uncertainties added in quadrature, while the outer band shows the total uncertainty, including the luminosity uncertainty. The latter is not visible since the the luminosity uncertainties almost entirely cancel in these ratios. The theory predictions are given with the corresponding PDF uncertainties shown as inner bars while the outer bars include the scale and α_S uncertainties added in quadrature.

	$\sigma_Z^{13\ \mathrm{TeV}}/\sigma_Z^{8\ \mathrm{TeV}}$	$\sigma_Z^{13\ \mathrm{TeV}}/\sigma_Z^{7\ \mathrm{TeV}}$	$\sigma_Z^{8\ \mathrm{TeV}}/\sigma_Z^{7\ \mathrm{TeV}}$
$\chi^2/N_{d.f.}$	0.4	0.5	0.4

Table 10.9: χ^2 values of the combination $Z \to e^+e^-$ and $Z \to \mu^+\mu^-$ channels at $\sqrt{s} = 13, 8$ and 7 TeV for the ratios $\sigma_Z^{13\ \mathrm{TeV}}/\sigma_Z^{8\ \mathrm{TeV}}$, $\sigma_Z^{13\ \mathrm{TeV}}/\sigma_Z^{7\ \mathrm{TeV}}$, and $\sigma_Z^{8\ \mathrm{TeV}}/\sigma_Z^{8\ \mathrm{TeV}}$.

Ratios of Z boson production cross sections

The resulting χ^2 values from the combination of the electron and muon channels for each cross section ratio are given in Table 10.9. Similarity among the values indicates that the combinations demonstrate very good compatibility. It was also verified that all combined $Z \to \ell\ell$ central values for a given $\sqrt{s}$ obtained in combinations for different ratios were consistent with each other (see Appendix G).

The dominant uncertainty for all Z-boson cross-section ratios is the luminosity uncertainty, since it is dominant for each separate measurement and taken as uncorrelated between the measurements at different $\sqrt{s}$. The largest cancellation is for the beam energy uncertainty, which is assumed to be 100% correlated for different beam energies.

For the ratio of the total cross sections there is a significant correlation of the A_Z factors. The scale and α_s parts of the A_Z uncertainties are assumed to be 100% correlated for the ratios while the PDF uncertainties are evaluated eigenvector-by-eigenvector, which allowed a partial cancellation.

Comparison to theory predictions The ratios of Z-boson production cross sections at different $\sqrt{s}$ are compared to predictions based on different PDF sets in Figure 10.8. The uncertainty on the measurements are dominated by the luminosity. Excluding the luminosity uncertainty, the experimental uncertainty is smaller for the fiducial ratios, since the total ratios contain partially cancelled uncertainties from the A_Z factors.

Most of the predictions for the ratios agree with the data within the experimental uncertainties, omitting the luminosity uncertainty. This observation may indicate that the luminosity-determination uncertainty in the measured ratio is conservative. The agreement among predictions and data within the experimental uncertainty holds for most of the PDFs, for both total and fiducial cross-section ratios, with the exception of the ATLAS-epWZ12 fiducial $\sqrt{s} = 13$ TeV to $\sqrt{s} = 7$ TeV cross section ratio. The different behaviour for this PDF set can be understood by the enhanced strangeness, which modifies the $y_{\ell\ell}$ rapidity distribution and thus the A_Z factor, compared to other PDFs.

The smallness of the PDF uncertainties for different predictions and the overall small spread among them suggest that the measured Z-boson data could be used to cross-normalise the measurements at the different centre-of-mass energies, thereby avoiding a large uncorrelated luminosity uncertainty. This aspect is explored by taking double ratios of $t\bar{t}$ to Z-boson cross sections, and is discussed in Section 10.3.3.

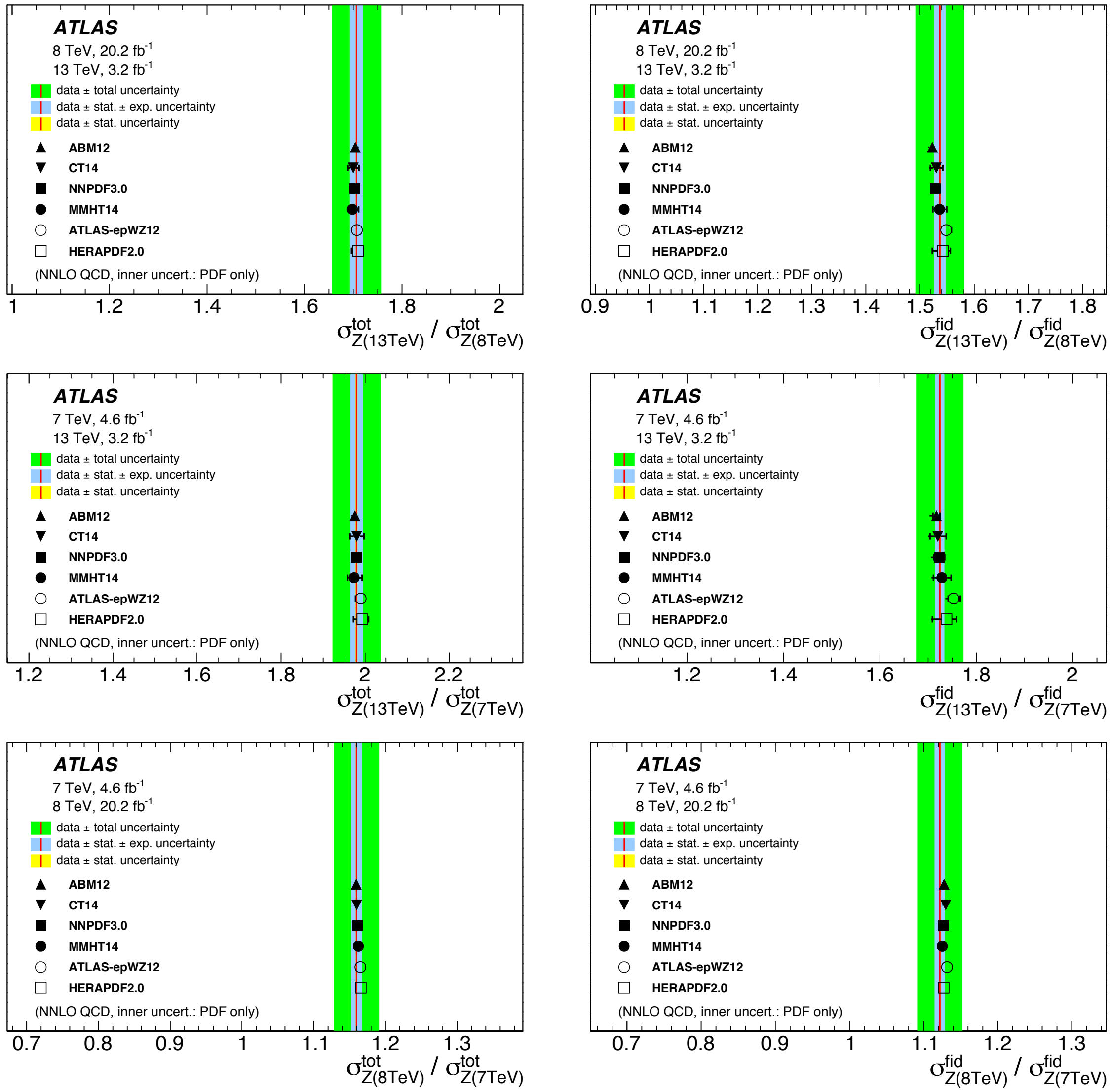

Figure 10.8: σ_Z^{tot}(13 TeV) to σ_Z^{tot}(8 TeV) (top left), σ_Z^{fid}(13 TeV) to σ_Z^{fid}(8 TeV) (top right), σ_Z^{tot}(13 TeV) to σ_Z^{tot}(7 TeV) (middle left), σ_Z^{fid}(13 TeV) to σ_Z^{fid}(7 TeV) (middle right), σ_Z^{tot}(8 TeV) to σ_Z^{tot}(7 TeV) (bottom left), σ_Z^{fid}(8 TeV) to σ_Z^{fid}(7 TeV) (bottom right) ratios of production cross sections compared to predictions based on different PDF sets. The inner shaded band (barely visible since it is small) corresponds to the statistical uncertainty, the middle band to the statistical and experimental systematic uncertainties added in quadrature, while the outer band shows the total uncertainty, including the luminosity uncertainty. The theory predictions are given with the corresponding PDF uncertainties, shown as inner bars while the outer bars, include the scale and α_S uncertainties added in quadrature.

Ratios of $t\bar{t}$ production cross sections

The measurements of $t\bar{t}$ cross sections at different $\sqrt{s}$ are more synchronised than for the Z-boson measurements, allowing for better control of correlations and uncertainty cancellations in the ratios. High correlations among the $t\bar{t}$ measurements, especially between $\sqrt{s} = 7$ TeV and 8 TeV, are shown in Tables 9.6 and 9.7.

The cross section ratios $\sigma^{tot(fid)}_{t\bar{t}(8\text{ TeV})}/\sigma^{tot(fid)}_{t\bar{t}(7\text{ TeV})}$ have been measured earlier [75] providing the result:

$$\begin{aligned}
\frac{\sigma^{tot}_{t\bar{t}(8\text{ TeV})}}{\sigma^{tot}_{t\bar{t}(7\text{ TeV})}} &= 1.326 \pm 0.024\ (\text{stat}) \pm 0.015\ (\text{syst}) \pm 0.049\ (\text{lumi}) \pm 0.001\ (\text{beam}) \\
\frac{\sigma^{fid}_{t\bar{t}(8\text{ TeV})}}{\sigma^{fid}_{t\bar{t}(7\text{ TeV})}} &= 1.319 \pm 0.024\ (\text{stat}) \pm 0.015\ (\text{syst}) \pm 0.049\ (\text{lumi}) \pm 0.001\ (\text{beam}).
\end{aligned} \tag{10.4}$$

Results of the current research for similar ratios as well ratios $\sigma^{tot(fid)}_{t\bar{t}(13\text{ TeV})}/\sigma^{tot(fid)}_{t\bar{t}(8\text{ TeV})}$ and $\sigma^{tot(fid)}_{t\bar{t}(13\text{ TeV})}/\sigma^{tot(fid)}_{t\bar{t}(7\text{ TeV})}$ are provided in Table 10.7. Both results for $\sigma^{tot(fid)}_{t\bar{t}(8\text{ TeV})}/\sigma^{tot(fid)}_{t\bar{t}(7\text{ TeV})}$ are in perfect agreement with each other. Such compatibility shows that the implementation of the methods used for ratio calculation as well as correlation model works as expected. The uncertainties for most of the experimental sources, except luminosity, are highly correlated, therefore the largest uncertainty on the $\sqrt{s} = 8$ TeV to 7 TeV cross section ratios stems from the luminosity. Moreover, the statistical component of the uncertainty is also sizeable, mostly due to the limited statistics at $\sqrt{s} = 7$ TeV.

Comparison to theory predictions The measured ratios $\frac{\sigma^{tot}_{t\bar{t}(13\text{ TeV})}}{\sigma^{tot}_{t\bar{t}(8\text{ TeV})}}$, $\frac{\sigma^{tot}_{t\bar{t}(13\text{ TeV})}}{\sigma^{tot}_{t\bar{t}(7\text{ TeV})}}$, and $\frac{\sigma^{tot}_{t\bar{t}(8\text{ TeV})}}{\sigma^{tot}_{t\bar{t}(7\text{ TeV})}}$ are compared with the theory predictions based on different PDF sets in Figure 10.9.

The predictions follow a similar pattern for all ratios. The PDF sets used in the PDF4LHC prescription [30] (CT14nnlo, NNPDF3.0, and MMHT14nnlo) predict the smallest values for the ratios. They are followed by HERA-data based PDF sets (ATLAS-epWZ12 and HERAPDF2.0) which predict a bit larger values, and the ABM12 predictions are the largest. Such a pattern can be explained by the different dependences of the gluon distribution on Bjorken-x in the PDF sets. The gluon distribution at low x region is measured at HERA and used for all presented PDF sets, therefore better agreement with data is observed for all of them. At high x, ABM12 and HERA-data based PDF sets have lower gluon density than other PDF sets. Thus, as the $\sqrt{s}$ increases, resulting in decrease of the average value of x, the ABM12 and HERA-based sets exhibit a stronger $\sqrt{s}$ dependence than the PDF4LHC PDFs. Since the observed spread of theoretical predictions is sizeable compared to the experimental uncertainties, omitting the luminosity uncertainty, these measurements do not test the consistency of the luminosity calibrations at different $\sqrt{s}$ to the same precision as it was observed for the Z-boson cross-section ratios at Section 10.3.2.

The measured ratio $\frac{\sigma^{tot}_{t\bar{t}(13\ \mathrm{TeV})}}{\sigma^{tot}_{t\bar{t}(8\ \mathrm{TeV})}}$ agrees with all predictions within the total experimental uncertainty. The prediction based on the HERAPDF2.0 PDF set shows the best agreement within the statistical uncertainty of the data. The central values of the measured cross-section ratios which involve $\sqrt{s} = 7$ TeV data are lower with respect to all predictions. The highest difference between the measured and predicted cross-section ratio is observed for $\frac{\sigma^{tot}_{t\bar{t}(8\ \mathrm{TeV})}}{\sigma^{tot}_{t\bar{t}(7\ \mathrm{TeV})}}$, where experimental result deviates from all predictions by about 2σ. Such a deviation was previously observed and published by the ATLAS collaboration [75]. The disagreement between predictions and measurement for the $\frac{\sigma^{tot}_{t\bar{t}(8\ \mathrm{TeV})}}{\sigma^{tot}_{t\bar{t}(7\ \mathrm{TeV})}}$ ratio is difficult to explain by the x-dependence of the gluon distribution, because the difference in average x is much higher between $\sqrt{s} = 13$ TeV and 8 TeV or 13 TeV and 7 TeV than for $\sqrt{s} = 8$ TeV and 7 TeV. This tension between measured and predicted result for $\frac{\sigma^{tot}_{t\bar{t}(8\ \mathrm{TeV})}}{\sigma^{tot}_{t\bar{t}(7\ \mathrm{TeV})}}$ can be investigated by taking the double ratio, which can provide a higher precision due to the cancellation of the luminosity uncertainty. The double ratio results are discussed in the next section.

10.3.3 Double ratios of $t\bar{t}$ and Z cross sections at different $\sqrt{s}$

The double ratio measurements benefit from the cancellation of uncertainties which occur in different channels at a given $\sqrt{s}$ as well as the same channel at different $\sqrt{s}$. Each double ratio contains two ratios at the same $\sqrt{s}$, providing almost entire cancellation of the luminosity uncertainty. Uncertainties on the theoretical predictions also cancel in the double ratios, due to the correlation between PDF eigenvectors for the same channel calculations. Thereby, such measurements provide a luminosity-uncertainty-independent check of the Standard Model. The double ratios are also intended to shine light on the observed tension between measurement and predictions for the single ratio of $t\bar{t}$ cross sections.

The combination of the electron and muon channels for each double ratio is performed separately. The resulting χ^2 values are given in Table 10.10, which demonstrate a very good compatibility among the three combinations. The combined electron and muon channel cross sections for the Z boson at different $\sqrt{s}$ that are used in the double ratios are compared to results obtained from the combination for the single ratios introduced earlier. The comparison is provided in Appendix G and demonstrates a high consistency among the results. Both suggest that the combination procedure is stable.

Comparison to theory predictions The double ratio results are compared to the theory predictions, based on different PDF sets, in Figure 10.10. The trends in the theory

	$\frac{\sigma_{t\bar{t}(13\text{ TeV})}}{\sigma_{Z(13\text{ TeV})}} / \frac{\sigma_{t\bar{t}(8\text{ TeV})}}{\sigma_{Z(8\text{ TeV})}}$	$\frac{\sigma_{t\bar{t}(13\text{ TeV})}}{\sigma_{Z(13\text{ TeV})}} / \frac{\sigma_{t\bar{t}(7\text{ TeV})}}{\sigma_{Z(7\text{ TeV})}}$	$\frac{\sigma_{t\bar{t}(8\text{ TeV})}}{\sigma_{Z(8\text{ TeV})}} / \frac{\sigma_{t\bar{t}(7\text{ TeV})}}{\sigma_{Z(7\text{ TeV})}}$
$\chi^2/N_{d.f.}$	0.4	0.5	0.4

Table 10.10: χ^2 values for the combination of the $Z \to e^+e^-$ and $Z \to \mu^+\mu^-$ channels at $\sqrt{s} = 13, 8$, and 7 TeV for the double ratios.

predictions and between the data and the predictions observed for the double ratios are similar to the single ratios of $t\bar{t}$ cross sections at different $\sqrt{s}$. The total uncertainties are smaller than those in the $t\bar{t}$ cross-section ratios due to the almost complete cancellation of the luminosity uncertainty, which more than compensates for the uncertainties that the Z-boson cross sections bring to these double ratios. The double ratio of $\sqrt{s} = 13$ TeV to $\sqrt{s} = 8$ TeV is consistent with all predictions at the 1σ level, where σ is the total experimental uncertainty.

The tension of the $\sqrt{s} = 8$ TeV over $\sqrt{s} = 7$ TeV ratio with respect to the theory predictions is increased, due to the reduced uncertainty in the data. The statistical uncertainty is the dominant source of experimental uncertainty in this ratio, where the main contribution comes from the $t\bar{t}$ measurement at $\sqrt{s} = 7$ TeV. The deviation of the ABM12 PDF is at the 4σ level, while for all other PDFs it is at the $\sim 3\sigma$ level. The closest to the observed ratio is given by the ATLAS-epWZ12 PDF set at the level of 2.9σ.

To understand the influence of the correlation model on the size of the tensions in both of the single and double $\sqrt{s} = 8$ TeV over $\sqrt{s} = 7$ TeV ratios the de-correlation model was studied. Systematic sources which potentially have the strongest influence on the ratios were de-correlated. The study showed that de-correlated beam energy and signal modelling uncertainties lead to a maximal increase of the experimental uncertainty, providing a reduction on the discrepancy to 1.9σ between data and the prediction based on the CT14 PDF set (more details are in Appendix H). Therefore, the source of the observed tensions in both the single and double ratios are statistical fluctuations rather than a systematic effect of the measurement.

10.4 PDF profiling

Using the PDF profiling technique introduced in Section 2.5, the measured cross sections, along with the complete correlation information, can be compared in a quantitative way to the predictions based on different PDF sets. In addition, the impact of the ATLAS data on the PDF uncertainties can be quantified. It is preferable to estimate the impact of the ATLAS data by using PDFs that do not include the cross-section data used in the analysis. Given that PDF groups often use tolerance criteria which are different compared to the $\Delta\chi^2 = 1$ rule employed in the profiling estimates, the impact of the data on PDF uncertainties can be different. The PDF profiling method works best for PDFs which

	CT14	MMHT14	NNPDF30	ABM12
χ^2/NDF	1.9/3	1.4/3	5.9/3	5.0/3
p-value	0.58	0.71	0.11	0.17

Table 10.11: χ^2 values for the comparisons of the ATLAS W and Z cross section data (50 ns bunch spacing at $\sqrt{s} = 13$ TeV) to the predictions based on the CT14, MMHT14, NNPDF3.0, and ABM12 PDF sets, along with the probability of finding the observed value or larger.

use the $\Delta\chi^2 = 1$ criterion for uncertainty estimation, and which agree well with the measurement ensuring small pulls of the PDF eigenvectors. The PDF sets which provide uncertainties at the 90% confidence level only (CT14) are re-scaled to 68% C.L. prior to profiling. For both W, Z and $t\bar{t}$, Z measurements, the comparison with predictions and profiling are performed using the xFitter package, which allows PDF and other theoretical uncertainties to be included via asymmetric error propagation.

10.4.1 W, Z measurements

The measured fiducial W and Z cross sections, including their correlations, as reported in Section 9.4, are quantitatively compared to predictions based on the CT14, MMHT14, NNPDF3.0, and ABM12 PDF sets. The resulting χ^2 values corresponding to the different PDFs are given in Table 10.11. All comparisons give a reasonable χ^2 value. Figure 10.11 visually compares the measurements, with both the total and the uncorrelated components of the uncertainties, to the predictions. Both Table 10.11 and Figure 10.11 demonstrate a good agreement between the CT14 and MMHT14 predictions and the ATLAS data.

The impact of the W, Z ATLAS data on the CT14 and MMHT14 PDF sets is quantified with the PDF profiling method, providing a shifted set of parton distributions with reduced uncertainties to some extent. The light sea-quark distributions, $x\bar{u}, x\bar{d}$ and xs, before and after profiling with the MMHT14 set, are shown in Figure 10.12. The strange-quark distribution after profiling is increased, and the uncertainties are slightly reduced compared to the reference PDF set. This in turn leads to the reduction of $x\bar{u}$ and $x\bar{d}$ at low x. However, the uncertainties on the $x\bar{u}$ and $x\bar{d}$ distributions are not visibly reduced. Some reduction of the uncertainty is also observed for the valence-quark distributions, xu_v and xd_v, as is illustrated in Figure 10.13, for the CT14 and MMHT14 sets. The small impact of the measured data on the s, u_v and d_v distributions indicate that the level of precision in the measured data does not provide a meaningful QCD fit analysis. The enlarged strangeness fraction of the light sea quarks after profiling is in agreement with other ATLAS measurements [54, 178]. Results with a similar pattern, but higher constraining power, are shown using ATLAS W, Z data with higher precision in Ref. [54].

	ATLAS-epWZ12	CT14	MMHT14	NNPDF30	HERAPDF2.0	ABM12
χ^2/NDF	8.3/6	15/6	13/6	17/6	10/6	25/6
p-value	0.22	0.02	0.05	0.01	0.11	< 0.001

Table 10.12: χ^2 values for the comparisons of the ATLAS $t\bar{t}$ and Z cross sections data at $\sqrt{s} = 13, 8, 7$ TeV to the predictions based on ATLAS-epWZ12, CT14, MMHT14, NNPDF3.0, HERAPDF2.0, ABM12 PDF sets along with the probability of finding the observed value or larger.

10.4.2 $t\bar{t}$, Z measurements

The measured cross sections of $t\bar{t}$ and Z boson production at $\sqrt{s} = 13, 8$, and 7 TeV are quantitatively compared to the predictions based on different PDF sets following similar strategy as for the W and Z measurements. The baseline comparison is performed for the total cross sections for $t\bar{t}$ and fiducial cross sections for Z-boson production, including their correlations. The quantitative assessment of the level of agreement between data and predictions are presented in Table 10.12. All comparisons provide an acceptable χ^2 value except for the ABM12 PDF set, which is disfavoured by the data. The covariance matrix is decomposed so as to extract the uncorrelated component of the uncertainties. A visual representation of the data compared to predictions is given in Figure 10.14. From Figure 10.14 and Table 10.12, the HERAPDF2.0 and ATLAS-epWZ12 PDF sets show good compatibility with the ATLAS data, and the agreement is improved when the measurement of the $t\bar{t}$ cross section at 7 TeV is excluded.

The effect of the measured data on the light-quark sea and gluon distributions is examined with the profiling method. The HERAPDF2.0 and ATLAS-epWZ12 sets can be used for this purpose, since neither of them includes the cross-section data used in this analysis. Given that the ATLAS-epWZ12 set provides smaller uncertainties for the predicted cross sections compared to HERAPDF2.0, it is chosen for the study. The profiling of the ATLAS-epWZ12 PDF set is performed only with the components related to the uncertainties of the HERA [70] and 2010 ATLAS [72] W, Z-boson data, to mimic the inclusion of the new ATLAS data in the PDF fit. The effect of the additional uncertainties arising from the model and PDF-parameterisation variations estimated in the ATLAS-epWZ12 PDF fit are not further investigated.

Figure 10.15 shows the light-quark sea $\Sigma = \bar{u} + \bar{d} + \bar{s}$ and gluon g distributions before and after the profiling, including their uncertainties at the scales of $Q^2 = M_Z^2$ and $Q^2 = M_t^2$, respectively. The upper plots show the profiled distributions divided by the central value of the ATLAS-epWZ12 PDF set and demonstrate that the central values of the profiled distributions agree very well with the original set. The lower plots show that the ATLAS $t\bar{t}$ and Z-boson cross-section data impose visible constraints on the light-quark sea distribution at $x < 0.02$ and on the gluon distribution at $x \sim 0.1$. These data constrain the least-well-understood component of the light-quark sea distribution, namely the strange-quark distribution while the other quark PDFs are not significantly constrained [163]. The lower plots also show the impact of the $t\bar{t}$ data only, which contribute significantly to the constraint on the gluon distribution, while the Z-boson data help to constrain both the light-quark-sea and gluon distributions.

Profiling is additionally performed with the MMHT14 PDF set using the Z-boson and $t\bar{t}$ cross-section data at $\sqrt{s} = 13, 8$, and 7 TeV, as well as excluding $t\bar{t}$ results at $\sqrt{s} = 7$ TeV and $\sqrt{s} = 8$ TeV. Figure 10.16 demonstrates the distributions for the light-quark sea and gluon divided by the central value of the MMHT14 PDF. In all cases a significant reduction of the PDF uncertainties for both the gluon and the sea-quark distributions is observed. The sea-quark distribution is pulled up at low x by $\sim 1.5\%$, while the gluon distribution is pulled down at low x. The pull is stronger when the $\sqrt{s} = 7$ TeV data are excluded. Compatibility tests with the MMHT14 predictions when the $t\bar{t}$ cross-section data at $\sqrt{s} = 7$ TeV or $\sqrt{s} = 8$ TeV are excluded give good $\chi^2/NDF = 4.7/5$ and $\chi^2/NDF = 3.6/5$, respectively, indicating that the relatively poor $\chi^2/NDF = 13/6$ when all data are used for profiling is driven by the tension between the $t\bar{t}$ measurements at $\sqrt{s} = 7$ TeV and $\sqrt{s} = 8$ TeV.

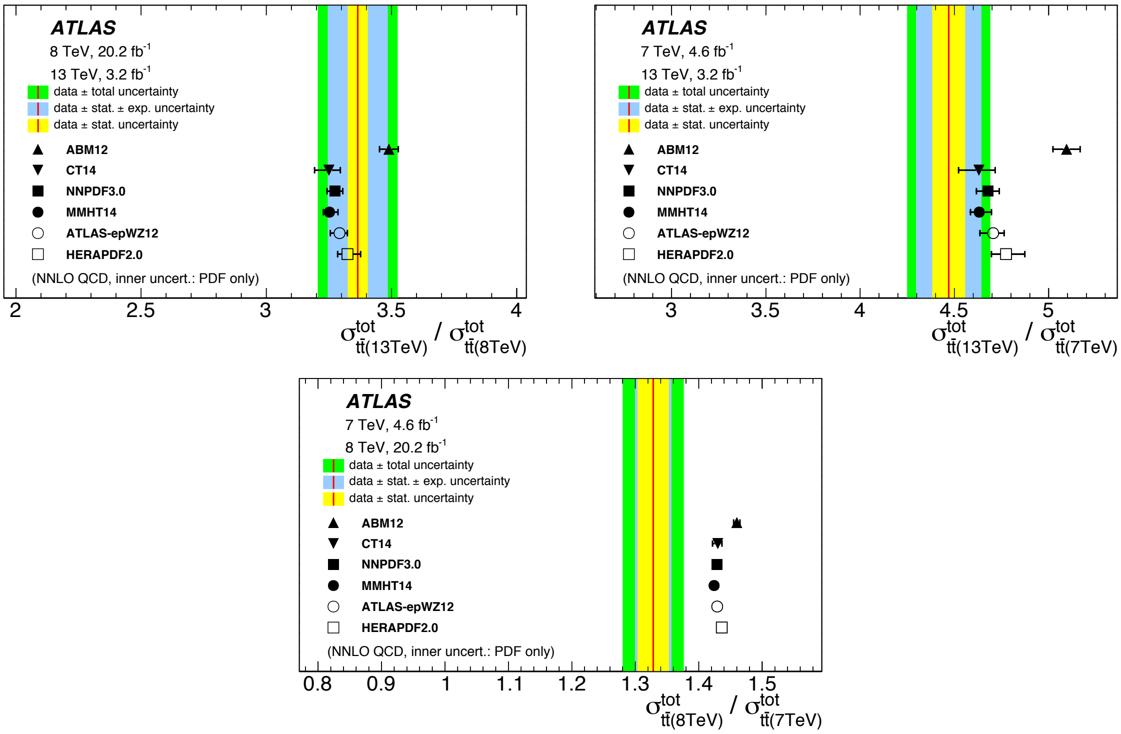

Figure 10.9: $\sigma^{\mathrm{tot}}_{t\bar{t}}(13\text{ TeV})$ to $\sigma^{\mathrm{tot}}_{t\bar{t}}(8\text{ TeV})$ (top left), $\sigma^{\mathrm{tot}}_{t\bar{t}}(13\text{ TeV})$ to $\sigma^{\mathrm{tot}}_{t\bar{t}}(7\text{ TeV})$ (top right), $\sigma^{\mathrm{tot}}_{t\bar{t}}(8\text{ TeV})$ to $\sigma^{\mathrm{tot}}_{t\bar{t}}(7\text{ TeV})$ (bottom) ratios of production cross sections compared to predictions based on different PDF sets. The inner shaded band corresponds to the statistical uncertainty, the middle band to the statistical and experimental systematic uncertainties added in quadrature, while the outer band shows the total uncertainty, including the luminosity uncertainty. For the 8-to-7 TeV ratio, the experimental systematic uncertainty band is too small to be clearly visible. The theory predictions are given with the corresponding PDF uncertainties shown as inner bars while the outer bars include the scale and α_S uncertainties added in quadrature.

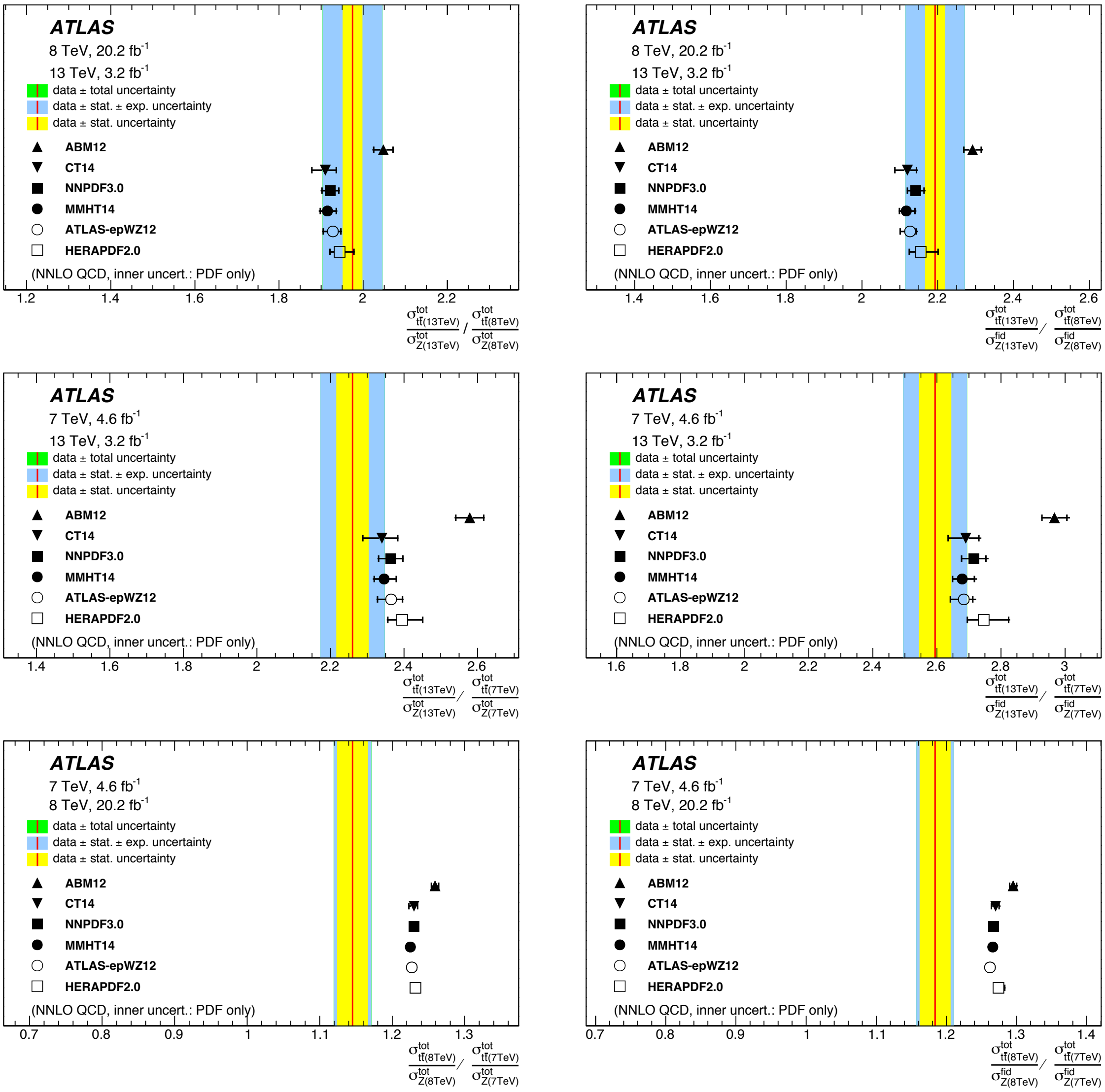

Figure 10.10: $\sqrt{s} = 13$ TeV to $\sqrt{s} = 8$ TeV (top two plots), $\sqrt{s} = 13$ TeV to $\sqrt{s} = 7$ TeV (middle two plots), and $\sqrt{s} = 8$ TeV to $\sqrt{s} = 7$ TeV (bottom two plots) double ratios of production cross sections compared to predictions based on different PDF sets. The inner shaded band corresponds to the statistical uncertainty, the middle band to the statistical and experimental systematic uncertainties added in quadrature, while the outer band shows the total uncertainty, including the luminosity uncertainty. The latter is not visible since the the luminosity uncertainties almost entirely cancel in these ratios. The theory predictions are given with the corresponding PDF uncertainties shown as inner bars while the outer bars include the scale and α_S uncertainties added in quadrature.

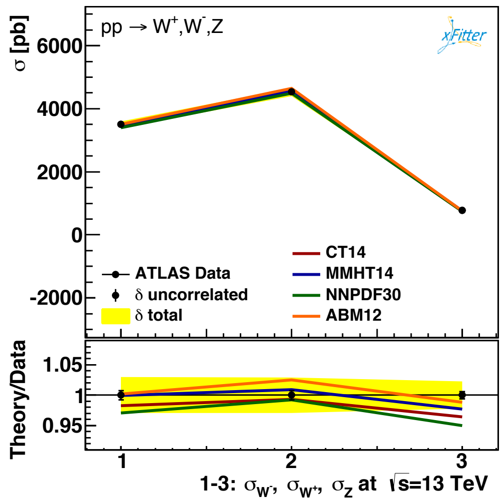

Figure 10.11: Comparison of the measured fiducial W^-, W^+ and Z cross-sections $(\sigma_{W^-}, \sigma_{W^+}, \sigma_Z)$ to predictions based on different PDF sets. The lower panel shows the total and uncorrelated uncertainties, δ, associated with the ratios of the predictions to the data.

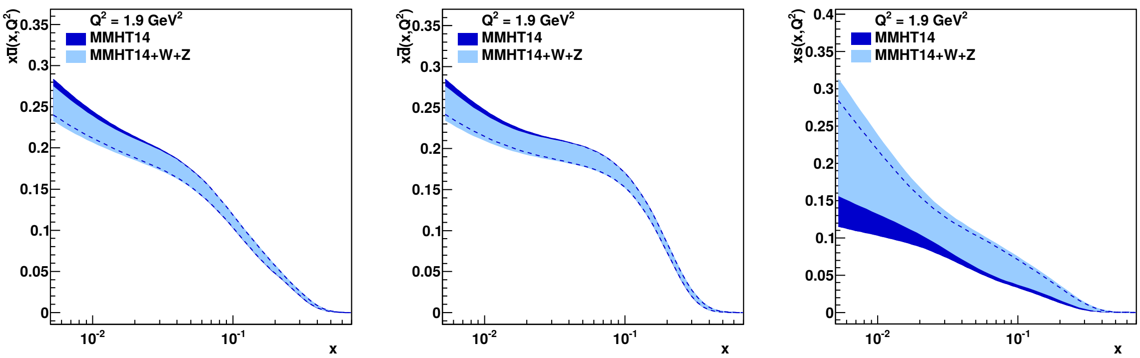

Figure 10.12: Distribution of the $x\bar{u}$ (left), $x\bar{d}$ (middle) and xs (right) PDFs as a function of Bjorken-x at a scale of $Q^2 = 1.9$ GeV^2 for the MMHT14 PDF set, before and after profiling.

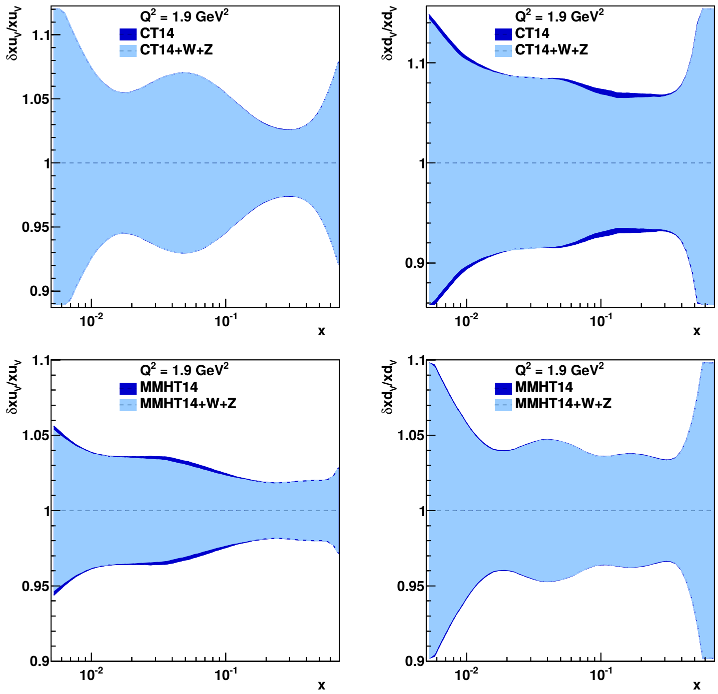

Figure 10.13: Effect of profiling on the relative uncertainties of the valence up-quark distribution $\delta x u_v(x)/x u_v(x)$ (left) and the valence down-quark distribution $\delta x d_v(x)/x d_v(x)$ (right) as a function of Bjorken-x at a scale of $Q^2 = 1.9$ GeV^2. The top row shows the CT14 PDF set and the bottom row shows the MMHT14 PDF set.

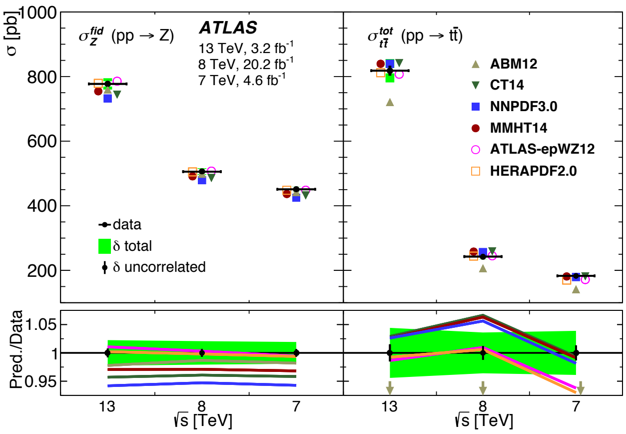

Figure 10.14: Comparison of the σ_Z^{fid} and $\sigma_{t\bar{t}}^{\text{tot}}$ cross sections with the predictions based on different PDF sets. Bins 1 to 3 correspond to σ_Z and 4 to 6 to $\sigma_{t\bar{t}}$ for $\sqrt{s} = 13$ TeV $\sqrt{s} = 8$ TeV and $\sqrt{s} = 7$ TeV, respectively.

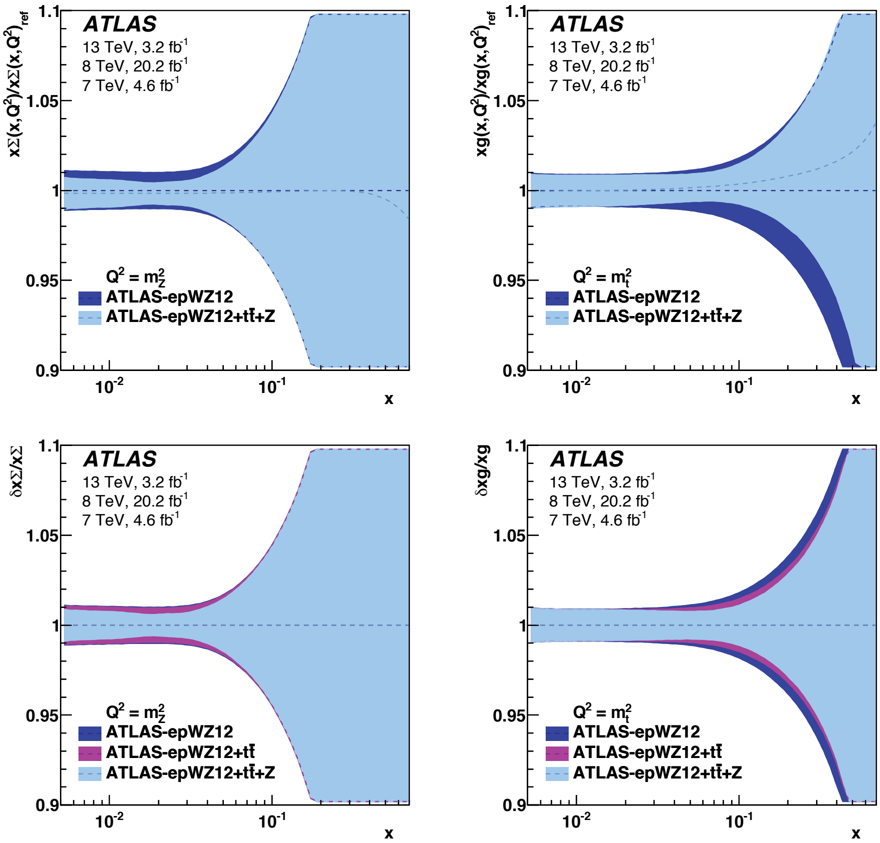

Figure 10.15: Impact of the ATLAS Z-boson and $t\bar{t}$ cross-section data on the determination of PDFs. The bands represent the uncertainty for the ATLAS-epWZ12 PDF set and the uncertainty of the profiled ATLAS-epWZ12 PDF set using $t\bar{t} + Z$ data as a function of x for the total light-quark-sea distribution, $x\Sigma$, at $Q^2 \approx m_Z^2$ (left) and for the gluon density, xg, at $Q^2 \approx m_t^2$ (right). In the upper plots, the profiled PDF set is divided by the central value of ATLAS-epWZ12 PDF set, "ref", while in the lower plots, the relative uncertainty, δ, is given. The lower plots also show the impact of only including the ATLAS $t\bar{t}$ data set. In the upper plots, the dashed blue curve represents the ratio of the central value of the profiled result to ATLAS-epWZ12 PDF set.

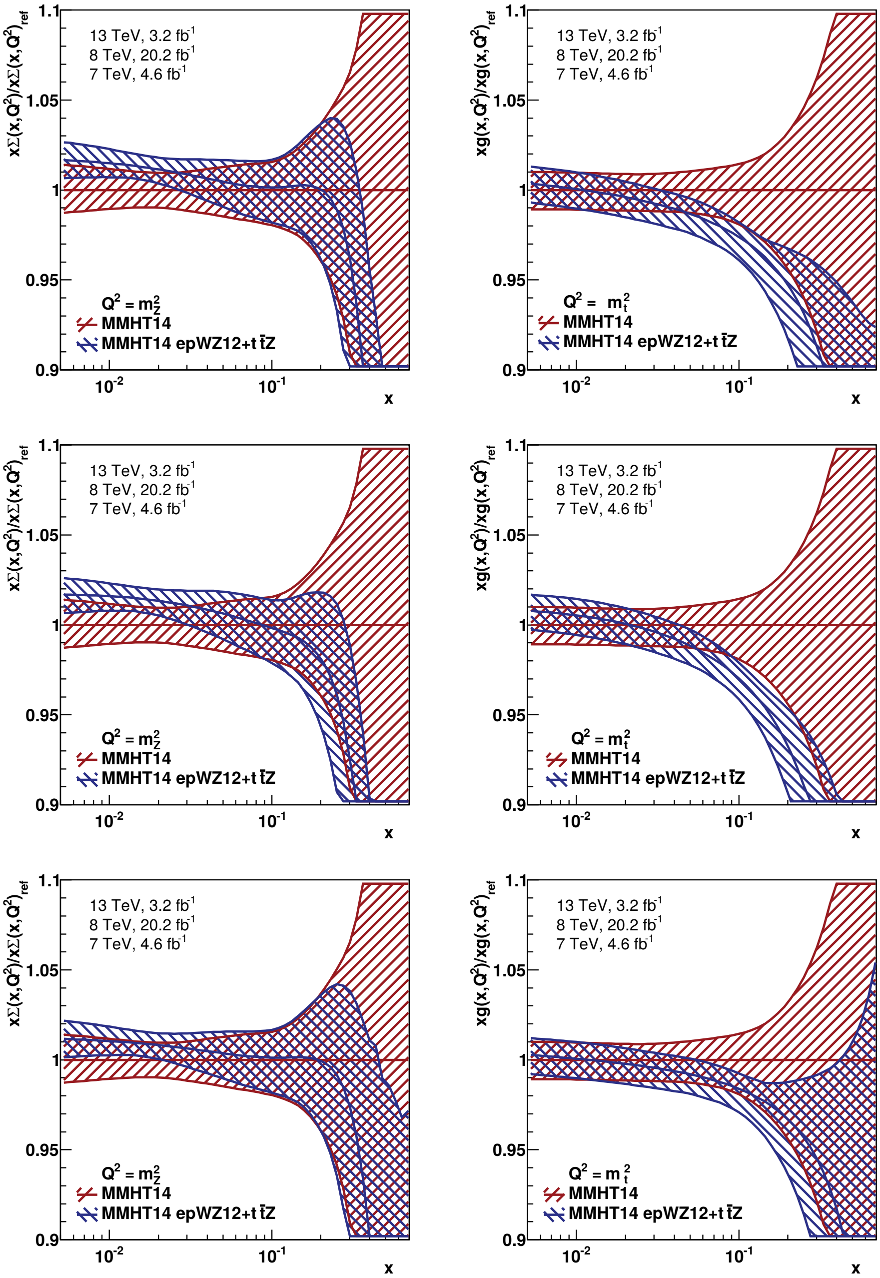

Figure 10.16: Impact of the ATLAS Z-boson and $t\bar{t}$ cross-section data on the determination of PDFs. The bands represent the uncertainty for the MMHT14 PDF set and the uncertainty of the profiled MMHT14 PDF set using $t\bar{t}+Z$ data as a function of x for the total light-quark-sea distribution, $x\Sigma$, at $Q^2 \approx m_Z^2$ (left) and for the gluon density, xg, at $Q^2 \approx m_t^2$ (right). The profiled PDF set is divided by the central value of MMHT14 PDF set ("ref"). The upper two plots represent profiling results using Z-boson and $t\bar{t}$ cross-section data at $\sqrt{s} = 13, 8$, and 7 TeV. The middle two plots represent result after excluding $t\bar{t}$ data at $\sqrt{s} = 7$ TeV from the profiling, the bottom two plots demonstrate results excluding $t\bar{t}$ data at $\sqrt{s} = 8$ TeV.

Chapter 11

Summary

This thesis presents measurements of the Z-boson production cross sections at $\sqrt{s} =$ 13 TeV using 81 pb^{-1} and 3.2 fb^{-1} of pp collisions with 50 ns and 25 ns bunch spacing configurations from the LHC, together with the evaluations of single and double ratios involving Z, $W^{\pm}$-boson and $t\bar{t}$ production cross sections. The measurements of Z-boson production at $\sqrt{s} = 13$ TeV are fully synchronised to the corresponding $W^{\pm}$ and $t\bar{t}$ analyses to improve the cancellation of the uncertainties in the ratios.

The contribution of background processes to the measurements of the $Z \to \ell^+\ell^-$ production cross sections, where $\ell^{\pm} = e^{\pm}, \mu^{\pm}$, is estimated using both Monte Carlo simulation and data-driven techniques. The dominant contribution to electron and muon channels at both bunch spacing configurations came from top-pair production and found to be at the level of $0.2 - 0.3\%$. The systematic uncertainties related to the experimental and theoretical aspects of the measurements are considered. Apart from the determination of the luminosity, the dominant systematic uncertainties in the cross-section evaluations are the lepton reconstruction and identification efficiencies. The measured cross sections with both data sets showed excellent compatibility within the statistical uncertainty.

The measured Z and $W^{\pm}$-boson fiducial cross sections for the electron and muon decay channels with 50 ns configuration are used for evaluation of the ratios $R_{W^{\pm}} = \sigma^{\text{fid}}_{W^{\pm}\to e\nu}/\sigma^{\text{fid}}_{W^{\pm}\to\mu\nu}$ and $R_Z = \sigma^{\text{fid}}_{Z\to e^+e^-}/\sigma^{\text{fid}}_{Z\to\mu^+\mu^-}$. The obtained results showed good agreement with the Standard Model expectations of lepton universality. The datasets for electron and muon decay channels are then combined using a methodology which accounts for the correlations of the experimental systematic uncertainties. The measured fiducial and total cross sections are found to agree with theoretical calculations based on NNLO QCD with NLO EW corrections. Using the combined cross sections, the ratios of W^+ to W^- and $W^{\pm}$ to Z-boson production are evaluated. The W^+ to W^- measured ratio showed the best agreement with the prediction based on CT14nnlo PDF set, while $W^{\pm}$ to Z ratio is found to be in the best agreement with ATLAS-epWZ12nnlo. The impact of the W and Z ATLAS data on the CT14 and MMHT14 PDF sets is quantified with the PDF profiling method. The profiled distributions for light sea-quark showed increasing of the strange quark and reduction of $x\bar{u}$, $x\bar{d}$ at low x as well as slight reduction of uncertainties comparing to the reference PDF set. Also minor reduction of the uncertainty is observed for the up and down valence-quark distributions.

Using the measured Z-boson and top-quark pair production cross section at $\sqrt{s} =$ 13 TeV with 25 ns bunch spacing configuration as well as previously published cross-section measurements at $\sqrt{s} = 8$ TeV and 7 TeV corrected to a common phase space, the single ratios at a given $\sqrt{s}$ for the two processes ($R_{t\bar{t}/Z}(i$ TeV$)$) and at different $\sqrt{s}$ for each process (R_{Z_i/Z_j}, $R_{t\bar{t}_i/t\bar{t}_j}$) are estimated. The double ratios of the two processes at different center-of-mass energies $R_{t\bar{t}/Z}(i/j$ TeV$)$, where $i, j = 13, 8, 7$ TeV, are evaluated. The experimental results are compared to the state-of-the-art theoretical predictions, which are computed at NNLO (with NLO EW corrections) and NNLO+NNLL accuracy for Z-boson and $t\bar{t}$ production, respectively. Excellent agreement between data and predictions is observed in the Z-boson cross-section ratios at the various centre-of-mass energies, even omitting the luminosity uncertainties. These results indicate that such measurements could be used to normalise cross-section measurements at different $\sqrt{s}$, as well as provide stringent cross-checks on the corresponding ratios of absolute integrated luminosity values. The data are found to be in best agreement with the ATLAS-epWZ12 PDF set, closely followed by the HERAPDF2.0 set. The Z and $t\bar{t}$ data used for these measurements have significant power to constrain the gluon distribution function at Bjorken-$x \sim 0.1$ and the total light-quark sea at $x < 0.02$, as demonstrated from a profiling analysis involving the ATLAS-epWZ12 PDF set.

Appendix A

Detailed list of Toy Monte Carlo replicas

	$W^- \to e^- \nu$ ID	$W^- \to e^- \nu$ ISO	$W^- \to e^- \nu$ TG	$W^+ \to e^+ \nu$ ID	$W^+ \to e^+ \nu$ ISO	$W^+ \to e^+ \nu$ TG	$W^- \to \mu^- \nu$ TG	$W^+ \to \mu^+ \nu$ TG	$Z \to e^+ e^-$ ID	$Z \to e^+ e^-$ ISO	$Z \to e^+ e^-$ TG	$Z \to \mu^+ \mu^-$ TG
Seed	10	12	11	10	12	11	11	11	10	12	11	1234
Toy MC replica 1	-0.073	-0.008	0.086	-0.077	-0.062	0.116	0.178	0.174	0.5516	0.5526	0.5521	0.7115
Toy MC replica 2	-0.232	-0.304	0.105	-0.207	-0.333	0.084	-0.021	-0.031	0.5496	0.5497	0.552	0.7112
Toy MC replica 3	0.069	-0.212	0.109	0.098	-0.22	0.089	-0.128	-0.09	0.5505	0.5501	0.5523	0.7104
Toy MC replica 4	-0.028	0.129	-0.123	0.02	0.16	-0.146	0.01	0.011	0.5522	0.5536	0.5519	0.7111
Toy MC replica 5	-0.044	-0.262	0.088	0.006	-0.266	0.149	-0.242	-0.228	0.5509	0.5503	0.5521	0.7104
Toy MC replica 6	-0.239	0.013	-0.27	-0.241	0.052	-0.205	0.036	0.058	0.5497	0.5517	0.5517	0.7109
Toy MC replica 7	0.263	-0.008	0.48	0.277	-0.06	0.621	0.165	0.158	0.5547	0.5523	0.5522	0.7115
Toy MC replica 8	-0.412	0.108	0.041	-0.399	0.121	0.031	-0.189	-0.168	0.5475	0.5526	0.552	0.7105
Toy MC replica 9	0.546	-0.042	-0.349	0.565	-0.065	-0.345	0.195	0.201	0.5563	0.5522	0.5517	0.7114
Toy MC replica 10	-0.17	0.034	-0.104	-0.161	0.041	-0.104	-0.032	-0.039	0.5487	0.5522	0.552	0.711
Toy MC replica 11	0.333	0.305	0.123	0.44	0.316	0.05	0.199	0.164	0.5535	0.5555	0.5523	0.7122
Toy MC replica 12	0.306	-0.144	-0.106	0.285	-0.123	-0.075	0.148	0.179	0.5549	0.5501	0.5519	0.7112
Toy MC replica 13	-0.066	0.001	-0.395	-0.03	0.037	-0.475	0.297	0.304	0.5506	0.5513	0.5518	0.7118
Toy MC replica 14	-0.576	-0.344	-0.07	-0.607	-0.358	-0.085	-0.324	-0.326	0.5467	0.5486	0.552	0.71
Toy MC replica 15	0.183	-0.237	-0.014	0.182	-0.265	-0.05	0.021	0.028	0.5553	0.5502	0.552	0.711
Toy MC replica 16	0.172	0.365	-0.474	0.221	0.42	-0.595	0.301	0.316	0.5534	0.5544	0.5518	0.7122
Toy MC replica 17	-0.442	0.121	0.336	-0.463	0.164	0.288	-0.04	-0.056	0.549	0.5533	0.5522	0.7108
Toy MC replica 18	-0.097	0.093	0.041	-0.077	0.101	0.153	0.091	0.131	0.5516	0.5524	0.5518	0.7111
Toy MC replica 19	-0.073	-0.002	0.031	-0.042	0.03	-0.016	0.298	0.325	0.551	0.5515	0.552	0.7122
Toy MC replica 20	0.059	-0.108	0.425	0.062	-0.139	0.398	0.378	0.382	0.5526	0.5513	0.5524	0.7124
Toy MC replica 21	0.135	0.033	-0.171	0.116	0.024	-0.07	0.189	0.222	0.5535	0.5511	0.5516	0.7116
Toy MC replica 22	0.221	0.324	-0.336	0.221	0.314	-0.412	0.094	0.121	0.5536	0.5553	0.5518	0.7116
Toy MC replica 23	-0.017	0.003	-0.145	-0.042	-0.059	-0.199	-0.1	-0.137	0.552	0.5529	0.5518	0.7107
Toy MC replica 24	0.128	0.055	-0.189	0.199	0.022	-0.208	-0.111	-0.062	0.5518	0.5519	0.5519	0.7105
Toy MC replica 25	-0.285	-0.077	-0.095	-0.373	-0.046	-0.088	0.158	0.157	0.5513	0.5505	0.552	0.7116
Toy MC replica 26	0.18	0.049	-0.072	0.15	0.033	-0.066	-0.1	-0.035	0.5552	0.5525	0.5521	0.7101
Toy MC replica 27	0.397	-0.245	-0.01	0.431	-0.226	-0.033	0.073	0.095	0.5564	0.5503	0.5518	0.7112
Toy MC replica 28	0.128	0.31	-0.17	0.138	0.338	-0.179	-0.185	-0.161	0.5535	0.5545	0.552	0.71
Toy MC replica 29	0.109	-0.194	0.069	0.16	-0.17	0.139	-0.036	-0.026	0.5519	0.5503	0.5518	0.7109
Toy MC replica 30	0.579	0.284	-0.145	0.6	0.289	-0.209	-0.108	-0.081	0.5567	0.5546	0.5521	0.7107
Toy MC replica 31	-0.555	0.129	-0.102	-0.592	0.139	-0.114	-0.042	-0.026	0.5481	0.5526	0.5518	0.7113
Toy MC replica 32	-0.016	0.135	0.106	0.019	0.134	0.124	0.065	0.034	0.5513	0.554	0.5521	0.7118
Toy MC replica 33	0.35	-0.261	-0.428	0.35	-0.26	-0.395	-0.394	-0.368	0.5538	0.5499	0.5515	0.7095
Toy MC replica 34	0.005	0.1	-0.238	0.033	0.116	-0.199	-0.033	-0.093	0.5516	0.553	0.5517	0.7109
Toy MC replica 35	0.344	-0.021	-0.592	0.372	-0.014	-0.679	-0.243	-0.232	0.5545	0.5523	0.5517	0.7104
Toy MC replica 36	-0.41	-0.163	0.559	-0.473	-0.139	0.642	0.148	0.152	0.5489	0.55	0.5524	0.7118
Toy MC replica 37	-0.409	0.306	-0.164	-0.456	0.335	-0.193	-0.608	-0.584	0.5497	0.5546	0.5517	0.7093
Toy MC replica 38	-0.726	-0.106	0.344	-0.769	-0.134	0.379	0.217	0.218	0.5469	0.5512	0.5522	0.7118
Toy MC replica 39	-0.095	0.04	-0.059	-0.073	0.048	-0.086	0.02	0.046	0.551	0.5532	0.5519	0.7109
Toy MC replica 40	-0.533	0.038	-0.264	-0.584	0.008	-0.354	-0.261	-0.297	0.5476	0.5522	0.5517	0.7107
Toy MC replica 41	0.05	-0.261	0.026	0.054	-0.263	-0.04	-0.324	-0.332	0.5513	0.5502	0.5522	0.7101
Toy MC replica 42	0.6	-0.175	-0.125	0.623	-0.149	-0.21	-0.053	-0.058	0.557	0.5503	0.552	0.7111
Toy MC replica 43	-0.011	0.378	0.051	-0.055	0.434	0.129	0.303	0.301	0.5522	0.5551	0.552	0.712
Toy MC replica 44	-0.359	0.054	0.326	-0.409	0.048	0.376	0.152	0.165	0.5494	0.5522	0.5521	0.7117
Toy MC replica 45	-0.569	0.065	0.193	-0.577	0.055	0.146	0.092	0.053	0.5474	0.5526	0.5521	0.7113
Toy MC replica 46	-0.215	0.174	0.246	-0.269	0.179	0.283	-0.124	-0.101	0.5505	0.5522	0.552	0.7104
Toy MC replica 47	-0.182	0.143	0.414	-0.129	0.144	0.433	-0.132	-0.124	0.5501	0.5537	0.5522	0.7106
Toy MC replica 48	0.184	-0.042	-0.067	0.19	-0.012	-0.025	0.142	0.171	0.5535	0.5509	0.5519	0.7115
Toy MC replica 49	-0.369	0.236	0.012	-0.38	0.248	0.03	-0.124	-0.102	0.549	0.554	0.5519	0.7105
Toy MC replica 50	0.187	-0.148	-0.287	0.243	-0.166	-0.311	0.213	0.171	0.5527	0.551	0.5517	0.7123
Toy MC replica 51	0.19	0.062	0.18	0.143	0.06	0.115	0.555	0.534	0.553	0.5519	0.5524	0.7127
Toy MC replica 52	0.414	-0.091	-0.169	0.401	-0.094	-0.144	0.041	0.06	0.5569	0.5519	0.5518	0.7113
Toy MC replica 53	-0.177	0.022	-0.019	-0.149	0.018	-0.043	-0.04	-0.077	0.5496	0.5526	0.5519	0.7112
Toy MC replica 54	-0.374	0.121	0.197	-0.438	0.135	0.205	0.094	0.057	0.5479	0.553	0.5522	0.7111
Toy MC replica 55	0.553	-0.071	-0.367	0.613	-0.078	-0.464	0.003	-0.046	0.5559	0.551	0.5519	0.7115
Toy MC replica 56	0.029	-0.058	0.245	0.066	-0.049	0.245	-0.137	-0.128	0.5515	0.5515	0.5522	0.7108
Toy MC replica 57	-0.004	0.09	-0.113	0.021	0.081	-0.144	0.198	0.216	0.552	0.5533	0.5518	0.712
Toy MC replica 58	0.033	0.064	-0.52	-0.048	0.053	-0.604	-0.009	-0.058	0.553	0.5531	0.5515	0.7111
Toy MC replica 59	-0.181	0.27	0.353	-0.236	0.315	0.327	0.093	0.093	0.5503	0.5539	0.5523	0.7112
Toy MC replica 60	-0.295	-0.037	0.28	-0.303	-0.043	0.273	0.331	0.32	0.5487	0.5523	0.5521	0.712
Toy MC replica 61	0.015	0.229	0.331	0.068	0.212	0.326	0.011	0.004	0.5505	0.5548	0.5523	0.7113
Toy MC replica 62	-0.311	-0.035	0.013	-0.333	-0.034	0.076	0.203	0.233	0.5483	0.5506	0.5518	0.7116
Toy MC replica 63	-0.009	-0.301	-0.064	-0.011	-0.364	0.016	0.176	0.156	0.5507	0.5501	0.5516	0.7118
Toy MC replica 64	0.231	-0.15	-0.248	0.286	-0.138	-0.287	0.003	-0.026	0.5537	0.5507	0.5517	0.7112
Toy MC replica 65	0.561	0.096	-0.439	0.579	0.16	-0.487	0.071	0.073	0.5558	0.5526	0.5517	0.7116
Toy MC replica 66	0.259	-0.017	0.394	0.274	-0.044	0.339	0.262	0.248	0.554	0.5514	0.5524	0.7122
Toy MC replica 67	-0.071	0.181	-0.761	-0.039	0.211	-0.872	-0.105	-0.109	0.5515	0.5526	0.5514	0.7108
Toy MC replica 68	-0.088	0.091	-0.007	-0.101	0.067	-0.029	0.225	0.262	0.552	0.5525	0.5519	0.7117
Toy MC replica 69	-0.102	-	0.442	-0.131	-	0.532	-0.055	-0.074	0.5513	-	0.5521	0.7108
Toy MC replica 70	-0.236	-	0.009	-0.223	-	0.022	-0.086	-0.043	0.5503	-	0.5518	0.7104
Toy MC replica 71	-0.134	-0.171	-0.473	-0.188	-0.16	-0.545	-0.128	-0.117	0.5516	0.5508	0.5516	0.7108
Toy MC replica 72	-0.056	0.091	0.181	-0.013	0.089	0.135	-0.055	-0.09	0.5503	0.5544	0.5523	0.7108
Toy MC replica 73	0.283	0.231	0.209	0.337	0.265	0.28	-0.244	-0.256	0.5537	0.554	0.552	0.7102
Toy MC replica 74	-0.177	0.082	0.222	-0.217	0.115	0.258	0.173	0.158	0.5511	0.5521	0.5521	0.7117
Toy MC replica 75	-0.026	-0.005	0.256	0.004	-0.049	0.216	0.217	0.205	0.5517	0.5512	0.5522	0.7116
Toy MC replica 76	-0.749	0.014	0.019	-0.738	0.028	0.043	0.224	0.193	0.5451	0.5525	0.5516	0.7121
Toy MC replica 77	0.304	-0.034	-0.405	0.357	-0.04	-0.428	-0.016	-0.051	0.5534	0.5522	0.5515	0.7108
Toy MC replica 78	0.118	-0.097	0.098	0.1	-0.116	0.146	0.085	0.118	0.5531	0.5513	0.5521	0.7114
Toy MC replica 79	-0.223	0.101	0.766	-0.223	0.119	0.815	-0.205	-0.195	0.5503	0.553	0.5527	0.7101
Toy MC replica 80	-0.26	0.337	-0.284	-0.272	0.386	-0.323	0.313	0.328	0.5487	0.5551	0.5519	0.7122
Toy MC replica 81	-0.146	0.304	0.426	-0.196	0.34	0.385	-0.226	-0.246	0.5516	0.5554	0.5524	0.7101
Toy MC replica 82	0.496	-0.144	-0.03	0.509	-0.179	-0.016	-0.061	-0.048	0.5567	0.5505	0.552	0.7108
Toy MC replica 83	-0.013	0.135	-0.37	-0.016	0.162	-0.397	0.075	0.087	0.5511	0.5529	0.5516	0.7113
Toy MC replica 84	0.156	0.197	0.292	0.101	0.18	0.233	-0.032	-0.023	0.5536	0.554	0.5522	0.7112
Toy MC replica 85	-0.238	-0.374	0.304	-0.266	-0.401	0.341	0.033	0.031	0.5497	0.5493	0.552	0.7113
Toy MC replica 86	-0.258	0.38	0.04	-0.26	0.418	0.087	0.088	0.06	0.5495	0.5537	0.5519	0.7116
Toy MC replica 87	-0.217	0.149	-0.151	-0.258	0.163	-0.041	-0.007	-0.005	0.5501	0.5537	0.5517	0.7108
Toy MC replica 88	-0.239	0.227	0.364	-0.237	0.251	0.402	-0.158	-0.155	0.5499	0.5534	0.5521	0.7108
Toy MC replica 89	0.118	-0.209	0.015	0.143	-0.222	0.066	0.129	0.1	0.5516	0.5498	0.5518	0.7115
Toy MC replica 90	0.212	0.373	-0.293	0.22	0.361	-0.251	0.307	0.349	0.5536	0.5545	0.5517	0.712
Toy MC replica 91	-0.0	0.144	0.461	-0.013	0.15	0.453	-0.055	-0.077	0.5528	0.5527	0.5524	0.7111
Toy MC replica 92	0.036	0.013	-0.006	0.032	0.044	-0.083	-0.103	-0.06	0.5536	0.5517	0.5522	0.7105
Toy MC replica 93	0.11	-0.106	0.487	0.069	-0.102	0.507	-0.384	-0.421	0.5541	0.5507	0.5525	0.7099
Toy MC replica 94	0.377	0.019	-0.174	0.425	0.017	-0.163	0.232	0.218	0.5553	0.5525	0.5518	0.7119
Toy MC replica 95	-0.026	0.2	0.281	-0.01	0.211	0.355	0.009	0.014	0.5506	0.5546	0.5521	0.7113
Toy MC replica 96	-0.114	0.004	-0.533	-0.107	0.003	-0.49	0.135	0.124	0.5511	0.5525	0.5512	0.7116
Toy MC replica 97	-0.958	-0.077	0.288	-1.04	-0.068	0.265	-0.091	-0.054	0.5442	0.5506	0.5523	0.7106
Toy MC replica 98	0.58	-0.275	-0.003	0.613	-0.307	0.03	0.208	0.233	0.5565	0.5501	0.5519	0.7114
Toy MC replica 99	0.53	0.008	-0.257	0.635	-0.018	-0.222	-0.078	-0.067	0.5551	0.552	0.5514	0.7109
Toy MC replica 100	0.02	0.011	-0.019	0.044	-0.007	-0.006	-0.368	-0.331	0.5511	0.5514	0.5518	0.7096

Table A.1: All toy MC replicas and corresponding seeds for lepton identification, reconstruction, isolation, trigger efficiency sources for $t\bar{t}$ and Z channels at $13 TeV$ ($50 ns$ data).

	$t\bar{t}$ ID	$t\bar{t}$ RECO	$Z \to ee$ ID	$Z \to ee$ RECO	$Z \to ee$ ISO	$Z \to ee$ TG	$Z \to \mu\mu$ TG
Seed	10	13	10	13	12	11	1234
Toy MC replica 1	-0.022	-0.001	0.5548	0.5536	0.5528	0.5536	0.7064
Toy MC replica 2	-0.0216	-0.0006	0.5557	0.5536	0.5536	0.5536	0.7061
Toy MC replica 3	-0.0206	-0.0006	0.555	0.5539	0.5533	0.5536	0.7063
Toy MC replica 4	-0.0201	-0.0004	0.5545	0.5538	0.5539	0.5536	0.7065
Toy MC replica 5	-0.0228	-0.0003	0.5528	0.554	0.5534	0.5536	0.7064
Toy MC replica 6	-0.023	-0.0007	0.5528	0.5536	0.5532	0.5536	0.7063
Toy MC replica 7	-0.0231	-0.001	0.5531	0.5535	0.553	0.5536	0.7064
Toy MC replica 8	-0.0129	-0.0009	0.5567	0.5533	0.5542	0.5536	0.7064
Toy MC replica 9	-0.0271	-0.0004	0.5516	0.5539	0.5531	0.5536	0.7063
Toy MC replica 10	-0.0228	-0.0006	0.5512	0.5537	0.5529	0.5536	0.7064
Toy MC replica 11	-0.0202	-0.0005	0.556	0.5541	0.554	0.5537	0.7065
Toy MC replica 12	-0.0216	-0.0003	0.553	0.554	0.555	0.5535	0.7066
Toy MC replica 13	-0.0197	-0.0005	0.5564	0.5538	0.553	0.5536	0.7064
Toy MC replica 14	-0.024	0.0	0.5515	0.5542	0.553	0.5536	0.7062
Toy MC replica 15	-0.0198	-0.0008	0.5572	0.5538	0.5536	0.5537	0.7066
Toy MC replica 16	-0.0292	-0.0004	0.5479	0.5539	0.5538	0.5536	0.7067
Toy MC replica 17	-0.0307	-0.0007	0.5495	0.5535	0.5542	0.5536	0.7065
Toy MC replica 18	-0.0196	-0.0008	0.5534	0.5539	0.5547	0.5536	0.7063
Toy MC replica 19	-0.0251	-0.0006	0.552	0.5539	0.5547	0.5536	0.7068
Toy MC replica 20	-0.025	-0.0009	0.5511	0.5536	0.5537	0.5536	0.7067
Toy MC replica 21	-0.0225	-0.0012	0.5523	0.5535	0.5541	0.5537	0.7063
Toy MC replica 22	-0.0217	-0.0003	0.5542	0.5541	0.5532	0.5536	0.7065
Toy MC replica 23	-0.0243	-0.0009	0.5531	0.5534	0.5541	0.5536	0.7066
Toy MC replica 24	-0.0187	0.0003	0.5563	0.5542	0.5535	0.5536	0.7067
Toy MC replica 25	-0.0219	-0.0007	0.5559	0.5537	0.5539	0.5536	0.7062
Toy MC replica 26	-0.0248	-0.0004	0.5509	0.5537	0.5534	0.5536	0.7062
Toy MC replica 27	-0.0221	-0.0002	0.5523	0.5539	0.5542	0.5536	0.7064
Toy MC replica 28	-0.0237	-0.0008	0.5534	0.5536	0.5528	0.5537	0.7064
Toy MC replica 29	-0.0225	-0.001	0.5537	0.5535	0.5537	0.5536	0.7062
Toy MC replica 30	-0.0199	-0.0005	0.5532	0.5535	0.5533	0.5536	0.706
Toy MC replica 31	-0.02	-0.0004	0.5571	0.554	0.5524	0.5536	0.7062
Toy MC replica 32	-0.0271	-0.0005	0.5482	0.5537	0.5539	0.5536	0.7062
Toy MC replica 33	-0.02	-0.0011	0.5531	0.5537	0.5528	0.5536	0.7066
Toy MC replica 34	-0.0241	-0.0013	0.5523	0.5536	0.5546	0.5536	0.7063
Toy MC replica 35	-0.0263	-0.0014	0.5515	0.5533	0.5531	0.5536	0.7063
Toy MC replica 36	-0.0235	-0.0001	0.5515	0.5541	0.5547	0.5536	0.7064
Toy MC replica 37	-0.0194	-0.0013	0.5557	0.5532	0.5552	0.5536	0.7062
Toy MC replica 38	-0.0211	-0.0001	0.5545	0.554	0.5543	0.5536	0.7064
Toy MC replica 39	-0.0216	-0.0005	0.5549	0.5534	0.5531	0.5536	0.7063
Toy MC replica 40	-0.025	-0.0001	0.553	0.5537	0.5537	0.5536	0.706
Toy MC replica 41	-0.0203	-0.0006	0.5564	0.5533	0.5537	0.5536	0.7064
Toy MC replica 42	-0.021	-0.0014	0.5531	0.5533	0.5532	0.5536	0.7065
Toy MC replica 43	-0.0184	0.0001	0.555	0.5538	0.5539	0.5536	0.7062
Toy MC replica 44	-0.0161	-0.001	0.558	0.5537	0.5524	0.5536	0.7062
Toy MC replica 45	-0.0202	-0.0003	0.5534	0.5535	0.5542	0.5536	0.7066
Toy MC replica 46	-0.0245	-0.0002	0.5539	0.5542	0.5536	0.5536	0.7065
Toy MC replica 47	-0.0149	-0.0005	0.5569	0.5533	0.5544	0.5536	0.706
Toy MC replica 48	-0.0228	-0.0006	0.5516	0.5536	0.5534	0.5536	0.7062
Toy MC replica 49	-0.0202	-0.0005	0.5544	0.554	0.5532	0.5536	0.7066
Toy MC replica 50	-0.0262	-0.0002	0.5529	0.5537	0.552	0.5536	0.7063
Toy MC replica 51	-0.0169	-0.0007	0.5577	0.5538	0.5537	0.5536	0.7064
Toy MC replica 52	-0.025	-0.001	0.5528	0.5528	0.5527	0.5536	0.7065
Toy MC replica 53	-0.0204	-0.0008	0.5544	0.5533	0.5537	0.5536	0.7062
Toy MC replica 54	-0.0221	-0.0007	0.5514	0.5538	0.5534	0.5536	0.7061
Toy MC replica 55	-0.0208	-0.0007	0.5529	0.5536	0.5539	0.5537	0.7063
Toy MC replica 56	-0.0243	-0.0009	0.5541	0.5536	0.5538	0.5536	0.7065
Toy MC replica 57	-0.0194	-0.0006	0.5556	0.5536	0.5556	0.5536	0.7066
Toy MC replica 58	-0.0301	-0.0008	0.5504	0.5535	0.5539	0.5536	0.7062
Toy MC replica 59	-0.0227	-0.0008	0.5543	0.5533	0.5545	0.5536	0.7065
Toy MC replica 60	-0.0231	-0.0006	0.5518	0.5536	0.553	0.5536	0.7064
Toy MC replica 61	-0.0262	-0.0011	0.5508	0.5536	0.5561	0.5536	0.706
Toy MC replica 62	-0.023	-0.0017	0.5537	0.5533	0.5542	0.5536	0.7064
Toy MC replica 63	-0.0194	-0.0014	0.5548	0.5536	0.554	0.5536	0.7064
Toy MC replica 64	-0.0213	-0.0008	0.5527	0.5536	0.5534	0.5536	0.7063
Toy MC replica 65	-0.0223	-0.0007	0.5514	0.5539	0.5534	0.5536	0.7064
Toy MC replica 66	-0.0265	-0.001	0.5525	0.5536	0.5545	0.5536	0.7065
Toy MC replica 67	-0.0258	-0.0009	0.5511	0.553	0.5537	0.5536	0.7064
Toy MC replica 68	-0.0269	-0.0003	0.5508	0.5537	0.5544	0.5536	0.7066
Toy MC replica 69	-0.0193	0.0001	0.5547	0.5538	0.5524	0.5536	0.7067
Toy MC replica 70	-0.0191	-0.0004	0.556	0.5537	0.5539	0.5536	0.7062
Toy MC replica 71	-0.0239	-0.0008	0.553	0.5537	0.5542	0.5536	0.7063
Toy MC replica 72	-0.0232	-0.0013	0.5545	0.5533	0.5543	0.5537	0.7063
Toy MC replica 73	-0.0274	-0.0004	0.5504	0.5537	0.554	0.5536	0.7065
Toy MC replica 74	-0.0248	-0.0007	0.5517	0.5533	0.5528	0.5536	0.7065
Toy MC replica 75	-0.0216	-0.0007	0.5555	0.5535	0.5535	0.5536	0.7063
Toy MC replica 76	-0.0253	-0.0009	0.5535	0.5537	0.5532	0.5536	0.7064
Toy MC replica 77	-0.0187	-0.0011	0.5559	0.5537	0.5541	0.5536	0.7063
Toy MC replica 78	-0.0194	-0.0008	0.5553	0.5536	0.554	0.5535	0.7065
Toy MC replica 79	-0.0156	-0.0015	0.5575	0.5535	0.5518	0.5536	0.7066
Toy MC replica 80	-0.0201	-0.0005	0.5552	0.5536	0.5533	0.5536	0.7063
Toy MC replica 81	-0.0202	-0.001	0.5541	0.5539	0.5539	0.5536	0.7063
Toy MC replica 82	-0.0246	-0.0005	0.5514	0.5538	0.555	0.5535	0.7064
Toy MC replica 83	-0.0224	-0.0006	0.5526	0.5533	0.5539	0.5536	0.7063
Toy MC replica 84	-0.0211	-0.0012	0.5525	0.5533	0.555	0.5536	0.7067
Toy MC replica 85	-0.0214	-0.0009	0.5549	0.5535	0.5532	0.5536	0.7063
Toy MC replica 86	-0.025	-0.0004	0.5521	0.5538	0.5542	0.5536	0.7067
Toy MC replica 87	-0.0169	-0.0012	0.5543	0.5534	0.5545	0.5536	0.7066
Toy MC replica 88	-0.0235	-0.0005	0.5537	0.5535	0.5533	0.5536	0.7071
Toy MC replica 89	-0.0236	-0.0007	0.5516	0.5533	0.553	0.5536	0.7066
Toy MC replica 90	-0.0224	-0.0011	0.5534	0.5534	0.553	0.5536	0.7064
Toy MC replica 91	-0.027	-0.0008	0.5512	0.5537	0.5534	0.5536	0.7065
Toy MC replica 92	-0.0236	0.0001	0.5527	0.5541	0.5536	0.5536	0.7063
Toy MC replica 93	-0.0203	0.0001	0.5549	0.5538	0.5536	0.5536	0.7065
Toy MC replica 94	-0.0213	-0.0007	0.5535	0.5533	0.5518	0.5536	0.7064
Toy MC replica 95	-0.0233	0.0001	0.5513	0.554	0.5535	0.5536	0.7068
Toy MC replica 96	-0.0206	-0.0004	0.5509	0.5541	0.5545	0.5536	0.7063
Toy MC replica 97	-0.0261	-0.0007	0.5521	0.5536	0.5543	0.5536	0.7063
Toy MC replica 98	-0.0251	-0.0008	0.5482	0.5536	0.5552	0.5536	0.7065
Toy MC replica 99	-0.0252	-0.0003	0.5527	0.5539	0.5538	0.5536	0.7065
Toy MC replica 100	-0.0205	0.0004	0.554	0.5537	0.5541	0.5536	0.7064

Table A.2: All toy MC replicas and corresponding seeds for lepton identification, reconstruction, isolation, trigger efficiency sources for $t\bar{t}$ and Z channels at $13TeV$ ($25ns$ data).

Appendix B

Uncertainties on correlation coefficients among C factors

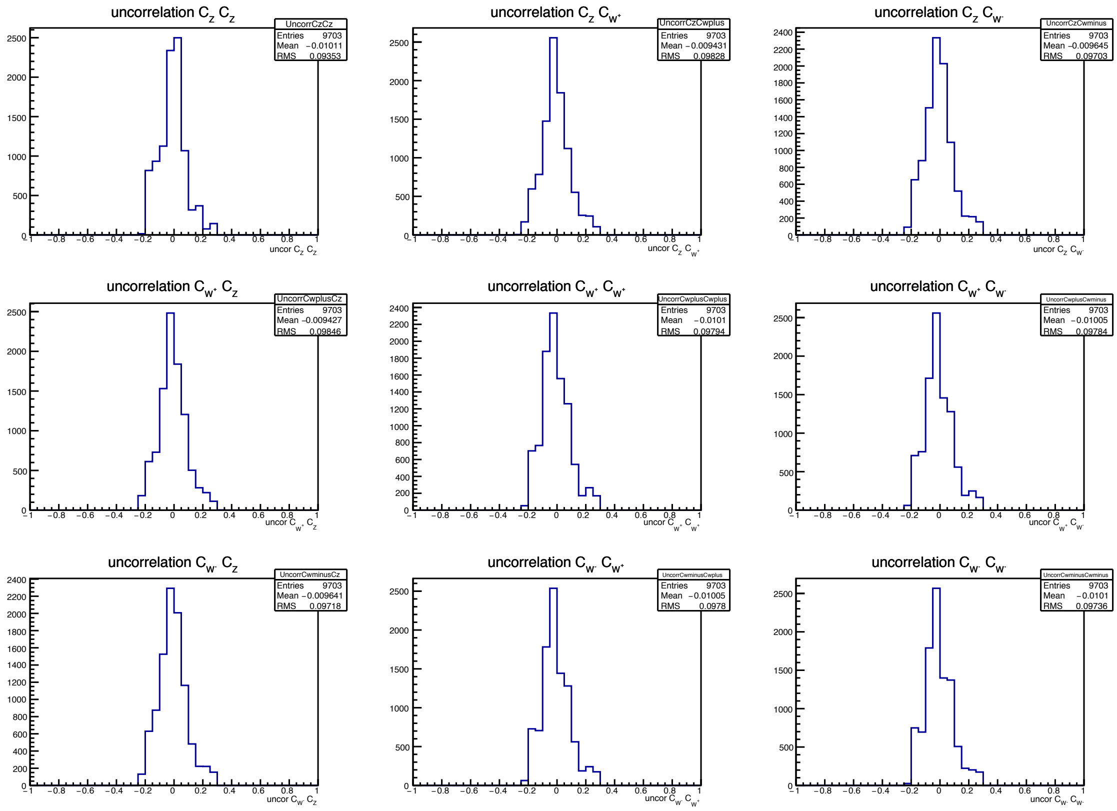

Figure B.1: All correlation of C factors in case of full decorrelation for all MC toys for electron identification source of systematics.

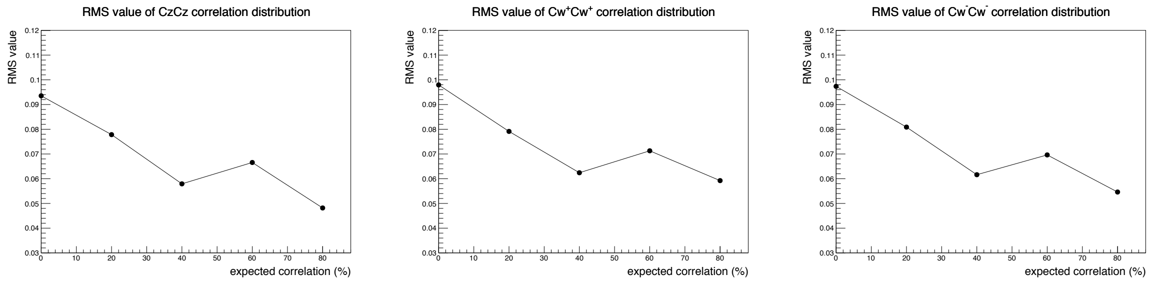

Figure B.2: $C_Z C_Z$ (left), $C_{W^+} C_{W^+}$ (middle), $C_{W^-} C_{W^-}$ (right) RMS as a function of number of correlated toys for electron identification systematics source.

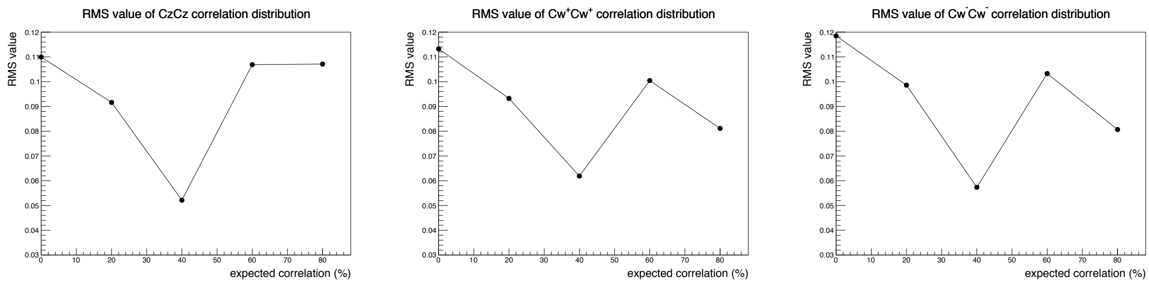

Figure B.3: $C_Z C_Z$ (left), $C_{W^+} C_{W^+}$ (middle), $C_{W^-} C_{W^-}$ (right) RMS as a function of number of correlated toys for electron trigger systematics source.

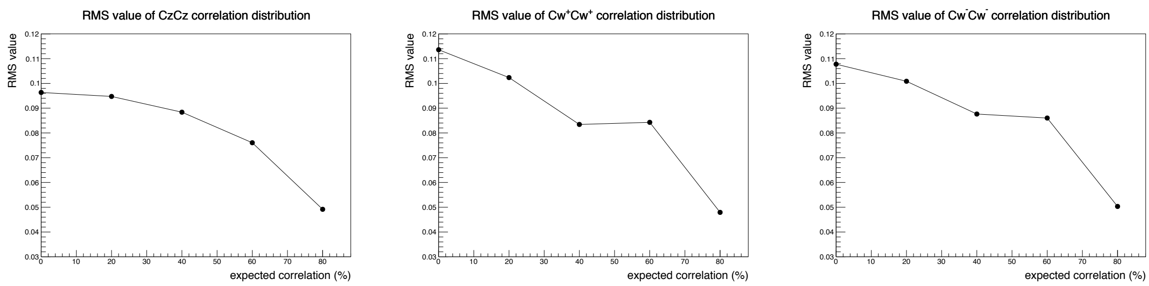

Figure B.4: $C_Z C_Z$ (left), $C_{W^+} C_{W^+}$ (middle), $C_{W^-} C_{W^-}$ (right) RMS as a function of number of correlated toys for muon trigger systematics source.

Appendix C

Details on the uncertainties used in the W and Z combination

Table C.1 contains nuisance parameters and symmetrized shifts of the C_W and C_Z factors for the inclusive combination. The names ended with `"__1_nui_0"` up to `"__1_nui_n-2"`, where `n` is a number of nuisance parameters for a given systematic source, represent fully correlated components, and names ended with `"__1_nui_n-1"` represent fully uncorrelated components.

Source	C_{Zmm} %	C_{Wmm} %	C_{Wmp} %	C_{Zee} %	C_{Wem} %	C_{Wep} %
ChargeIDZ	0			-0.15		
Charge_MisID_1					0.1	0.1
EG_RESOLUTION_ALL__1				-0.015	-0.0445	-0.0495
EG_SCALE_ALL__1				0.225	0.398	0.445
EL_EFF_ID_COMBMCTOY__1_nui_0				0.454	0.303	0.323
EL_EFF_ID_COMBMCTOY__1_nui_1				0.152	0.013	-0.013
EL_EFF_ID_COMBMCTOY__1_nui_2				0.038	-0.012	0.005
EL_EFF_Iso_COMBMCTOY__1_nui_0				0.27	0.131	0.142
EL_EFF_Iso_COMBMCTOY__1_nui_1				0.103	0.003	-0.007
EL_EFF_Iso_COMBMCTOY__1_nui_2				0.016	-0.01	0.004
EL_EFF_Reco_TotalCorrUncertainty__1				0.765	0.438	0.469
EL_EFF_Trig_COMBMCTOY__1_nui_0				0.041	0.288	0.308
EL_EFF_Trig_COMBMCTOY__1_nui_1				-0.022	-0.031	0.017
EL_EFF_Trig_COMBMCTOY__1_nui_2				0.019	0	0
JET_GroupedNP_1__1		-1.291	-1.2965		-1.421	-1.3865
JET_GroupedNP_2__1		-0.2115	-0.215		-0.231	-0.232
JET_GroupedNP_3__1		-0.888	-0.9625		-0.9245	-0.9675
JET_JER_SINGLE_NP__1		0.345	0.318		0.326	0.343
MET_SoftTrk_ResoPara		0.0855	0.1015		0.0805	0.0865
MET_SoftTrk_ResoPerp		0.0875	0.106		0.0785	0.0925
MET_SoftTrk_Scale__1		-0.095	-0.11		-0.0615	-0.073
MUONS_ID__1	-0.02	-0.0125	-0.0055			
MUONS_MS__1	-0.005	-0.0055	0.001			
MUONS_SCALE__1	-0.065	-0.128	-0.1445			
MUON_EFF_STAT__1	0.61	0.265	0.2635			
MUON_EFF_SYS__1	0.64	0.269	0.28			
MUON_EFF_TrigStatTOYUncertainty__1_nui_0	0.093	0.192	0.193			
MUON_EFF_TrigStatTOYUncertainty__1_nui_1	-0.025	-0.016	0.01			
MUON_EFF_TrigStatTOYUncertainty__1_nui_2	0.027	-0.002	0.001			
MUON_EFF_TrigSystUncertainty__1	0.17	0.5325	0.5415			
MUON_ISO_STAT__1	0.485	0.2595	0.2645			
MUON_ISO_SYS__1	0.215	0.1205	0.123			
MuTrigCharge		-0.25	0.25			
PDF	0.015	0.12	0.09	0.11	0.11	0.1
PILEUP_W__1	0.01	-0.22	-0.23	0.01	-0.36	-0.31
BgEWKLumi	0.01			0.01		
DiBosZ	0.01			0.01		
MJ_FitRegion_We_nui_0					2.806	1.545
MJ_FitRegion_We_nui_1					0.733	-0.779
MJ_FitRegion_Wm		0.5739	0.4422			
MJ_IsoChoice_We					1.21	0.515
MJ_IsoChoice_Wm		0.6782	0.5226			
MJ_PtVarMET_We_nui_0					-0.201	-0.384
MJ_PtVarMET_We_nui_1					-0.333	0.102
MJ_PtVarMET_Wm_nui_0		0.295	0.225			
MJ_PtVarMET_Wm_nui_1		0.216	-0.169			
MJ_PtVarMTW_We					0.256	0.251
MJ_PtVarMTW_Wm_nui_0		0.087	0.067			
MJ_PtVarMTW_Wm_nui_1		0.057	-0.045			
MJ_TopoEtMET_We_nui_0					-0.331	-0.607
MJ_TopoEtMET_We_nui_1					-0.606	0.194
MJ_TopoEtMET_Wm_nui_0		0.324	0.249			
MJ_TopoEtMET_Wm_nui_1		0.168	-0.131			
MJ_TopoEtMTW_We_nui_0					-0.308	-0.264
MJ_TopoEtMTW_We_nui_1					-0.136	0.093
MJ_TopoEtMTW_Wm_nui_0		0.137	0.105			
MJ_TopoEtMTW_Wm_nui_1		0.075	-0.059			
MultijetSigShape		0.2594	0.3199		0.549	0.42
Top		0.08356	0.06439		0.0844	0.0692
TopZ	0.02			0.02		
WBosZ	0			0		
Wtau		0.1342	0.1034		0.0938	0.0897
ZTauZ	0			0		
Zee					0.0654	0.0525
Zmumu		0.3079	0.2373			
Ztautau		0.01543	0.01189		0.0141	0.0111

Table C.1: Nuisance parameters and symmetrized shifts of the C_W C_Z factors for the inclusive combination.

Appendix D

Details on the uncertainties used in the $t\bar{t}$ and Z combination

Table D.1 presents the statistical, systematic and total uncertainties on the measured total cross-sections of $Z \rightarrow ee$, $Z \rightarrow \mu\mu$ and $t\bar{t}$ at $\sqrt{s} = 13, 8, 7$ TeV. The uncertainty names ended with `"__1_nui_0"` up to `"__1_nui_n-2"`, where `n` is a number of nuisance parameters for a given systematic source, represent fully correlated components, and names ended with `"__1_nui_n-1"` represent fully uncorrelated components.

Uncertainty	$\sigma^{tot}_{Z\to\mu\mu}$ (13 TeV), %	$\sigma^{tot}_{Z\to ee}$ (13 TeV), %	$\sigma^{tot}_{t\bar{t}}$ (13 TeV), %	$\sigma^{tot}_{Z\to\mu\mu}$ (8 TeV), %	$\sigma^{tot}_{Z\to ee}$ (8 TeV), %	$\sigma^{tot}_{t\bar{t}}$ (8 TeV), %	$\sigma^{tot}_{Z\to\mu\mu}$ (7 TeV), %	$\sigma^{tot}_{Z\to ee}$ (7 TeV), %	$\sigma^{tot}_{t\bar{t}}$ (7 TeV), %
ACoef				0	−0.065				
Angular_Resolution				0	−0.003				
Az	1.773 51	1.773 51		1.717 48	1.717 48		1.782 88	1.782 88	
BTAG						−0.391			−0.41
BTAG1			−0.29						
BTAG2			0.07						
BTAG3			0.1						
BTAG4			−0.01						
BTAG5			0						
BTAG6			0						
CTAG						0.016			0.027
CTAG1			0.04						
CTAG2			−0.02						
CTAG3			0						
CTAG4			0						
ChargeIDZ	0	−0.15							
DLumi13TeV	2.1	2.1	2.31						
DLumi7TeV							1.8	1.8	1.98
DLumi8TeV				1.9	1.9	2.1			
Di_Trig				−0.038					
EBEAM	0.69	0.69	1.5	0.62	0.62	1.72	0.6	0.6	1.79
EG_RESOLUTION_ALL__1		−0.025	−0.01		−0.002	−0.008			−0.022
EG_SCALE_ALL__1		0.245	0.2		0.025	0.51			0.213
EL_EFF_ID_COMBMCTOY__1_nui_0		−0.363	−0.32						
EL_EFF_ID_COMBMCTOY__1_nui_1		0.112	−0.115						
EL_EFF_ID_Z7TeV								0.163	
EL_EFF_ID_Z8TeV					0.798				
EL_EFF_ID_ttbar						0.403			0.087
EL_EFF_Iso_COMBMCTOY__1		0.14			0				
EL_EFF_Isott13TeV			0.39						
EL_EFF_Isott7TeV									0.59
EL_EFF_Isott8TeV						0.3			
EL_EFF_Reco_COMBMCTOY__1_nui_0		−0.047	−0.034						
EL_EFF_Reco_COMBMCTOY__1_nui_1		0.017	−0.021						
EL_EFF_Reco_Z7TeV								0.205	
EL_EFF_Reco_Z8TeV					0.087				
EL_EFF_Reco_ttbar						0.045			0.098
EL_EFF_Trig_COMBMCTOY__1		0.01	0.14		0.194			0.045	
EleScaleLArCalib					0.022			0.019	
EleScaleLArElecUnconv					0.039			0.036	
EleScaleMatCalo					−0.008			−0.008	
EleScaleMatCryo					−0.038			−0.036	
EleScaleMatID					−0.016			−0.016	
EleScalePS					0.016			0.018	
EleScaleS12					0.01			0.011	
ElecEnL1Gain					0			0.003	
ElecEnL2Gain					0.026			0.026	
ElecEnLArElecCalib					−0.004			−0.004	
ElecEn_G4								−0.004	
ElecEn_Pedestal								0.008	
ElecEn_SamplingTerm								0.009	
ElecEn_ZeeStat								0.018	
ElecEn_ZeeSyst								0.026	
Extrap_ME							−0.036	−0.002	
Extrap_PS							−0.029	−0.028	
Extrap_uncor							0.09	0.069	
FLOSR			0.52			0.247			0.268
FLSTAT1			0.16						
FLSTAT1_7TeV									0.213
FLSTAT1_8TeV						0.091			
FLSTAT2			0.03						
FLSTAT2_7TeV									0.027
FLSTAT2_8TeV						0.012			
GENIFSR			−0.4			−0.202			−0.301
GENTT			0.84			1.218			1.432
GENVV			−0.09			−0.128			−0.115
GENWIFSR			−0.21						
GENWT			−0.14			−0.37			−0.159
Generator				0	0				
HADRTT			−2.8						
JEFF						−0.016			0
JESBJET						−0.025			−0.044
JESCBY						0			0.055
JESDET1						0.041			0.011
JESDET2						0.012			−0.005
JESDET3						0.033			0
JESFCMP						0.317			0.213
JESFRES						0.181			0.115
JESFWD						0.128			0.027
JESFWDS						0.045			0.005
JESMIX1						0.008			−0.005
JESMIX2						0.033			0.005
JESMODE1						0.226			0.044
JESMODE2						−0.029			0.005
JESMODE3						0.025			0
JESMODE4						0.008			0
JESPMU						0.041			0.027
JESPT						0.016			0
JESPV						0.103			−0.022
JESRHO						0.173			0
JESSNGL						−0.016			0
JESSTAT1_7TeV									0.022
JESSTAT1_8TeV						0.049			
JESSTAT2_7TeV									0
JESSTAT2_8TeV						−0.016			
JESSTAT3_7TeV									−0.005
JESSTAT3_8TeV						0.037			
JET_19NP_JET_BJES_Response			−0.02						
JET_19NP_JET_EffectiveNP_1			−0.22						
JET_19NP_JET_EffectiveNP_2			0.02						
JET_19NP_JET_EffectiveNP_3			−0.01						
JET_19NP_JET_EffectiveNP_4			−0.01						
JET_19NP_JET_EffectiveNP_5			0.01						
JET_19NP_JET_EffectiveNP_6restTerm			−0.01						
JET_19NP_JET_EtaIntercalibration_Modelling			−0.04						
JET_19NP_JET_EtaIntercalibration_TotalStat			−0.03						
JET_19NP_JET_Flavor_Composition			−0.17						
JET_19NP_JET_Flavor_Response			0.1						
JET_19NP_JET_GroupedNP_1			−0.08						
JET_19NP_JET_Pileup_OffsetMu			0.08						
JET_19NP_JET_Pileup_OffsetNPV			0.08						
JET_19NP_JET_Pileup_PtTerm			0						
JET_19NP_JET_Pileup_RhoTopology			−0.07						
JET_19NP_JET_PunchThrough_MC15			0						
JET_19NP_JET_SingleParticle_HighPt			0						
JET_JER_SINGLE_NP__1			−0.16			−0.506			−0.301
JVF						−0.025			−0.06
LArUnconvCalib					−0.008			−0.008	
LEPTR						−0.165			−0.186
MCStatZ7TeV							0.023	0.038	
MCStatZ8TeV				0	0.011				
MISTAG						0.021			0.022
MISTAG1			0.05						
MISTAG10			0						
MISTAG11			0						
MISTAG12			0						
MISTAG2			0						
MISTAG3			0						
MISTAG4			0						
MISTAG5			0						
MISTAG6			0						
MISTAG7			0						
MISTAG8			0						
MISTAG9			0						
MUONS_ID__1	−0.005		−0.01	−0.003		−0.004	−0.001		0
MUONS_MS__1	−0.005		0	−0.004		−0.004	−0.003		0
MUONS_SCALE__1	−0.055		−0.04	−0.034		−0.012	−0.028		−0.142
MUON_EFF_ISO__1	0.41			0.036			0.147		
MUON_EFF_ISOtt13TeV			0.27						
MUON_EFF_ISOtt7TeV									0.437
MUON_EFF_ISOtt8TeV						0.218			
MUON_EFF_Rec_Z7TeV							0.303		
MUON_EFF_Rec_Z8TeV				0.449					
MUON_EFF_Rec__1	0.68		0.44						
MUON_EFF_Reco_ttbar						0.42			0.306
MUON_EFF_SingleTrig__1	0.12		0.05	0.545			0.049		
MUON_TTVA__1	0			0.054					
Mass_shape				0	0				
NSTTSYS			−0.3			−0.214			−0.213
PDFNNPDF30_nlo_as_0118_eigenset	0.02	0.1		0.038	0.02		0.069	0.09	
PDFtt			0.48			1.128			1.044
PILEUP_W__1	0.01	0.01		0.008	0.024				
R32			−0.39						
RZMSYS			0.15			0.021			0.049
SCALTT						−0.3			−0.301
TheoryME							−0.037	−0.027	
TheoryPS							−0.224	−0.18	
Unfolding				0	0				
WTDRS			−0.62			−0.152			−0.213
XSVV			0.02			0.029			0.027
XSWT			0.52			0.687			0.722
ZPTMismodel	−0.03	−0.07		−0.003	−0.004		−0.035	−0.006	
Zvtx				0	0				
BgEWKLumi	0.01	0.01		0.01	0.013				
BkgEWStat				0	0			0.002	
BkgEWSystgg				0.029	0.029				
DiBosZ	0.01	0.01		0.005	0.005		0.008	0.009	
MJBkg	0.05	0.05		0.032	0.138		0.069	0.028	
SingleTopZ				0.001	0.001				
TopZ	0.02	0.02		0.008	0.01		0.007	0.008	
WBosZ	0	0		0.002	0.014		0	0	
ZTauZ	0	0		0.004	0.005		0.003	0.003	
tWt							0.001		
Total Systematics	2.95	2.88	4.32	2.73	2.77	3.53	2.64	2.63	3.51
Stat	0.08	0.09	0.92	0.03	0.04	0.71	0.08	0.10	1.69
Total	2.95	2.88	4.42	2.73	2.77	3.60	2.64	2.63	3.89

Table D.1: Summary of the statistical, systematic and total uncertainties on the total cross-section measurements of $Z \to ee$, $Z \to \mu\mu$ and $t\bar{t}$ at $\sqrt{s} = 13, 8, 7$ TeV.

Appendix E

Kinematic distributions for 50 ns bunch spacing data

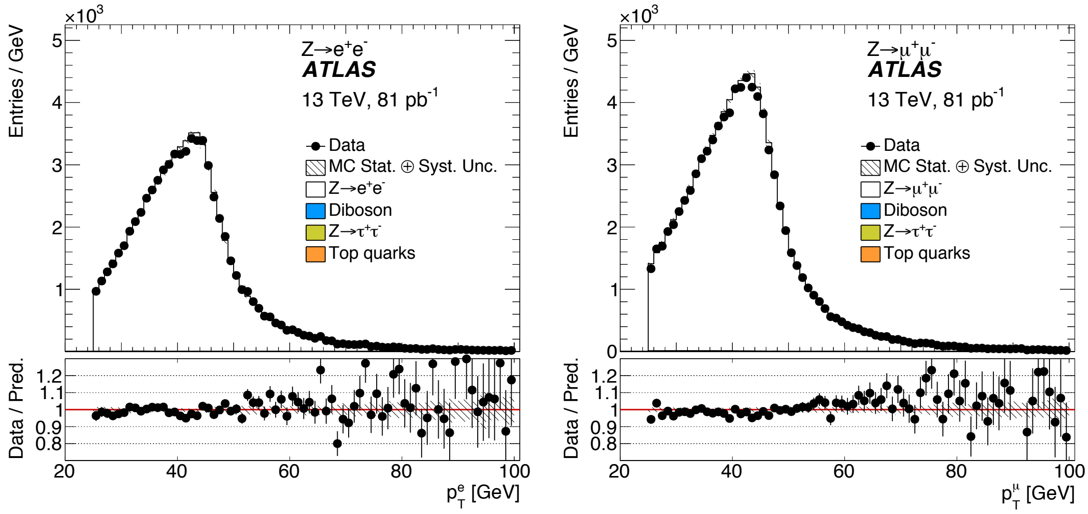

Figure E.1: Lepton transverse momentum distributions from the $Z \to e^+e^-$ selection (left) and the $Z \to \mu^+\mu^-$ selection (right). Systematic uncertainties for the signal and background distributions are combined in the shaded band, and statistical uncertainties are shown on the data points. Luminosity uncertainties are not included. There are two lepton entries in the histogram for each candidate event.

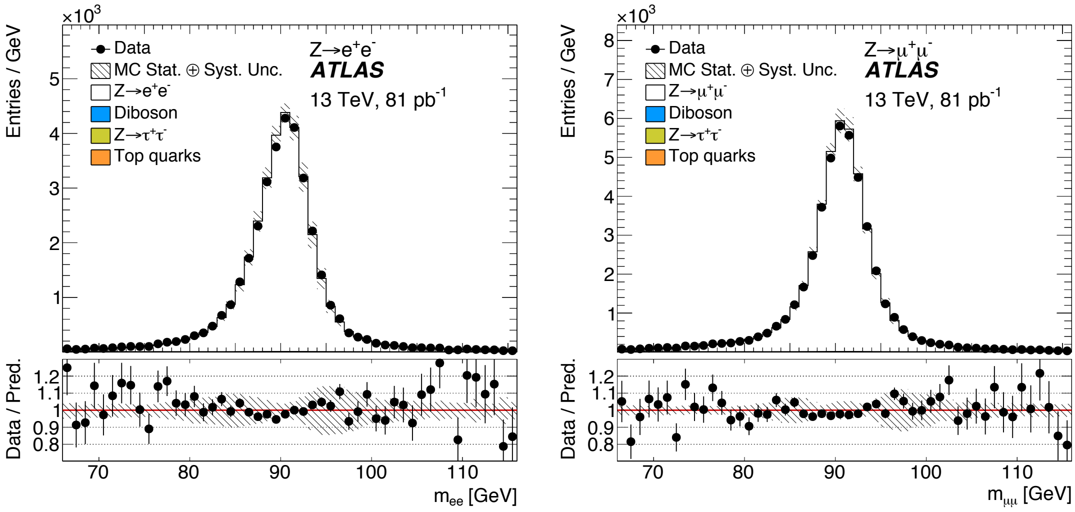

Figure E.2: Dilepton mass distribution after the $Z \rightarrow e^+e^-$ selection (left) and the $Z \rightarrow \mu^+\mu^-$ selection (right). Systematic uncertainties for the signal and background distributions are combined in the shaded band, and statistical uncertainties are shown on the data points. Luminosity uncertainties are not included.

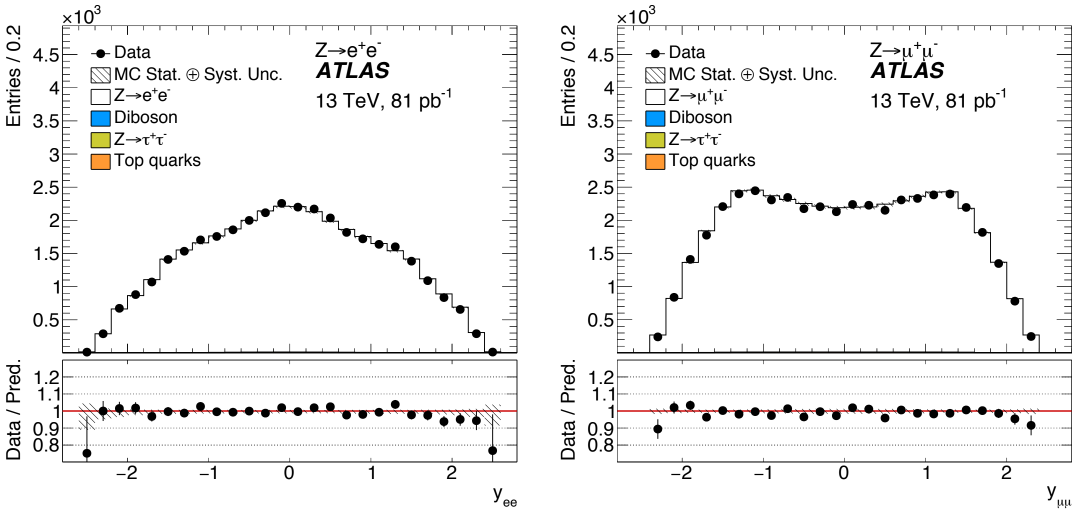

Figure E.3: Z boson rapidity distribution after the $Z \rightarrow e^+e^-$ selection (left) and the $Z \rightarrow \mu^+\mu^-$ selection (right). Systematic uncertainties for the signal and background distributions are combined in the shaded band, and statistical uncertainties are shown on the data points. Luminosity uncertainties are not included.

Appendix F

W/Z ratio results for the electron and muon channels separately

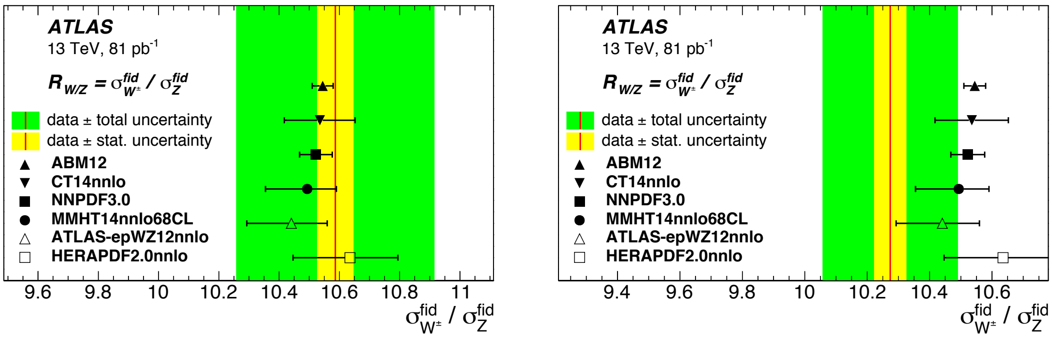

Figure F.1: Ratio of $W^{\pm}$ to Z-boson production fiducial cross sections in electron (left) and muon (right) channel compared to predictions based on different PDF sets. The inner shaded band corresponds to statistical uncertainty while the outer band shows statistical and systematic uncertainties added in quadrature. The theory predictions are given with the corresponding PDF uncertainties shown as error bands. Scale uncertainties are not included in the error bands.

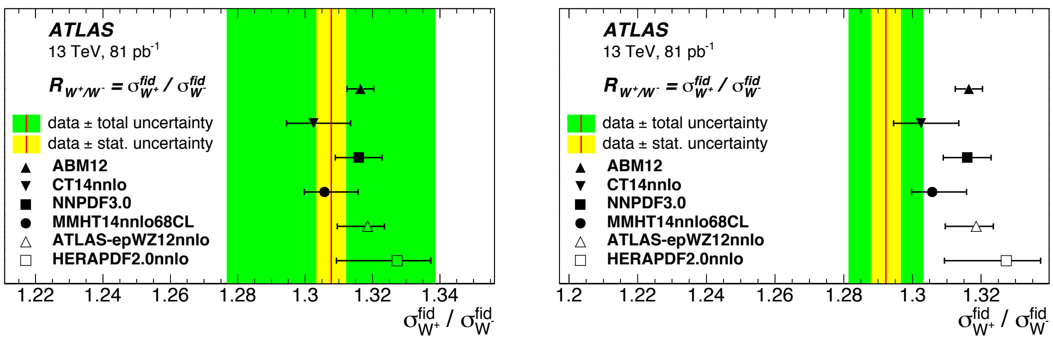

Figure F.2: Ratio of W^+ to W-boson production fiducial cross sections in electron (left) and muon (right) channel compared to predictions based on different PDF sets. The inner shaded band corresponds to statistical uncertainty while the outer band shows statistical and systematic uncertainties added in quadrature. The theory predictions are given with the corresponding PDF uncertainties shown as error bands. Scale uncertainties are not included in the error bands.

Appendix G

All combined cross sections

Combined $Z \rightarrow ee$ and $Z \rightarrow \mu\mu$ cross-sections obtained for each ratio measurement as well as for simultaneous combunation all cross-section measurements (also called as "grand combination") are shown in Table G.1. The $\chi^2/N_{d.f.}$ values of each combination are given in Sections 9.4, 10.3.2, 10.3.3. All the central values of combined cross sections at differnt types of measurements agree with each other within the statistical precision as well as all sources of uncertainties. Such compartibility shows the good stability of the combination method which was performed using the HERAverager [70, 164] software.

Combination type	$\sigma_{comb}^{Z\ fid}$(7 TeV) value ± stat ± syst ± lumi	$\sigma_{comb}^{Z\ fid}$(8 TeV) value ± stat ± syst ± lumi	$\sigma_{comb}^{Z\ fid}$(13 TeV) value ± stat ± syst ± lumi	$\sigma_{comb}^{t\bar{t}\ tot}$(7 TeV) value ± stat ± syst ± lumi	$\sigma_{comb}^{t\bar{t}\ tot}$(8 TeV) value ± stat ± syst ± lumi	$\sigma_{comb}^{t\bar{t}\ tot}$(13 TeV) value ± stat ± syst ± lumi
Single ratios						
Z(13 TeV)/Z(8 TeV)	—	$505.8 \pm 0.1 \pm 4.2 \pm 9.6$	$777.1 \pm 0.5 \pm 6.4 \pm 16.3$	—	—	—
Z(13 TeV)/Z(7 TeV)	$450.8 \pm 0.3 \pm 3.1 \pm 8.1$	—	$777.3 \pm 0.5 \pm 6.3 \pm 16.3$	—	—	—
Z(8 TeV)/Z(7 TeV)	$450.8 \pm 0.3 \pm 3.1 \pm 8.1$	$505.8 \pm 0.1 \pm 4.2 \pm 9.6$	—	—	—	—
$t\bar{t}/t\bar{t}$(13/8 TeV)	—	—	—	—	$242.9 \pm 1.7 \pm 6.9 \pm 5.1$	$817.5 \pm 7.5 \pm 29.8 \pm 18.9$
$t\bar{t}/t\bar{t}$(13/7 TeV)	—	—	—	$182.9 \pm 3.1 \pm 5.3 \pm 3.6$	—	$817.5 \pm 7.5 \pm 29.8 \pm 18.9$
$t\bar{t}/t\bar{t}$(8/7 TeV)	—	—	—	$182.9 \pm 3.1 \pm 5.3 \pm 3.6$	$242.9 \pm 1.7 \pm 6.9 \pm 5.1$	—
Double ratios						
$t\bar{t}/Z$(13/8 TeV)	—	$505.6 \pm 0.1 \pm 4.2 \pm 9.6$	$777.1 \pm 0.5 \pm 6.3 \pm 16.3$	—	$242.7 \pm 1.7 \pm 6.9 \pm 5.1$	$818.0 \pm 7.5 \pm 29.8 \pm 18.9$
$t\bar{t}/Z$(13/7 TeV)	$450.8 \pm 0.3 \pm 3.1 \pm 8.1$	—	$777.2 \pm 0.5 \pm 6.3 \pm 16.3$	$182.9 \pm 3.1 \pm 6.4 \pm 3.6$	—	$817.9 \pm 7.5 \pm 29.8 \pm 18.9$
$t\bar{t}/Z$(8/7 TeV)	$450.7 \pm 0.3 \pm 3.1 \pm 8.1$	$505.7 \pm 0.1 \pm 4.2 \pm 9.6$	—	$182.9 \pm 3.1 \pm 6.4 \pm 3.6$	$242.9 \pm 1.7 \pm 6.9 \pm 5.1$	—
Grand Combination	$450.7 \pm 0.3 \pm 3.1 \pm 8.1$	$505.8 \pm 0.1 \pm 4.2 \pm 9.6$	$777.3 \pm 0.5 \pm 6.3 \pm 16.3$	$182.9 \pm 3.1 \pm 6.4 \pm 3.6$	$242.8 \pm 1.7 \pm 6.9 \pm 5.1$	$818.0 \pm 7.5 \pm 29.8 \pm 18.9$

Table G.1: Summary of the combined fiducial $Z \to ee$ and $Z \to \mu\mu$ cross-sections at different cross-section ratio calculations. The cross-section ratios are shown with absolute values of statistical, systematic, and luminosity uncertainties.

Appendix H

Systematic sources decorrelation

To estimate influence of possible changes in correlation model (Table 9.1) on single $\sigma_{t\bar{t}}^{8\text{ TeV}}/\sigma_{t\bar{t}}^{7\text{ TeV}}$ and double $\frac{\sigma_{t\bar{t}}^{8\text{ TeV}}}{\sigma_{Z}^{8\text{ TeV}}}/\frac{\sigma_{t\bar{t}}^{7\text{ TeV}}}{\sigma_{Z}^{7\text{ TeV}}}$ ratios, de-correlations for some systematic sources were performed. Jet energy scale, flavour tagging, signal modelling and beam energy were taken as uncorrelated. Table H.1 contains numerical evolution of the discrepancy (in terms of number of standard deviations σ) between experimental result (with total experimental uncertainty) and predicted result based on CT14 PDF set.

Signal modelling (incl. PDF), beam energy, jet energy scale and flavour tagging (placed in descending order) have the strongest influence for decreasing disagreement of measured and predicted central values within the total experimental uncertainty. De-correlation of jet energy scale, flavour tagging and signal modelling (incl. PDF) together gives 1.7σ discrepancy for single ratio and 2σ for double ratio. De-correlation of beam energy and signal modelling (incl. PDF) provides the smallest discrepancy, 1.5σ for single ratio and 1.9σ for double ratio.

	$\sigma_{t\bar{t}}^{8\text{ TeV}}/\sigma_{t\bar{t}}^{7\text{ TeV}}$		$\frac{\sigma_{t\bar{t}}^{8\text{ TeV}}}{\sigma_{Z}^{8\text{ TeV}}}/\frac{\sigma_{t\bar{t}}^{7\text{ TeV}}}{\sigma_{Z}^{7\text{ TeV}}}$	
Uncorrelated systematic source	**ratio (value ± stat ± syst ± lumi)**	**N of σ from CT14**	**ratio (value ± stat ± syst ± lumi)**	**N of σ from CT14**
Lepton trigger	1.328 ± 0.024(1.83%) ± 0.015(1.14%) ± 0.038(2.89%)	2.047	1.184 ± 0.022(1.83%) ± 0.015(1.30%) ± 0.003(0.24%)	3.098
Muon reco and ID	1.328 ± 0.024(1.83%) ± 0.016(1.23%) ± 0.038(2.89%)	2.033	1.184 ± 0.022(1.83%) ± 0.016(1.36%) ± 0.003(0.28%)	3.033
Muon momentum scale	1.328 ± 0.024(1.83%) ± 0.015(1.11%) ± 0.038(2.89%)	2.047	1.184 ± 0.022(1.83%) ± 0.015(1.27%) ± 0.003(0.26%)	3.098
All muon systematics	1.328 ± 0.024(1.83%) ± 0.017(1.26%) ± 0.038(2.89%)	2.019	1.184 ± 0.022(1.83%) ± 0.016(1.39%) ± 0.003(0.25%)	3.033
Electron reco and ID	1.328 ± 0.024(1.83%) ± 0.015(1.14%) ± 0.038(2.89%)	2.047	1.184 ± 0.022(1.83%) ± 0.015(1.30%) ± 0.003(0.27%)	3.098
Electron energy scale	1.328 ± 0.024(1.83%) ± 0.016(1.20%) ± 0.038(2.89%)	2.033	1.184 ± 0.022(1.83%) ± 0.016(1.34%) ± 0.003(0.27%)	3.033
All electron systematics	1.328 ± 0.024(1.83%) ± 0.017(1.27%) ± 0.038(2.89%)	2.019	1.184 ± 0.022(1.83%) ± 0.017(1.40%) ± 0.003(0.27%)	2.968
Jet energy scale	1.328 ± 0.024(1.83%) ± 0.018(1.33%) ± 0.038(2.89%)	2.004	1.184 ± 0.022(1.83%) ± 0.017(1.45%) ± 0.003(0.26%)	2.968
Flavour tagging	1.328 ± 0.024(1.83%) ± 0.017(1.25%) ± 0.038(2.89%)	2.019	1.184 ± 0.022(1.83%) ± 0.016(1.39%) ± 0.003(0.28%)	3.033
Signal modelling (incl. PDF)	1.328 ± 0.024(1.83%) ± 0.036(2.69%) ± 0.038(2.89%)	1.685	1.184 ± 0.022(1.83%) ± 0.033(2.76%) ± 0.005(0.46%)	2.087
Beam energy	1.328 ± 0.024(1.83%) ± 0.036(2.70%) ± 0.038(2.89%)	1.685	1.184 ± 0.022(1.83%) ± 0.024(2.06%) ± 0.002(0.13%)	2.539
Jet energy scale and flavour tagging	1.328 ± 0.024(1.83%) ± 0.019(1.44%) ± 0.038(2.89%)	1.988	1.184 ± 0.022(1.83%) ± 0.018(1.56%) ± 0.003(0.25%)	2.904
All lepton systematics, jet energy scale and flavour tagging	1.328 ± 0.024(1.83%) ± 0.022(1.64%) ± 0.038(2.89%)	1.939	1.184 ± 0.022(1.83%) ± 0.021(1.75%) ± 0.003(0.26%)	2.716
Jet energy scale, flavour tagging, signal modelling (incl. PDF)	1.328 ± 0.024(1.83%) ± 0.038(2.88%) ± 0.038(2.89%)	1.648	1.184 ± 0.022(1.83%) ± 0.035(2.94%) ± 0.004(0.34%)	2.002
Beam energy and signal modelling (incl. PDF)	1.328 ± 0.024(1.83%) ± 0.049(3.69%) ± 0.038(2.89%)	1.459	1.184 ± 0.022(1.83%) ± 0.038(3.20%) ± 0.006(0.48%)	1.886

Table H.1: Decorrelation effect of the $t\bar{t}$ at 7 and 8 TeV systematic sources on single $\sigma_{t\bar{t}}^{8\text{ TeV}}/\sigma_{t\bar{t}}^{7\text{ TeV}}$and double $\frac{\sigma_{t\bar{t}}^{8\text{ TeV}}}{\sigma_{Z}^{8\text{ TeV}}}/\frac{\sigma_{t\bar{t}}^{7\text{ TeV}}}{\sigma_{Z}^{7\text{ TeV}}}$ ratios. Obtained cross section ratios and its total uncertainties compared to predictions based on CT14 PDF set in terms of number of standard deviations from prediction.

Appendix I

Correlation ellipse details

To compare measured electron to muon channel cross section ratios simultaneously to the Standard Model prediction as well as PDG values, the covariance matrix of the measured R_W and R_Z was constructed:

$$\Sigma = \begin{pmatrix} c_{11} & c_{12} \\ c_{21} & c_{22} \end{pmatrix} = \begin{pmatrix} \delta^2_{R_W} & \rho_{R_W R_Z}\delta_{R_W}\delta_{R_Z} \\ \rho_{R_W R_Z}\delta_{R_W}\delta_{R_Z} & \delta^2_{R_Z} \end{pmatrix}, \tag{I.1}$$

where $\delta_{R_{W(Z)}}$ the total statistical and systematic uncertainty in the ratio $R_{W(Z)}$ and $\rho_{R_W R_Z}$ is the correlation coefficient between the R_W and R_Z measurements. The correlation coefficient

$$\rho_{R_W R_Z} = \frac{cov[R_W R_Z]}{\delta_{R_W}\delta_{R_Z}} \tag{I.2}$$

is determined using the statistic and full list of systematic uncertainties for both R_W and R_Z measurements and found to be 0.27. The elements of the covariance matrix I.1 and the central values of R_W, R_Z can be used for construction of the uncertainty ellipse. The lengths of the ellipse axes defined as the square root of the eigenvalues of the covariance matrix obtained as 0.029 and 0.015. The angle θ of the major axis of the ellipse is given by

$$\theta = \frac{1}{2}\arctan\frac{2c_{12}}{c_{11}c_{22}} \tag{I.3}$$

and found to be -0.21 rad. It helps represent visually the level and sign of correlation among R_W and R_Z measurements.

Appendix J

Detailed breakdown of uncertainties on $t\bar{t}/Z$ ratios

Uncertainty	$\sigma^{\text{tot}}_{Z\to\mu\mu}$(13 TeV), [%]	$\sigma^{\text{tot}}_{Z\to ee}$(13 TeV), [%]	$\sigma^{\text{tot}}_{t\bar{t}}$(13 TeV) , [%]	$R_{t\bar{t}(\text{tot 13 TeV})/Z(\text{tot 13 TeV})}$
BTAG1			−0.29	−0.29
BTAG2			0.07	0.07
BTAG3			0.1	0.10
BTAG4			−0.01	−0.01
BTAG5			0	0.00
BTAG6			0	0.00
CTAG1			0.04	0.04
CTAG2			−0.02	−0.02
CTAG3			0	0.00
CTAG4			0	0.00
ChargeIDZ	0	−0.15		0.08
DLUMI_13TeV	2.1	2.1	2.31	0.21
EBEAM	0.69	0.69	1.5	0.81
EG_RESOLUTION_ALL__1		−0.025	−0.01	0.00
EG_SCALE_ALL__1		0.245	0.2	0.08
EL_EFF_ID_COMBMCTOY__1_nui_0		−0.363	−0.32	−0.14
EL_EFF_ID_COMBMCTOY__1_nui_1		0.112	−0.115	−0.17
EL_EFF_Iso_COMBMCTOY__1		0.14		−0.07
EL_EFF_Isott13TeV			0.39	0.39
EL_EFF_Reco_COMBMCTOY__1_nui_0		−0.047	−0.034	−0.01
EL_EFF_Reco_COMBMCTOY__1_nui_1		0.017	−0.021	−0.03
EL_EFF_Trig_COMBMCTOY__1		0.01	0.14	0.13
FLOSR			0.52	0.52
FLSTAT1			0.16	0.16
FLSTAT2			0.03	0.03
GENIFSR			−0.4	−0.40
GENTT			0.84	0.84
GENVV			−0.09	−0.09
GENWIFSR			−0.21	−0.21
GENWT			−0.14	−0.14
HADRTT			−2.8	−2.80
JET_19NP_JET_BJES_Response			−0.02	−0.02
JET_19NP_JET_EffectiveNP_1			−0.22	−0.22
JET_19NP_JET_EffectiveNP_2			0.02	0.02
JET_19NP_JET_EffectiveNP_3			−0.01	−0.01
JET_19NP_JET_EffectiveNP_4			−0.01	−0.01
JET_19NP_JET_EffectiveNP_5			0.01	0.01
JET_19NP_JET_EffectiveNP_6restTerm			−0.01	−0.01
JET_19NP_JET_EtaIntercalibration_Modelling			−0.04	−0.04
JET_19NP_JET_EtaIntercalibration_TotalStat			−0.03	−0.03
JET_19NP_JET_Flavor_Composition			−0.17	−0.17
JET_19NP_JET_Flavor_Response			0.1	0.10
JET_19NP_JET_GroupedNP_1			−0.08	−0.08
JET_19NP_JET_Pileup_OffsetMu			0.08	0.08
JET_19NP_JET_Pileup_OffsetNPV			0.08	0.08
JET_19NP_JET_Pileup_PtTerm			0	0.00
JET_19NP_JET_Pileup_RhoTopology			−0.07	−0.07
JET_19NP_JET_PunchThrough_MC15			0	0.00
JET_19NP_JET_SingleParticle_HighPt			0	0.00
JET_JER_SINGLE_NP__1			−0.16	−0.16
MISTAG1			0.05	0.05
MISTAG10			0	0.00
MISTAG11			0	0.00
MISTAG12			0	0.00
MISTAG2			0	0.00
MISTAG3			0	0.00
MISTAG4			0	0.00
MISTAG5			0	0.00
MISTAG6			0	0.00
MISTAG7			0	0.00
MISTAG8			0	0.00
MISTAG9			0	0.00
MUONS_ID__1	−0.005		−0.01	−0.01
MUONS_MS__1	−0.005		0	0.00
MUONS_SCALE__1	−0.055		−0.04	−0.01
MUON_EFF_ISOtt13TeV			0.27	0.27
MUON_EFF_STAT__1	0.33		0.19	0.03
MUON_EFF_SYS__1	0.59		0.4	0.11
MUON_EFF_TrigStatTOYUncertainty__1	0.03		0.05	0.04
MUON_EFF_TrigSystUncertainty__1	0.12		0.02	−0.04
MUON_ISO_STAT__1	0.07			−0.03
MUON_ISO_SYS__1	0.4			−0.20
MUON_TTVA_STAT__1	0			0.00
MUON_TTVA_SYS__1	0			0.00
NSTTSYS			−0.3	−0.30
PDFNNPDF30_nlo_as_0118_eigenset	0.02	0.1		−0.06
PDFtt			0.48	0.48
PILEUP_W__1	0.01	0.01		−0.01
R32			−0.39	−0.39
RZMSYS			0.15	0.15
WTDRS			−0.62	−0.62
XSVV			0.02	0.02
XSWT			0.52	0.52
ZPTMismodel	−0.03	−0.07		0.05
AZ	1.77	1.77		1.77
BgEWKLumi	0.01	0.01		−0.01
DiBosZ	0.01	0.01		−0.01
MJBkg	0.05	0.05		−0.05
TopZ	0.02	0.02		−0.02
WBosZ	0	0		0.00
ZTauZ	0	0		0.00
Total Systematics	2.95	2.88	4.32	3.83
Stat	0.08	0.09	0.92	0.92
Total	2.95	2.88	4.42	3.94

Table J.1: Summary of the statistical, systematic and total uncertainties on the $Z \to ee$, $Z \to \mu\mu$ and $t\bar{t}$ ($e\mu$ channel) total cross-section measurements, together with the corresponding uncertainties on the ratio for the $\sqrt{s} = 13$ TeV data. Values given in a single (different) row are considered to be 100% (0%) correlated. Values given as 0.0 are smaller than 0.05%.

Uncertainty	$\sigma^{\text{tot}}_{Z\to\mu\mu}$(8 TeV), [%]	$\sigma^{\text{tot}}_{Z\to ee}$(8 TeV), [%]	$\sigma^{\text{tot}}_{t\bar{t}}$(8 TeV), [%]	$R_{t\bar{t}(\text{tot 8 TeV})/Z(\text{tot 8 TeV})}$
ACoef	0	−0.065		0.03
Angular_Resolution	0	−0.003		0.00
BTAG			−0.391	−0.39
CTAG			0.016	0.02
DLUMI_8TeV	1.9	1.9	2.1	0.20
Di_Trig	−0.038			0.02
EBEAM	0.62	0.62	1.72	1.10
EG_RESOLUTION_ALL__1		−0.002	−0.008	−0.01
EG_SCALE_ALL__1		0.025	0.51	0.50
EL_EFF_ID_Z8TeV		0.798		−0.40
EL_EFF_ID_ttbar			0.403	0.40
EL_EFF_Iso_COMBMCTOY__1		0		0.00
EL_EFF_Isott8TeV			0.3	0.30
EL_EFF_Reco_Z8TeV		0.087		−0.04
EL_EFF_Reco_ttbar			0.045	0.05
EL_EFF_Trig_COMBMCTOY__1		0.194		−0.10
EleScaleLArCalib		0.022		−0.01
EleScaleLArElecUnconv		0.039		−0.02
EleScaleMatCalo		−0.008		0.00
EleScaleMatCryo		−0.038		0.02
EleScaleMatID		−0.016		0.01
EleScalePS		0.016		−0.01
EleScaleS12		0.01		−0.01
ElecEnL1Gain		0		0.00
ElecEnL2Gain		0.026		−0.01
ElecEnLArElecCalib		−0.004		0.00
FLOSR			0.247	0.25
FLSTAT1_8TeV			0.091	0.09
FLSTAT2_8TeV			0.012	0.01
GENIFSR			−0.202	−0.20
GENTT			1.218	1.22
GENVV			−0.128	−0.13
GENWT			−0.37	−0.37
Generator	0	0		0.00
JEFF			−0.016	−0.02
JESBJET			−0.025	−0.03
JESCBY			0	0.00
JESDET1			0.041	0.04
JESDET2			0.012	0.01
JESDET3			0.033	0.03
JESFCMP			0.317	0.32
JESFRES			0.181	0.18
JESFWD			0.128	0.13
JESFWDS			0.045	0.05
JESMIX1			0.008	0.01
JESMIX2			0.033	0.03
JESMODE1			0.226	0.23
JESMODE2			−0.029	−0.03
JESMODE3			0.025	0.03
JESMODE4			0.008	0.01
JESPMU			0.041	0.04
JESPT			0.016	0.02
JESPV			0.103	0.10
JESRHO			0.173	0.17
JESSNGL			−0.016	−0.02
JESSTAT1_8TeV			0.049	0.05
JESSTAT2_8TeV			−0.016	−0.02
JESSTAT3_8TeV			0.037	0.04
JET_JER_SINGLE_NP__1			−0.506	−0.51
JVF			−0.025	−0.03
LArUnconvCalib		−0.008		0.00
LEPTR			−0.165	−0.17
MCStatZ8TeV	0	0.011		−0.01
MISTAG			0.021	0.02
MUONS_ID__1	−0.003		−0.004	0.00
MUONS_MS__1	−0.004		−0.004	0.00
MUONS_SCALE__1	−0.034		−0.012	0.00
MUON_EFF_ISO__1	0.036			−0.02
MUON_EFF_ISOtt8TeV			0.218	0.22
MUON_EFF_Rec_Z8TeV	0.449			−0.22
MUON_EFF_Reco_ttbar			0.42	0.42
MUON_EFF_SingleTrig__1	0.545			−0.27
MUON_TTVA__1	0.054			−0.03
Mass_shape	0	0		0.00
NSTTSYS			−0.214	−0.21
PDFNNPDF30_nlo_as_0118_eigenset	0.038	0.02		−0.03
PDFtt			1.128	1.13
PILEUP_W__1	0.008	0.024		−0.02
RZMSYS			0.021	0.02
SCALTT			−0.3	−0.30
Unfolding	0	0		0.00
WTDRS			−0.152	−0.15
XSVV			0.029	0.03
XSWT			0.687	0.69
ZPTMismodel	−0.003	−0.004		0.00
Zvtx	0	0		0.00
AZ8TeV	1.72	1.72		1.72
BgEWKLumi	0.01	0.013		−0.01
BkgEWStat	0	0		0.00
BkgEWSystgg	0.029	0.029		−0.03
DiBosZ	0.005	0.005		−0.01
MJBkg	0.032	0.138		−0.09
SingleTopZ	0.001	0.001		0.00
TopZ	0.008	0.01		−0.01
WBosZ	0.002	0.014		−0.01
ZTauZ	0.004	0.005		0.00
Total Systematics	2.73	2.77	3.53	3.10
Stat	0.03	0.04	0.71	0.71
Total	2.73	2.77	3.60	3.18

Table J.2: Summary of the statistical, systematic and total uncertainties on the $\sigma^{\text{tot}}_{t\bar{t}}$(8 TeV) to σ^{tot}_{Z}(8 TeV) cross sections ratio for the measurement at $\sqrt{s} = 8$ TeV.

Uncertainty	$\sigma^{\text{tot}}_{Z\to\mu\mu}(7\text{ TeV}), [\%]$	$\sigma^{\text{tot}}_{Z\to ee}(7\text{ TeV}), [\%]$	$\sigma^{\text{tot}}_{t\bar{t}}(7\text{ TeV}), [\%]$	$R_{t\bar{t}(\text{tot 7 TeV})/Z(\text{fid 7 TeV})}$
BTAG			−0.41	−0.41
CTAG			0.027	0.03
DLUMI_7TeV	1.8	1.8	1.98	0.18
EBEAM	0.6	0.6	1.79	1.19
EG_RESOLUTION_ALL__1			−0.022	−0.02
EG_SCALE_ALL__1			0.213	0.21
EL_EFF_ID_Z7TeV		0.163		−0.08
EL_EFF_ID_ttbar			0.087	0.09
EL_EFF_Isott7TeV			0.59	0.59
EL_EFF_Reco_Z7TeV		0.205		−0.10
EL_EFF_Reco_ttbar			0.098	0.10
EL_EFF_Trig_COMBMCTOY__1		0.045		−0.02
EleScaleLArCalib		0.019		−0.01
EleScaleLArElecUnconv		0.036		−0.02
EleScaleMatCalo		−0.008		0.00
EleScaleMatCryo		−0.036		0.02
EleScaleMatID		−0.016		0.01
EleScalePS		0.018		−0.01
EleScaleS12		0.011		−0.01
ElecEnL1Gain		0.003		0.00
ElecEnL2Gain		0.026		−0.01
ElecEnLArElecCalib		−0.004		0.00
ElecEn_G4		−0.004		0.00
ElecEn_Pedestal		0.008		0.00
ElecEn_SamplingTerm		0.009		0.00
ElecEn_ZeeStat		0.018		−0.01
ElecEn_ZeeSyst		0.026		−0.01
Extrap_ME	−0.036	−0.002		0.02
Extrap_PS	−0.029	−0.028		0.03
Extrap_uncor	0.09	0.069		−0.08
FLOSR			0.268	0.27
FLSTAT1_7TeV			0.213	0.21
FLSTAT2_7TeV			0.027	0.03
GENIFSR			−0.301	−0.30
GENTT			1.432	1.43
GENVV			−0.115	−0.11
GENWT			−0.159	−0.16
JEFF			0	0.00
JESBJET			−0.044	−0.04
JESCBY			0.055	0.06
JESDET1			0.011	0.01
JESDET2			−0.005	−0.01
JESDET3			0	0.00
JESFCMP			0.213	0.21
JESFRES			0.115	0.11
JESFWD			0.027	0.03
JESFWDS			0.005	0.01
JESMIX1			−0.005	−0.01
JESMIX2			0.005	0.01
JESMODE1			0.044	0.04
JESMODE2			0.005	0.01
JESMODE3			0	0.00
JESMODE4			0	0.00
JESPMU			0.027	0.03
JESPT			0	0.00
JESPV			−0.022	−0.02
JESRHO			0	0.00
JESSNGL			0	0.00
JESSTAT1_7TeV			0.022	0.02
JESSTAT2_7TeV			0	0.00
JESSTAT3_7TeV			−0.005	−0.01
JET_JER_SINGLE_NP__1			−0.301	−0.30
JVF			−0.06	−0.06
LArUnconvCalib		−0.008		0.00
LEPTR			−0.186	−0.19
MCStatZ7TeV	0.023	0.038		−0.03
MISTAG			0.022	0.02
MUONS_ID__1	−0.001		0	0.00
MUONS_MS__1	−0.003		0	0.00
MUONS_SCALE__1	−0.028		−0.142	−0.13
MUON_EFF_ISO__1	0.147			−0.07
MUON_EFF_ISOtt7TeV			0.437	0.44
MUON_EFF_Rec_Z7TeV	0.303			−0.15
MUON_EFF_Reco_ttbar			0.306	0.31
MUON_EFF_SingleTrig__1	0.049			−0.02
NSTTSYS			−0.213	−0.21
PDFNNPDF30_nlo_as_0118_eigenset	0.069	0.09		−0.08
PDFtt			1.044	1.04
RZMSYS			0.049	0.05
SCALTT			−0.301	−0.30
TheoryME	−0.037	−0.027		0.03
TheoryPS	−0.224	−0.18		0.20
WTDRS			−0.213	−0.21
XSVV			0.027	0.03
XSWT			0.722	0.72
ZPTMismodel	−0.035	−0.006		0.02
AZ7TeV	1.78	1.78		1.78
BkgEWStat		0.002		0.00
DiBosZ	0.008	0.009		−0.01
MJBkg	0.069	0.028		−0.05
TopZ	0.007	0.008		−0.01
WBosZ	0	0		0.00
ZTauZ	0.003	0.003		0.00
tWt	0.001			0.00
Total Systematics	2.64	2.63	3.51	3.15
Stat	0.08	0.10	1.69	1.69
Total	2.64	2.63	3.89	3.57

Table J.3: Summary of the statistical, systematic and total uncertainties on the $\sigma^{\text{tot}}_{t\bar{t}}(8\text{ TeV})$ to $\sigma^{\text{tot}}_{Z}(8\text{ TeV})$ cross sections ratio.

Bibliography

[1] K. G. Wilson, *Confinement of Quarks*, *Phys. Rev.* **D10** (1974) 2445–2459.

[2] P. W. Higgs, *Broken Symmetries and the Masses of Gauge Bosons*, *Phys. Rev. Lett.* **13** (1964) 508–509.

[3] Super-Kamiokande Collaboration, Y. Fukuda et al., *Evidence for oscillation of atmospheric neutrinos*, *Phys. Rev. Lett.* **81** (Aug, 1998) 1562–1567.

[4] SNO Collaboration, Q. R. Ahmad et al., *Measurement of the rate of $\nu_e + d \to p + p + e^-$ interactions produced by ^8B solar neutrinos at the Sudbury Neutrino Observatory*, *Phys. Rev. Lett.* **87** (Jul, 2001) 071301.

[5] SNO Collaboration, Q. R. Ahmad et al., *Direct evidence for neutrino flavour transformation from neutral-current interactions in the Sudbury Neutrino Observatory*, *Phys. Rev. Lett.* **89** (Jun, 2002) 011301.

[6] Particle Data Group Collaboration, C. Patrignani et al., *Review of Particle Physics*, *Chin. Phys.* **C40** (2016), no. 10 100001.

[7] C. S. Wu, E. Ambler, R. W. Hayward, D. D. Hoppes, and R. P. Hudson, *Experimental test of parity conservation in beta decay*, *Phys. Rev.* **105** (Feb, 1957) 1413–1415.

[8] R. L. Garwin, L. M. Lederman, and M. Weinrich, *Observations of the failure of conservation of parity and charge conjugation in meson decays: the magnetic moment of the free muon*, *Phys. Rev.* **105** (Feb, 1957) 1415–1417.

[9] S. Weinberg, *A Model of Leptons*, *Phys. Rev. Lett.* **19** (1967) 1264–1266.

[10] A. S. J. Goldstone and S. Weinberg., *Broken Symmetries*, *Phys. Rev.* **127** (1962) 965970.

[11] S. L. Glashow, *Partial Symmetries of Weak Interactions*, *Nucl. Phys.* **22** (1961) 579–588.

[12] G. 't Hooft, *Renormalization of Massless Yang-Mills Fields*, *Nucl. Phys.* **B33** (1971) 173–199.

[13] G. 't Hooft, *Renormalizable Lagrangians for Massive Yang-Mills Fields*, *Nucl. Phys.* **B35** (1971) 167–188.

[14] R. Devenish and A. Cooper-Sarkar, "Deep inelastic Scattering." Oxford University Press, 2011.

[15] J. D. Bjorken, E. A. Paschos, *Inelastic Electron-Proton and γ-Proton Scattering and the Structure of the Nucleon*, *Phys. Rev.* **185**, (1969) 1975–1982.

[16] C. A. Dominguez, *Introduction to QCD sum rules*, *Mod. Phys. Lett.* **A28**, (2013) 1360002, [arXiv:1305.7047].

[17] T. Gleisberg, S. Hoeche, F. Krauss, M. Schonherr, S. Schumann, F. Siegert, and J. Winter, *Event generation with SHERPA 1.1*, *JHEP* **02** (2009) 007, [arXiv:0811.4622].

[18] Y. L. Dokshitzer, *Calculation of the Structure Functions for Deep Inelastic Scattering and e^+ e^- Annihilation by Perturbation Theory in Quantum Chromodynamics.*, *Sov. Phys. JETP* **46** (1977) 641–653. [Zh. Eksp. Teor. Fiz.73,1216(1977)].

[19] V. N. Gribov and L. N. Lipatov, *Deep inelastic e p scattering in perturbation theory*, *Sov. J. Nucl. Phys.* **15** (1972) 438–450. [Yad. Fiz.15,781(1972)].

[20] G. Altarelli and G. Parisi, *Asymptotic Freedom in Parton Language*, *Nucl. Phys.* **B126** (1977) 298–318.

[21] Particle Data Group Collaboration, *REVIEW OF PARTICLE PHYSICS*, *JP* **G37** (2010) 075021.

[22] "W.J. Stirling, private communication.", http://www.hep.ph.ic.ac.uk/~wstirlin/plots/plots.html.

[23] S. Alekhin, J. Blumlein, and S. Moch, *Parton Distribution Functions and Benchmark Cross Sections at NNLO*, *Phys. Rev.* **D86** (2012) 054009, [arXiv:1202.2281].

[24] H.-L. Lai et al., *New parton distributions for collider physics*, *Phys. Rev.* **D82** (2010) 074024, [hep-ph/1007.2241].

[25] A. D. Martin, W. J. Stirling, R. S. Thorne, and G. Watt, *Parton distributions for the LHC*, *Eur. Phys. J.* **C63** (2009) 189–285, [arXiv:0901.0002].

[26] R. D. Ball et al., *Parton distributions with LHC data*, *Nucl. Phys.* **B867** (2013) 244–289, [arXiv:1207.1303].

[27] ZEUS and H1 Collaborations, F. D. Aaron et al., *Combined Measurement and QCD Analysis of the Inclusive $e^{\pm}p$ Scattering Cross Sections at HERA*, *JHEP* **01** (2010) 109, [arXiv:0911.0884].

[28] M. Gluck, P. Jimenez-Delgado, and E. Reya, *Dynamical parton distributions of the nucleon and very small-x physics*, *Eur. Phys. J.* **C53** (2008) 355–366, [arXiv:0709.0614].

[29] S. D. et al., *The CT14 Global Analysis of Quantum Chromodynamics*, *Phys. Rev.* **D 93** (2016) 033006, [arXiv:1506.0744].

[30] J. Rojo et al., *The PDF4LHC report on PDFs and LHC data: Results from Run I and preparation for Run II*, *J. Phys.* **G42** (2015) 103103, [arXiv:1507.0055].

[31] S. Drell and T.-M. Yan, *Partons and their Applications at High-Energies*, *Annals Phys.* **66** (1971) 578.

[32] Andraz Lipanje, *Testing universality of lepton couplings*, Univerza v Ljubljani (2015).

[33] S. Catani, L. Cieri, G. Ferrera, D. de Florian, M. Grazzini, *Vector boson production at hadron colliders: a fully exclusive QCD calculation at NNLO*, *Phys. Rev. Lett.* **103** (2009) 08200 [arXiv: 0903.2120].

[34] S. Catani and M. Grazzini, *An NNLO subtraction formalism in hadron collisions and its application to Higgs boson production at the LHC*, *Phys. Rev. Lett.* **98** (2007) 222002, [arXiv:0703012].

[35] Y. Li and F. Petriello, *Combining QCD and electroweak corrections to dilepton production in FEWZ*, *Phys. Rev.* **D86** (2012) 094034, [arXiv:1208.5967].

[36] D. A. Kosower, *Antenna factorization in strongly ordered limits*, *Phys. Rev.* **D71** (2005) 045016.

[37] Particle Data Group Collaboration, J. Beringer et al., *Review of Particle Physics (RPP)*, *Phys. Rev.* **D86** (2012) 010001.

[38] R. Gavin, Y. Li, F. Petriello, and S. Quackenbush, *FEWZ 2.0: A code for hadronic Z production at next-to-next-to-leading order*, *Comput. Phys. Commun.* **182** (2011) 2388–2403, [arXiv:1011.3540].

[39] T. Binoth and G. Heinrich, *An automatized algorithm to compute infrared divergent multiloop integrals*, *Nucl. Phys.* **B585** (2000) 741–759, [arXiv:0004013].

[40] T. Hahn, *CUBA: A Library for multidimensional numerical integration*, *Comput. Phys. Commun.* **168** (2005) 78–95, [arXiv:0404043].

[41] M. R. Whalley, D. Bourilkov, and R. C. Group, *The Les Houches accord PDFs (LHAPDF) and LHAGLUE*, in *HERA and the LHC: A Workshop on the implications of HERA for LHC physics. Proceedings, Part B*, pp. 575–581, 2005. arXiv:0508110.

[42] "Lhapdf web-page." http://lhapdf.hepforge.org.

[43] M. Czakon and A. Mitov, *Top++: A program for the calculation of the top-pair cross-section at hadron colliders*, *Comput. Phys. Commun.* **185** (2014) 2930, [arXiv:1112.5675].

[44] M. Czakon, P. Fiedler, and A. Mitov, *Total Top-Quark Pair-Production Cross Section at Hadron Colliders Through $O(\frac{4}{S})$*, *Phys. Rev. Lett.* **110** (2013) 252004, [arXiv:1303.6254].

[45] M. Czakon and A. Mitov, *NNLO corrections to top pair production at hadron colliders: the quark-gluon reaction*, *JHEP* **01** (2013) 080, [arXiv:1210.6832].

[46] M. Czakon and A. Mitov, *NNLO corrections to top-pair production at hadron colliders: the all-fermionic scattering channels*, *JHEP* **12** (2012) 054, [arXiv:1207.0236].

[47] P. Brnreuther, M. Czakon, and A. Mitov, *Percent Level Precision Physics at the Tevatron: First Genuine NNLO QCD Corrections to $q\bar{q} \to t\bar{t} + X$*, *Phys. Rev. Lett.* **109** (2012) 132001, [arXiv:1204.5201].

[48] M. Beneke, P. Falgari, and C. Schwinn, *Soft radiation in heavy-particle pair production: All-order colour structure and two-loop anomalous dimension*, *Nucl. Phys.* **B828** (2010) 69–101, [arXiv:0907.1443].

[49] M. Czakon, A. Mitov, and G. F. Sterman, *Threshold Resummation for Top-Pair Hadroproduction to Next-to-Next-to-Leading Log*, *Phys. Rev.* **D80** (2009) 074017, [arXiv:0907.1790].

[50] P. M. Nadolsky and Z. Sullivan, *PDF uncertainties in WH production at Tevatron*, *eConf* **C010630** (2001) P510, [arXiv:0110378].

[51] NNPDF Collaboration, R. D. Ball, V. Bertone, F. Cerutti, L. Del Debbio, S. Forte, A. Guffanti, J. I. Latorre, J. Rojo, and M. Ubiali, *Unbiased global determination of parton distributions and their uncertainties at NNLO and at LO*, *Nucl. Phys.* **B855** (2012) 153–221, [arXiv:1107.2652].

[52] D. Bardin, S. Bondarenko, P. Christova, L. Kalinovskaya, L. Rumyantsev, A. Sapronov, and W. von Schlippe, *SANC integrator in the progress: QCD and EW contributions*, *JETP Lett.* **96** (2012) 285–289, [arXiv:1207.4400].

[53] Particle Data Group Collaboration, K. A. Olive et al., *Review of Particle Physics*, *Chin. Phys.* **C38** (2014) 090001.

[54] ATLAS Collaboration, M. Aaboud et al., *Precision measurement and interpretation of inclusive W^+ , W^- and Z/γ^* production cross sections with the ATLAS detector*, *Eur. Phys. J.* **C77** (2017), [arXiv:1612.03016].

[55] Particle Data Group Collaboration, H. Ogul et al., *High order QCD predictions for inclusive production of W bosons in pp collisions at $\sqrt{s} = 13$ TeV*, *Advances in High Energy Physics* (2016).

[56] NNPDF Collaboration, R. D. Ball et al., *Parton distributions for the LHC Run II*, *JHEP* **04** (2015) 040, [arXiv:1410.8849].

[57] L. A. Harland-Lang, A. D. Martin, P. Motylinski, and R. S. Thorne, *Parton distributions in the LHC era: MMHT 2014 PDFs*, *Eur. Phys. J.* **C75** (2015), no. 5 204, [arXiv:1412.3989].

[58] S. Alekhin, J. Bluemlein, and S. Moch, *The ABM parton distributions tuned to LHC data*, *Phys. Rev.* **D89** (2014), no. 5 054028, [arXiv:1310.3059].

[59] ZEUS, H1 Collaboration, H. Abramowicz et al., *Combination of measurements of inclusive deep inelastic $e^{\pm}p$ scattering cross sections and QCD analysis of HERA data*, *Eur. Phys. J.* **C75** (2015), no. 12 580, [arXiv:1506.0604].

[60] ATLAS Collaboration, ATLAS Collaboration, *Determination of the strange quark density of the proton from ATLAS measurements of the $W \to \ell\nu$ and $Z \to \ell\ell$ cross sections*, *Phys. Rev. Lett.* **109** (2012) 012001, [arXiv:1203.4051].

[61] ATLAS Collaboration, G. Aad et al., *Simultaneous measurements of the $t\bar{t}$, W^+W^-, and $Z/\gamma^* \to \tau\tau$ production cross-sections in pp collisions at $\sqrt{s} = 7$ TeV with the ATLAS detector*, *Phys. Rev.* **D91** (2015), no. 5 052005, [arXiv:1407.0573].

[62] S. Alekhin et al., *HERAFitter*, *Eur. Phys. J.* **C75** (2015), no. 7 304, [arXiv:1410.4412].

[63] "xfitter web-page." https://www.xfitter.org/xFitter/xFitter.

[64] M. Ciafaloni, *Coherence Effects in Initial Jets at Small q**2 / s*, *Nucl. Phys.* **B296** (1988) 49–74.

[65] F. James and M. Roos, *Minuit: A System for Function Minimization and Analysis of the Parameter Errors and Correlations*, *Comput. Phys. Commun.* **10** (1975) 343–367.

[66] M. Botje, *Error estimates on parton density distributions*, *J. Phys.* **G28** (2002) 779–790, [`arXiv:0110123`].

[67] W. T. Giele and S. Keller, *Implications of hadron collider observables on parton distribution function uncertainties*, *Phys. Rev.* **D58** (1998) 094023, [`arXiv:9803393`].

[68] H. Paukkunen and P. Zurita, *PDF reweighting in the Hessian matrix approach*, *JHEP* **12** (2014) 100, [`arXiv:1402.6623`].

[69] HERAFitter developers' Team Collaboration, S. Camarda et al., *QCD analysis of W- and Z-boson production at Tevatron*, *Eur. Phys. J.* **C75** (2015), no. 9 458, [`arXiv:1503.0522`].

[70] F. D. Aaron et al., *Measurement of the Inclusive ep Scattering Cross Section at Low Q^2 and x at HERA*, *Eur. Phys. J.* **C 63** (2009) 625, [`arXiv:0904.0929`].

[71] J. Gao, M. Guzzi, J. Huston, H.-L. Lai, Z. Li, P. Nadolsky, J. Pumplin, D. Stump, and C. P. Yuan, *CT10 next-to-next-to-leading order global analysis of QCD*, *Phys. Rev.* **D89** (2014), no. 3 033009, [`arXiv:1302.6246`].

[72] ATLAS Collaboration, G. Aad et al., *Measurement of the inclusive $W^{\pm}$ and Z/gamma cross sections in the electron and muon decay channels in pp collisions at $\sqrt{s} = 7$ TeV with the ATLAS detector*, *Phys. Rev.* **D85** (2012) 072004, [`arXiv:1109.5141`].

[73] CMS Collaboration, S. Chatrchyan et al., *Measurement of the Inclusive W and Z Production Cross Sections in pp Collisions at $\sqrt{s} = 7$ TeV*, *JHEP* **10** (2011) 132, [`arXiv:1107.4789`].

[74] CMS Collaboration, S. Chatrchyan et al., *Measurement of inclusive W and Z boson production cross sections in pp collisions at $\sqrt{s} = 8$ TeV*, *Phys. Rev. Lett.* **112** (2014) 191802, [`arXiv:1402.0923`].

[75] ATLAS Collaboration, ATLAS Collaboration, *Measurement of the $t\bar{t}$ production cross-section using $e\mu$ events with b-tagged jets in pp collisions at $\sqrt{s} = 7$ and 8 TeV with the ATLAS detector*, *Eur. Phys. J.* **C74** (2014) no.10, 3109, Addendum: *Eur. Phys. J.* **C76** (2016) no.11, 642, `arXiv:1406.5375`.

[76] UA1 Collaboration, G. Arnison et al., *Experimental Observation of Isolated Large Transverse Energy Electrons with Associated Missing Energy at s**(1/2) = 540-GeV*, *Phys. Lett.* **122B** (1983) 103–116.

[77] UA2 Collaboration, M. Banner et al., *Observation of Single Isolated Electrons of High Transverse Momentum in Events with Missing Transverse Energy at the CERN anti-p p Collider*, *Phys. Lett.* **122B** (1983) 476–485.

[78] UA1 Collaboration, G. Arnison et al., *Experimental Observation of Lepton Pairs of Invariant Mass Around 95-GeV/c**2 at the CERN SPS Collider*, *Phys. Lett.* **126B** (1983) 398–410.

[79] CDF Collaboration, F. Abe et al., *Observation of top quark production in pp collisions with the collider detector at Fermilab*, *Phys. Rev. Lett.* **74** (1995) 26262631.

[80] D0 Collaboration, S. Abachi et al., *Observation of the top quark*, *Phys. Rev. Lett.* **74** (1995), 2632-2637.

[81] Particle Data Group Collaboration, W-M Yao et al., *Review of Particle Physics*, *J. Phys. G: Nucl. Part. Phys.* **33** (2006), 1232.

[82] ATLAS Collaboration, G. Aad et al., *Observation of a new particle in the search for the Standard Model Higgs boson with the ATLAS detector at the LHC*, *Phys. Lett.* **B716** (2012) 1–29, [arXiv:1207.7214].

[83] CMS Collaboration, S. Chatrchyan et al., *Observation of a new boson at a mass of 125 GeV with the CMS experiment at the LHC*, *Phys. Lett.* **B716** (2012) 30–61, [arXiv:1207.7235].

[84] O. S. Bruning, P. Collier, P. Lebrun, S. Myers, R. Ostojic, J. Poole, and P. Proudlock, *LHC Design Report Vol.1: The LHC Main Ring*, .

[85] L. Evans and P. Bryant, *LHC Machine*, *JINST* **3** (2008) S08001.

[86] ATLAS Collaboration, G. Aad et al., *The ATLAS Experiment at the CERN Large Hadron Collider*, *JINST* **3** (2008) S08003.

[87] CMS Collaboration, S. Chatrchyan et al., *The CMS Experiment at the CERN LHC*, *JINST* **3** (2008) S08004.

[88] LHCb Collaboration, A. A. Alves, Jr. et al., *The LHCb Detector at the LHC*, *JINST* **3** (2008) S08005.

[89] LHCf Collaboration, O. Adriani et al., *The LHCf detector at the CERN Large Hadron Collider*, *JINST* **3** (2008) S08006.

[90] K. K. Phua, L. C. Kwek, N. P. Chang, and A. H. Chan, eds., *Proceedings, Conference in Honor of the 90th Birthday of Freeman Dyson*, (Singapore), World Scientific, World Scientific, 2014.

[91] TOTEM Collaboration, G. Anelli et al., *The TOTEM experiment at the CERN Large Hadron Collider*, *JINST* **3** (2008) S08007.

[92] ALICE Collaboration, K. Aamodt et al., *The ALICE experiment at the CERN LHC*, *JINST* **3** (2008) S08002.

[93] C. Lefvre, "The CERN accelerator complex. Complexe des acclrateurs du CERN." Dec, 2008.

[94] *"The accelerator complex web-page."* `https://home.cern/about/accelerators`.

[95] J. Pequenao, *"Computer generated image of the whole ATLAS detector"*, CERN-GE-0803012, 2008.

[96] G. Aad et al., *ATLAS pixel detector electronics and sensors*, *JINST* **3** (2008) P07007.

[97] H. Pernegger on behalf of the ATLAS Pixel collaboration, *The Pixel Detector of the ATLAS experiment for LHC Run-2*, *JINST* **10** (2014) C06012.

[98] A. Miucci, *The ATLAS Insertable B-Layer project*, *JINST* **9** (2014) C02018.

[99] T. A. T. collaboration, *The ATLAS Transition Radiation Tracker (TRT) proportional drift tube: design and performance*, *JINST* **3** (2008) P02013.

[100] ATLAS Collaboration, *ATLAS liquid-argon calorimeter: Technical Design Report.* Technical Design Report ATLAS. CERN, Geneva (1996).

[101] J. Pequenao, *"Computer Generated image of the ATLAS calorimeter"*, CERN-GE-0803015, 2008.

[102] ATLAS Collaboration, G. Aad et al., *Commissioning of the ATLAS Muon Spectrometer with Cosmic Rays*, *Eur. Phys. J.* **C70** (2010) 875–916, [`arXiv:1006.4384`].

[103] ATLAS Collaboration, M. Aaboud et al., *Performance of the ATLAS Trigger System in 2015*, *Eur. Phys. J.* **C77** (2017), no. 5 317, [`arXiv:1611.0966`].

[104] A. Collaboration, *FTK: A Hardware Real-Time Track Finder for the ATLAS Trigger System*, Tech. Rep. ATL-DAQ-PROC-2016-006, CERN, Geneva, Mar, 2016.

[105] M. Shochet, L. Tompkins, V. Cavaliere, P. Giannetti, A. Annovi, and G. Volpi, *Fast TracKer (FTK) Technical Design Report*, Tech. Rep. CERN-LHCC-2013-007, ATLAS-TDR-021, Jun, 2013.

[106] *"GRL package web-page"*, `https://twiki.cern.ch/twiki/bin/view/Atlas/GoodRunsLists`.

[107] *"The ATLAS ATHENA framework"*, `https://twiki.cern.ch/twiki/bin/view/AtlasComputing/WorkBookAthenaFramework`.

[108] *"Analysis good-run list web-page"*, `https://twiki.cern.ch/twiki/bin/viewauth/AtlasProtected/GoodRunListsForAnalysis`.

[109] ATLAS Collaboration, "Summary of ATLAS Pythia 8 tunes", ATL-PHYS-PUB-2012-003, 2012.

[110] *"MC15a web page"*, `https://twiki.cern.ch/twiki/bin/view/AtlasProtected/AtlasProductionGroupMC15a#Production_details_for_MC15a`.

[111] *"MC15b web page"*, `https://twiki.cern.ch/twiki/bin/view/AtlasProtected/AtlasProductionGroupMC15b`.

[112] S. Agostinelli et al., *GEANT4: A Simulation toolkit*, *Nucl. Instrum. Meth.* **A506** (2003) 250.

[113] P. Nason, *A New method for combining NLO QCD with shower Monte Carlo algorithms*, *JHEP* **11** (2004) 040, [`arXiv:0409146`].

[114] S. Frixione and C. Oleari, *Matching NLO QCD computations with Parton Shower simulations: the POWHEG method*, *JHEP* **1** (2007) 070, [`arXiv:0709.2092`].

[115] S. Alioli, P. Nason, C. Oleari, E. Re, *A general framework for implementing NLO calculations in shower Monte Carlo programs: the POWHEG BOX*, *JHEP* **06** (2010) 043, [`arXiv:1002.2581`].

[116] T. Sjöstrand, S. Mrenna, P. Skands, *A Brief Introduction to PYTHIA 8.1*, *Comput. Phys. Commun.* **178** (2008) 852, [`arXiv:0710.3820`].

[117] ATLAS Collaboration, *Measurement of the Z/γ^* boson transverse momentum distribution in pp collisions at $\sqrt{s} = 7$ TeV with the ATLAS detector*, *JHEP* **1409** (2014) 145, [`arXiv:1406.3660`].

[118] D. J. Lange, *The EvtGen particle decay simulation package*, *Nucl. Instrum. Meth.* **A462** (2001) 152.

[119] T. Przedzinski and Z. Was, *Photos interface in C++: Technical and physics documentation*, arXiv:1011.0937.

[120] T. Gleisberg, S. Hoeche, F. Krauss, M. Schoenherr, S. Schumann, F. Siegert, J. Winter., *Event generation with SHERPA 1.1*, *JHEP* **02** (2009) 007, [arXiv:0811.4622].

[121] P. Z. Skands, *Tuning Monte Carlo Generators: The Perugia Tunes*, *Phys. Rev.* **D 82** (2010) 074018, [arXiv:1005.3457].

[122] ATLAS Collaboration, *Summary of ATLAS Pythia 8 tunes*, *Comput. Phys. Commun.* [ATLAS-PHYS-PUB-2012-003].

[123] S. M. T. Sjöstrand and P. Z. Skands, *PYTHIA 6.4 Physics and Manual*, *JHEP* **05** (2006) 026, [arXiv:0603175].

[124] N. Zakharchuk, "Measurement of Z-boson production cross sections at $\sqrt{s} = 13$ TeV and $t\bar{t}$ to Z-boson cross-section ratios with the ATLAS detector at the LHC." Ph.D. thesis, Hamburg University, Hamburg, 2017.

[125] J. Wenninger, *Energy Calibration of the LHC Beams at 4 TeV*, CERN-ATS-2013-040.

[126] ATLAS Collaboration, *Performance of the ATLAS Track Reconstruction Algorithms in Dense Environments in LHC run 2*, arXiv:1704.0798.

[127] T. Cornelissen et al., *The new ATLAS track reconstruction (NEWT)*, *J. Phys. Conf.* **Ser. 119** (2008).

[128] A. Rosenfeld and J. Faltz, *Sequential Operations in Digital Picture Processing*, *J. ACM* **13** (1966) 471.

[129] R. Frhwirth, *Application of Kalman Filtering to Track and Vertex Fitting*, *Nucl. Instrum. Meth.* **A 262** (1987) 444.

[130] ATLAS Collaboration, *A neural network clustering algorithm for the ATLAS silicon pixel detector*, *JINST* **9** (2014) P09009, [arXiv:1406.7690].

[131] P. Akesson, T. Atkinson, M. Costa, M. Elsing, S. Fleischmann, A. Gaponenko, W. Liebig, E. Moyse, A. Salzburger, M. Siebel, *ATLAS Tracking Event Data Model*, ATL-SOFT-PUB-2006-004, 2006.

[132] G. Piacquadio, K. Prokofiev, A. Wildauer, *Primary Vertex Reconstruction in the ATLAS Experiment at LHC*, *J. Phys.* **Conf. Ser. 119** (2008) 032033.

[133] Eva Bouhova-Thacker et al., *Expected Performance of Vertex Reconstruction in the ATLAS Experiment at the LHC*, *IEEE* **VOL. 57, NO. 2** (2010) 760 – 767.

[134] C. Patrignani et al., *Particle Data Group*, *Chin. Phys. C* **40** (2016) 100001.

[135] *"Track to vertex association tool"*, `https://twiki.cern.ch/twiki/bin/view/AtlasProtected/TrackVertexAssociationTool`.

[136] *"e/γ software for electron reconstruction"*, `https://twiki.cern.ch/twiki/bin/viewauth/AtlasProtected/EGammaSoftware`.

[137] W. Lampl et al., *"Calorimeter Clustering Algorithms: Description and Performance"*, ATL-LARG-PUB-2008-002, 2008.

[138] R. Fruhwirth, *A Gaussian-mixture approximation of the Bethe-Heitler model of electron energy loss by bremsstrahlung*, *Comput. Phys. Commun.* **154** (2003) 131.

[139] ATLAS Collaboration, *"Improved electron reconstruction in ATLAS using the Gaussian Sum Filter-based model for bremsstrahlung"*, ATLAS-CONF-2012-047, 2003.

[140] *"Emtrackmatchbuilder software for matching tracks in inner detector to electromagnetic clusters"*, `http://acode-browser.usatlas.bnl.gov/lxr/source/athena/Reconstruction/egamma/egammaTools/src/EMTrackMatchBuilder.cxx`.

[141] *"Photon conversion vertices finder tool (version 00-04-12)"*, `https://svnweb.cern.ch/trac/atlasoff/browser/InnerDetector/InDetRecTools/InDetConversionFinderTools/tags/InDetConversionFinderTools-00-04-12`.

[142] *"Egamma ambiguity tool (e/γ software)"*, `https://twiki.cern.ch/twiki/bin/view/AtlasProtected/EGammaIdentificationRun2#Using_the_Ambiguity_tool_in_anal`.

[143] ATLAS Collaboration, *"Electron efficiency measurements with the ATLAS detector using the 2015 LHC proton-proton collision data"*, ATLAS-CONF-2016-024, 2016.

[144] *"Lepton isolation selection tool"*, `https://twiki.cern.ch/twiki/bin/view/AtlasProtected/IsolationSelectionTool#Current_official_working_points`

[145] R. Achenbach et al., *Upgrades to the ATLAS Level-1 Calorimeter Trigger*, *JINST* **3** (2008) P03001.

[146] ATLAS Collaboration, *Performance of the ATLAS Trigger System in 2015*, [arXiv:1611.0966].

[147] *"Trigger recommendations for electron selection"*, https://twiki.cern.ch/twiki/bin/view/Atlas/TrigEgammaRecommendedTriggers2015.

[148] *"Electron trigger matching tool"*, https://twiki.cern.ch/twiki/bin/view/Atlas/TrigEgammaAnalysisTools#Trigger_Matching

[149] ATLAS Collaboration, *Performance of the ATLAS Silicon Pattern Recognition Algorithm in Data and Simulation at $\sqrt{s} = 7$ TeV*, ATLAS-CONF-2010-072, 2010.

[150] J. Illingworth and J. Kittler, *A survey of the Hough transform*, *Computer Vision, Graphics, and Image Processing archive* **44** (1988) 87-116.

[151] ATLAS Collaboration, *Muon reconstruction performance of the ATLAS detector in protonproton collision data at $\sqrt{s} = 13$ TeV*, arXiv:1603.0559.

[152] *"Muon trigger matching tool web-page"*, https://twiki.cern.ch/twiki/bin/view/AtlasProtected/MCPAnalysisGuidelinesMC15#Muon_trigger_matching.

[153] R. J. Barlow and C. Beeston, *R. J. Barlow and C. Beeston*, "*Fitting using finite Monte Carlo samples*", *Comput. Phys. Commun.* **77** (1993) 219.

[154] ATLAS Collaboration, "*Measurement of the W and Z-boson cross section and cross-section ratios at $\sqrt{s} = 13$ TeV*", ATL-COM-PHYS-2015-1308, 2015.

[155] ATLAS Collaboration, "*Measurement and QCD analysis of differential inclusive $W^{\pm} \to \ell\nu$ and $Z \to \ell\ell$ production and leptonic decay cross sections with ATLAS*", ATL-COM-PHYS-2013-217, 2013.

[156] "*Electron efficiency scale factors, Run II pre-recommendations*", https://twiki.cern.ch/twiki/bin/view/AtlasProtected/ElectronEfficiencyRun2.

[157] "*Pile-up re-weighting web-page, Run II pre-recommendations*", https://twiki.cern.ch/twiki/bin/view/AtlasProtected/PileupReweighting.

[158] "*Proposal for pileup re-weighting*", https://indico.cern.ch/event/437993/contribution/1/attachments/1138739/1630981/spagan_MuRescaling.pdf.

[159] "*Muon efficiency scale factors, run 2 pre-recommendations, muon CP group web-page*", `https://twiki.cern.ch/twiki/bin/view/AtlasProtected/MuonPerformance#AnchorReconstruction`.

[160] ATLAS Collaboration, "*Muon reconstruction performance in ATLAS at $\sqrt{s} = 13$ TeV*", ATL-COM-PHYS-2015-1149, 2015.

[161] ATLAS Collaboration, "*Measurement of the transverse momentum and ϕ^*_η distributions of Drell-Yan lepton pairs in proton-proton collisions at $\sqrt{s} = 8$ TeV with the ATLAS detector*", *Eur. Phys. J.* **C 76(5)** (2016) 1-61, [`arXiv:1512.02192`].

[162] ATLAS Collaboration, "*Jet Calibration and Systematic Uncertainties for Jets Reconstructed in the ATLAS Detector at $\sqrt{s} = 13$ TeV*", ATL-PHYS-PUB-2015-015, 2015.

[163] ATLAS Collaboration, *Measurements of top-quark pair to Z-boson cross-section ratios at $\sqrt{s} = 13, 8, 7$ TeV with the ATLAS detector*, *JHEP* **02** (2017) 117, [`arXiv:1612.03636`].

[164] A. Glazov, "*Averaging of DIS cross section data*", AIP Conf. Proc. 792, 2005.

[165] A. Glazov et al., "*Heraverager, Data combination package, Manual*", 2015.

[166] J. Dassoulas, "Measurement of Z Boson production with the ATLAS Experiment at the LHC." Ph.D. thesis, Hamburg University, Hamburg, 2014.

[167] ATLAS Collaboration, *Measurement of $W^\pm$ and Z-boson production cross sections in pp collisions at $\sqrt{s} = 13$ TeV with the ATLAS detector*, *Phys. Lett. B* **759** (2016) 601, [`arXiv:1603.09222`].

[168] K. A. Olive et al, *Review of Particle Physics*, *Chin. Phys. C* **38** (2014) 090001.

[169] The ALEPH, DELPHI, L3, OPAL Collaborations, the LEP Electroweak Working Group, *Electroweak Measurements in Electron-Positron Collisions at W-Boson-Pair Energies at LEP*, *Phys. Rept.* **532** (2013) 119, [`arXiv:1302.3415`].

[170] UA1 Collaboration, C. Albajar et al., *Intermediate Vector Boson Cross-Sections at the CERN Super Proton Synchrotron Collider and the Number of Neutrino Types*, DOI: 10.1016/0370-2693(87)91510-3.

[171] UA2 Collaboration, J. Alitti et al., *A measurement of the W and Z production cross sections and a determination of Γ_W at the CERN $p\bar{p}$ collider*, DOI: 10.1016/0370-2693(92)90333-Y.

[172] CDF Collaboration, A. Abulencia et al., *Measurements of inclusive W and Z cross sections in p anti-p collisions at s**(1/2) = 1.96-TeV*, [arXiv:0508029].

[173] DO Collaboration, V. Abazov. et al., *Measurement of the Cross Section for W and Z Production to Electron Final States with the D0 Detector at* $\sqrt{s} = 1.96$ *TeV*, 4403-CONF and 4750-CONF.

[174] PHENIX Collaboration, A. Adare. et al., *Cross Section and Parity Violating Spin Asymmetries of $W^{\pm}$ Boson Production in Polarized $p + p$ Collisions at* $\sqrt{s} = 500$ *GeV*, DOI: 10.1103/PhysRevLett.106.062001,[arXiv:1009.0505].

[175] ATLAS Collaboration, *Measurement of the $t\bar{t}$ production cross-section using $e\mu$ events with b-tagged jets in pp collisions at* $\sqrt{s} = 13$ *TeV with the ATLAS detector*, *Phys.Lett.* **B761** (2016) 136, [arXiv:1606.02699].

[176] ATLAS Collaboration, *Measurement of the $t\bar{t}$ production cross-section in pp collisions at* $\sqrt{s} = 13$ *TeV using $e\mu$ events with b-tagged jets*, ATLAS-CONF-2015-033.

[177] ATLAS Collaboration, *Measurements of the $t\bar{t}$ production cross-section in the dilepton and lepton-plus-jets channels and of the ratio of the $t\bar{t}$ and Z boson cross-sections in pp collisions at* $\sqrt{s} = 13$ *TeV with the ATLAS detector*, ATLAS-CONF-2015-049

[178] ATLAS Collaboration, *Determination of the strange quark density of the proton from ATLAS measurements of the $W \to \ell\nu$ and $Z \to \ell\ell$ cross sections*, *Phys. Rev. Lett.* **109** (2012) 012001, [arXiv:1203.4051].

Acknowledgements

This work would not have been possible without the help and support of a lot of people, whom I would like to thank here.

First of all I would like to thank my supervisor Alexander Glazov for guidance and support during my PhD. I am grateful for regular discussions and countless help during the first steps in the analysis. You showed me how to work both in a group, relying on other people, and autonomous, taking decisions by myself. Thank you for introducing me to the ATLAS Standard Model community and giving the opportunity to prove myself.

I am very pleased to thank my supervisor for hardware-related work, Ingrid-Maria Gregor, who opened the word of particle detectors for me. Thank you for organizing the work in the best and most effective way. Also thank you for fruitful discussions of the physical results which lead to choosing the vector of the next steps in measurements.

I would like to thank Manuella Vincter with whom I had a great pleasure to work. You played a role of "mammy" in our W, Z family during both analyses that I was involved. Thank you for pushing our results to publication and providing a lot of inspiration on this way. Also I want to thank members our W, Z family in the person of Nataliia Zakharchuk, Ludovica Aperio Bella, Federico Sforza, Chiara Debenedetti, Hayk Pirumov, and Ulla Blumenschein without whom these results would not be possible. I am very thankful to Richard Hawkings and Barbara Alvarez Gonzalez for very productive meetings and discussions of $t\bar{t}$ and Z analyses synchronization and constructing the correlation model.

I want to express my appreciation to Dario Ariza and Ulrich Kötz for help during my work in the laboratory. Moreover, I want to thank Kerstin Tackmann and Eda Yildirim for efficient discussions of the measured results. I am also grateful to Philip Sommer and Kristin Lohwasser for introduction to me the methods for efficiency scale factors estimation in the $e\gamma$ group.

Apart from written above I also want to reiterate the profound gratitude to Ingrid-Maria Gregor as a leader of the ATLAS group at DESY for creation a friendly spirit in the group and approving all my work-related travels to different institutions and collaborations, where I contacted many interesting people and gain a lot of experience.

In addition to scientific research I spend time with my friends doing sport activities, hiking, travelling, and discussing different topics. Therefore, I want to thank V. Libov, N. Bartosik, R. Shevchenko, V. Myronenko, A. Singh, A. Martinez, and many others for the great time spent with you.

I am very grateful to all my family for the constant support. Thank you for always believing in me, being proud of me, loving me unconditionally.

Eidesstattliche Versicherung

Hiermit erkläre ich an Eides statt, dass ich die vorliegende Dissertationsschrift selbst verfasst und keine anderen als die angegebenen Quellen und Hilfsmittel benutzt habe.

Declaration on oath

I hereby declare, on oath, that I have written the present dissertation by my own and have not used other than the acknowledged resources and aids.

Hamburg, October 2017